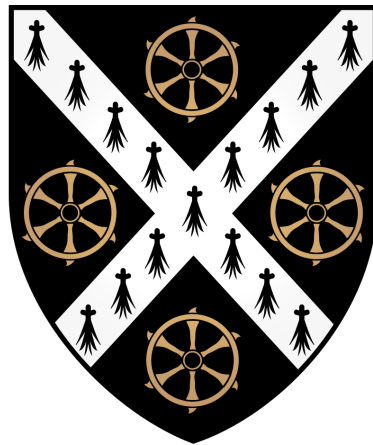


Studies for Upgrading and Optimising the CLEAR
Beamline, and Generating Uniform Electron-Beam
Profiles for Irradiation Experiments



Luke Aidan Dyks
St. Catherine's College, Oxford

Thesis submitted in fulfilment of the requirements for the degree of Doctor
of Philosophy at the University of Oxford

Trinity Term, 2022

Abstract

Irradiation facilities around the world are used to investigate the effect of high-energy particle beams on electronics, to study the makeup of historical objects and art, and for medical applications, notably radiotherapy. The CERN Linear Electron Accelerator for Research (CLEAR) is an irradiation facility that produces 200 MeV beams of electrons with parameters tuned to the needs of users.

One of the most commonly requested beam parameters is for bunch lengths of less than 1 ps, which was not previously possible for high-charge bunches. In this thesis, the ability to compress high-charge bunches to sub-ps bunch lengths, using the velocity bunching technique, is shown in simulation. The simulations are then verified with experimental measurements taken at CLEAR. The ability to reduce the emittance of the beam during compression is also presented.

Potential upgrades to the CLEAR facility are proposed, namely a new laser system and the installation of an additional klystron. The benefits of these upgrades are explored in simulation, demonstrating that they would allow the production of shorter bunches, with lower energy spread, and lower emittance.

It is shown that by using a modified version of the CLEAR photoinjector it is possible to produce bunches with a uniform transverse profile using a simple Gaussian laser with a 1 ps pulse length. A compact irradiation facility was proposed consisting of the CLEAR photoinjector, an X-band linac using cavities similar to those developed for the Compact Linear Collider, and a quadrupole matching section. It was shown that such a facility could produce beams of different sizes with uniform beam profiles. The stability of such a facility was investigated, demonstrating that beam jitters do not significantly reduce beam uniformity.

To me really, I wrote the damn thing.

Acknowledgements

If I'm totally honest, at the outset of my DPhil I didn't really believe that I'd be able to pay attention for a long enough period of time to get the damn thing written down! It's only been through the support of others that I've been able to achieve this.

First and foremost there are my two supervisors, Phil Burrows and Roberto Corsini. I'd like to thank both for allowing the freedom to let my creativity run wild, whilst keeping me on the right path. As well as my supervisors, there are many other colleagues that I'd like to thank. Much of this thesis would not have been possible without the sorcerer of simulation that is Andrea Latina. Then there's the CLEAR team, Wilfrid Farabolini, Pierre Korysko, Antonio Gilardi, Kyrre Sjøbæk, Davide Gamba, Joe Bateman, Cameron Robertson and Vilde Rieker. Additionally my progression as a scientist has been greatly mentored by Manjit Dosanjh and Steinar Stapnes. Finally there's the rest of the old FONT group at Oxford, who's help, particularly in the early part of my DPhil, was vital.

Of course, none of my work would have been possible without my friends providing me with a release, particularly during the living hell that was the Covid lockdown. I don't think that it will be possible to get round to all of you, but here are a few people I'd particularly like to thank. Firstly, Danielle Hodgkinson, I hope that I've managed to be as supportive to you in your PhD journey as you've been to mine. Then there's my former housemates, Rebecca Ramjiawan and Sophie Moualed, thank you for putting up with my eccentricities! Then there's all of the CERN people who've allowed me to be my loud, annoying self, so I'd like to thank Hans Baechle, Adam Powell, Adam Rennie, Savannah Clawson, and Victor Guillen. I'd also like to thank my overseas friends for their support. In particular, Lauren Rhodes, Tom Fox, Charlotte Cooke, Leo Carella, Andy Bees, and George Dobson.

Although these friends have helped so much, it's nothing compared to the support I've received from my family. So to my Mum, Dad, and even my brother, thank you.

I'm sure I've forgotten people. If your name is missing, I blame the general state of sleep deprivation that I live in. But seriously, thank you. I hope that you all continue to travel with me on the chaotic roller-coaster that is my life.

Contents

| | | |
|----------|--|-----------|
| 1 | Introduction | 1 |
| 1.1 | The Standard Model | 1 |
| 1.2 | Particle Accelerators and Colliders | 3 |
| 1.2.1 | Particle Accelerators | 3 |
| 1.2.2 | Colliders | 5 |
| 1.2.3 | Proposed Future Colliders | 7 |
| 1.3 | The Compact Linear Collider | 8 |
| 1.3.1 | Physics Potential | 8 |
| 1.3.2 | CLIC Accelerator Technology | 12 |
| 1.3.3 | Implementation of CLIC | 14 |
| 1.4 | The CLEAR User Facility | 14 |
| 1.5 | Very High Energy Electron Radiotherapy | 20 |
| 1.5.1 | The Present State of Radiotherapy | 20 |
| 1.5.2 | Very High Energy Radiotherapy | 23 |
| 1.6 | FLASH Radiotherapy | 25 |
| 1.6.1 | Status of FLASH Radiotherapy | 25 |
| 1.6.2 | Mechanisms and Beam Characteristics | 26 |
| 1.6.3 | Translation of FLASH to the Clinic | 29 |
| 1.7 | Thesis Outline | 30 |
| 2 | Beam Dynamics | 31 |
| 2.1 | Coordinate System | 31 |
| 2.2 | Transverse beam dynamics | 32 |
| 2.2.1 | Single Particle Motion | 32 |
| 2.2.2 | Motion of Beams | 33 |

| | | |
|----------|--|------------|
| 2.3 | Velocity Bunching | 34 |
| 2.4 | RF Photoinjectors | 35 |
| 2.4.1 | Emittance Growth in a Photoinjector | 36 |
| 3 | Beam Dynamics in the CLEAR Linac | 38 |
| 3.1 | Beamline Components | 38 |
| 3.1.1 | CLEAR Injector | 38 |
| 3.1.2 | Experimental Beamline | 41 |
| 3.1.3 | Measurement of Bunch Length | 43 |
| 3.2 | User Requirements | 45 |
| 3.3 | ASTRA Model of CLEAR | 48 |
| 3.4 | Bunch Compression | 51 |
| 3.4.1 | RF Gun | 52 |
| 3.4.2 | Bunching Cavity | 59 |
| 3.4.3 | Emittance Growth Compensation | 64 |
| 3.4.4 | Experimental Verification of Compression | 66 |
| 3.4.5 | Compression at Reduced Gun Phases | 69 |
| 3.5 | Summary | 74 |
| 4 | Potential Upgrades to CLEAR | 76 |
| 4.1 | Reduced laser pulse length | 76 |
| 4.1.1 | RF Gun | 78 |
| 4.1.2 | Bunching Cavity | 82 |
| 4.2 | Additional Klystron | 85 |
| 4.2.1 | Reduced Buncher Field | 86 |
| 4.2.2 | Higher Gun Field | 93 |
| 4.3 | Summary | 105 |
| 5 | Generation of Uniform Beam Profiles | 109 |
| 5.1 | Defining Uniformity | 110 |
| 5.2 | Generating Uniform Beams | 111 |
| 5.3 | Proposed Linear Accelerator | 116 |
| 5.4 | Accelerator Optimisation | 120 |

| | | |
|----------|---------------------------------------|------------|
| 5.4.1 | RF Gun | 121 |
| 5.4.2 | Linac | 123 |
| 5.4.3 | Quadrupole Matching Section | 126 |
| 5.4.4 | Stability | 130 |
| 5.5 | Summary | 133 |
| 6 | Conclusions | 136 |
| 6.1 | Summary | 136 |
| 6.2 | Future Work | 138 |
| | Bibliography | 139 |

List of Figures

| | | |
|-----|--|----|
| 1.1 | A map of the three stages of CLIC in comparison to the current CERN accelerator Complex [34]. | 9 |
| 1.2 | Cross section of Higgs production processes in an e^+e^- collider vs CM energy [36]. | 10 |
| 1.3 | Feynman diagrams for the Higgs production processes with the largest cross section at CLIC, (a) Higgsstrahlung, (b) WW-fusion, and (c) ZZ-fusion [36]. | 10 |
| 1.4 | Cross section of top quark pair production processes in an e^+e^- collider vs CM energy [37] | 11 |
| 1.5 | Feynman diagrams for the top production processes with the largest cross section at CLIC [37]. | 12 |
| 1.6 | The CLEAR User Facility. | 15 |
| 1.7 | Tumour control probability and normal tissue complication probability vs. increased dose. | 21 |
| 1.8 | Percentage dose deposited vs. depth through water for different RT treatment modalities: 5 MeV electrons, 15 MeV electrons, 2.5 MeV X-ray photons (γ), 150 MeV protons, 250 MeV carbon-12 ions, and 150 MeV electrons, calculated from TOPAS Monte Carlo simulations [100]. | 22 |
| 1.9 | Temporal characteristics of several in-vitro and in-vivo irradiations at UHDRs, showing whether the flash effect was achieved (dots) or not (crosses) [129]. Black or grey crosses signify a study at a single dose-rate. Crosses and dots of the same colour signify a study with an escalation of dose-rate. | 27 |
| 2.1 | The Frenet-Serret coordinate system describing a reference particle (red) at distance s along an ideal path. \hat{x} , \hat{y} and \hat{z} are the orthogonal unit vectors relative to the reference particle in the horizontal, vertical and longitudinal directions respectively. | 31 |

| | | |
|------|--|----|
| 2.2 | General ellipse in horizontal phase-space, showing the relation of x and x' to $\alpha_x(s)$, $\beta_x(s)$ and $\gamma_x(s)$ | 33 |
| 2.3 | Sample RF wave vs time showing the centre, head and tail of a bunch undergoing velocity bunching. | 35 |
| 3.1 | A diagram of the current CLEAR injector (top) and experimental (bottom) beamlines with the positions of magnets, RF elements, beam instrumentation and Experiments shown [154]. | 39 |
| 3.2 | A photograph of the VESPER test stand [161]. An SRAM board from the ESA JUICE irradiation experiment is installed [57]. | 41 |
| 3.3 | A photograph of the in-air test stand with two copper beam scatterers installed on a movable stage. | 42 |
| 3.4 | A diagram of an RF deflecting cavity being used for bunch length measurement. | 43 |
| 3.5 | The RF deflecting cavity presently installed on the CLEAR beamline. | 45 |
| 3.6 | Transverse beam profiles measured on screen BTV 390 with the RFD extracted (a) and inserted into the beam (b). | 46 |
| 3.7 | Measured bunch lengths vs bunch charge from previously undertaken bunch compression since the first beam operation in CLEAR in 2017. | 48 |
| 3.8 | (a) The normalised electric field of the RF gun and (b) the normalised magnetic field of the solenoid magnet surrounding the gun vs distance from the photocathode. | 50 |
| 3.9 | The approximate radius of the CLEAR aperture as a function of distance from the photocathode to the first quadrupole triplet. | 51 |
| 3.10 | ASTRA simulation of the total bunch charge extracted from the RF gun with a 2D Gaussian laser profile of spot size (a) 0.4 mm and (b) 0.8 mm vs gun phase as a percentage of the generated bunch charge. | 53 |
| 3.11 | ASTRA simulation of the bunch energy of bunches of different charge vs the RF phase of the gun for bunches produced with a 0.8 mm laser spot. | 54 |
| 3.12 | The bunch length of bunches of different charge bunches vs gun RF phase simulated in ASTRA, for a laser spot size of (a) 0.4 mm and (b) 0.8 mm. | 55 |

| | | |
|------|---|----|
| 3.13 | The simulated longitudinal space charge field vs distance from the photocathode acting on 30 probe particles randomly selected from a bunch produced by a 0.4 mm laser spot accelerated at the peak-energy phase. | 56 |
| 3.14 | ASTRA simulation of energy spread of several bunches of different charge vs the RF phase of the gun for bunches generated from a laser spot of 0.8 mm. | 57 |
| 3.15 | The normalised transverse emittance of bunches of various charges, produced by a 0.8 mm laser spot size vs the RF phase of the gun, without the presence of a solenoid field. | 58 |
| 3.16 | (a) The minimum emittance value of bunches of different spot size simulated to the entrance to the bunching cavity vs charge. (b) The solenoid field strength required to minimise the beam emittance vs charge. | 59 |
| 3.17 | ASTRA simulation of the bunch energy of several bunches of different charge, all produced from a laser spot of 0.8 mm, vs the RF phase of the buncher. | 60 |
| 3.18 | ASTRA simulation of the bunch length of several bunches of different charge, all produced from a laser spot of 0.8 mm, vs the RF phase of the buncher. | 61 |
| 3.19 | The minimum bunch lengths achievable for bunches of different charges simulated in ASTRA vs laser spot size. | 62 |
| 3.20 | ASTRA simulation of the energy spread of several bunches of different charge, all produced from a laser spot of 0.8 mm, vs the RF phase of the buncher. | 62 |
| 3.21 | The evolution of energy spread vs distance from the photocathode for several 500 pC bunches, each generated from a laser spot of 0.8 mm, and accelerated at different phases in the bunching cavity. | 63 |
| 3.22 | The evolution of bunch length vs distance from the photocathode for several 500 pC bunches, each generated from a laser spot of 0.8 mm, and accelerated at different phases in the bunching cavity. | 64 |
| 3.23 | (a) ASTRA simulations of the beam emittance vs buncher phase of bunches of different charge, all produced from a laser spot of 0.8 mm, at the end of the bunching cavity with no solenoid field around the buncher. (b) ASTRA simulations of the minimum beam emittance achievable with a tuned solenoid field vs buncher phase for bunches of different charge, all produced from a laser spot of 0.8 mm, at the end of the bunching cavity. | 65 |

| | | |
|------|--|----|
| 3.24 | Comparison between ASTRA simulation and experimental data of the bunch length vs buncher phase of a bunch charge 0.5 nC created from a laser spot of 0.6 mm. A range of $\pm 5^\circ$ in gun phase is shown. The error bars show the statistical uncertainty. | 67 |
| 3.25 | Comparison between ASTRA simulation and experimental data of the bunch length vs buncher phase of a bunch charge 0.3 nC created from a laser spot of 0.5 mm. A range of $\pm 5^\circ$ in gun phase is shown. The error bars show the statistical uncertainty. | 67 |
| 3.26 | Comparison of the minimum bunch lengths achievable in ASTRA simulation and experimentally vs bunch charge for bunches produced from a 0.5 mm laser spot. The error bars show the statistical uncertainty. | 68 |
| 3.27 | ASTRA simulation of the bunch length vs buncher phase for bunches of charge 0.5 nC produced from a 0.8 mm laser spot, and accelerated at different gun phases. | 69 |
| 3.28 | The minimum bunch lengths achievable for bunches of different charge, produced from a laser spot of 0.8 mm, vs RF gun phase. | 70 |
| 3.29 | ASTRA simulations of the energy spread of bunches of different charge, all produced from a laser spot of 0.8 mm, at the end of the bunching cavity set to, (a) the peak accelerating phase, and (b) the phase of minimum bunch length vs RF gun phase. | 72 |
| 3.30 | The minimum emittance achievable at the entrance of the bunching cavity, following an optimisation of the gun solenoid vs gun phase for bunches of different charge, produced from a laser spot of 0.8 mm. | 73 |
| 4.1 | ASTRA simulation of the percentage bunch charge extracted from the RF gun for a 2 nC total charge, produced by laser pulses of different length and a laser spot of (a) 0.4 mm, and (b) 0.8 mm, vs gun phase. | 78 |
| 4.2 | The bunch length at the entrance of the bunching cavity of bunches of various charge, generated from a laser spot of 0.8 mm, accelerated at the maximum energy phase of the RF gun vs the laser pulse length. | 79 |

| | | |
|------|--|----|
| 4.3 | The energy spread at the entrance of the bunching cavity of bunches of various charge, generated from a laser spot of 0.8 mm, accelerated at the maximum energy phase of the RF gun vs the laser pulse length. | 80 |
| 4.4 | (a) The minimum emittance and (b) the solenoid strength required to minimise emittance of bunches of different charge produced from a laser spot of 1.2 mm vs laser pulse length. | 81 |
| 4.5 | ASTRA simulation of the bunch length vs buncher phase for bunches of 2 nC produced from a 0.8 mm laser spot and different laser pulse lengths. | 82 |
| 4.6 | The minimum bunch lengths achievable for bunches of different charge produced from a laser spot of (a) 0.8 mm, and (b) 1.2 mm, vs laser pulse length. | 83 |
| 4.7 | ASTRA simulation of the energy spread vs buncher phase for bunches of 2 nC, generated from a 0.8 mm laser spot and different laser pulse lengths. | 84 |
| 4.8 | The energy spread of bunches of different charge, all produced from a laser spot of 0.8 mm at the end of the bunching cavity set to, (a) the peak accelerating phase, and (b) the phase of minimum bunch length, vs laser pulse length. . . | 84 |
| 4.9 | The minimum normalised emittance for bunches of different charge produced from a laser spot of 1.2 mm, accelerated at (a) the maximum energy phase in the buncher, and (b) the phase of the minimum bunch length, vs laser pulse length. | 86 |
| 4.10 | ASTRA simulation of the bunch energy of a 0.5 nC bunch, generated from a laser spot of 0.8 mm, vs the phase of buncher, for several different maximum buncher electric field strengths. | 87 |
| 4.11 | ASTRA simulation of the bunch length of a 0.5 nC bunch, generated from a laser spot of 0.8 mm, vs the phase of buncher, for several different maximum buncher electric field strengths. | 88 |
| 4.12 | The minimum bunch lengths achievable for bunches of different charges, generated from a laser spot of 0.8 mm, vs maximum electric field in the bunching cavity. | 89 |
| 4.13 | ASTRA simulation of the energy spread of a 0.5 nC bunch, generated from a laser spot of 0.8 mm, vs the buncher phase, for several different maximum buncher electric field strengths. | 90 |

| | | |
|------|--|-----|
| 4.14 | The energy spread for bunches of different charges, generated from a laser spot of 0.8 mm, at the phase of minimum bunch length in the bunching cavity vs maximum electric field in the bunching cavity. | 91 |
| 4.15 | The minimum emittance of bunches of different charge, all produced from a laser spot of 0.8 mm, at the end of the bunching cavity set to (a) the maximum energy phase, and (b) the phase of minimum bunch length vs the maximum electric field in the buncher. | 92 |
| 4.16 | ASTRA simulation of (a) the energy, and (b) the percentage bunch charge extracted from the RF gun for a bunch of 2 nC total charge, generated from a 0.4 mm laser spot and accelerated at different gun electric fields, vs gun phase. | 94 |
| 4.17 | The bunch length at the entrance of the bunching cavity for bunches of various charge, generated from a laser spot of (a) 0.4 mm, and (b) 0.8 mm accelerated at the maximum energy phase of the RF gun vs maximum electric field strength in the gun. | 95 |
| 4.18 | The energy spread at the entrance of the bunching cavity for bunches of various charge, generated from a laser spot of 0.8 mm, accelerated at the maximum energy phase of the RF gun vs maximum electric field strength in the gun. | 96 |
| 4.19 | (a) The normalised emittance, following an optimisation of the gun solenoid, at the entrance of the bunching cavity for bunches of various charge, generated from a laser spot of 0.8 mm, accelerated at the maximum energy phase of the RF gun vs gun field strength. (b) The magnetic field strength of the solenoid magnet required to minimise emittance growth vs gun field strength. | 97 |
| 4.20 | ASTRA simulation of the bunch energy of a 1.0 nC bunch, generated from a laser spot of 0.8 mm, vs the phase of the buncher, for several different maximum gun electric field strengths. | 99 |
| 4.21 | ASTRA simulation of the bunch length of a 1.0 nC bunch, generated from a laser spot of 0.8 mm, vs the phase of the buncher, for several different maximum gun electric field strengths. | 100 |
| 4.22 | The minimum bunch lengths achievable for bunches of different charge produced from a laser spot of (a) 0.4 mm, and (b) 0.8 mm, vs maximum electric field strength in the gun. | 100 |

| | | |
|------|--|-----|
| 4.23 | ASTRA simulation of the energy spread of a 1.0 nC bunch, generated from a laser spot of 0.8 mm, vs the phase of the buncher, for several different maximum gun electric field strengths. | 102 |
| 4.24 | The energy spread of bunches of various charge generated from a laser spot of 0.8 mm vs the electric field strength in the RF gun at (a) the maximum energy phase of the buncher, and (b) the phase of minimum bunch length in the buncher. | 103 |
| 4.25 | The minimum emittance of bunches of different charge, all produced from a laser spot of 0.8 mm, at the end of the bunching cavity set to (a) the maximum energy phase, and (b) the phase of minimum bunch length vs the maximum electric field in the gun. | 103 |
| 5.1 | Sample distributions in x with their kurtosis labelled. | 110 |
| 5.2 | Transverse phase space of two sample distributions, one under the influence of linear forces and one under the influence of non-linear focusing forces. . . | 112 |
| 5.3 | Horizontal beam size vs distance from the photocathode for a bunch of charge 0.4 nC generated from a laser spot of 1.6 mm with different solenoid magnetic field strengths. | 112 |
| 5.4 | Particle distributions in x across a slice in y of width $\pm\sigma_y/4$ measured at a distance of 1.5 m from the photocathode for a bunch of charge 0.4 nC generated from a laser spot of 1.6 mm. | 113 |
| 5.5 | The phase space of a bunch of charge 0.4 nC generated from a laser spot of 1.6 mm focused by a solenoid magnet of strength 0.29 T measured at (a) $s = 0.3$ m, (b) $s = 0.6$ m, and (c) $s = 1.0$ m. | 114 |
| 5.6 | Kurtosis vs distance from the photocathode for a bunches of charge 0.4 nC generated from a laser spot of 1.6 mm and focused by different solenoid fields. | 115 |
| 5.7 | Normalised emittance vs distance from the photocathode for bunches of charge 0.4 nC generated from a laser spot of 1.6 mm and focused by different solenoid fields. | 116 |
| 5.8 | Diagram of the irradiation facility beamline. | 117 |

| | | |
|------|--|-----|
| 5.9 | Real and imaginary longitudinal electric field profiles, normalised to the maximum real component, of the X-band cavities vs distance from the entrance to the cavity for (a) an unloaded cavity, and (b) a loaded cavity. | 118 |
| 5.10 | Beam size vs distance from the entrance to the first X-band structure for a 0.4 nC bunch produced with different $\alpha_{x,y}$ | 119 |
| 5.11 | Beam transport vs distance from the entrance to the first X-band structure for a 0.4 nC bunch produced with different $\alpha_{x,y}$ | 120 |
| 5.12 | (a) The beam spot size, (b) the bunch length, and (c) the kurtosis of a 0.4 nC bunch generated from a laser spot of 0.8 mm, vs distance from the photocathode. | 121 |
| 5.13 | Transverse phase space of a 0.4 nC bunch, 1.2 m from the photocathode, generated from a laser spot of 0.8 mm. | 122 |
| 5.14 | Longitudinal phase space of a 0.4 nC bunch, 1.2 m from the photocathode, generated from a laser spot of 0.8 mm. | 123 |
| 5.15 | Bunch energy vs distance from the entrance of the first X-band cavity for a bunch of charge 0.4 nC generated from a laser spot of 0.8 mm. | 124 |
| 5.16 | Maximum particle radius and rms bunch size vs distance from the entrance of the first X-band cavity for a bunch of charge 0.4 nC generated from a laser spot of 0.8 mm. | 124 |
| 5.17 | Transverse phase space of a 0.4 nC bunch at the exit of the linac. | 125 |
| 5.18 | Longitudinal phase space of a 0.4 nC bunch at the exit of the linac. | 126 |
| 5.19 | Projected transverse phase space of a 0.4 nC bunch at the exit of the linac. | 127 |
| 5.20 | Transverse phase space measured at the experimental target location 0.3 m from the exit of the final quadrupole for the (a) small-, (b) medium-, and (c) large-diameter beam optics. | 128 |
| 5.21 | Beam size vs distance from the linac exit for the (a) small-, (b) medium-, and (c) large-diameter beam optics. | 129 |
| 5.22 | Transverse beam profiles for the large-beam optics measured (a) 0.1 m, (b) 0.5 m, and (c) 1.0 m, from the exit of the final quadrupole. | 131 |
| 5.23 | Maximum particle radius vs distance from the linac exit for the large beam optics. | 131 |

| | | |
|------|--|-----|
| 5.24 | Beam profiles of bunches produced on photocathode with a uniform quantum efficiency, and one produced with a quantum efficiency with a 50% gradient for (a) a uniform, and (b) a Gaussian laser spot. | 132 |
| 5.25 | (a) Particle distributions in x across a slice in y of width $\pm\sigma_y/4$ measured at a distance of 1.2 m from the photocathode for bunches produced with a uniform cathode and a cathode with a 50% slope in quantum efficiency. (b) The transverse profile for a bunch produced from a cathode with a 50% slope in quantum efficiency at a distance of 1.2 m. | 134 |

List of Tables

| | | |
|-----|--|-----|
| 1.1 | Fundamental fermions of the Standard Model. | 2 |
| 3.1 | Available beam parameters in CLEAR. | 46 |
| 5.1 | Beam Parameters at the linac exit. | 123 |
| 5.2 | Maximum amplitude of variations of beam parameters across a specified variation tolerance. | 132 |

Chapter 1

Introduction

1.1 The Standard Model

The notion that the universe is made of small, indivisible atomic building blocks can be traced back to the ancient Greek philosopher Democritus in the 5th century BC [1]. By the mid-19th century this idea was accepted scientific knowledge. However, towards the end of that century a problem had emerged. The discovery of the electron, by Thomson in 1897 [2], showed that the atom was in fact not an indivisible unit. Thomson later suggested in 1904, that atoms were rather like a “plum pudding”, with negatively charged electrons embedded in positively charged matter [3]. Within seven years this idea was disproved by Rutherford with the discovery of the nucleus in 1911 [4]. The discovery of the nucleus was followed by its constituents, the proton in 1919 by Rutherford [5], and the neutron by Chadwick in 1932 [6, 7]. Throughout the subsequent few decades more particles were observed resulting in a complex zoo of known particles. During this time, theoretical work was ongoing in order to attempt to explain the particles in the zoo, with the idea that many of these particles were formed of more fundamental particles gaining prominence. The development of this theoretical work, in conjunction with further experimental discoveries, led to the formulation of the Standard Model of particle physics.

The Standard Model (SM) describes the fundamental particles of matter and how they interact with three of the four fundamental forces thought to exist in the universe, the electromagnetic (EM) force, the strong force, and the weak force [8]. In the SM there are twelve particles of matter, known as fermions (Table 1.1), which can be split into two groups; quarks, which interact with all three fundamental forces; and leptons, which do not interact

Table 1.1: Fundamental fermions of the Standard Model.

| Generation | Leptons | | Quarks | |
|------------|----------------|---------------------------|-----------|-------------|
| 1 | Electron e^- | Electron Neutrino ν_e | Up u | Down d |
| 2 | Muon μ^- | Muon Neutrino ν_μ | Charm c | Strange s |
| 3 | Tau τ^- | Tau Neutrino ν_τ | Top t | Bottom b |

with the strong force. Each of these particles has a corresponding antiparticle, which has the same mass, but an opposite electric charge. There are three charged leptons in matter, with an electric charge of -1, with three associated neutrinos of a neutral charge. Six quarks are found in the SM, the up, charm and top carrying a charge of $+2/3$, and the down, strange and bottom carrying a charge of $-1/3$. Quarks are not found in isolation and are instead bound into composite particles with integer electric charge, known as hadrons. Combinations of three quarks are known as baryons, and quark-antiquark pairs known as mesons. The fermions can be classified in three generations with increasing mass. All atomic matter is formed of charged fermions of the first generation.

The fermions have half-integer spin. They interact with each other via the three fundamental forces which are carried by integer-spin particles known as bosons. The strong interaction is carried by the gluon (g), the EM by the photon (γ), and the weak by the W and Z bosons (W^\pm, Z^0).

With the discovery of the tau neutrino in 2001 [9], there was evidence for the existence of all of the fermions and force carrying bosons in the SM. However, a potential issue still existed. There was no evidence for a mechanism to explain the masses of the particles. A solution to this problem had been proposed by Higgs and other theorists in 1964 [10], via the existence of the so-called Higgs field. Higgs postulated that if the Higgs field existed, then there would be an associated boson, the Higgs boson. Evidence for the Higgs boson, at a mass of around 125 GeV, was found in 2012 at the European Organisation for Nuclear Research (CERN) in the ATLAS [11] and CMS [12] detectors of the Large Hadron Collider (LHC). Studies of the properties of the Higgs boson have continued since 2012, with its mass currently measured to be 125.25 ± 0.17 GeV [13], but several of its properties, such as its self-coupling, remain unmeasured.

The SM successfully describes many processes. However, there are many aspects of

the universe that it fails to describe. There is no attempt made in the SM to explain the fourth fundamental force, gravity. Furthermore, astronomical observations suggest that the majority of the mass content of the universe is in the form of so-called dark matter and dark energy [14]. The SM does not describe the nature of either. The SM initially predicted that the neutrinos are massless. However, observations of neutrino oscillations suggest that they do have mass [15]. In addition, it is unlikely that the small amount of charge-parity (CP) violation in the SM can account for the asymmetry between matter and antimatter necessary to explain why we live in a matter dominated universe [16]. A goal of modern particle physics is, therefore, to explain these areas of physics that lie beyond the SM (BSM). To reach that goal will require new facilities, providing higher energies and intensities, as well as higher precision measurement techniques.

1.2 Particle Accelerators and Colliders

Since the discovery of the neutron, the main tools physicists have used to investigate the particles of the SM are particle accelerators [17]. Accelerators use radio-frequency (RF) EM waves to transfer energy to beams of charged particles. Magnets of different order are used to control the beams on their trajectories, dipoles to bend the beams, quadrupoles to focus them, as well as higher order magnets to provide corrections to the beam. When at high energies, the particle beams can be impacted upon a target, which can either be a fixed-target, or another high-energy particle beam in a collider.

1.2.1 Particle Accelerators

Modern particle accelerators are typically built in one of two configurations, circular or linear. A circular accelerator uses magnetic fields to bend the beams in a circular trajectory. A particle of charge, q , and momentum, p , passing through a dipole magnetic field of strength, B , will follow a circular path governed by the following relation,

$$B\rho = \frac{p}{q}, \quad (1.1)$$

where ρ is the radius of curvature of the particle trajectory. The quantity, $B\rho$, is known as the beam rigidity [18].

Beams are injected into a circular accelerator at an initial energy. The beams then circulate in the accelerator, passing through RF cavities, gaining a small amount of energy each turn. As they gain energy the rigidity increases. Therefore, to maintain a constant trajectory, the strength of the magnetic field of the dipoles has to be increased. Accelerators that maintain a constant radius are known as synchrotrons. As the beam is accelerated, the orbit period is reduced, meaning that the frequency of the RF cavities must be increased. When the beams are moving at ultra-relativistic velocities the required increase is negligible. When accelerated to a desired energy the beams can either be maintained at that energy, known as a storage ring, or extracted.

The maximum energy achievable in a synchrotron depends on the type of particle accelerated. In a proton synchrotron the maximum beam energy is limited by the maximum strength of the dipole magnets, and the bending radius of the trajectory. However, for beams of electrons or positrons, the maximum energy in a synchrotron is limited by the power lost through radiation. When following a curved path, charged particles emit radiation. At ultra-relativistic velocities, the radiation is emitted tangentially, and is known as synchrotron radiation. The power loss, P , of a beam due to synchrotron radiation is,

$$P \propto \frac{1}{\rho^2} \frac{E^4}{m^4}, \quad (1.2)$$

where ρ is the radius of curvature, m is the mass of the particles, and E is the energy of the beam. For proton synchrotrons the power loss is negligible up to energies of several hundred TeV. However, as electrons and positrons have a mass around 1800 times less than protons, the amount of synchrotron radiation emitted can be significant above beam energies of a few hundred MeV. The maximum energy, therefore, in a circular electron or positron accelerator is limited by the amount of power it is possible to input to the beam in the RF cavities. It is possible to reduce the synchrotron radiation losses by building an accelerator with a larger radius, however, the costs of such a machine rise significantly.

To accelerate electron or positron beams to energies higher than a few hundred GeV, it is not practical to use a circular accelerator. Linear accelerators, or linacs, accelerate particles in a straight path using sequential RF cavities. In a linear accelerator, the maximum energy achieved is dependent on its length and the acceleration gradient of the RF cavities used. To build cheaper, compact linear accelerators, cavities with high-gradients should be used.

Once built, it is relatively easy to upgrade the energy of a linac by extending its length, or replacing the cavities with cavities of a higher gradient.

1.2.2 Colliders

For use in particle physics, beams accelerated to high energy can be extracted from an accelerator and either impacted upon a fixed-target or collided. A detector can be located at the collision point, known as the interaction point (IP), and used to identify particles created in the collisions. The physics potential of a collision depends on the type of particles involved, as well as two figures of merit, the energy in the centre-of-mass (CM) reference frame of the collision, and the luminosity. In a collision at a CM energy, E_{CM} , the rate of interaction X occurring is given by,

$$R_X = \mathcal{L}\sigma_X(E_{CM}), \quad (1.3)$$

where \mathcal{L} is the luminosity, and σ_X is the cross-section of the interaction. The cross-section describes the probability of X occurring, and depends on both the CM energy as well as the type of particles involved in the collision. The luminosity is a property of the experimental setup. The luminosities of fixed-target experiments tend to be higher than in colliders as the target tends to have a larger number of particles than a beam in a collider. However, it is easier to reach higher CM energies in colliders than in fixed-target experiments. For a beam of energy E_b , much greater than the mass of the particles in the beam, impacting upon a target with particles of mass m_t , the CM energy is,

$$E_{CM} \approx \sqrt{2m_t E_b}. \quad (1.4)$$

Whereas, in a collider of beams of energy E_1 and E_2 , the CM energy is,

$$E_{CM} \approx 2\sqrt{E_1 E_2}. \quad (1.5)$$

Furthermore, momentum in a collision must be conserved. As the particles in a fixed target are at rest, any particles following the collision must carry the momentum of the beam. In a collider, the magnitude of the two beam momenta can be similar, but with opposite sign, allowing the products of a collision to be easily identified.

In a collider with two beams of n_1 and n_2 particles, the luminosity is given by,

$$\mathcal{L} = f_r \frac{n_1 n_2}{4\pi\sigma_x^* \sigma_y^*} \mathcal{F} \quad (1.6)$$

where f_r is the repetition frequency of the collisions, σ_x^* and σ_y^* are the transverse beam sizes in the horizontal and vertical axes, and \mathcal{F} is a correction factor that describes any geometric or dynamic factors that affect the beams as they cross [13]. The revolution frequency of a circular collider is typically higher than the repetition frequency in a linear collider. Therefore, to achieve comparable luminosities, the beam size must be significantly smaller in a linear collider. Further to this, in a circular collider it is possible to have several IPs positioned around the circumference of the collider, whereas in linear collider designs it is common to have only one.

The highest energy collider to have operated to date is the Large Hadron Collider, which began operation in 2008 [19]. The LHC is a proton synchrotron of 27 km circumference, which using 8.3 T superconducting dipole magnets, can achieve a design CM energy of 14 TeV. Operation of the LHC led to the discovery of the Higgs boson in 2012 [11, 12]. Since 2012, the properties of the Higgs boson and other SM particles and processes have been studied further. To increase the precision of measurements taken at the LHC, upgrades are being made to increase its luminosity in the so-called high-luminosity LHC (HL-LHC) [20].

The precision of measurements possible in the HL-LHC is limited by the nature of the proton beams themselves. Protons are baryons and, therefore, not fundamental particles. In any collision between two baryons it is the constituent quarks and gluons that collide. The collisions, therefore, produce a high level of background in the detector making it difficult to identify individual particles, adding a level of uncertainty to any measurement. Furthermore, the colliding quarks and gluons carry an unknown fraction of each proton's energy, making the CM energy of each collision unknown.

Leptons are fundamental particles, so collisions in a lepton collider produce a much lower background. Prior to the installation of the LHC, the same 27 km tunnel housed an e^+e^- collider, known as the Large Electron-Positron (LEP) collider [21]. LEP is the highest CM energy lepton collider to have operated. However, the maximum CM energy was only 209 GeV due to synchrotron radiation losses [22].

1.2.3 Proposed Future Colliders

The consensus amongst particle physicists is that the next collider to be built should be an e^+e^- collider to explore the properties of the Higgs boson [23]. There are currently two linear, e^+e^- collider projects under development, the superconducting International Linear Collider (ILC) [24] and the normal conducting Compact Linear Collider (CLIC) [25, 26, 27]. Both the ILC and CLIC propose to build initial stages with CM energies of 250 GeV and 380 GeV respectively. These stages will be used to study the properties of the Higgs boson, also the top quark at CLIC, with high-precision. Due to their linear design both projects can potentially be upgraded to significantly higher energies. The CLIC project will be discussed in detail in the following section.

The initial stage of the ILC would be 20.5 km long and would use 1.3 GHz superconducting RF cavities of gradient 31.5 MV/m to produce a CM energy of 250 GeV [28]. The first stage is targeted to produce a luminosity of $1.35 \times 10^{34} \text{ cm}^{-2}\text{s}^{-1}$, and could achieve an integrated luminosity of 2 ab^{-1} following around a decade of operation [24]. The length of the accelerator could then be extended to 31 km to produce a CM energy of 500 GeV and luminosity of $1.8 \times 10^{34} \text{ cm}^{-2}\text{s}^{-1}$, followed by a further extension to 40 km for a CM energy of 1 TeV and luminosity of $4.9 \times 10^{34} \text{ cm}^{-2}\text{s}^{-1}$.

There are also proposals to build a circular e^+e^- collider, the Future Circular Collider (FCC-ee) [29] which would be built at CERN, and the Circular Electron-Positron Collider (CEPC) [30, 31], which would be built in China. FCC-ee, would consist of a synchrotron of a circumference of 100 km, which would use normal conducting bending dipoles and could produce a maximum CM energy of 350 GeV. The maximum energy is limited by the power use of the superconducting RF cavities. Following the e^+e^- operation at FCC-ee, the tunnel could be re-used to host a superconducting hadron collider, FCC-hh, with a CM energy of up to 100 TeV [32].

The CEPC would also consist of a synchrotron built from mostly normal conducting magnets and superconducting RF cavities in a 100 km tunnel [30, 31]. The CM energy would be slightly lower than FCC-ee at 240 GeV, restricted by synchrotron radiation losses. Following several years of operation the tunnel would be re-used to host a proton-proton collider, the Super Proton-Proton Collider (SPPC), with a CM energy of 75 TeV. Unlike

the FCC, the CEPC tunnel is large enough to host both accelerators which would allow high-energy lepton-hadron collisions.

In addition there are preliminary studies ongoing to build a circular muon collider [23]. Muons are leptons but have a larger mass than electrons, and so synchrotron radiation losses are not as significant as in an e^+e^- collider. Therefore, it may be possible to achieve an order of a few TeV CM energy in a muon collider in a significantly smaller synchrotron than FCC. However, muons have to be produced and cooled sufficiently to be accelerated. Furthermore, muons have a lifetime of 2.2 μs , and would decay as they move through a collider.

1.3 The Compact Linear Collider

The Compact Linear Collider is a proposed e^+e^- collider which aims to reach a CM energy of up to 3 TeV [25, 26, 27]. The implementation of CLIC could take place in three stages, all located on the CERN site. A possible arrangement of these stages is shown in Figure 1.1. The initial stage would be an 11 km accelerator, powered by either klystrons or a novel two-beam accelerating scheme, to produce a CM energy of 380 GeV. Two extensions to CLIC have been envisaged. The first involves extending the accelerator to 29 km to produce a CM energy of 1.5 TeV, before a final extension to a length of 50 km producing a CM energy of 3 TeV. The baseline luminosity for the initial stage is $1.5 \times 10^{34} \text{ cm}^{-2}\text{s}^{-1}$, with the second and third stages having targeted luminosities of $3.7 \times 10^{34} \text{ cm}^{-2}\text{s}^{-1}$ and $5.9 \times 10^{34} \text{ cm}^{-2}\text{s}^{-1}$ respectively. Over the full CLIC operational timeline this would provide integrated luminosities of 1 ab^{-1} for the 380 GeV stage, 2.5 ab^{-1} for the 1.5 TeV stage, and 5 ab^{-1} for the 3.0 TeV stage [33].

1.3.1 Physics Potential

The main goal of the 380 GeV stage is take high-precision measurements of known SM particles, particularly the Higgs boson, the top quark, and the W and Z bosons [26]. The higher energy stages will mostly focus on searching for BSM physics processes through both direct and indirect searches. As CLIC is the only proposed e^+e^- collider that will be able to reach multi-TeV CM energies, it possesses significant advantages in its physics reach [35].

The main physics goals of CLIC will be summarised here, for a more in depth analysis

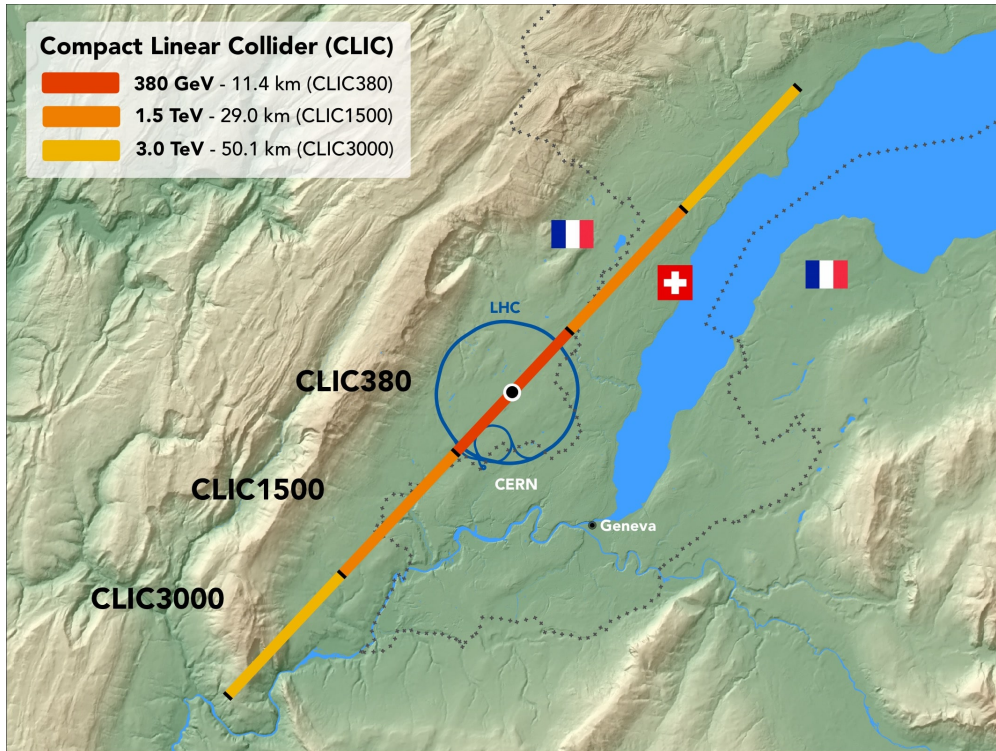


Figure 1.1: A map of the three stages of CLIC in comparison to the current CERN accelerator Complex [34].

refer to [35].

1.3.1.1 Higgs Physics

There are several mechanisms for the production of the Higgs boson. The cross section of each of the mechanisms depends on the CM energy, the most common are shown in Figure 1.2. In the SM, the coupling strength of a fermion to the Higgs boson is proportional to the mass of the fermion [36]. Deviations from this relationship could be a sign of a BSM process. To investigate these processes, high-precision measurements of Higgs-fermion couplings must be taken. Three Higgs production processes have the largest cross section at all CM energies of the CLIC program, the Feynman diagrams of which are shown in Figure 1.3. For the first energy stage, the largest cross section for Higgs production is the Higgsstrahlung process ($e^+e^- \rightarrow ZH$), although WW-fusion is significant. The first stage of CLIC should allow most Higgs couplings in both of these processes to be measured to a precision of less than 1 %.

Analysis of the decay products of the ZH produced by Higgsstrahlung will allow a high-precision measurement of the Higgs mass to be made [36]. The Z boson can either decay

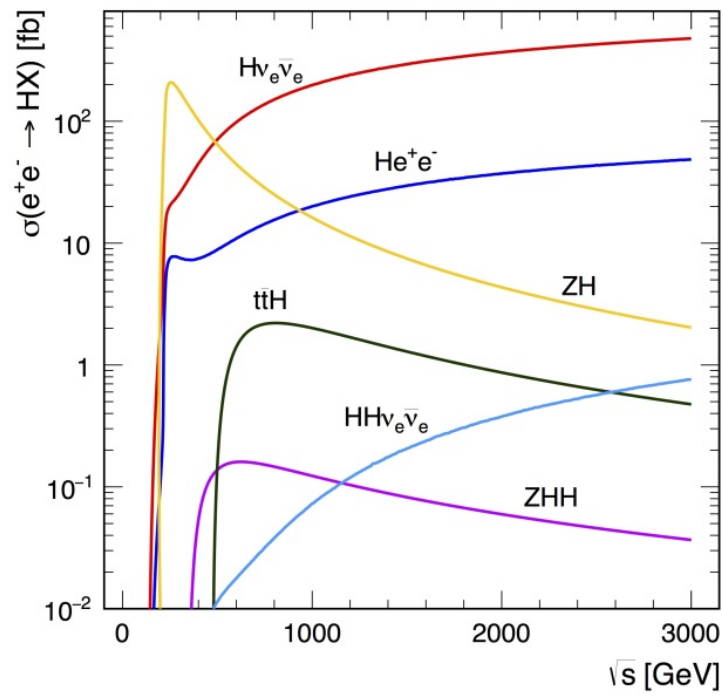


Figure 1.2: Cross section of Higgs production processes in an e^+e^- collider vs CM energy [36].

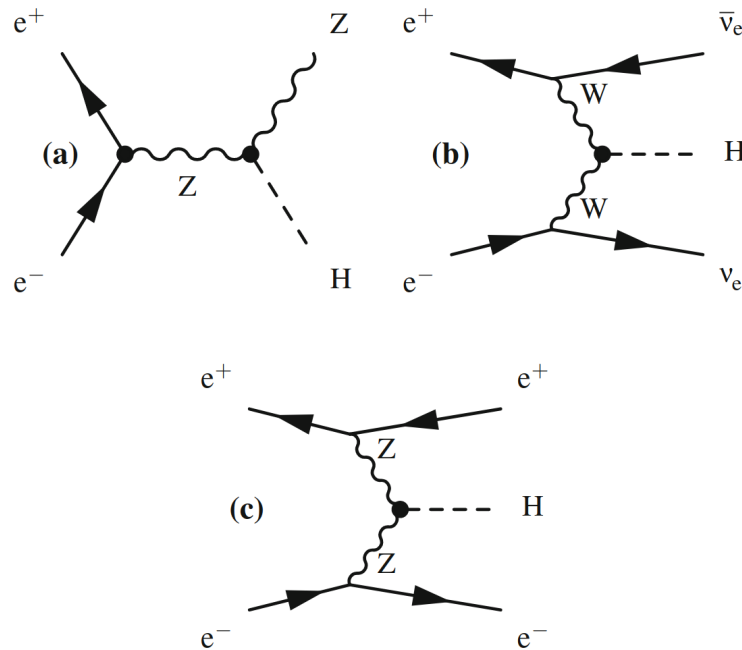


Figure 1.3: Feynman diagrams for the Higgs production processes with the largest cross section at CLIC, (a) Higgsstrahlung, (b) WW-fusion, and (c) ZZ-fusion [36].

into an e^+e^- pair, a $\mu^+\mu^-$ pair, a $\tau^+\tau^-$ pair, a $\nu\bar{\nu}$ pair or a $q\bar{q}$ pair. By identifying these products, and using them to reconstruct the decay, it is possible to measure the recoil mass of the Higgs which sharply peaks around the Higgs mass itself.

In the higher energy stages of CLIC, WW-fusion becomes the dominant Higgs production mechanism, with ZZ-fusion being another important mechanism. Furthermore, at higher energies it is possible to measure the strength of the Higgs self-coupling by measuring $e^+e^- \rightarrow ZHH$ and $e^+e^- \rightarrow HH\nu_e\bar{\nu}_e$. Like many of the couplings, the strength of the Higgs self-coupling is important to understanding the properties of the Higgs potential. Differences between theoretical predictions of the Higgs potential and experimental measurements could be the result of BSM processes.

1.3.1.2 Top Physics

Top-quark pair production in CLIC would provide the first measurements of the properties of the top quark in an e^+e^- collider, which could significantly improve their precision relative to measurements taken in the LHC [37]. The cross sections for the dominant top quark pair production processes in CLIC are shown in Figure 1.4. At all CM energies the dominant processes are via coupling to photons and Z bosons, shown in Figure 1.5. Many BSM theories effect this coupling strength, therefore, measurement in CLIC could provide evidence for or against BSM physics.

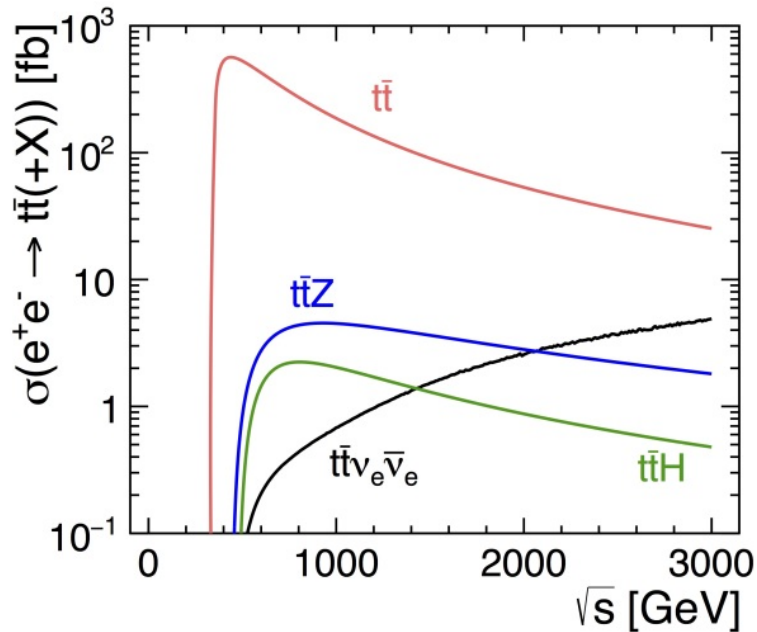


Figure 1.4: Cross section of top quark pair production processes in an e^+e^- collider vs CM energy [37]

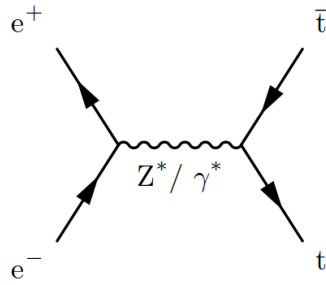


Figure 1.5: Feynman diagrams for the top production processes with the largest cross section at CLIC [37].

By gradually increasing the CM energy around 350 GeV, a so-called threshold scan, it is possible to gain a more precise measurement of the top quark mass than has previously been taken. Furthermore, precision measurements of other top quark production mechanisms and couplings could shed light upon certain BSM theories.

1.3.2 CLIC Accelerator Technology

In order to keep costs low, and to allow CLIC to fit in the area surrounding CERN, CLIC has been designed to be as compact as possible, whilst maintaining its physics potential. For this purpose, the main CLIC accelerator will use normal conducting copper cavities at the X-band frequency of 12 GHz. The maximum acceleration gradient that will be used for CLIC will be 100 MV/m, which will be used in the second two stages. However, the luminosity targets of the first stage require a higher beam current than the second two, for which the optimal gradient is 72 MV/m.

To achieve these acceleration gradients, CLIC requires a very high peak power. To provide this, a novel two-beam acceleration technique has been proposed, rather than using high-power, X-band klystrons. A long, high-current drive beam is accelerated to an energy of 2.38 GeV by efficient, 1 GHz klystrons. Pulses in the drive beam are interleaved to increase the bunch frequency to 12 GHz. The drive beam then passes through so-called power extraction and transfer structures. The extracted power is then transferred to the main CLIC beam through waveguides. The two-beam acceleration method was successfully tested at the CLIC Test Facility (CTF3), and should be scalable [38, 39]. The two-beam scheme significantly reduces the costs and increases the efficiency of CLIC especially at higher energies, although an alternative design for the first stage, powered by klystrons has also

been completed.

The design luminosity of CLIC will be degraded by any imperfections in the physical machine compared to a machine that matches the design perfectly. The imperfections can either be static or dynamic, and can cause the emittance to grow, or cause beam-beam offsets at the IP. Static imperfections are mostly due to the misalignment of components or errors in the machining of components. Sources of static imperfections include misaligned: beam position monitors (BPM), which will cause the beam to be mis-corrected on its path to the IP; magnets, that can give unwanted kicks to the beam, thereby altering its trajectory; and RF cavities, in which the beam can generate wakefields that degrade the beam quality. It is, therefore, vital to machine and align CLIC components to a high degree of accuracy [40, 41].

Dynamic imperfections can occur on different timescales and can cause variations to individual bunches within a train or between different trains. Sources of dynamic imperfections include: beam jitters introduced by the kicker magnets which direct the beams into the main linacs; timing errors that lead to different bunches being accelerated at different RF phases; time varying misalignment of components caused by component vibrations or ground movement; power fluctuations; and stray magnetic fields produced by nearby currents. It must be noted that dynamic imperfections occurring at the train repetition frequency appear static to the train.

To reduce the effect of both static and dynamic imperfections on the luminosity there are beam-based feedback and feedforward systems, and an IP feedback system. It has recently been shown that such systems could increase the expected luminosity of the 380 GeV stage to $2.8 \times 10^{34} \text{ cm}^{-2}\text{s}^{-1}$, around a factor two increase above the baseline target [42, 43].

The research effort undertaken to realise CLIC has led to the development and improvement of several accelerator technologies. Chief among these is the development of X-Band RF structures which are already being used, or planned to be used, in several facilities such as: the Deep Electron FLASH Therapy facility (DEFT), a proposed radiotherapy facility using very high energy electron beams to treat patients via the FLASH effect [44]; the injector linac of the eSPS, a proposed project at CERN to search for dark matter particles in the MeV - GeV mass range [45]; the CompactLight X-ray free electron laser [46, 47]; the in-

jector linac of the EuPRAXIA facility, a proposed plasma wakefield acceleration test facility [48]; Smart*Light, a compact inverse Compton scattering source for producing hard X-rays [49]; and the PolariX-TDS (Polarizable X-Band Transverse Deflection Structure), used for high resolution measurements of transverse beam properties [50, 51]. Important in their own right, these projects will provide vital experience with X-band technology, improving its performance and efficiency for future implementation in CLIC [23].

1.3.3 Implementation of CLIC

It would be possible to begin construction of CLIC soon after approval. An updated proposal from the CLIC project will be submitted to the European Strategy for Particle Physics Update in 2026. In the case that the project is approved, construction of the tunnel could begin as early as 2030. The projected cost of the 380 GeV stage of CLIC is 5.9 billion CHF [52], significantly lower than the combined 4 billion CHF machine cost and 7.6 billion CHF infrastructure cost projected for FCC-ee [29]. Following construction and commissioning, the first collisions at CLIC could take place in 2037. The first stage would then operate for eight years. There would then be a two year period spent re-configuring the accelerator complex and commissioning it for 1.5 TeV operation, which would last for another eight years. Following another two year interval to reconfigure the site for 3.0 TeV operation, operation could continue for a final seven or more years. Construction of most of the second and third stages can be undertaken in parallel to data taking with the earlier stages. The second and third stages are projected to cost an additional 5.9 billion CHF and 7.3 billion CHF respectively.

1.4 The CLEAR User Facility

The CERN Linear Electron Accelerator for Research (CLEAR), is a user facility that has been operating at CERN since 2017 [53, 54, 55]. CLEAR was developed from the CALIFES accelerator, which produced the probe beam used to test the novel two-beam acceleration concept for CLIC in the CLIC Test Facility (CTF3) [39]. The main purpose of CLEAR is to act as a general R&D facility for a wide range of accelerator-based technology. The beamline consists of a 20 m long electron linac which can accelerate electron beams to energies between

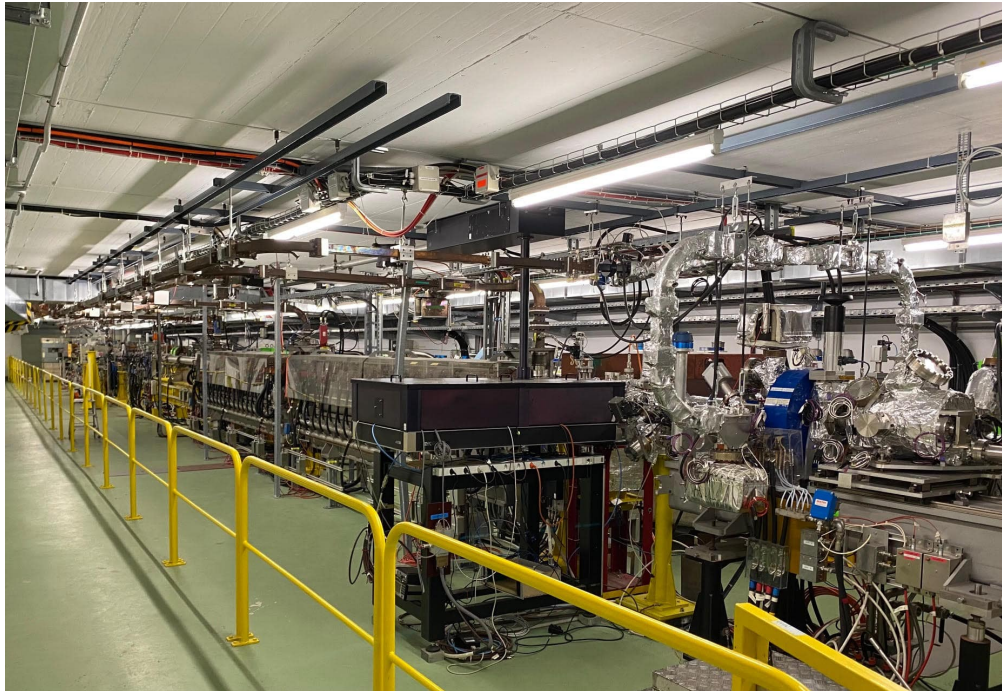


Figure 1.6: The CLEAR User Facility.

60 MeV and 220 MeV, followed by an experimental beamline, and two in-air test stands. CLEAR operation is independent of CERN's long shutdowns of the LHC beam complex and thus has been able to operate for around 35 weeks a year since 2018, with only short technical shutdowns in the summer and winter [56].

Internal and external users are able to perform experiments on the CLEAR beamline which include the following:

Irradiation of Electronics One of the first users to experiment at CLEAR was a team from the European Space Agency (ESA) in collaboration with the Radiation to Electronics (R2E) group at CERN. The group irradiated electronic components from the JUICE mission to the planet Jupiter with 100 - 200 MeV electron beams. Four static random-access memories (SRAM) mounted onto a single board, were irradiated in the VESPER (Very energetic Electron facility for SPace Planetary Exploration missions in harsh Radiative environments) test stand to study their performance in a high electron flux environment. These studies provided experimental evidence for electron induced single event upsets (SEU) [57], suggesting that the high flux of electrons trapped in Jupiter's radiation belts could be a significant contribution to the overall SEU rate in the probe's electronics. Further studies have been

undertaken to understand and characterise these SEUs and their mechanisms [58, 59, 60, 61].

In addition to their work with the ESA, the R2E group have performed several other irradiation experiments at CLEAR [62], including: investigating the effects of dose-rate on SEUs; the mechanisms that electron beams can cause stuck bits in dynamic random-access memories; and investigating displacement damage in diodes. Many of these studies can be done with proton beams, however, they are more difficult to undertake as the protons produce a higher level of activation in the sample.

CLIC Related Research Two prototype CLIC accelerating structures are installed in the CLEAR beamline. Originally installed to test the two-beam acceleration scheme, the structures are not currently connected to RF power. At present, the structures are used to study short-range wakefield kicks induced on beams as they pass through [63, 64], and to test the performance of the wakefield monitors installed [65].

In addition, there are four prototype CLIC cavity BPMs installed downstream of the CLIC structure [66]. The performance of the BPMs, in conjunction with their associated electronics and acquisition systems, is being studied [67]. If successfully demonstrated to give reliable, high-resolution measurements, these BPMs will be used to compliment the measurements taken of wakefield effects in the CLIC structures.

Medical Irradiation Experiments CLEAR is currently a unique user facility for undertaking medical research using high-current, 200 MeV electron beams. Electron beams at this energy are of particular interest in investigating very high-energy electron (VHEE) radiotherapy and the so-called FLASH effect, discussed in Sections 1.5 and 1.6. Several experiments, summarised in [68], for investigating dosimetry at ultra high dose-rates, strong focusing of VHEE beams, and the biological effects of VHEE beams have been performed on CLEAR. To prepare for these studies, significant work was done to improve the machine stability and the uniformity of doses on the target.

In addition to radiotherapy-related research, tests into the sterilisation of personal protective equipment with high-energy electron beams has been undertaken [69]

Beam Instrumentation CLEAR is a powerful facility for completing research into beam instrumentation [70]. The low levels of activation mean that it is possible to access the machine several times a day; there is a flexible range of beam parameters available to users; and a large amount of existing high-quality beam diagnostics, largely re-purposed from CTF3. Several beam instrumentation experiments are installed on the beamline, as well as others installed temporarily in the in-air stands [71].

One early test was the first observation, and investigation of strong shadowing effects between two optical transition radiation (OTR) screens positioned close together [72]. The results of this study could have implications for the design of several diagnostic devices that use more than one OTR source.

CLEAR has also been used to test novel BPMs based on the emission of Cherenkov diffraction radiation (ChDR) [71]. The Cherenkov BPMs consist of chambers containing dielectric inserts. As the beam passes the inserts, Cherenkov diffraction radiation is emitted over a defined solid angle, allowing for a high signal strength with a low background [73]. By analysing the light, it is possible to measure transverse and longitudinal beam properties.

Several prototype devices utilising ChDR have been tested at CLEAR. One of the prototypes will be used on the AWAKE experiment to differentiate the signals of the co-propagating proton and electron beams [74]. In conventional BPMs the signal given by the proton beam will mask the signal of the electron beam. The prototype Cherenkov BPM will operate at a detection frequency of 30 GHz, allowing the differentiation of the two signals due to their differing bunch lengths.

Devices utilising ChDR could be used to take non-destructive, high-precision measurements of bunch length. A study completed at CLEAR [75] and the Compact Linear Accelerator for Research and Applications (CLARA) facility [76], demonstrated that by using ChDR it is possible to measure the longitudinal profile of sub-ps bunches, with a precision similar to conventional methods. Further work is being undertaken at CLEAR to explore the use of ChDR devices to measure bunch lengths at AWAKE. Furthermore it has been shown that Cherenkov devices could be a useful diagnostic for the LHC [77]. Some preliminary tests of a system compatible with the LHC are being undertaken at CLEAR.

The theoretical model behind ChDR has not yet been fully verified experimentally.

Therefore, a simplified setup is being investigated at CLEAR [71]. Verification of the model is needed to both improve the performance of ChBPMs for current beamlines, as well as to allow their use to be extended to higher energy beams, for example in the FCC.

Work is ongoing towards developing a beam loss monitoring system based on optical fibres [78]. Lost particles that pass through the optical fibre create Cherenkov light that can be measured, with the time delay used to pinpoint the location the light was emitted. If optimised, such a beam loss monitor would allow localised beam losses to be measured continuously over long distances. Currently two optical fibres are installed close to the beampipe, along the entire length of the experimental beamline, and will be tested further in 2022.

AWAKE and Plasma Applications There is a strong collaboration between CLEAR and the Advanced Wakefield (AWAKE) experiment at CERN, a facility used to investigate proton-driven plasma wakefield acceleration [79, 80]. Several beam diagnostics used, and to be used, on the AWAKE beamline were first tested and optimised at CLEAR. The spectrometer screen used to measure the energy distribution of the order 1 GeV electrons accelerated by AWAKE was calibrated and studied at CLEAR [81]. An initial investigation confirmed the uniformity of the screen, which was then followed by subsequent investigations looking to calibrate the measured light with charge impacted upon the screen and the time-dependant properties of this light. The charge calibration is currently the primary way to quantify the charge of accelerated electron bunches in AWAKE [82].

An electro-optical sampling (EOS) system is installed on the CLEAR injector [83]. The EOS system is able to perform high-resolution bunch length measurements, by analysing the modulation of a chirped laser field caused by an electro-optical crystal when exposed to the electric field of the bunch. The method is non-destructive and works with a single bunch, and may be used in AWAKE run 2c to provide real-time measurements of bunch length [80]. The system is currently being optimised at CLEAR to improve its resolution and ease of use.

Rubidium vapour is used as a plasma source on AWAKE. A potential rubidium vapour source for run 2c will include an OTR or scintillating screen to measure beam profiles [80]. The screen will be exposed to rubidium vapour and will be cyclically heated to 200° C. The

performance of the screens during and after this cycle is not known. Therefore, experiments are ongoing in CLEAR to measure the response of the screens to the beam during a heat cycle, with out without rubidium vapour.

AWAKE run 2c requires a second electron source [80]. The new source is currently being commissioned at CERN ready for installation at AWAKE for 2026 [84]. Following commissioning the source will be used as part of CLEAR, either in the current CLEAR beam hall injecting beams into the current beamline, or in a separate hall as its own low-energy test beam. As well as providing potential users with beams, the installation of the new source will allow the AWAKE collaboration to address performance challenges prior to its main installation.

Further plasma based research is undertaken at CLEAR, and an active plasma lens is installed on the beamline [85]. Such lenses can provide focusing in both the horizontal and vertical planes simultaneously, unlike quadrupole magnets, with significantly larger focusing gradients than can be achieved with magnets. Experiments were performed at CLEAR with different gases, ionised by high currents generated with a compact Marx bank [86]. The experimenters were able to demonstrate that by using argon gas, a linear magnetic field, of gradient 0.3 kT/m, can be produced, preserving beam emittance [87]. By using a 500 μm diameter capillary and argon gas, a linear focusing field of 3.6 kT/m was produced, an order of magnitude higher than magnetic elements [88].

Generation of THz Radiation Radiation in the THz frequency range has a variety of different uses ranging from imaging and security scanning, to the quantum control of materials [89]. Compact linac-based sources of THz radiation have the potential to provide advantages relative to other sources, such as significantly higher photon fluxes. Studies have been ongoing into producing THz radiation with the CLEAR electron beam [90]. By using trains of sub-ps bunches, it was shown that THz radiation can be generated through coherent transition radiation in thin metal foils, through Coherent Cherenkov radiation, and through coherent Smith-Purcell radiation in periodic gratings [90, 91, 45]. The peak power emitted at a frequency of 0.3 THz in these experiments was 0.1 MW for electron bunches of around 1 ps. By reducing the bunch length to 0.1 ps, for bunches of several hundred pC charge, it may be possible to generate a peak power of order 100 MW.

Particle Detector Research The CLEAR beamline is of use to some of the detector collaborations at CERN. A prototype photonic crystal developed by the LHCb RICH group was irradiated at CLEAR looking to observe Cherenkov light emitted at specific angles [92]. Such a detector could distinguish a greater range of particles, whilst being more compact, than a conventional Cherenkov radiator.

A team from the ATLAS detector group working on wireless data transmission for silicon tracker detectors irradiated a 60 GHz receiver/transmitter to test its radiation hardness [55].

1.5 Very High Energy Electron Radiotherapy

The development of compact, high-gradient cavities for projects such as CLIC, as well as novel laser wakefield based accelerators [93], has led to a recent surge in interest of using very-high energy electron beams (VHEE), between 50 - 250 MeV, for radiotherapy (RT). Radiotherapy is one of the main tools used in the treatment of cancers, with around half of all cancer patients requiring at least one course of RT in their treatment [94]. Globally cancer resulted in 9.6 million deaths in 2018, a figure which could grow to over 16 million annual deaths by 2040 without improved treatment. Therefore, developing innovative and widely available cancer treatments will be a key challenge for the coming decades. Although still at a relatively early stage of development, VHEE has the potential to become a useful treatment modality, providing potential advantages in both medical outcomes and financial costs [95].

1.5.1 The Present State of Radiotherapy

The goal of radiotherapy is to successfully kill the cells of a tumour whilst reducing damage to surrounding healthy tissue. In RT, ionising radiation is delivered to the tumour from an external source over a time period of several minutes. As the radiation passes through, energy is deposited into the cells of the tumour damaging their DNA, preventing the cell from reproducing [96]. The probability that all cells in a tumour are controlled or eradicated by a treatment is defined as the tumour control probability (TCP) and typically increases with radiation dose with a relation illustrated in Figure 1.7. As the radiation passes through healthy tissue in the body, damage is also done to healthy cells. The damage caused to

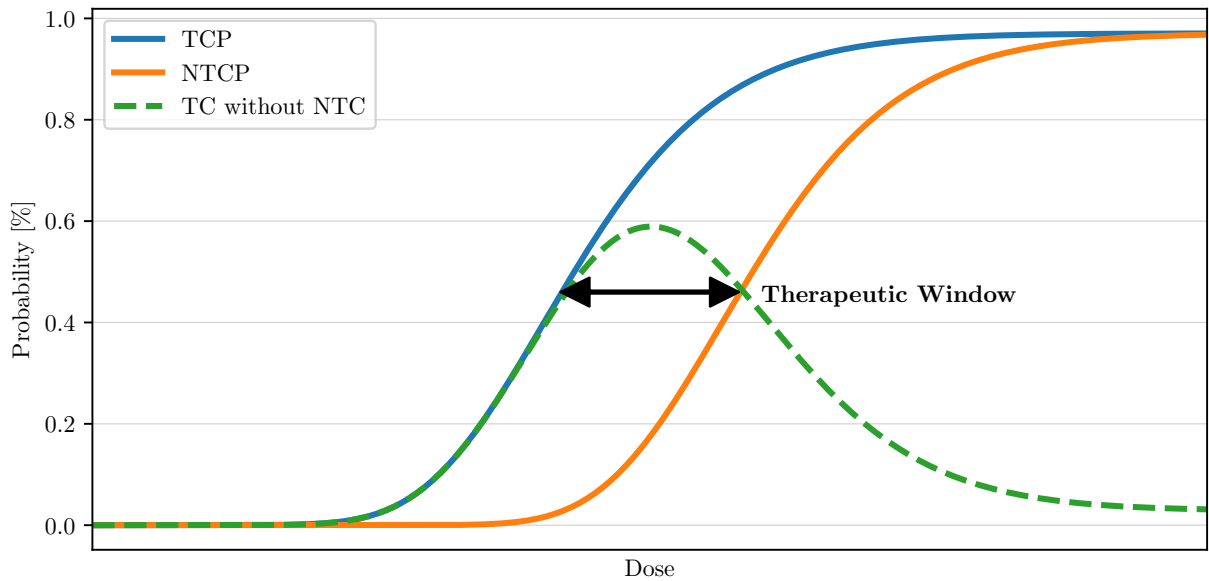


Figure 1.7: Tumour control probability and normal tissue complication probability vs. increased dose.

healthy cells can lead to normal tissue complications (NTC), with a likelihood described by a NTC probability (NTCP). All cells have repair mechanisms to allow the repair of damaged DNA. It is thought that the repair mechanisms in most tumour cells are not as effective as in healthy cells [96], resulting in a larger TCP than NTCP for a given dose, up to large doses. The separation between the two probabilities gives rise to a therapeutic window, in which the probability of tumour control without NTC,

$$P = TCP(1 - NTCP), \quad (1.7)$$

is maximised [97, 98]. The therapeutic window can be enlarged by employing a variety of different methods such as; the fractionation of the overall RT dose into around 30 or 40 individual dose fractions, of around 2 Gy each, delivered over several weeks allowing healthy tissue to recover in between fractions; collimating and shaping the beam profile to improve its uniformity in order to reduce the uncertainty in dose delivery; Using collimators to deliver conformally shaped beams that closely fit the tumour volume reducing the dose incident upon healthy tissue; delivering the dose from several angles surrounding the tumour, again to maximise the tumour dose whilst minimising NT dose; utilising more precise imaging of the target volume allowing the use of more precisely targeted RT beams onto the tumour; as well as using different RT modalities for different tumour types [96, 99].

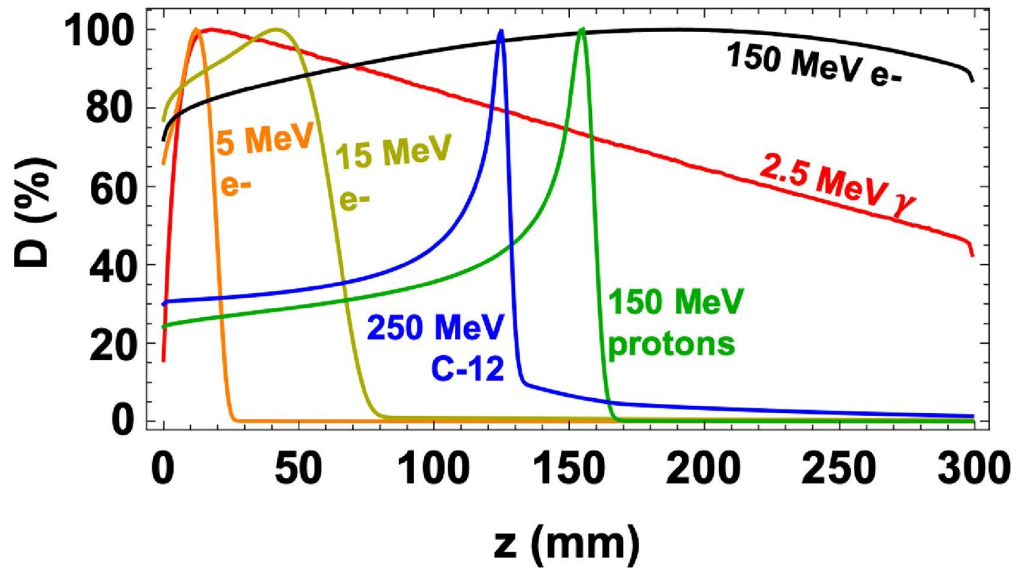


Figure 1.8: Percentage dose deposited vs. depth through water for different RT treatment modalities: 5 MeV electrons, 15 MeV electrons, 2.5 MeV X-ray photons (γ), 150 MeV protons, 250 MeV carbon-12 ions, and 150 MeV electrons, calculated from TOPAS Monte Carlo simulations [100].

There are three main types of particle beams currently available for RT: low-energy electrons, X-rays, and hadrons (protons and heavier ions). The depth-dose profiles of the three different modalities are shown in Figure 1.8. X-rays are by far the most commonly used beam in RT. Typically a small linac is used to accelerate electron beams to between 6 and 25 MeV [101]. The electrons are bent and focused towards the patient and are collided into a target, typically made from tungsten, where X-rays are produced by bremsstrahlung. The X-rays produced can have energies between 4 and 25 MV. The dose deposited upon entry into the patient is very low, meaning that damage to the skin of the patient is low. There is then a rapid rise in dose followed by a steady drop off, meaning that from a single beam, healthy tissue before the tumour receives a higher dose than the tumour. To reduce the dose on healthy tissue the linac is mounted upon a gantry that can be rotated around the patient. In this case the integrated dose delivered to the tumour can be significantly higher than the dose to surrounding healthy tissue.

By removing the X-ray producing target from the RT machine, it is possible to treat patients with low-energy electrons. The dose deposited by low-energy electrons is relatively flat from entrance until passing through a few centimetres when there is a rapid drop. Because of this, low-energy electrons are typically used to treat skin cancers and superficial tumours.

Hadrons, such as protons and ions, of energies ranging between 50 and 300 MeV/u are also used for radiotherapy. One benefit of using hadrons is that they deposit most of their dose in a single, sharp peak, known as the Bragg peak, which can be targeted on the tumour, thereby reducing the damage done to healthy tissue [101]. As the hadrons move through the body they deposit a small dose to tissue preceding the Bragg peak and almost no dose following the Bragg peak. The depth of the Bragg peak depends both on the energy of the hadron beam and the tissue that it passes through. The width of the Bragg peak is typically a few millimetres, much smaller than the typical size of a tumour. Therefore, beams of several energies are delivered to the patient to create a spread out Bragg peak (SOBP). The relatively large mass of hadrons means that the beams are less affected by scattering in the body and spread out less, again reducing the dose given to healthy tissue. The production of hadron beams of sufficient energy to reach deep-seated tumours requires the use of cyclotrons and synchrotrons, which are significantly larger and more complicated than the compact electron linacs mentioned previously. Furthermore, due to the relatively high rigidity of these beams, the beam delivery systems and gantries are also significantly larger than those required for low-energy electron or X-ray RT. The size and complexity of the accelerators and beam delivery systems make a hadron RT facility around three times more expensive than a photon facility [102]. Therefore, hadron therapy is often reserved for cancers that require the highest sensitivity in terms of dose delivery, such as paediatric tumours and brain tumours, and is virtually non-existent outside of high-income countries.

1.5.2 Very High Energy Radiotherapy

The first detailed investigation of the use of VHEE beams for radiotherapy was undertaken in 2000 [103]. Prior to this, the accelerators required to create beams of sufficient energies were considered too large and costly for use in hospitals, with most conventional RT linacs operating at gradients far lower than 100 MV/m. However, projects such as CLIC have opened the door to accelerators compact enough to produce VHEE beams in a typical hospital campus [95]. The cost of such a facility, therefore, could be relatively low compared to hadron therapy, although it would still likely be more expensive than X-ray RT.

Furthermore, VHEE beams could have several clinical advantages over other RT modalities. Unlike low-energy electrons, VHEE beams penetrate deep into the body to allow the

treatment of deep-seated tumours. The depth-dose profile of VHEE beams, shown in Figure 1.8, is flatter than that of X-rays, which could reduce the dose given to healthy tissue before the tumour. It was shown in simulation, and experimentally at CLEAR, that the depth-dose profile is relatively insensitive to tissue heterogeneities [100], compared to both X-ray and hadron beams. Therefore, VHEE-RT could potentially reduce range uncertainties when treating tumours in inhomogeneous areas of the body, such as the lungs or prostate.

Unlike X-rays, electron beams can be bent and focused using magnetic elements. By focusing a VHEE beam it is possible to change both the on-axis and transverse dose distribution profiles, potentially targeting the maximum dose to the tumour [104, 105, 106]. Again, the first experimental verification of the depth-dose profile of focused VHEE beams was performed at CLEAR. Simulations have recently shown that by varying the strength of a single quadrupole in the focusing system it is possible to create a spread out electron peak (SOEP), with several pulses, similar to a SOBPs [107]. An experimental verification of the SOEP at CLEAR has been planned.

The magnets used in VHEE systems will be significantly smaller than those used in hadron beam delivery systems due to the lower rigidity of electron beams of equal energy, reducing the size and cost of the system. The lower rigidity of electron beams also means that magnetic elements required to perform scanning of pencil beams can both be smaller and operate at a significantly higher rate.

One of the main advantages of VHEE-RT is that it is relatively easier to create a high-current beam. It would, therefore, be easier to perform RT at ultra-high dose-rates (UHDR) with VHEE beams than both X-rays and hadron beams [95]. UHDRs are interesting for RT as they have the potential to generate the so-called FLASH effect, discussed in section 1.6, which may significantly widen the therapeutic window.

A vital step in the clinical realisation of VHEE-RT, is to complete treatment plans that demonstrate that it can provide clinical advantages over current technology. Several treatment plans have been done for non-focused, scanned VHEE beams and compared to conventional techniques. The general conclusion from these studies is that scanned VHEE beams sit between X-ray and hadron therapy in the ability to reduce dose to sensitive organs surrounding tumours [95]. Concepts such as the SOEP and FLASH may increase the clinical

viability of VHEE-RT, however, detailed treatment plans have not been completed.

One potential source of uncertainty in these treatment plans is that there is very little direct data on the interaction of VHEE beams and living tissue, particularly the high-energy secondary X-rays that may be produced. However, Monte Carlo simulations have shown that the neutron yield for VHEE should be at least an order of magnitude lower than with X-ray and hadron beams [108, 95]. Furthermore, simulations have been done that suggest that the relative biological effectiveness of VHEE beams should be similar to low-energy electrons [109]. The first step towards an experimental verification of this was done at CLEAR when it was demonstrated that there was a very small difference in the damage done to plasmid DNA relative to low-energy electrons [110]. Future investigation of the biological effects of VHEE beams will require both improved simulations, including all focusing and scanning effects, as well as dedicated beam facilities that will allow experimental studies to be undertaken.

1.6 FLASH Radiotherapy

Recent RT studies in which doses were delivered at UHDRs, typically greater than 40 Gy/s, have shown the potential of shifting the therapeutic window in RT significantly [111, 112]. In this UHDR regime, there appears to be a significant drop in NTCs relative to RT at conventional dose-rates, without reducing tumour control. The FLASH effect could make RT treatments faster, cheaper, and with fewer NTCs. FLASH could also allow the treatment of tumours quickly enough to eliminate dose deposition errors due to the patient moving.

1.6.1 Status of FLASH Radiotherapy

The potential tissue sparing of UHDR beams was first noted in 1959 in bacterial cells [113], followed by mammalian cells in 1967 [114]. By 1969 the use of UHDR beams in radiotherapy was being discussed, noting that whilst technically challenging the use of these beams was feasible with contemporary accelerator technology [115]. Further studies were completed through the 1970s and early 1980s, although the use of UHDR beams for RT was largely forgotten until the field was sparked into life in 2014 [111]. In 2014, a study was published in which doses of up to 30 Gy were delivered to lung tumours in mice at either conventional dose-rates (< 0.03 Gy/s) or at UHDRs. The tumour control of both dose regimes was

shown to be similar, however, the level of NTCs was significantly lower for the doses given at UHDRs. The biological effect seen in this study was named the FLASH effect.

The 2014 study demonstrated that FLASH-RT could widen the therapeutic window between tumour control and NTCs. It has since been followed by experimental demonstrations of the FLASH effect in several different tissue types, in several different organisms. The FLASH effect in mice has been studied further with studies of the brain [116], skin [117], and intestines [118] undertaken. The effect has also been shown to be present in zebrafish [119], cats and pigs [120]. In 2019, a successful treatment of a human patient was completed with FLASH doses for a patient who had undertaken several RT courses at conventional dose-rates [121]. In each of the studies done so far no reduction of tumour control has been seen at UHDRs [122, 123]. At present several further studies are being undertaken with different types of beams, organisms, tissue, and dose characteristics, and even a clinical trial to treat bone metastases [122].

1.6.2 Mechanisms and Beam Characteristics

The mechanisms that lead to the FLASH effect are not well understood. Early studies suggested that the relative sparing of healthy tissue was caused by oxygen depletion in the cells [113]. It is known that cells with a low oxygen content, known as hypoxic cells, are 2-3 times more resistant to RT doses than cells that have normal oxygen levels. If the RT dose is delivered at UHDRs it is reasoned that oxygen cannot resupply the cells quickly enough, causing a transient hypoxia. Levels of oxygen depletion have been shown to be present in UHDR studies, however, the level of oxygen depletion is not high enough to fully explain the FLASH effect [124, 125]. Other mechanisms have been proposed such as, differential DNA damage at UHDRs, and differences in immune response to dose-rate [123, 126]. However, the overall mechanism is likely to involve several different factors and must be studied systematically in future.

It is generally thought that the FLASH effect can be achieved with a dose of at least 1 Gy delivered at a dose-rate of more than 40 Gy/s over a maximum irradiation time of ~ 100 ms. However, as the mechanisms behind FLASH are not understood, the optimal dose delivery is difficult to predict. The temporal characteristics of doses delivered at UHDRs on different

machines are different. For example, a 3 GHz low-energy electron linac will typically operate with a series of pulses firing at 10s to 100s of Hz. Each individual pulse will consist of a bunch train of between a few ns and a few μ s long. Within each train there are individual bunches of lengths of ~ 10 ps at a frequency of 3 GHz [111]. In comparison, a proton beam accelerated by a cyclotron is effectively a series of continuous pulses with pulse frequencies of MHz [127]. The conditions to achieve a FLASH effect in several studies are shown in Figure 1.9. From these studies, it is clear that the ability to achieve the FLASH effect or not depends on [128]: the total dose per pulse, with the threshold for FLASH thought to lie above ~ 1 Gy; the dose-rate intra-pulse, typically above $\sim 10^6$ Gy/s; the pulse repetition frequency; the mean dose-rate, thought to be above ~ 40 Gy/s; and the total irradiation time, thought to be ~ 100 ms. It is typically thought that the lower the number of pulses, the stronger the FLASH effect, but this remains to be shown conclusively. The different types of particle beam may also have a significant effect. Furthermore, different tissue types may have different responses to the same UHDR dose [128].

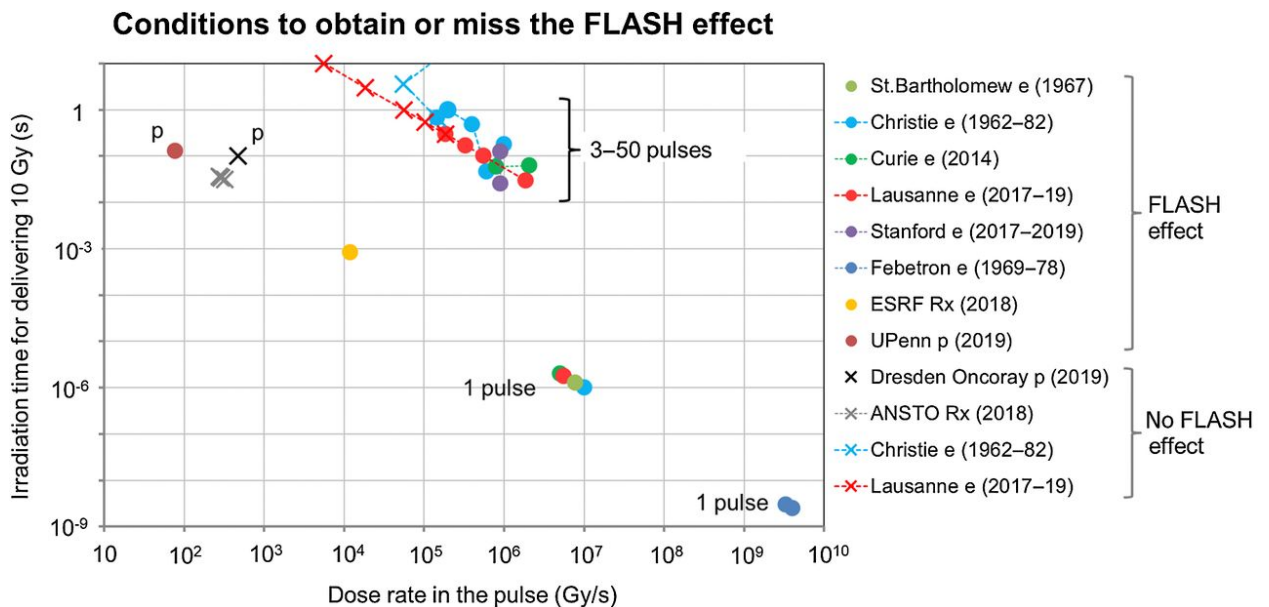


Figure 1.9: Temporal characteristics of several in-vitro and in-vivo irradiations at UHDRs, showing whether the flash effect was achieved (dots) or not (crosses) [129]. Black or grey crosses signify a study at a single dose-rate. Crosses and dots of the same colour signify a study with an escalation of dose-rate.

Most pre-clinical demonstrations of the FLASH effect have used low-energy electron beams, which cannot treat deep-seated tumours directly. Although low-energy electron FLASH-RT could be useful if undertaken during an operation, when the tumour is directly

exposed to the electron beam [130].

It has been shown that the short, high-intensity beams of X-rays produced through synchrotron radiation can induce the FLASH effect in cells [131]. However, building synchrotron light sources would not be practical or cost effective. It has so far only been possible to use UHDR X-rays produced by conventional linacs, over a small volume, diameter ~ 1 cm and a depth of 2 mm [132]. Whilst potentially useful for in-vitro research into the FLASH effect, such beams may have little clinical use. The UHDR volume is limited by the inefficiency of the X-ray producing target [128]. Most of the energy of the incoming electron beam is lost as heat in the target, thus it is not trivial to increase the X-ray flux simply by increasing the electron current without damaging the target. Any clinical UHDR X-ray machine will, therefore, require a new generation of target or have several conventional X-ray sources irradiating the patient simultaneously [128].

It is difficult to produce UHDRs across a large volume with current medical proton accelerators [133]. The only current technology able to produce high enough beam currents are cyclotrons, and even then only at when operating at high energy. At these high-energies it is impossible to target the Bragg peak inside the patient, so current proposed trials use transmission proton beams [122]. Losing the beneficial effects of the Bragg peak may counter some the benefits of delivering the dose at UHDRs, which will need to be studied in future. To perform proton FLASH-RT at lower energies, utilising the Bragg peak, will require a generation of new accelerators. Furthermore, the biological effect of producing a SOBP at UHDRs is not known. The low dose given to tissue before the tumour in each individual shot may not be high enough to produce the FLASH effect, which appears to have a threshold dose of ~ 1 Gy.

The relative ease of reaching high beam currents with VHEE beams make them a promising modality for FLASH-RT. Collider projects such as CLIC have several commonalities with the technology necessary to produce VHEE beams at UHDRs; both need high beam currents, for high luminosity at the IP in a collider, and to provide UHDRs for FLASH-RT; both need precisely controlled beams, to increase luminosity and decrease power consumption in a collider, and to safely treat patients in a FLASH facility; and both need to be compact, to reduce the costs of a collider, and for a FLASH-RT machine to fit in a hospital campus. Several pre-clinical linacs exist to investigate VHEE-FLASH. At present, CLEAR

provides a unique combination of beam current, beam energy, and availability of use [68]. However, the studies that can be performed on CLEAR are limited to small volumes as well as to non-living organisms. Further investigation of VHEE-FLASH will require dedicated accelerator facilities [44].

1.6.3 Translation of FLASH to the Clinic

Successful translation of studies of the FLASH effect to the clinic will require both technological and biological advances [122]. Previous RT technology was used clinically before the biological mechanisms were fully understood. At present FLASH is undergoing clinical trials, which may demonstrate the potential of FLASH in widening the therapeutic window, but will leave many potential issues. At present, no studies of the FLASH effect have investigated the long term impacts to patients. A cautious approach should be taken, as without proper knowledge of the mechanisms behind FLASH, these impacts will be difficult to predict. It will also be difficult to predict which modalities suit different tumour types [128], and whether we will still need to fractionate FLASH doses.

To understand the biology it will be necessary to complete systematic studies of the physical, chemical and cellular effects of UHDR radiation on tissue. Different modalities, with their different dose characteristics will be required for this. Therefore, it will be necessary to build new, dedicated beam facilities for each modality. The facilities built will need to be able to produce high-current beams and particle fluxes, that are easy to control, and have uniform beam profiles. It will also be necessary to define a so-called biological dosimeter to compare the FLASH effect induced by different dose-rates. It is thought that a simple organism such as zebrafish embryos could be used for this purpose [134].

In addition to new beam facilities, new diagnostic technology will be required. Conventional RT uses dosimetry devices such as ionisation chambers to measure the amount of dose deposited into a patient in real time, ensuring that the total dose delivered can be corrected. Studies of ionisation chambers have shown that at UHDRs they exhibit highly non-linear behaviour [135, 68]. For the successful operation of FLASH in clinics, these ionisation chambers will either need to be developed, or new technology, possibly from the world of particle physics, used in their place.

1.7 Thesis Outline

The work in this thesis builds on irradiation experiments performed at CLEAR. Technical details of the CLEAR facility are described in Chapter 3, with a beam dynamics model used to optimise the beamline proposed. The model is used to optimise the beamline for bunch compression, as well as the reduction of emittance growth. The model is then extended in Chapter 4 to investigate several proposed upgrades to CLEAR and assess their effect. The model of the CLEAR photoinjector is then used to demonstrate that beams with uniform transverse profiles can be produced from a simple photoinjector set up. Beams with uniform profiles could be very useful for irradiation experiments, therefore, a compact irradiation facility is proposed in order to produce such beams. As several key accelerator physics concepts are mentioned in the course of this thesis, they are detailed in Chapter 2. The thesis closes with a series of conclusions in Chapter 6.

Chapter 2

Beam Dynamics

To avoid confusion, the following chapter will discuss some of the key definitions and concepts in accelerator physics that are used later in this thesis. The chapter is meant to summarise these concepts. A more exhaustive description can be found in several specialised books such as [136, 17, 137].

2.1 Coordinate System

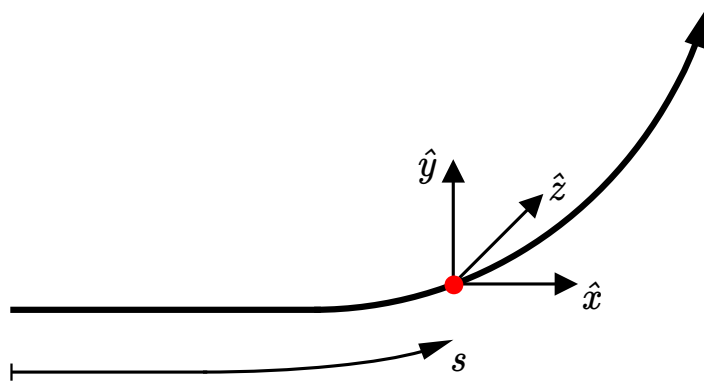


Figure 2.1: The Frenet-Serret coordinate system describing a reference particle (red) at distance s along an ideal path. \hat{x} , \hat{y} and \hat{z} are the orthogonal unit vectors relative to the reference particle in the horizontal, vertical and longitudinal directions respectively.

For the remainder of this thesis, the motion of each particle is defined with respect to the Frenet-Serret coordinate system, shown in Figure 2.1. In this coordinate system, particles are measured relative to a reference particle of momentum P_0 , following an ideal trajectory through the accelerator at a path length s . The horizontal, vertical, and longitudinal dis-

placements of these particles to the reference are given by x , y , and z respectively. The coordinates x' , y' describe angles in transverse phase-space, defined as,

$$x' = \frac{dx}{ds} \qquad y' = \frac{dy}{ds}. \quad (2.1)$$

The fractional offset in longitudinal momentum of each particle is given by,

$$\delta = \frac{p - P_0}{P_0}. \quad (2.2)$$

The coordinates in the horizontal, vertical and longitudinal motion can be combined into the 6-dimensional vector,

$$\vec{x}(s) = \begin{pmatrix} x \\ x' \\ y \\ y' \\ z \\ \delta \end{pmatrix}, \quad (2.3)$$

to fully define the motion of each particle.

2.2 Transverse beam dynamics

2.2.1 Single Particle Motion

As they pass through the magnets located in an accelerator lattice, particles undergo oscillations in the transverse plane known as betatron oscillations [136, 17, 137]. The transverse particle motion of these particles is described by Hill's equations,

$$\frac{d^2x(s)}{ds^2} + K_x(s)x(s) = F_x(s), \qquad \frac{d^2y(s)}{ds^2} + K_y(s)y(s) = F_y(s), \quad (2.4)$$

where $K_x(s)$ and $K_y(s)$ are focusing functions dependant on the magnetic lattice, and $F_x(s)$ and $F_y(s)$ are forces due interactions of the particles with other particles in the beam or external fields. The solution to Hill's equation in the horizontal direction, x , is given by,

$$x(s) = \sqrt{A_x \beta_x(s)} \cos(\mu(s) + \mu_0), \quad (2.5)$$

where $\beta_x(s)$ is an amplitude factor known as the beta function, A_x is the action, $\mu(s)$ is the betatron phase, and μ_0 is a constant. According to Liouville's theorem, the action is

constant under the influence of conservative fields. However, this is not the case when the particles are emitting energy due to effects such as synchrotron radiation.

The motion of a particle in an accelerator will trace an ellipse in phase-space described by,

$$2A_x = \gamma_x(s)x^2 + 2\alpha_x(s)xx' + \beta_x(s)x'^2, \quad (2.6)$$

where,

$$\alpha_x(s) = -\frac{1}{2} \frac{d\beta_x(s)}{ds} \quad \gamma_x(s) = \frac{1 + \alpha_x(s)^2}{\beta_x(s)}. \quad (2.7)$$

The relationship between, $\alpha_x(s)$, $\beta_x(s)$ and $\gamma_x(s)$ to the phase-space ellipse is shown in Figure 2.2. The area of the phase-space ellipse is equal to $2\pi A_x$. The solution to Hill's equation in the vertical plane is similar to the horizontal.

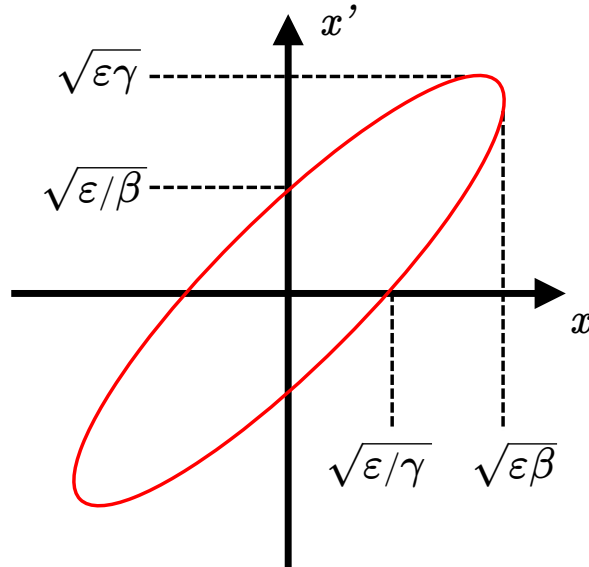


Figure 2.2: General ellipse in horizontal phase-space, showing the relation of x and x' to $\alpha_x(s)$, $\beta_x(s)$ and $\gamma_x(s)$.

2.2.2 Motion of Beams

Beams in particle accelerators consist of more than a single particle. It is, therefore, necessary to define the motion of the ensemble of particles in a beam. It is possible to represent the motion in phase-space of a beam of individual particles, each with its own action, by selecting an area in phase-space that encompasses a specific proportion of the beam. The area of this phase-space is defined as the emittance of the beam. In order to describe a beam of arbitrary

shape in phase-space it is necessary to define the root mean square (rms) emittance, ϵ_{rms} , of the beam distribution. The rms emittance is defined using the moments of the distribution such that,

$$\epsilon_{x,rms} = \sqrt{\langle x^2 \rangle \langle x'^2 \rangle - \langle xx' \rangle^2}. \quad (2.8)$$

The relations shown in Figure 2.2 remain valid for a beam of particles of emittance $\epsilon_{x,rms}$. Notably, the beam size, $\sigma_{x,rms}$ is given by,

$$\sigma(s)_{x,rms} = \sqrt{\epsilon_{x,rms} \beta_x(s)}. \quad (2.9)$$

If the momentum of the beam is increased, as occurs during acceleration, the angles in transverse phase-space reduce in a process known as adiabatic damping. Therefore, the emittance of the beam also decreases. It is, therefore, useful to normalise the emittance in order that it remains constant during acceleration. The normalised emittance of a beam, $\epsilon_{x,n}$ is given by,

$$\epsilon_{x,n} = \gamma \beta \epsilon_{x,rms}, \quad (2.10)$$

where γ and β are the Lorentz gamma and beta of the beam. As mentioned previously, Liouville's theorem means that the action of particles at a constant energy is conserved. However, the rms emittance of a beam can be degraded by effects such as space-charge [136].

2.3 Velocity Bunching

It is often desirable to compress the length of the bunch. One way of performing bunch compression in a linac is to use the velocity bunching technique. Originally proposed in 1965, the technique was not regularly used to compress bunches to ultra-short lengths, with magnetic compression often preferred [138, 139]. However, with the development of the high-brightness beams that can be produced in photoinjectors, the idea was renewed in order to avoid the emittance growth associated with magnetic compression of high-brightness beams, caused by effects such as coherent synchrotron radiation [140].

Velocity bunching involves inducing a higher velocity to particles at the tail of the bunch than particles at the head. To achieve this, the phase of an RF cavity must be shifted from the peak accelerating phase to a phase at which the head of the bunch receives a lower

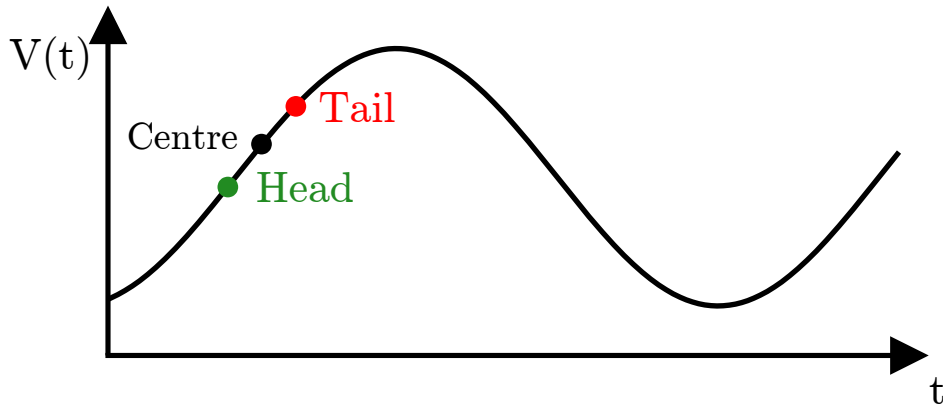


Figure 2.3: Sample RF wave vs time showing the centre, head and tail of a bunch undergoing velocity bunching.

accelerating field than the tail, as shown in Figure 2.3. To maximise the velocity difference, the technique should be used when the beam is at a low energy. In velocity bunching a phase-space rotation occurs, with a length spread being converted to an energy spread. The maximum rate of compression is achieved when the cavity RF phase has been shifted from the peak accelerating phase by 90° , known as zero crossing. The beam is accelerated simultaneously to being compressed. As the beam gains energy, the rate of compression drops. Presently velocity bunching is used for bunch compression at several accelerator facilities including CLEAR [84, 141, 142]

2.4 RF Photoinjectors

Photoinjectors are electron sources that produce beams with compact 6D phase-space, known as high-brightness beams. First proposed in the 1980s [143, 144], they are used to produce beams with low emittance and short bunch length without the need to use additional bunching systems following the RF gun. Because of this, it is possible to produce very compact photoinjectors compared to other electron bunch sources. Presently photoinjectors are used in a wide range of different accelerator facilities such as free electron lasers [145, 76], energy recovery linacs [146], future electron positron colliders such as CLIC [147], and experimental facilities such as CLEAR.

Photoinjectors consist of a laser beam that is directed onto a photocathode. The laser

beam liberates electrons from the surface of the photocathode, via the photoelectric effect, which can then be accelerated by a surrounding RF cavity of a few RF cells. The number of electrons produced per photon in the laser beam is defined as the quantum efficiency. The photocathode can be made of metals such as tungsten or copper [148, 76], which tend to have low quantum efficiency but are more durable, or semi-conductors such as Cs₂Te or CsK₂Sb which have quantum efficiencies several order of magnitude higher, but are less durable [53, 149]. It is necessary to use a laser of a specific frequency on each photocathode type. By using a pulsed laser it is possible to produce short bunches, with complex time structures, in a relatively small space. The parameters of the laser such as the transverse spot size and pulse length can be varied to produce beams with different parameters.

2.4.1 Emittance Growth in a Photoinjector

The emittance of the bunches produced in a photoinjector depends on several effects. The emittance is typically dominated by RF focusing effects and the space-charge forces within the bunch [150], however, other sources of emittance growth exist. The lower limit of emittance is give by thermal effects in the photocathode [151]. The contribution to the rms emittance due to thermal effects, ϵ_{th} , is given by,

$$\epsilon_{th} = \frac{\gamma\beta\sigma_{x,y}}{2} \sqrt{\frac{k_B T_c}{m_e c^2}}, \quad (2.11)$$

where $\sigma_{x,y}$ is the laser spot size, k_B is Boltzmann's constant, T_c is the temperature of the photocathode, γ and β are the Lorentz gamma and beta factors, and m_e is the electron rest mass. Typically the contribution to the normalised emittance due to thermal effects is small, often less than 1 π mm mrad [152].

A more significant contribution to the emittance is caused by RF focusing effects. Electrons at different phases in an RF field experience different focusing forces from the field. As electrons produced in a photoinjector are spread across the bunch length there is a time dependent variation in RF focusing in the gun of a photoinjector. The variation in RF focusing causes an emittance growth relative to ϵ_{th} . The contribution to the rms emittance, ϵ_{RF} , given by RF focusing can be written in practical units as,

$$\epsilon_{RF} = 2.73 \times 10^{-11} E_0 [MV/m] f^2 [MHz] \sigma_{x,y}^2 [mm] \sigma_t^2 [ps], \quad (2.12)$$

where E_0 is the maximum electric field strength of the gun, f is the frequency of the gun RF, and σ_t is the laser pulse length.

The third main contributor to the emittance of the beam is caused by space-charge forces within the beam. Space-charge forces are the result of the Coulomb interaction between particles in the bunch, and rapidly decreases with increased bunch energy. However, the forces can be large inside the RF gun. The space-charge contribution to rms emittance is given in practical units by,

$$\epsilon_{sc} = 3.76 \times 10^3 \frac{Q[nC]}{E_0[MV/m](2\sigma_{x,y}[mm] + \sigma_t[ps])}, \quad (2.13)$$

where Q is the bunch charge. The total rms emittance, ϵ_{tot} , of the bunch is given by,

$$\epsilon_{tot} = \sqrt{\epsilon_{th}^2 + \epsilon_{RF}^2 + \epsilon_{sc}^2}. \quad (2.14)$$

For high-brightness beams ϵ_{sc} is often the main contribution to emittance growth. However, emittance growth caused by space-charge forces can be compensated for. At many facilities, including CLEAR, emittance growth compensation is achieved by surrounding the RF gun with a solenoid magnet [153].

Chapter 3

Beam Dynamics in the CLEAR Linac

Since the beginning of user operation at CLEAR, significant work has been put in to consolidating and improving the performance of the facility. The following chapter will detail a study of the beam dynamics in the current CLEAR beamline. Primarily this will involve simulation studies of bunch compression in the CLEAR linac with experimental verification following.

3.1 Beamline Components

The CLEAR facility is composed of two sections as shown in Figure 3.1. The first section is the CLEAR injector, also known as CALIFES, which is 20 m long and was used as the probe beam injector in CTF3. Following the injector is the 16 m long experimental beamline.

3.1.1 CLEAR Injector

The CLEAR facility reuses the photoinjector designed for the probe beam of CTF3 [155] to generate electron bunches. The bunches are produced by a pulsed UV laser, with a pulse frequency of 1.5 GHz, directed onto a Cs₂Te photocathode [156]. The laser can deposit an energy of up to 1.6 μ J onto the photocathode, with a Gaussian laser spot of size variable between 0.4 and 2.5 mm rms, and a pulse length of 4.7 ps. The repetition rate of laser pulses incident on the photocathode can be increased to 3 GHz by means of an optical double pulse system.

The beams are accelerated to an energy of around 5 MeV by a 2.5 cell RF gun. RF power

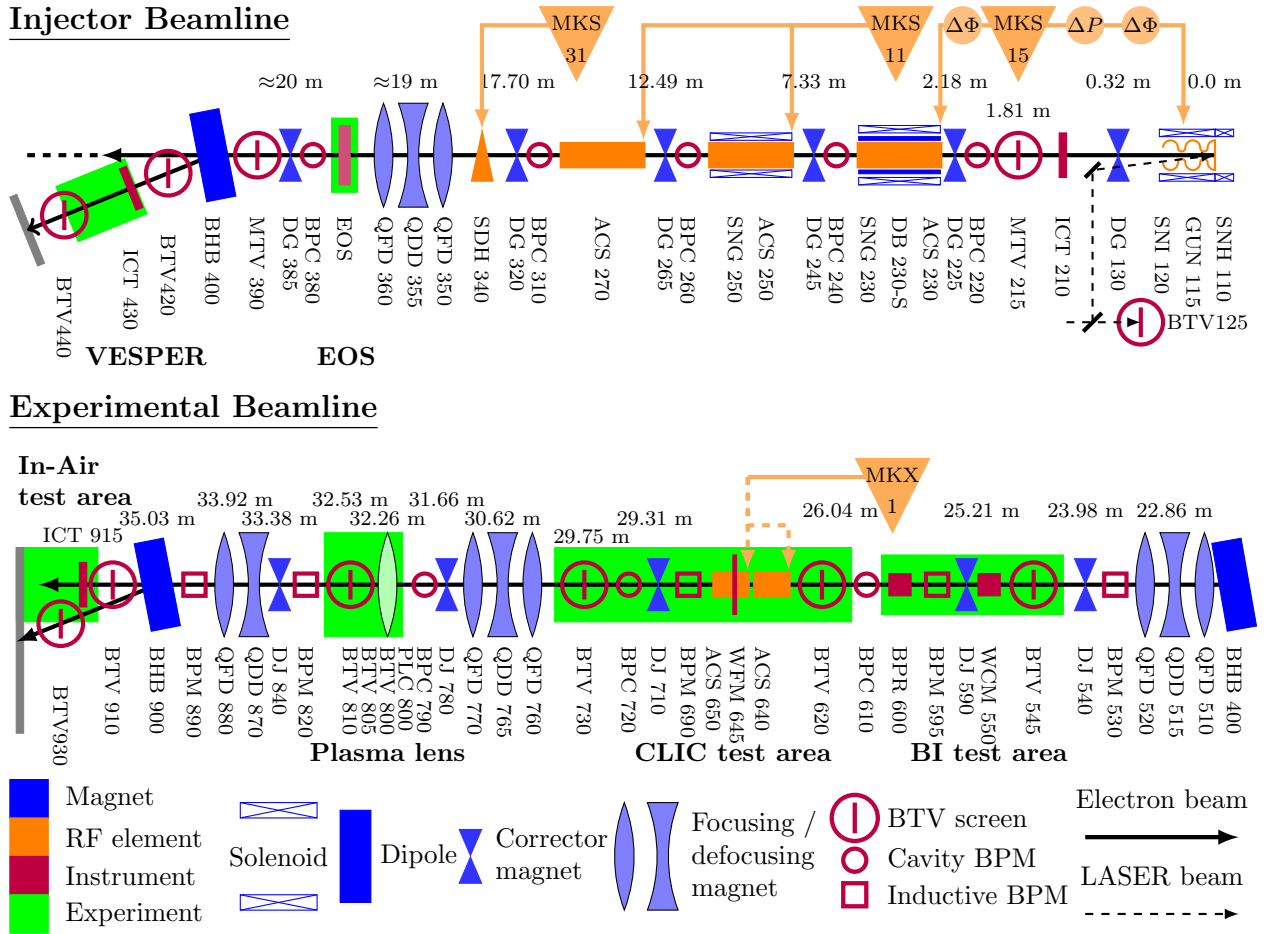


Figure 3.1: A diagram of the current CLEAR injector (**top**) and experimental (**bottom**) beamlines with the positions of magnets, RF elements, beam instrumentation and Experiments shown [154].

is supplied to the gun from a klystron with a frequency of 2.99855 GHz, and has an on-axis accelerating field of around 80 MV/m. The RF phase of the gun can be shifted with a phase shifter. The power can also be attenuated independently of the klystron power. Surrounding the gun there are two solenoid magnets to provide emittance growth compensation. One solenoid provides a focusing magnetic field to the beam travelling out of the gun and one provides a bucking field to ensure that the overall magnetic field is zero on the photocathode.

Following the RF gun there are three travelling wave accelerating cavities from the LEP Injector Linac (LIL) [157, 158, 159]. Each 4.5 m long cavity has 135 accelerating cells, with a decreasing iris diameter in order to provide a quasi-constant gradient. The first accelerating cavity, known as the bunching cavity or buncher, is powered by the same klystron as the RF gun. Independent control of the buncher phase is achieved with a mechanical phase shifter.

However, there is no individual control of the RF power which has a peak on-axis field of 18 MV/m. The following two accelerating cavities are connected to a single klystron. The RF pulse of this klystron is compressed such that the peak on-axis field is around 21 MV/m. By varying the power and phase of these cavities the beam energy can be adjusted in the range 60 - 220 MeV. The buncher can be used for both bunch compression through velocity bunching as well as acceleration. Both the buncher and the first accelerating cavity are surrounded across their entire length by 9 SNS type solenoid magnets from LIL to provide emittance growth compensation and beam focusing [158].

Further along the beamline there is an RF deflecting cavity (RFD) used to measure the bunch length (section 3.1.3). The cavity was originally designed for use in the LIL complex [160].

A quadrupole triplet is positioned after the RFD. The triplet provides strong focusing in order to aid beam transport and improve beam quality, and can be used to increase the resolution of bunch length measurements made with the RFD. The beam then passes through the Electro-Optical bunch profile experiment which is permanently installed on the beamline [83]. At the end of the injector beamline there is a dipole magnet used to measure the beam energy as well as to direct the beam to the Very energetic Electron facility for Space Planetary Exploration missions in harsh Radiative environments (VESPER) test stand (Fig. 3.2). The dipole magnet can be reversed in polarity to allow a de-Gaussing procedure to remove hysteresis effects in the iron core in order to improve the accuracy of energy measurements and aid beam transport. Several corrector magnets are installed along the beamline to provide orbit corrections to the beam to ensure good beam transport.

Along the length of the injector there are several beam diagnostics installed. Integrated Current Transformers (ICT) [162] are installed following the gun and in the VESPER test stand. The ICTs are used to measure the beam charge and assess beam transport. Several cavity Beam Position Monitors (BPM), used to measure the position and intensity of the beam in the beam pipe, are positioned along the beamline after the gun, each accelerating structure, and the quadrupole triplet [163]. Further measurements of the beam position and size can be made using the Beam Television screens (BTV) shown in Figure 3.1. A phosphor BTV screen installed after the RF gun is used to characterise the gun performance. The second BTV is used for general beam optimisation and bunch length measurements in

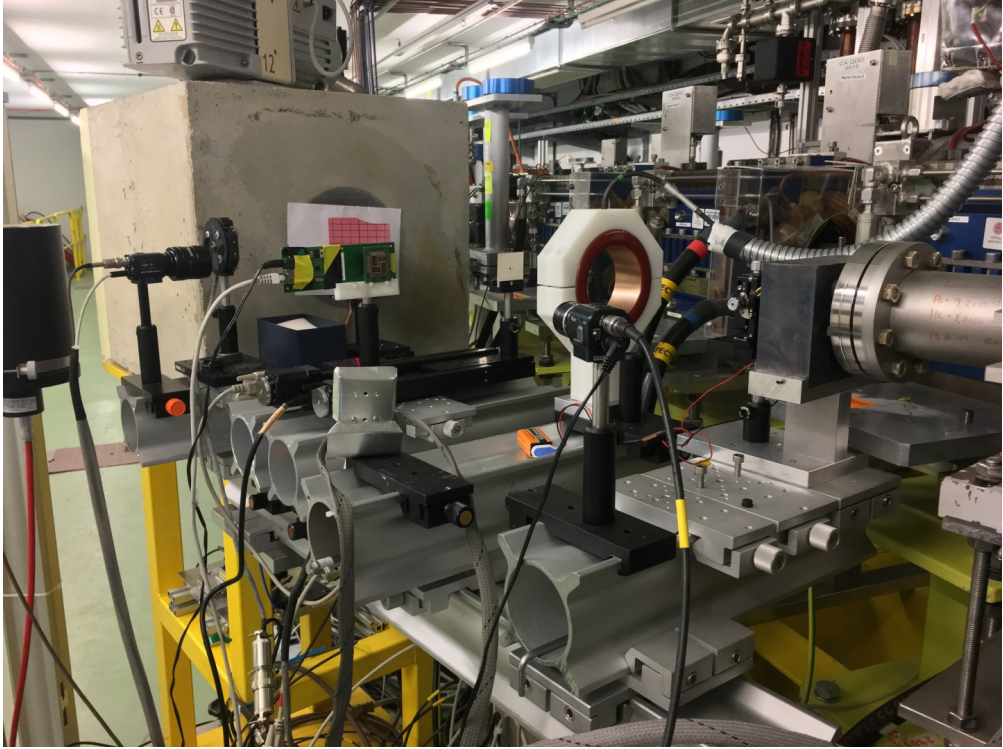


Figure 3.2: A photograph of the VESPER test stand [161]. An SRAM board from the ESA JUICE irradiation experiment is installed [57].

conjunction with the RFD and can either be used with an optical transition radiation (OTR) screen or a Yttrium Aluminium Garnet (YAG) scintillating screen [164]. There is a Chromox screen installed in vacuum following the VESPER dipole to measure the beam energy and another Chromox screen installed in air to measure the bunch profile for users. All of the BTV screens in the injector use analogue cameras to measure the beam profile. Movable filters are installed on most BTV cameras at CLEAR to avoid saturation of the cameras.

3.1.2 Experimental Beamline

The first element in the experimental beamline is a quadrupole triplet. There is a second quadrupole triplet on the experimental beamline following the CLIC structures and a doublet just before the in-air test stand.

Two X-band CLIC prototype accelerating structures are installed in the experimental beamline and are currently used to measure wakefield effects in X-band structures. The structure is not currently connected to an X-band power source, however, this is proposed for the future [84]. Following the CLIC structures is a removable section of beampipe, in

which four experimental CLIC cavity BPMs can be installed [66]. As the CLIC cavity BPMs provide a significant aperture restriction, when they are not being tested they are removed from the beamline. There is also a plasma lens experiment installed on the experimental beamline, which is used to investigate the focusing effect of a small plasma cell. At the end of the beamline is a dipole magnet which is used to measure the beam energy. Following the dipole magnet is the in-air test stand. As shown in figure 3.3 the in-air test stand is used to perform irradiation experiments as well as other experiments that can be undertaken in air. The exit window of the beampipe before the in-air test stand is made of kapton. An alignment laser is directed onto a mirror on the back of the BTV 910 screen, and reflected through the kapton window. The laser spot can then be used by users to align their experiments.

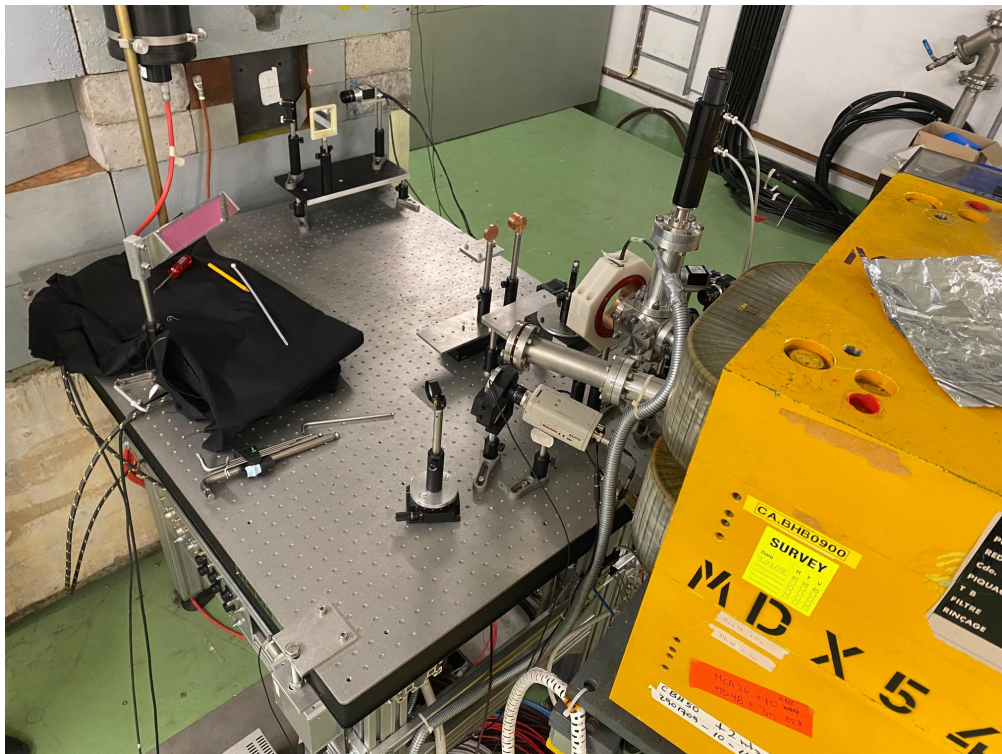


Figure 3.3: A photograph of the in-air test stand with two copper beam scatterers installed on a movable stage.

As with the injector beamline, the experimental beamline has several cavity BPMs and BTVs installed. Two BTVs, BTV620 and BTV800 use OTR screens, BTV930 uses a Chromox screen, with other BTVs using YAG screens. All screens other than BTV620 use analogue cameras. BTV620 is positioned before the CLIC structures and has a digital camera installed to improve the resolution of beam profile measurements for wakefield tests [165]. It is also possible to install up to four YAG screens and digital cameras on the in-air test stand

to provide beam profile measurements for users. The use of digital cameras on CLEAR will be increased in future with the development of a new control system. Further beam diagnostics have been taken from the former CTF3 drive beam and installed in CLEAR with their electronics adjusted for the lower beam currents and shorter bunch trains of CLEAR. Of these, several inductive BPMs have been installed which have recently been calibrated to provide beam charge and beam position measurements [166]. A wall current monitor has also been taken from the drive beam and installed on CLEAR [167]. A third ICT is installed in the in-air test stand to provide beam charge measurements to users and assess beam transport. As with the injector, several corrector magnets are used to improve beam transport.

3.1.3 Measurement of Bunch Length

Bunch lengths can be measured on CLEAR using the RFD and the downstream BTV 390. The principle of this technique involves using an RF field to deflect a bunch, as shown in Figure 3.4. The deflection of the bunch induces a correlation between the transverse bunch size and the bunch length [168].



Figure 3.4: A diagram of an RF deflecting cavity being used for bunch length measurement.

The RFD provides a deflecting force which imparts a time-dependent transverse kick to the bunch. Therefore, as the bunch passes through the RFD, particles along its length are deflected by a different amount. It is assumed that the RFD provides no accelerating field to the bunch. For transverse kicks of a small angle and bunches of length $\sigma_z \ll \lambda/2\pi$, the

deflection to the beam centroid, Δy , is given by,

$$\Delta y = \frac{eV_0}{E_0} \sqrt{\beta_c \beta_p} \sin \Delta\psi_y \sin \phi_{RF}, \quad (3.1)$$

where β_c and β_p are the beta function at the cavity and at the screen, E_0 is the beam energy, V_0 is the deflecting voltage, $\Delta\psi_y$ is the phase advance between the deflector and the screen, and ϕ_{RF} is phase of the RF deflector. ϕ_{RF} is defined as 0° at zero crossing. The vertical size of the beam, σ_y , after it has been deflected is given by,

$$\sigma_y = \sqrt{\sigma_{y_0}^2 + \sigma_z^2 \beta_c \beta_p \left(\frac{2\pi eV_0}{\lambda_{RF} E_0} \sin \Delta\psi_y \cos \phi_{RF} \right)^2}, \quad (3.2)$$

where σ_{y_0} is the vertical size of the bunch without the deflecting cavity, and λ_{RF} is the RF deflector wavelength. From equation 3.1 it is clear that when the RFD is phased at zero crossing there is no deflection to the bunch centroid.

It has been shown that quadrupole elements can be used to improve the resolution of the measurement without introducing any systematic errors [169, 170]. A limitation on the resolution of the technique is the size and resolution of the measurement screen relative to σ_{y_0} and σ_y . By using the quadrupole triplet on the CLEAR injector to minimise the size of σ_{y_0} , it is easier to determine the contribution to σ_y associated with the bunch length.

The RFD used on CLEAR has 6 cells each 25 mm long and is shown in figure 3.5. The frequency of the cavity is 2.99855 GHz and it is powered by an individual klystron. The timing of the RF pulse in the deflector can be adjusted to “insert” or “extract” the deflector pulse from the beam. To ensure an accurate measurement of the bunch length, the beam must pass through the centre of the cavity. The nearby screens and BPMs are used to check this. The first step in measuring the bunch length is to use the quadrupole triplet to minimise σ_{y_0} on the screen, an example of a beam profile measurement for a focused beam is shown in Figure 3.6a. The deflecting cavity must then be turned on, inserted, and ϕ_{RF} adjusted to locate zero crossing. The bunch is now extended in the vertical direction but not the horizontal as shown in Figure 3.6b. It must be noted that the position of the bunch centroid (Figure 3.6) does not move when the RFD is inserted, suggesting that beam is well aligned and the centroid is at zero crossing. The phase of the RFD is then varied to shift the bunch centroid to the two extremities of the screen. The phase of the RFD is then scanned across this range, with σ_y being measured at each phase step. The

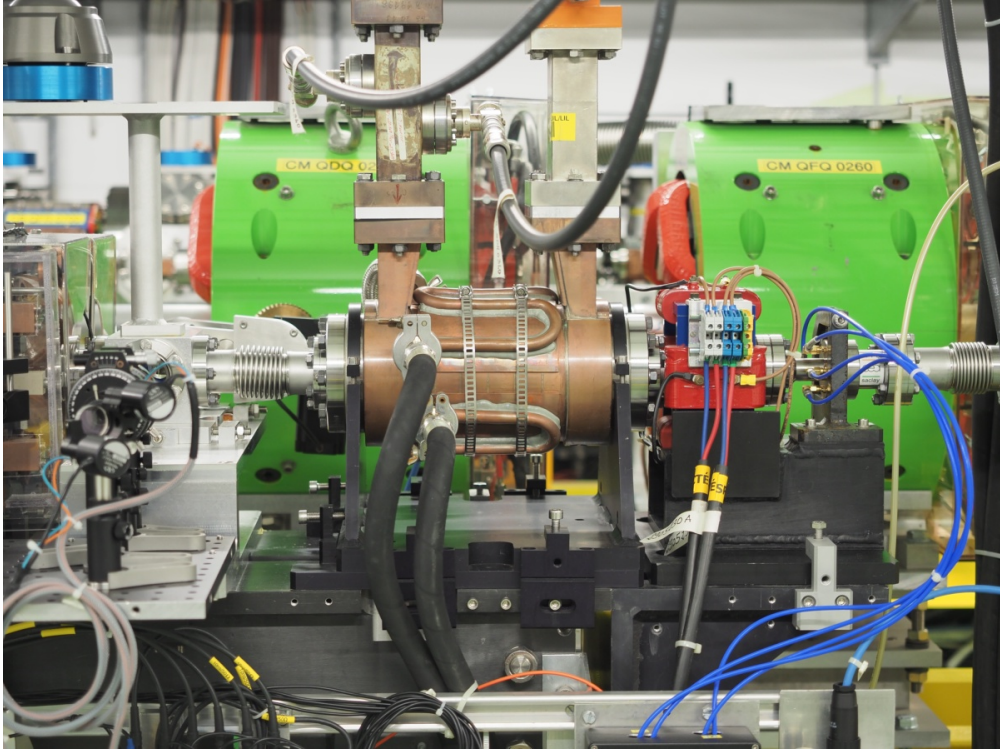


Figure 3.5: The RF deflecting cavity presently installed on the CLEAR beamline.

deflection of the bunch centroid and σ_y are then used to calculate the bunch length from equations 3.1 and 3.2. Any misalignment of the beam passing through the RFD could cause a systematic error. To reduce this, the phase of the RFD is shifted by 180° and the length measurement retaken. The final value of the bunch length measurement is taken to be the mean of the two. Using this method on CLEAR, it is possible to determine the bunch length to a resolution of around 0.2 ps. The method outlined here has been shown to give good agreement in bunch length measurement to measurements performed with a streak camera and for bunches longer than 1 ps, the minimum resolution of the streak camera [171], and to measurements taken using Cherenkov diffraction radiation for bunches of length between 0.5 ps and 2 ps [75]. Furthermore measurements taken of bunches shorter than 0.5 ps have given good agreement to several user experiments.

3.2 User Requirements

In order to satisfy the requirements of each specific user, the beam parameters available on CLEAR can be adjusted over a wide range. A list of typical beam parameters are given in Table 3.1. It must be noted that many of these parameters are not independent of each

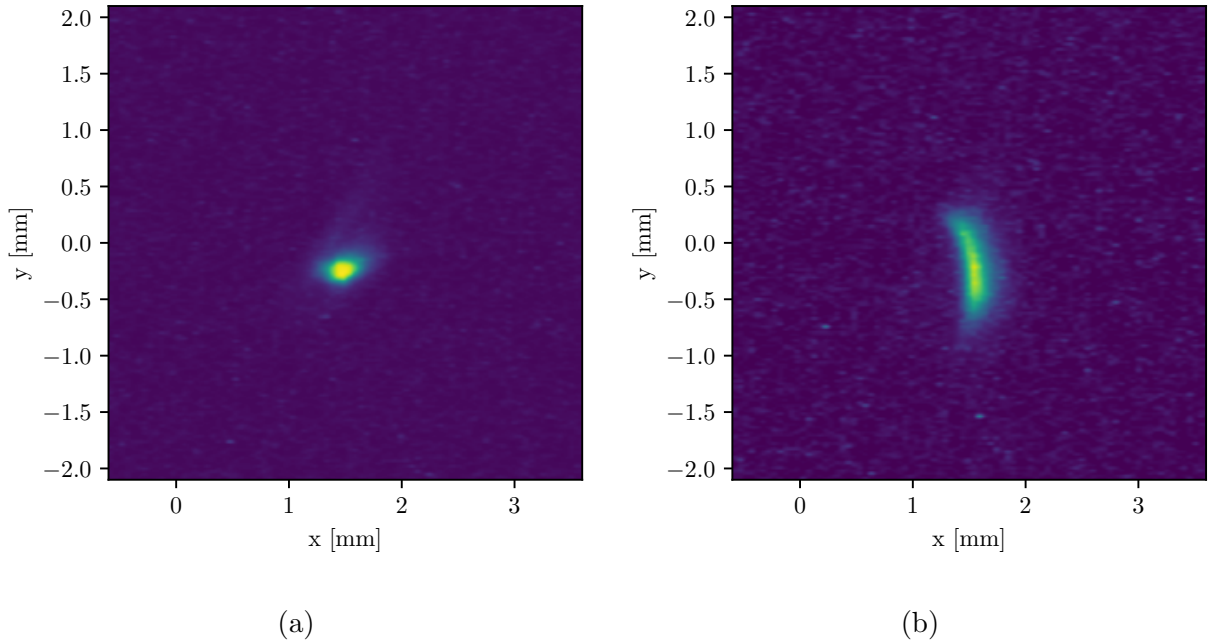


Figure 3.6: Transverse beam profiles measured on screen BTV 390 with the RFD extracted (a) and inserted into the beam (b).

other, for example, the emittance of beams with higher bunch charge will be higher than that of low-charge bunches.

Table 3.1: Available beam parameters in CLEAR.

| Parameter | Value or Range |
|-----------------------------------|---------------------------|
| Energy [MeV] | 60 – 220 |
| Energy Spread | < 0.2% rms (< 1 MeV FWHM) |
| Bunch length rms [ps] | 0.1 – 10 |
| Bunch charge [nC] | 0.001 – 3.0 |
| Norm. emittance [μm] | 1 – 20 |
| Bunch frequency [GHz] | 1.5 (3 with double pulse) |
| RF frequency [GHz] | 3.0 |
| Bunches per pulse | 1 – 150 |
| Max. charge per pulse [nC] | 30 |
| Beam repetition rate [Hz] | 0.8333 – 10 |

Typically irradiation experiments do not require specific beam properties other than a total amount of charge to impact upon a desired area. Normally these experiments are installed in-air on one of the two test stands. If the beam is required to be symmetric in x and y , then the experiment must be installed in the in-air test stand at the end of the beam line as the energy spread of the beam causes dispersion in the beam when bent

into the VESPER test stand. The transverse size of the beam at the experiment can be adjusted using the beam optics and adjusting the distance between the vacuum window and the target, which changes the amount scattering with the air undergone by the beam. The size of the beam can be further increased by introducing additional scattering elements, either inserting a previous BTV screen, by installing a water phantom, or metal or plastic scatterer between the beam and the target. Beam sizes for irradiation experiments typically range between a few mm, requiring a focused beam close to the exit window, and a few cm, following a scatterer. The number of bunches per train and the total irradiation time can then be adjusted to satisfy the user's needs.

Other experiments require beams with specific optical properties and specific bunch lengths. For example beams of normalised emittance of $\sim 3 - 5 \pi$ mm mrad were used to demonstrate the first aberration-free active plasma lens at CLEAR [87]. For this care must be taken to set up the beam correctly to avoid emittance growth. The laser must be positioned on the photocathode in order to minimise the strength of the first two correctors in the beamline, so to not introduce dispersion to the beam when the energy spread is relatively high out of the gun. In addition to this the strengths of the various solenoid magnets early in the beamline must be optimised to provide the greatest amount of emittance growth compensation.

One of the most common beam requests from users is to have beams of a specific bunch length. Some users require beams with ultra-short bunch lengths. Experiments, such as ones in the generation of THz radiation, Electro-Optical bunch profile measurements, and non-invasive measurements of bunch length with Cherenkov radiation, require bunches shorter than 1 ps [90, 83, 75]. Bunch compression can be done on CLEAR using the velocity bunching technique, and bunch lengths of less than 1 ps and even as short as 0.1 ps have been produced previously. However, as shown in Figure 3.7, these highly compressed bunch lengths were only possible for bunches of charge less than 0.2 nC, too low for many users' requests. If CLEAR is to provide beams across the full parameter range requested by users, higher charge bunches must be compressed.

Additionally, in the present design of the eSPS, it is proposed that the CLEAR injector be reinstalled in a different beam hall to its current installation and used as an injector to the eSPS linac [45]. The eSPS linac consists of a 70 m X-band linac used to accelerate electron

beams from 0.2 GeV, from the injector, to 3.5 GeV, when they are then injected into the SPS. In order to preserve beam quality in the X-band linac, the bunch length produced in the injector must be less than 1 ps in bunch length for charges up to 1.7 nC. If the CLEAR injector is to be used for the eSPS injector then high-charge bunch compression must first be demonstrated.

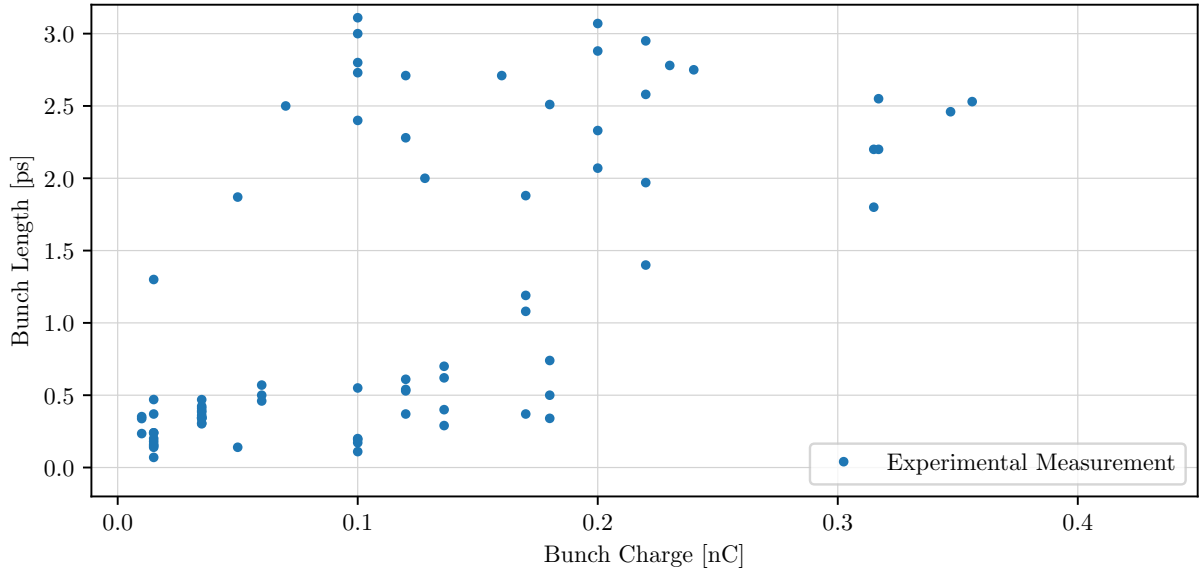


Figure 3.7: Measured bunch lengths vs bunch charge from previously undertaken bunch compression since the first beam operation in CLEAR in 2017.

3.3 ASTRA Model of CLEAR

In order to study and optimise the machine performance, a model of the CLEAR beam-line was produced and simulations were done. As the beam in CLEAR is produced from a photocathode any start-to-end simulations of the beam need to include the space-charge forces that are dominant in low energy beams. To simulate the beam with these space-charge forces, the particle tracking code ASTRA (A Space Charge Tracking Algorithm) was used [172]. ASTRA is a commonly used code in the design of photoinjectors [76, 145, 173], allowing beams to be produced from a photocathode and tracked through an accelerator. Furthermore, ASTRA simulations are used to inform the commissioning and optimisation of photoinjectors, and the code is well base lined against experimental data [174, 175, 176]. Unlike many other particle tracking codes, external RF and magnetic fields can be overlapped, allowing the simulation of RF elements surrounded by solenoid magnets. As beams

are tracked, ASTRA computes and inputs the effect of space-charge forces on the beam.

ASTRA simulates the beam as a collection of macro-particles and applies both the internal space-charge forces and external electric and magnetic fields to the beam. Space-charge forces can be calculated using a cylindrically symmetric grid algorithm or a fully 3D Fast-Fourier-Transform algorithm, the details of which can be found in [172]. In order to ease the computation time required for simulations, the tracking of the beam in CLEAR was completed using the cylindrically symmetric algorithm.

Photo-emission of the beam can be simulated in ASTRA. By inputting the parameters of the photoinjector, such as the effective work function, φ_{eff} , and photon energy, E_{photon} , ASTRA simulates the emission of the beam from a Fermi-Dirac distribution. In this distribution the values of rms transverse momentum, $\sigma_{p_{x,y}}$, electron energy, σ_E , and thermal emittance, $\epsilon_{t_{x,y}}$ are defined by,

$$\sigma_{p_x} = \sigma_{p_y} = \sqrt{\frac{E_{photon} - \varphi_{eff}}{3m_e c^2}}, \quad (3.3)$$

$$\sigma_E = \frac{1}{3\sqrt{2}}(E_{photon} - \varphi_{eff}), \quad (3.4)$$

$$\epsilon_{t_{x,y}} = \sqrt{\frac{E_{photon} - \varphi_{eff}}{3m_e c^2}}, \quad (3.5)$$

respectively. The laser used at CLEAR has a wavelength of 262 nm and, therefore, $E_{photon} = 4.73$ eV. For a Cs₂Te photocathode the value of φ_{eff} is 3.5 eV. ASTRA is also able to simulate the mirror charge that prevents the emission of electrons from the photocathode in high space-charge bunches.

The fields of RF cavities and solenoid magnets can be input into ASTRA using field tables. Since in CLEAR there is a rotational symmetry about the beam axis of both the RF cavities and the solenoid magnets, only the longitudinal component of each field is required. ASTRA calculates the radial and azimuthal components of the field from this longitudinal component by way of a field expansion. The normalised longitudinal components of the electric field of the RF Gun and the magnetic field of the surrounding solenoid used in the model of CLEAR are shown in Fig. 3.8a and Fig. 3.8b respectively. The magnetic field of the 9 solenoids, surrounding both the bunching cavity and the first accelerating cavity,

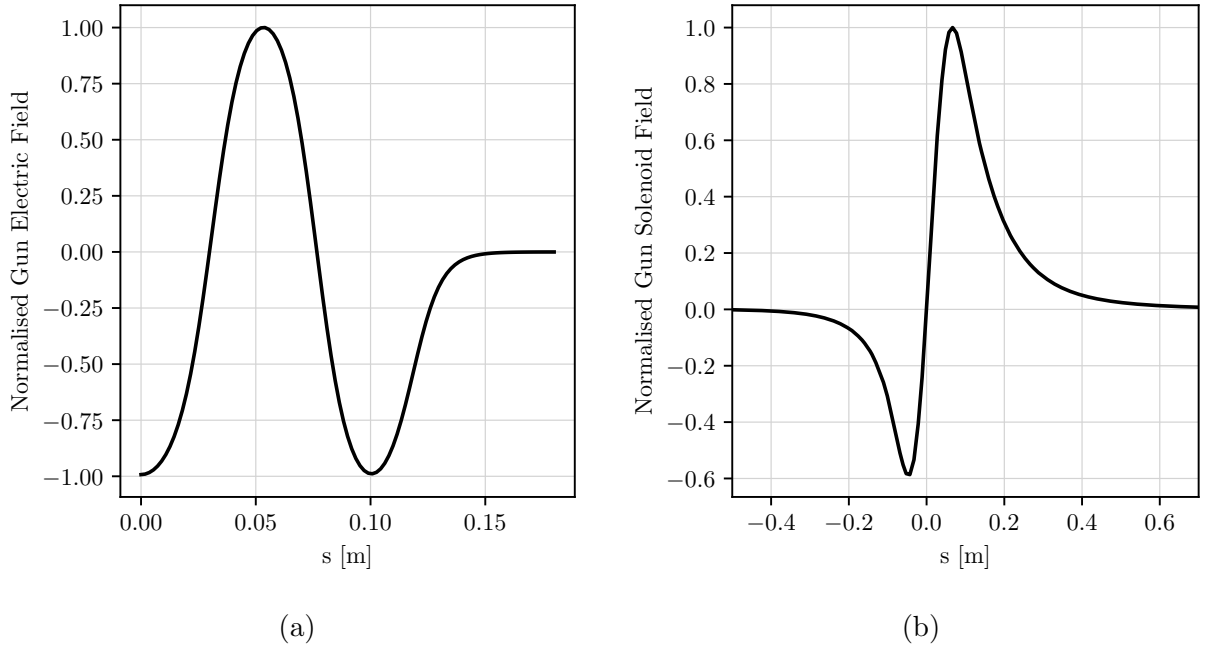


Figure 3.8: **(a)** The normalised electric field of the RF gun and **(b)** the normalised magnetic field of the solenoid magnet surrounding the gun vs distance from the photocathode.

is modelled as a single finite continuous solenoid. The longitudinal component of a finite continuous solenoid, B_z , of length, l , radius, R , is given by,

$$B_z = \frac{\mu_0 N I}{2} \left(\frac{l/2 - z}{l \sqrt{R^2 + (l/2 - z)^2}} + \frac{l/2 + z}{l \sqrt{R^2 + (l/2 + z)^2}} \right), \quad (3.6)$$

where N is the number of coils and I is the current. Each SNS type solenoid has a length of 236 mm, a radius of 90 mm and 95 coils. The maximum operating current in CLEAR is 200 A which leads to a maximum magnetic field of approximately, 0.1 T. The input and output fields of the LIL accelerating structures, as well as the repeating cell field are used to generate the full field of these cavities in ASTRA. The full ASTRA model of CLEAR can be accessed via [177].

The aperture of the CLEAR beamline has been approximated using the design documents of each beamline component and is shown in Figure 3.9. The tightest aperture restrictions on CLEAR are the RF elements, the accelerating cavities, the cavity BPMs, and the RFD cavity. It must be noted that the aperture of the accelerating structures is an approximation, assuming that the aperture is defined by the iris diameter and varies constantly from input to output. In reality the iris diameter varies discretely over eight radius transitions.

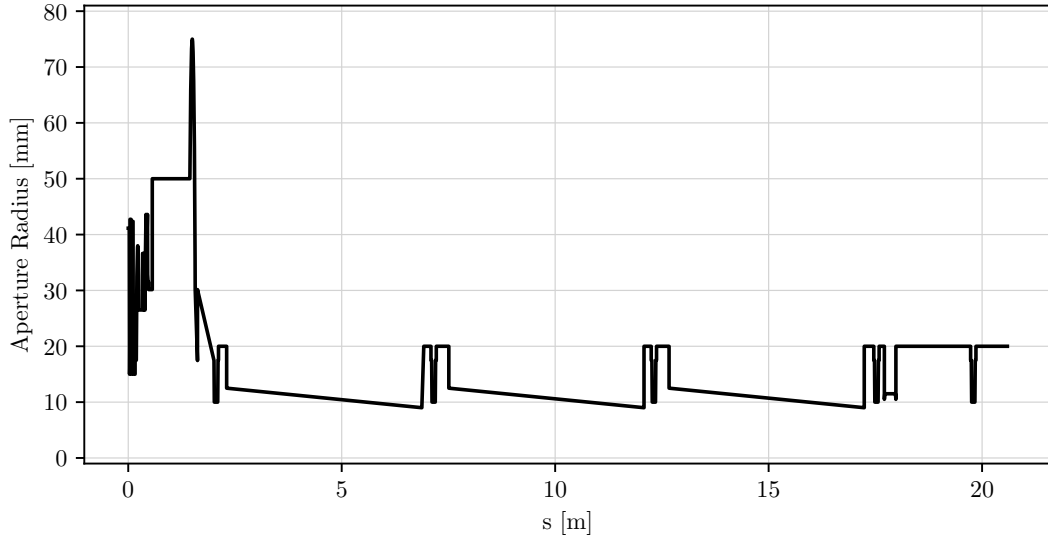


Figure 3.9: The approximate radius of the CLEAR aperture as a function of distance from the photocathode to the first quadrupole triplet.

3.4 Bunch Compression

To satisfy user demands for high-charge bunches with sub-ps bunch lengths an optimisation of bunch compression was performed. Compression of the electron bunches in CLEAR can be performed using the velocity bunching technique outlined in section 2.3. Velocity bunching is performed on CLEAR by first turning off the klystron used to power the second and third cavities. By doing this we are able to adjust the phase of the bunching cavity in order to maximise the beam energy and minimise the energy spread. The RF power is then returned to the two accelerating cavities and the beam energy is again maximised. The settings of the beam orbit correctors are optimised to ensure good beam transport. The phase of the bunching cavity is then slowly shifted towards zero crossing. As the phase of the buncher is shifted, the phase of the two accelerating cavities is shifted, again to maximise the beam energy and minimise the energy spread. As the phase of the buncher is lower the beam energy drops relative to on-crest acceleration, therefore, the settings of the correctors and solenoid magnets have to be adjusted to ensure good beam transport. In addition to the bunching cavity, the phase of the RF gun can also be shifted to provide additional compression.

To demonstrate that high-charge bunch compression is possible in CLEAR, simulations of the beamline were undertaken using the ASTRA model. The simulation work was completed

in a piecewise fashion, with each element of the beamline looked at in turn and optimised to give the maximum level of compression and beam quality. Bunches of charges 0.01, 0.1, 0.5, 1.0, 1.5, and 2.0 nC were tracked from the photocathode to the beginning of the bunching cavity without the presence of a solenoid field. After the optimal setting of the phase of the RF gun was chosen, the optimum setting of the gun solenoid was found. Following this, the bunches were tracked through the buncher to the beginning of the first accelerating cavity. The phase of the bunching cavity was varied to investigate velocity bunching and following this the setting of the buncher solenoid magnet was optimised. For most simulations described in this section, tracking to the end of the CLEAR injector is not shown. When accelerated on the peak-energy phase of the two following accelerating cavities the emittance and length of the bunches do not alter significantly, as will be discussed.

Unless otherwise stated each simulation in this section assumes the standard conditions available on CLEAR: the peak electric field in the gun and buncher of 80 MV/m and 18 MV/m respectively. The solenoid strength of the bunching cavity solenoid was set to a maximum of 0.1 T. The maximum magnetic field of the gun solenoid currently available on CLEAR is 0.24 T, however, as this limit is caused by the control system and is not a physical limit the potential maximum field strength was set to 0.3 T. The simulations were done assuming no beam losses in order to reduce the computation time. In operation, there are typically around 10 % beam losses in the CLEAR injector, which will likely cause a small change to measured beam properties. The beams were produced from three 2D Gaussian laser profiles, with spot sizes, 0.4, 0.8 and 1.2 mm. The laser pulse length was set to 4.7 ps.

Experimental analyses of bunch compression on CLEAR have also been undertaken. These analyses will be reported in this section and compared with the simulation results.

3.4.1 RF Gun

The phase of the RF gun was the first parameter to be optimised. A scan was performed of the RF phase for each different charge and each laser spot size. A phase of zero degrees corresponds to the field shown in Figure 3.8a. Figure 3.10a shows the percentage charge extracted from the photocathode for a laser spot size of 0.4 mm as the phase is varied. The mirror charge induced on the photocathode causes some particles to be shielded from the

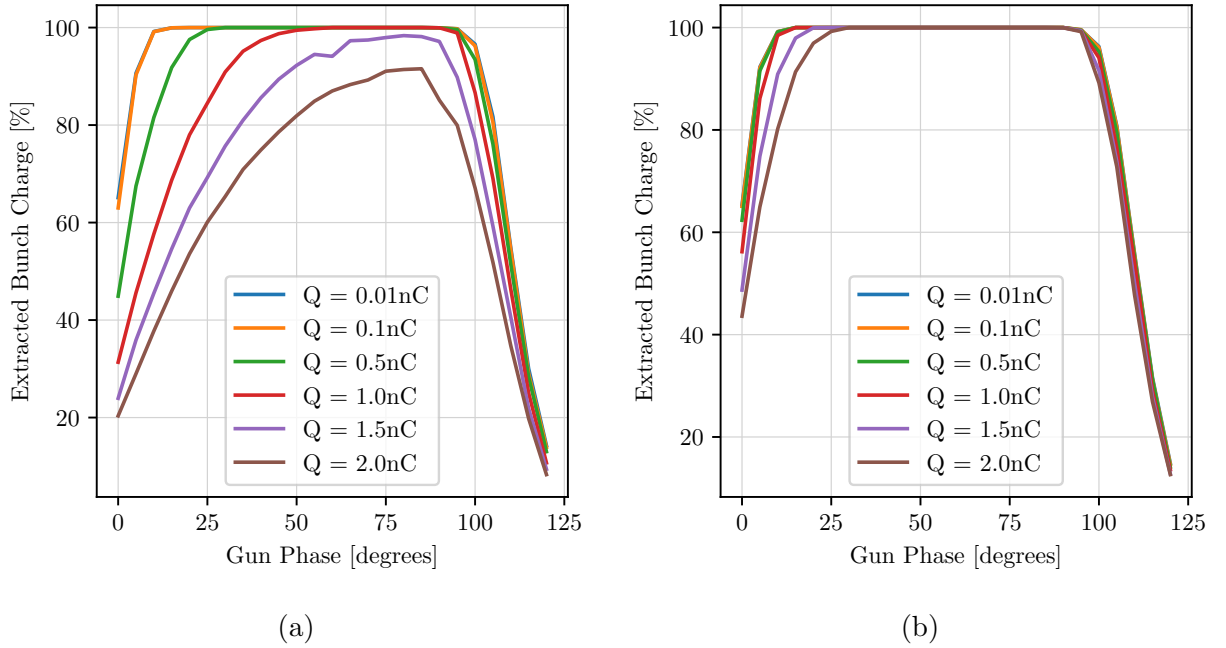


Figure 3.10: ASTRA simulation of the total bunch charge extracted from the RF gun with a 2D Gaussian laser profile of spot size (a) 0.4 mm and (b) 0.8 mm vs gun phase as a percentage of the generated bunch charge.

accelerating electric field, hence they are not extracted from the photocathode. For bunches of low charge, 100 % of the bunch is extracted at phases higher than 10° . The effect of the mirror charge is larger for higher-charge bunches meaning that a lower fraction of the created bunch is extracted. It is evident in the simulation that there is an increase in charge extracted with higher phases up to $\sim 90^\circ$ when there is a sudden drop off. At higher phases, the peak accelerating field occurs later relative to the laser pulse, meaning that more of the bunch sees a high accelerating phase. The drop off in charge extracted occurs just before the sign change of the electric field, where the bunch is no longer in an accelerating phase. It is clear that for low bunch charges the level of extraction is high for a large phase range; this is not the case for the high-charge bunches.

As shown in figure 3.10b, when the laser spot size is increased to 0.8 mm a larger proportion of the bunch charge is extracted at lower phases. The charge density is a factor four lower than 0.4 mm, therefore, the effect of the mirror charge is diminished. The extraction curve for the 0.01 nC and 0.1 nC charged bunches is identical to the 0.4 mm case, due to the space charge being low in both cases. If the laser spot is increased further, the charge extraction curves for all bunch charges are similar to the 0.01 nC bunch. From this, it can

be concluded that in order to produce a high-charge bunch in CLEAR a laser spot size of larger than 0.4 mm is needed.

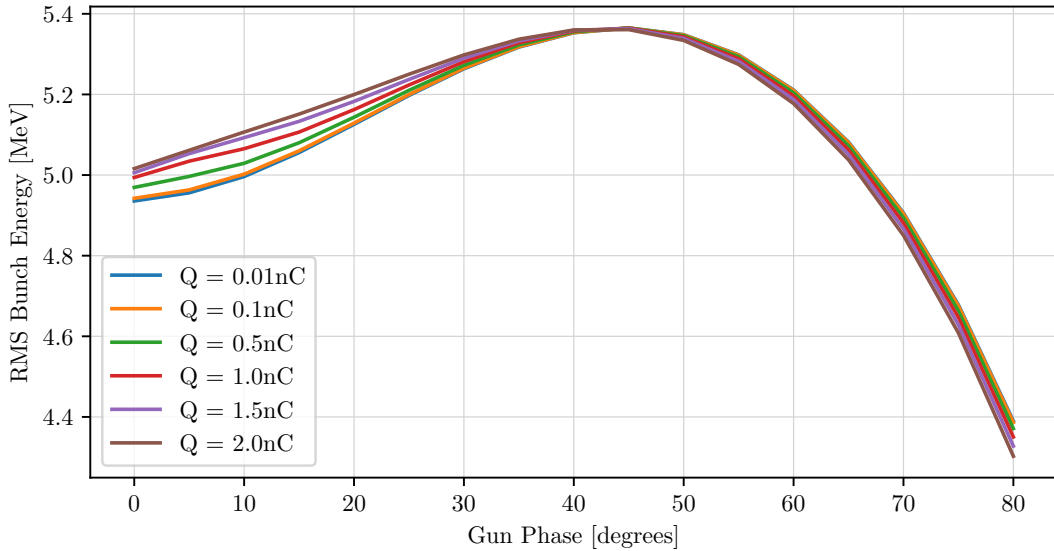


Figure 3.11: ASTRA simulation of the bunch energy of bunches of different charge vs the RF phase of the gun for bunches produced with a 0.8 mm laser spot.

As the RF phase of the gun is varied the average energy of the extracted bunch changes. The variation of bunch energy for bunches produced from a laser spot of 0.8 mm is shown in Figure 3.11. For all bunch charges there is an increase in bunch energy as the phase is increased from 0° to a peak energy around 45° of 5.35 MeV. As the phase is increased past the peak-energy phase the bunch energy drops until at around 80° the bunches begin to stop being extracted from the photocathode and the beam quality significantly drops. The dependence of the bunch energy on bunch charge is very small for most phases as there is a low amount of beam loading in the gun. At phases lower than $\sim 30^\circ$, bunches of higher charge appear to have a higher average energy. The difference in energy is due to higher charge bunches not being fully extracted. The energy gained by each bunch particle is time dependent and at phases lower than 45° particles emitted later receive a lower acceleration gradient. Thus if fewer of the generated particles are extracted, the average accelerating field seen by the bunch and, therefore, its average energy, will be higher.

Simulations of bunches with a different spot size show the same variation in bunch energy with RF phase as the 0.8 mm case, with each fully extracted bunch seeing an energy peak at around 45° . In the case that the entire bunch is not extracted over the entire phase range,

such as for 1.5 nC and 2.0 nC bunches produced from a 0.4 mm spot, the peak in average energy occurs at a lower phase than 45° .

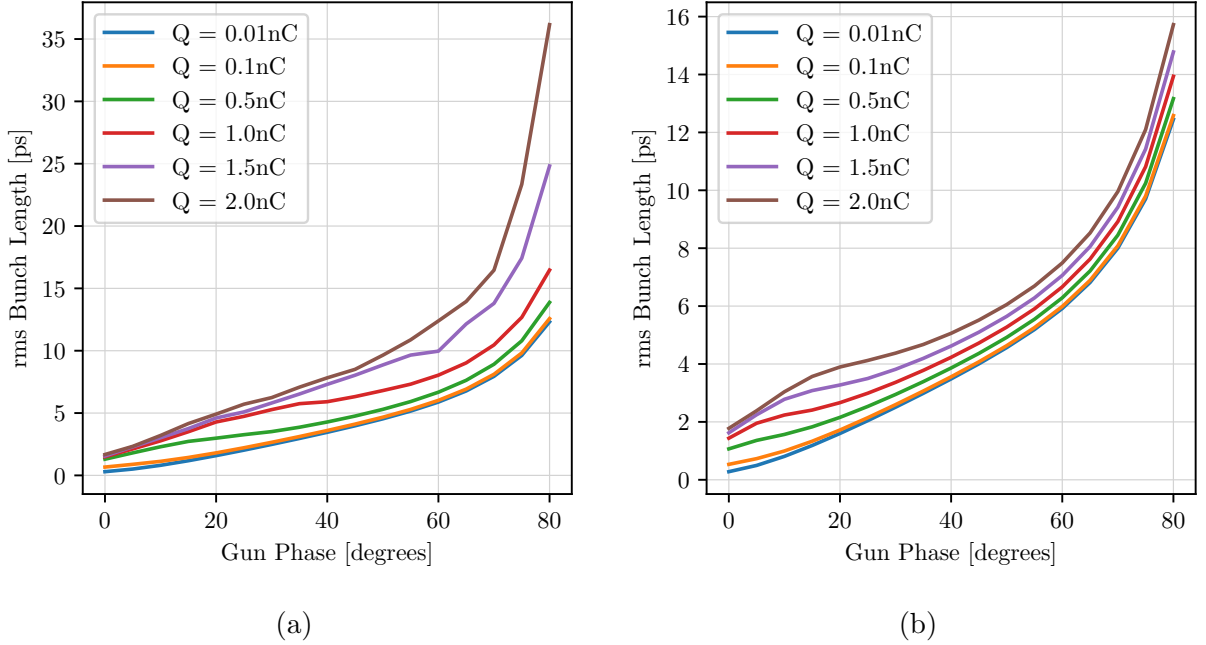


Figure 3.12: The bunch length of bunches of different charge bunches vs gun RF phase simulated in ASTRA, for a laser spot size of **(a)** 0.4 mm and **(b)** 0.8 mm.

The lengths of bunches extracted from the RF gun are also very dependent on both the space charge forces present and the RF phase. As can be seen in Figure 3.12, bunches of higher charge have a longer bunch length than lower charge bunches. The increase in length mostly occurs in the first few centimetres of the gun when the bunch energy is low and space charge forces are high. An example of the change in the longitudinal space charge fields seen by 30 randomly selected probe particles over the first 0.5 m of the linac is shown in Figure 3.13. The fields seen by the probe particles are around three orders of magnitude higher at the cathode than at 15 cm, the exit of the gun. The reduction is mostly due to the energy gain of the bunch and visible drops can be seen after each accelerating cell in the gun.

For higher-charge bunches some elongation also occurs over the drift between the gun and the bunching cavity due to the longitudinal space forces present. For bunches of 0.01 nC, where space charge effects in the drift are relatively low for all laser spot sizes, we see that in phases lower than the peak-energy phase the bunch length is less than the 4.7 ps length of the laser pulse due to velocity bunching. At the peak-energy phase the bunch length is

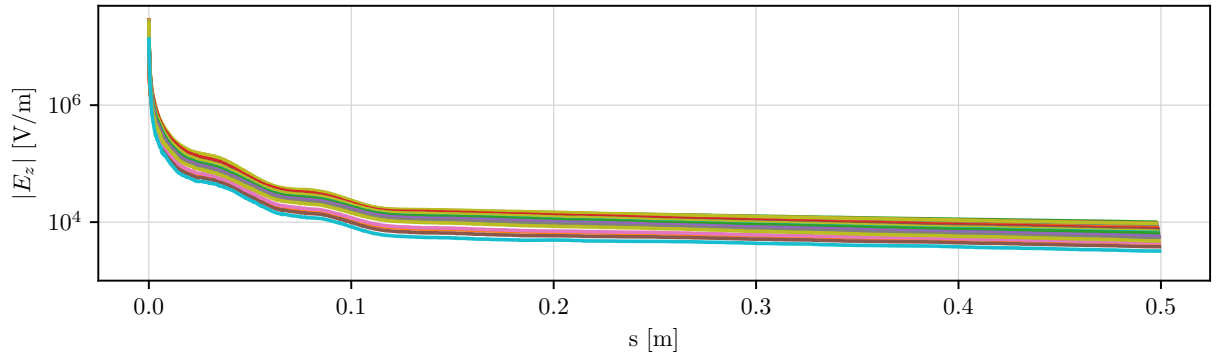


Figure 3.13: The simulated longitudinal space charge field vs distance from the photocathode acting on 30 probe particles randomly selected from a bunch produced by a 0.4 mm laser spot accelerated at the peak-energy phase.

around 4 ps, with some velocity bunching occurring in the first few centimetres of the gun. Following the peak-energy phase, the bunches become longer due to the bunch tail seeing a lower field than the bunch head.

For a laser spot of 0.4 mm, as shown in Figure 3.12a, the space charge forces cause elongation of bunch length with bunch charge, for all phases of the RF. The relative elongation appears to be lower at low RF phases than at high RF phases. However, this is due to a lower charge being extracted at low phases.

When the bunch is produced from a larger laser spot, the bunch elongation with an increase in bunch charge is reduced, as can be seen for a spot size of 0.8 mm in Figure 3.12b. For a laser spot of 0.4 mm, a bunch of charge 1 nC accelerated at the peak-energy phase has a length of 6.3 ps as it enters the buncher. However, a bunch of the same charge accelerated at the same phase has a bunch length of 4.7 ps, identical to the laser pulse length, when produced from a spot of 0.8 mm. Larger laser spot sizes than 0.8 mm result in even lower bunch lengths, although up to a 2 nC charge the difference is small. It is, therefore, clear that the larger the spot size the smaller the bunch length achievable at the end of the CLEAR accelerator.

For RF phases lower than the peak-energy phase, the energy spread of the bunches is low, as shown in Figure 3.14. There is an initial rise in energy spread until it begins to fall at around 20° . For bunches of low charge, the energy spread is minimised at 0.3 % at the peak-energy phase. For higher bunch charges the energy spread is minimised at a lower RF

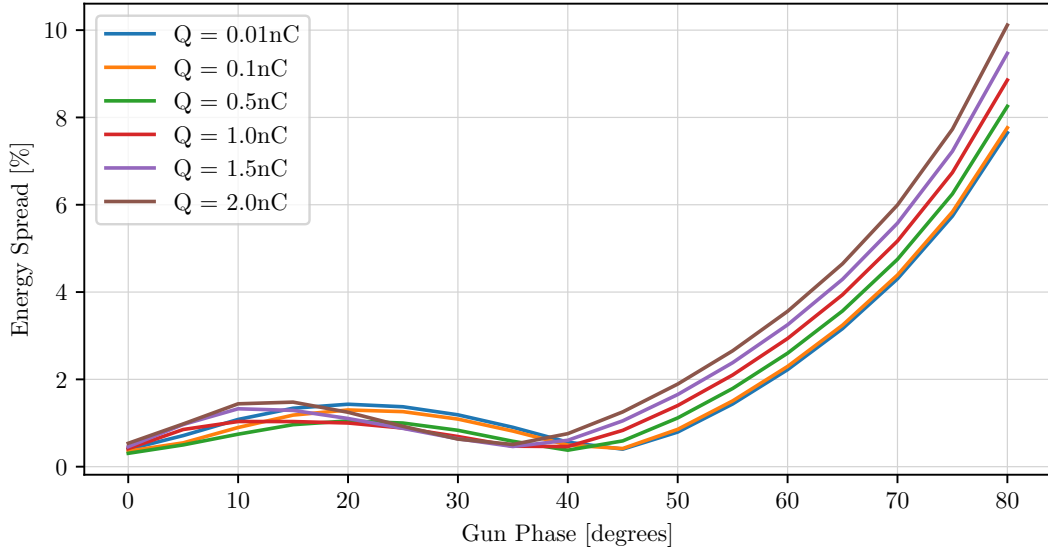


Figure 3.14: ASTRA simulation of energy spread of several bunches of different charge vs the RF phase of the gun for bunches generated from a laser spot of 0.8 mm.

phase than the peak-energy phase. The minimum energy spread possible is also larger for bunches of a higher charge. Both of these effects are likely to be caused by the longer bunch lengths of higher-charged bunches in the gun. Following the energy peak phase there is a large increase in energy spread. The energy spread is lower for bunches generated from a larger laser spot. Again this is likely due to these bunches having a shorter bunch length in the gun.

The emittance of each bunch varies with RF phase as shown in Figure 3.15. The variation in emittance corresponds to the variation in energy spread, namely that RF phases that result in a large energy spread also result in a large emittance. The minimum emittances can be found at the same RF phases as the minimum energy spread. It is also clear that space-charge forces cause the emittance of high charge bunches to grow relative to low-charge bunches when no solenoid field is present. The increase in emittance with charge is largely driven by space charge forces and there is a large emittance growth for beams produced from a smaller laser spot.

However, we can optimise the strength of the solenoid field to suppress the emittance growth significantly. The minimum emittances possible through this optimisation for bunches accelerated at the peak-energy phase of the gun are shown in Figure 3.16a. Bunches with higher charge, produced from the same laser spot size, have a larger minimum emittance due

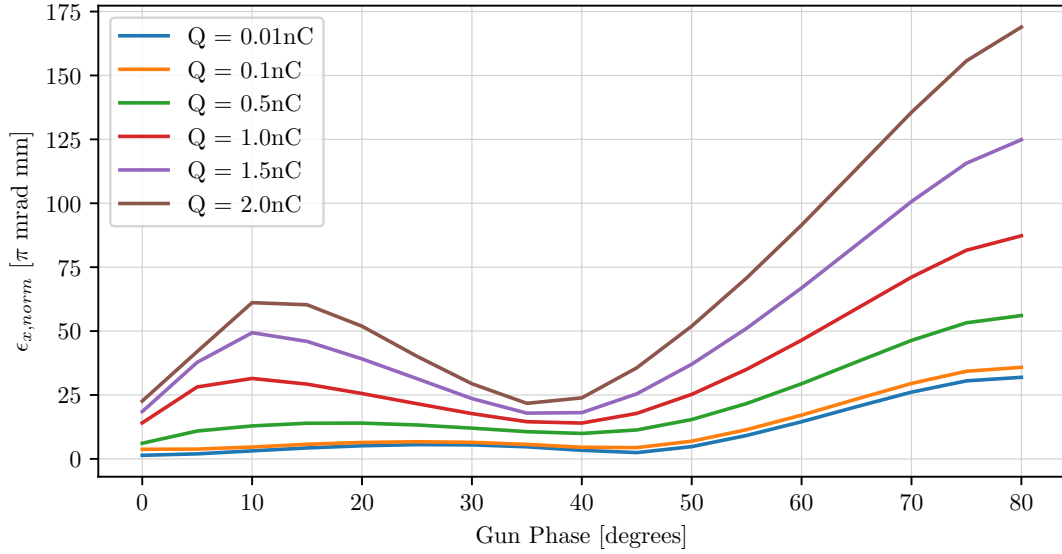


Figure 3.15: The normalised transverse emittance of bunches of various charges, produced by a 0.8 mm laser spot size vs the RF phase of the gun, without the presence of a solenoid field.

to increased space-charge forces. Although bunches produced from a larger spot size have a lower emittance when there is no magnetic focusing, the minimum emittance achievable with focusing is higher for larger laser spot sizes. These simulations suggest that it is possible to reduce the emittance growth for bunches up to 2.0 nC to less than 15π mm mrad for all laser spot sizes.

Although bunches generated with a larger laser spot have a larger emittance, a lower solenoid field is required to achieve the minimum value, as shown in Figure 3.16b. For bunches generated from a 0.4 mm laser spot, the minimum emittance is produced at magnetic field strengths higher than the current maximum of 0.24 T when the charge is over 0.1 nC. The same is true of bunches up to a charge of 0.5 nC, and 1.5 nC for bunches generated from laser spots of 0.8 mm and 1.2 mm respectively. Therefore, achieving these emittances would require a new control system to be installed. The maximum field required to minimise emittance in any simulation was 0.27 T. If the field is too high the beam is focused too much causing an increase in charge density and, therefore, space charge forces which drive a growth in emittance. The solenoid magnet only had a small impact on the longitudinal properties of the bunches until the strength of the magnetic field caused the beam to be over focused, when the increase in space charge forces increased the bunch length slightly.

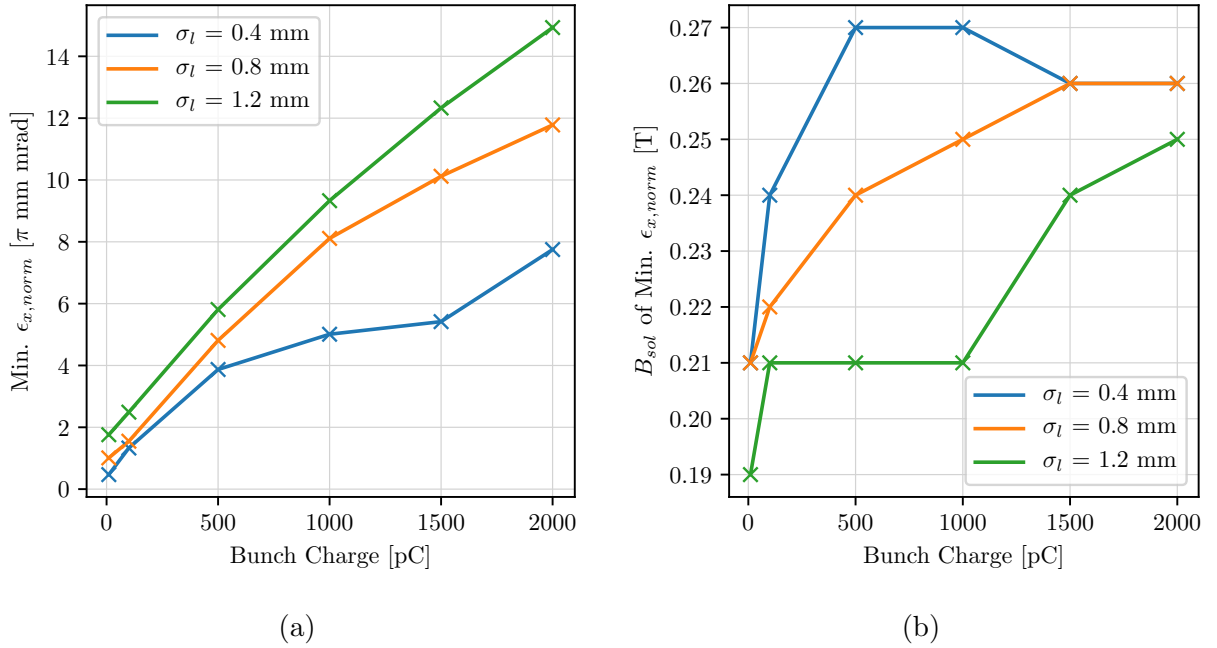


Figure 3.16: (a) The minimum emittance value of bunches of different spot size simulated to the entrance to the bunching cavity vs charge. (b) The solenoid field strength required to minimise the beam emittance vs charge.

It must be noted that the long drift space between the photocathode and the bunching cavity on CLEAR may prevent experimental optimisation of the beam emittance. In order to reduce beam losses, photoinjectors are typically designed such that the first accelerating structure is positioned at a beam waist, when the beam has the smallest transverse profile. The bunching cavity in CLEAR is ~ 2.4 m after the photocathode. It is impossible to create a beam waist at this distance in the current CLEAR setup, and the beam is typically significantly larger than at the waist when entering the cavity, which could cause losses. For experiments requiring high bunch charges, the typical experimental procedure is to reduce these beam losses and not to optimise the beam for minimum emittance.

3.4.2 Bunching Cavity

The next component of the CLEAR beamline to be optimised was the bunching cavity. A phase of 0° in the buncher was defined as the peak accelerating phase for the central particle in the initial bunch. As a compromise between bunch quality and charge extraction, the phase of the gun was set to the peak-energy phase. The strength of the gun solenoid was set to minimise the bunch emittance, with a maximum field strength of 0.24 T.

As with the RF gun, the first parameter to be optimised for compression in the bunching cavity is the RF phase. As can be seen in Figure 3.17 the bunch energy varies sinusoidally between 65 MeV and 20 MeV with the RF phase of the buncher. The phase with the minimum bunch energy is around -90° , zero crossing. At phases lower than zero crossing the bunch initially sees a decelerating field as it enters the cavity, which causes the bunch to slip in phase relative to the RF towards an accelerating field.

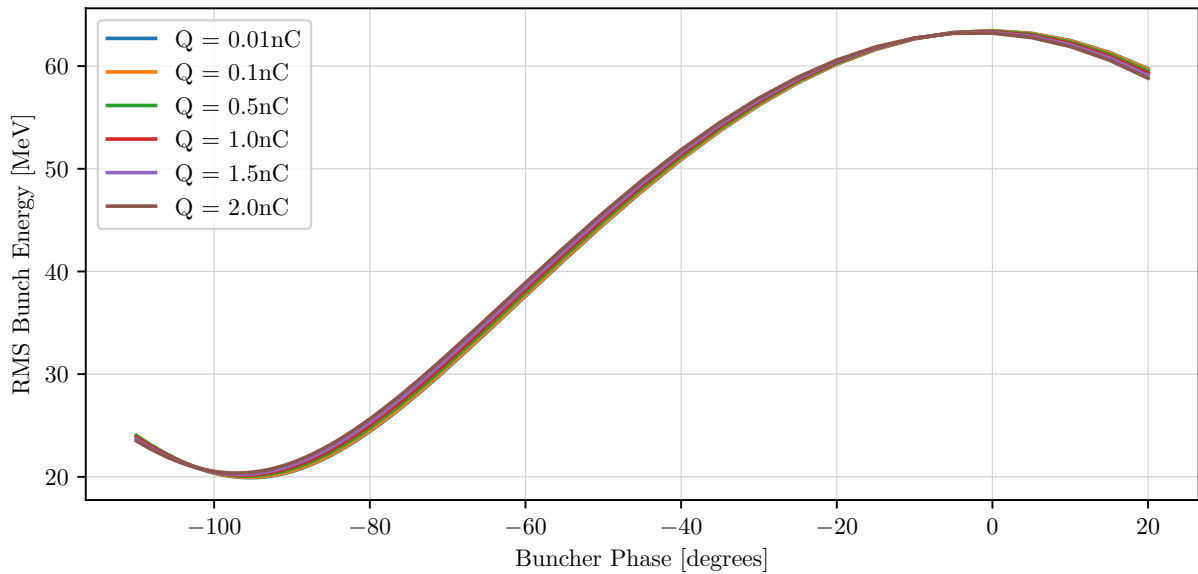


Figure 3.17: ASTRA simulation of the bunch energy of several bunches of different charge, all produced from a laser spot of 0.8 mm, vs the RF phase of the buncher.

As can be seen in Figure 3.18, we can perform bunch compression by moving the RF phase of the buncher closer to zero crossing. When accelerated on the energy crest bunches are not compressed. Low-charge bunches remain at the same length as they were when they entered the buncher. There is a small increase in bunch length at the exit of the buncher relative to the beginning for bunches above 1 nC, which is caused by space-charge forces still present in the early section of the buncher. There is a slow drop in bunch length over the first 50° of de-phasing, followed by a more rapid drop off until a minimum bunch length is achieved between -85° and -90° . At phases lower than zero crossing the bunch length grows again. The minimum bunch length of higher-charge bunches is longer than that of lower-charge bunches. The reason for this is both that space charge forces in the buncher prevent further compression and that higher charge bunches have a longer bunch length when entering the buncher.

The minimum bunch length of high-charge bunches is achieved closer to zero crossing than for low-charge bunches. The ideal phase for bunch compression causes the bunch to reach its minimum length at the exit of the bunching cavity. If a bunch is compressed too much in the buncher then the bunch length will begin to grow after reaching an initial minimum as the phase space is over-rotated. If the bunch is at a low energy when it is compressed, longitudinal space charge forces can grow causing further bunch lengthening.

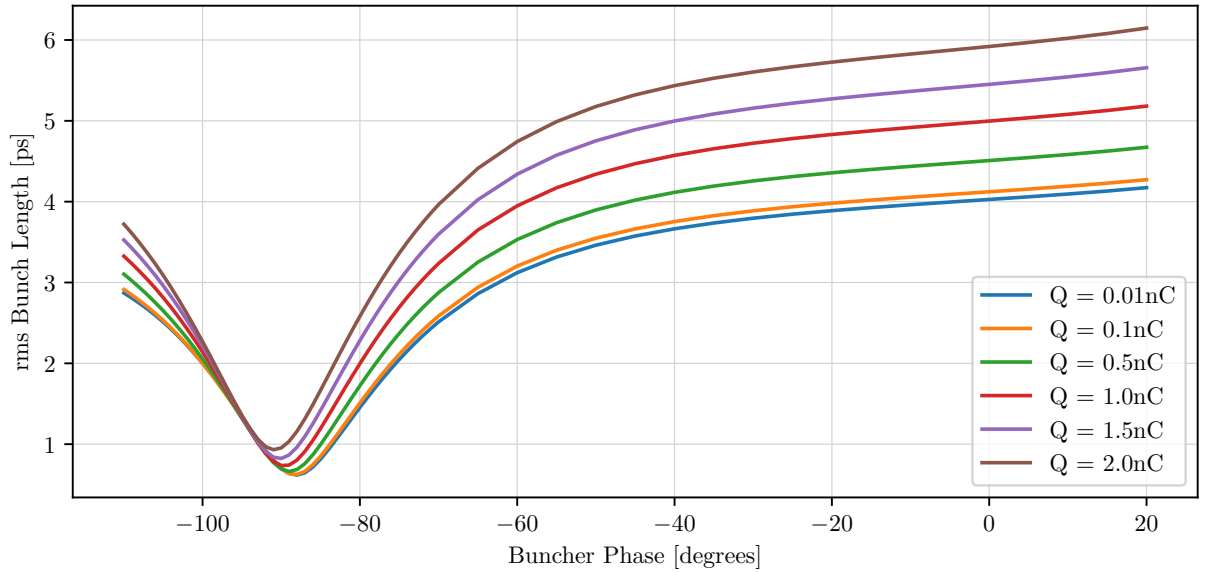


Figure 3.18: ASTRA simulation of the bunch length of several bunches of different charge, all produced from a laser spot of 0.8 mm, vs the RF phase of the buncher.

The minimum achievable bunch length depends on the laser spot size that the bunch was generated from. As can be seen in Figure 3.19, the minimum bunch length for bunches produced from a laser spot of 0.4 mm grows significantly for charges greater than 0.5 nC. It is impossible to achieve sub-ps bunch lengths for charges of 1.0 nC or higher with this spot size. However, by increasing the spot size to 0.8 mm or 1.2 mm we can achieve much more compression, being able to produce sub-ps bunches of 2 nC charge.

When compressing the bunches there is an increase in energy spread, as shown in Figure 3.20. At the peak-energy phase the bunch energy spread at the exit of the cavity decreases slightly relative to the energy spread at the entrance. When the phase is reduced from the peak-energy phase there is an increase in the energy spread to a maximum at a phase of around -80° . There is a sharp decrease in energy spread until a phase just lower than zero crossing when it begins to rise again. The reason for this is that at phases below -80° ,

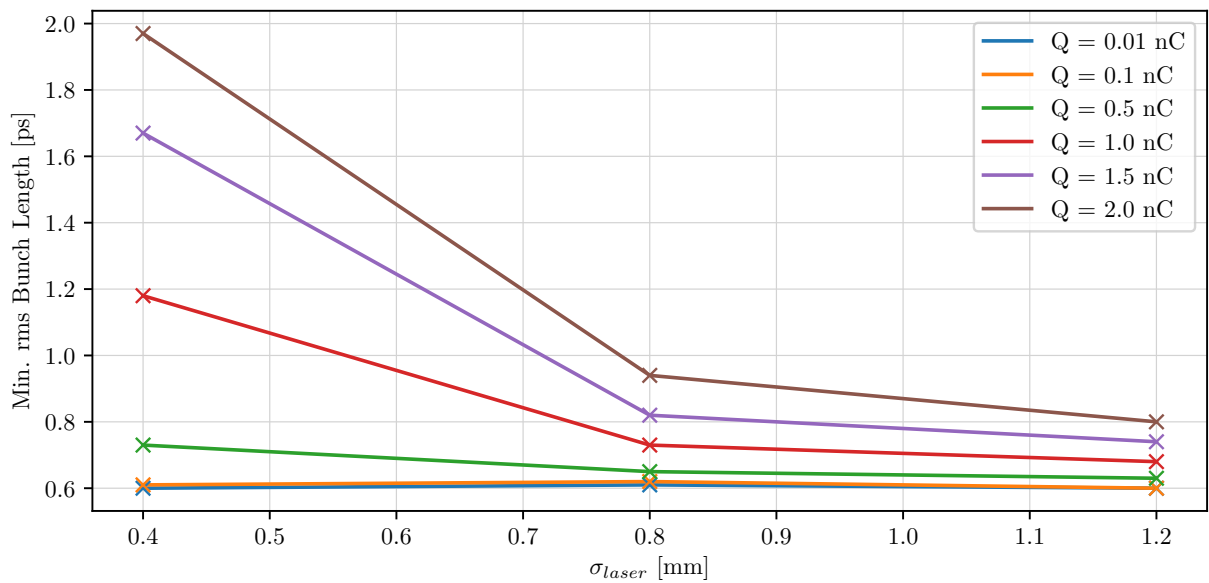


Figure 3.19: The minimum bunch lengths achievable for bunches of different charges simulated in ASTRA vs laser spot size.

bunches slip into a more highly accelerating phase. In Figure 3.21, this early increase in energy spread followed by a decrease can be clearly seen for phase of -80° and to an even greater extent for a phase of -90° . Generally, the energy spread increases with bunch charge due to the longer bunch lengths of bunches with higher charge. The energy spread decreases for larger spot sizes, again due to the increases in bunch length.

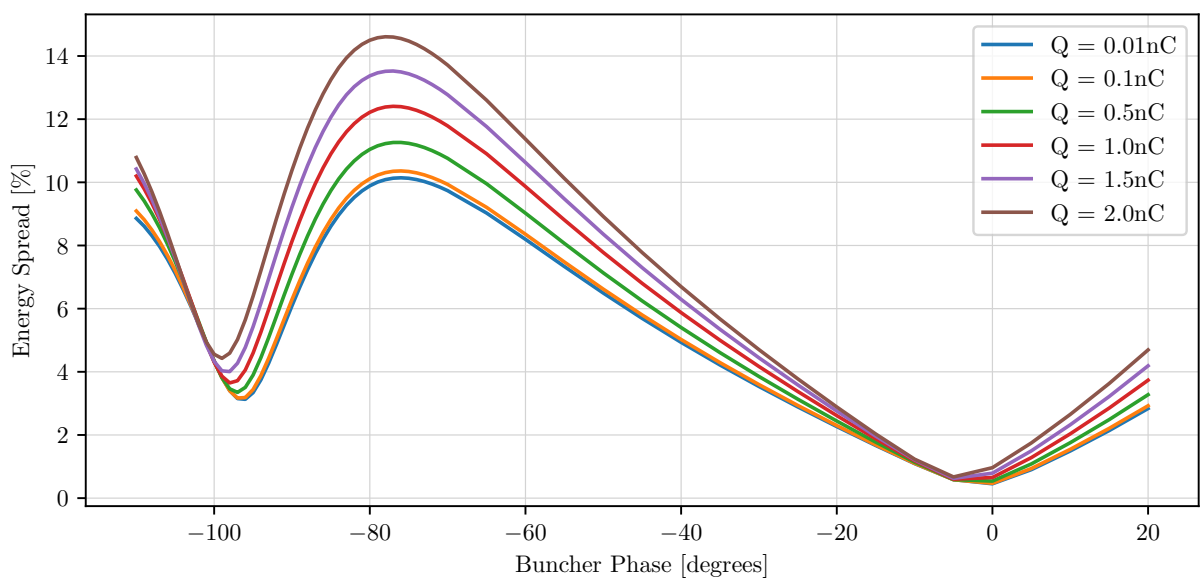


Figure 3.20: ASTRA simulation of the energy spread of several bunches of different charge, all produced from a laser spot of 0.8 mm, vs the RF phase of the buncher.

Although the energy spread at the exit of the bunching cavity is very large for phases other than the peak-energy phase, the energy spread drops after on-crest acceleration in the two following accelerating cavities, as can be seen in Figure 3.21. For a bunch of charge 500 pC generated from a 0.8 mm laser spot, the energy spread at the end of the whole CLEAR injector is less than 2 % for all buncher phases. The rate of decrease in energy spread over the following two accelerating cavities is proportional to the bunch length as is typical in linear accelerators. Bunches that have been compressed in the buncher, such as those accelerated at phases of -80° and -90° , see the biggest falls in energy spread.

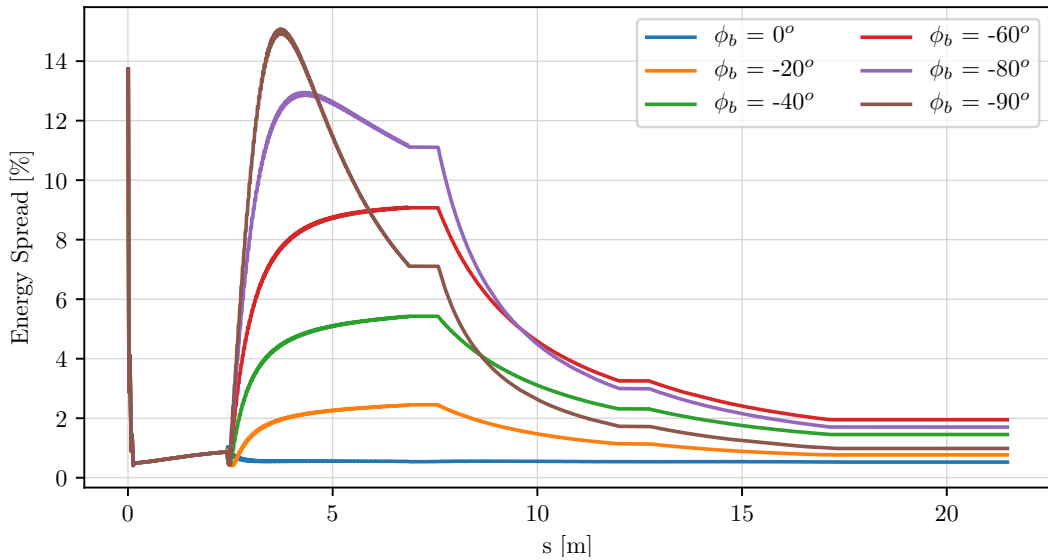


Figure 3.21: The evolution of energy spread vs distance from the photocathode for several 500 pC bunches, each generated from a laser spot of 0.8 mm, and accelerated at different phases in the bunching cavity.

The bunch length is unaltered by on-crest acceleration in the two following cavities as shown in Figure 3.22. By de-phasing these two cavities a marginal amount of bunch length compression can be achieved, although at the cost of significantly worse energy spread and emittance. As the energy of the beam drops as it is compressed the energy at the end of the injector is lower. Therefore, although the normalised emittance of the bunch is conserved along the rest of the accelerator, its geometric emittance is not, resulting in larger beam sizes along the rest of the beamline.

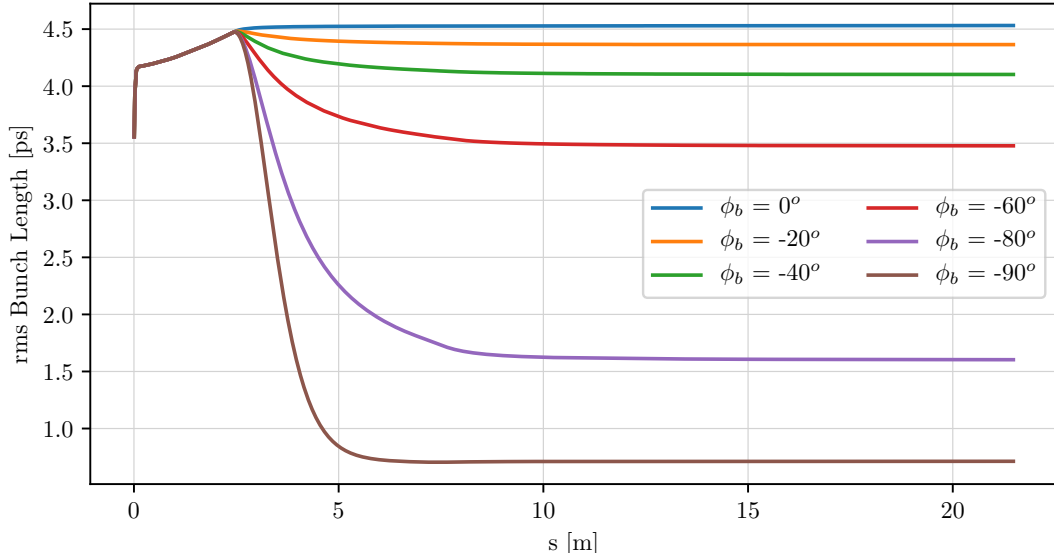


Figure 3.22: The evolution of bunch length vs distance from the photocathode for several 500 pC bunches, each generated from a laser spot of 0.8 mm, and accelerated at different phases in the bunching cavity.

3.4.3 Emittance Growth Compensation

When there is no solenoid field present in the bunching cavity, velocity bunching leads to growth in the emittance of the beam, as shown in Figure 3.23a. The growth in emittance is caused by both space charge forces in the shorter bunches and transverse RF fields. When accelerated on the peak-energy phase of the buncher the incoming emittance of the bunch from the gun is conserved for low-charge bunches. Bunches of higher charge have a higher incoming emittance. As well as this, the space charge forces cause a slight increase in emittance over the length of the bunching cavity for high-charge bunches. As the phase is reduced there is a large emittance growth, to a maximum at around 75° . There is then a drop towards zero crossing. At phases below zero crossing there is a large blow up in beam emittance. The relative emittance increase when compressed compared to the peak-energy phase is larger for higher charged bunches than lower charged bunches. For beams produced from a laser spot of 0.8 mm there is an increase of a factor three for a bunch charge of 0.01 nC but a factor four for a 2.0 nC bunch. Bunches produced from larger laser spots have a larger beam emittance than those produced from smaller laser spots.

It is possible to suppress some of this emittance growth by optimising the strength of the buncher solenoid magnet. In Figure 3.23b, we can see that it is possible to completely

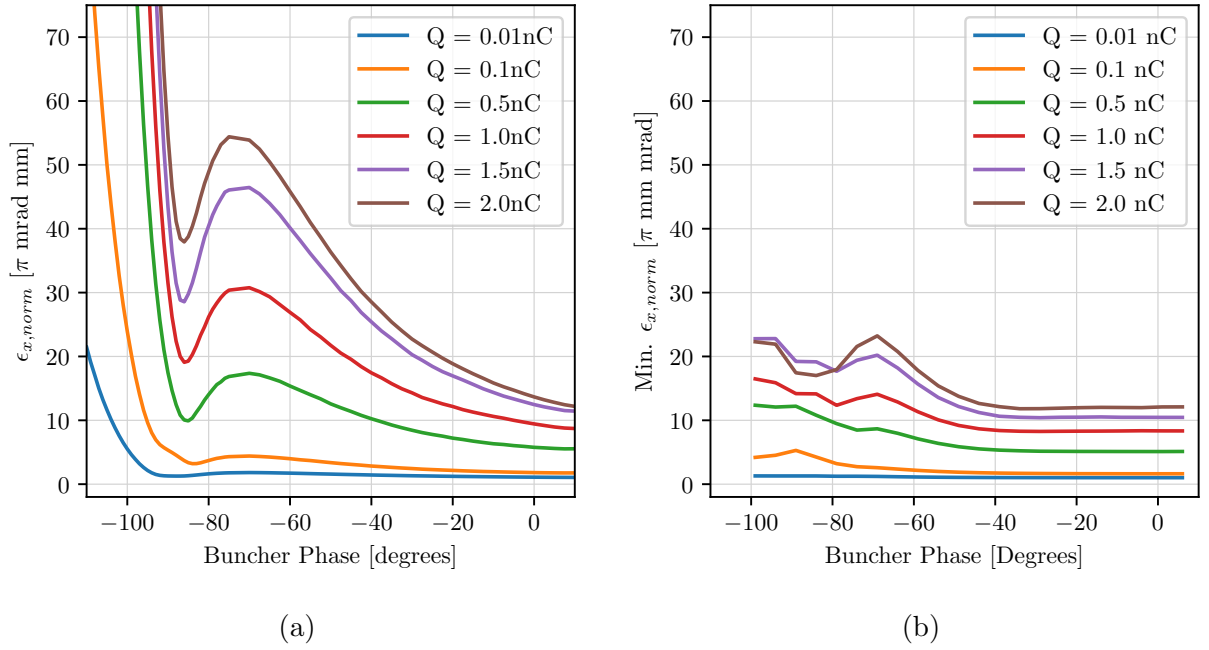


Figure 3.23: **(a)** ASTRA simulations of the beam emittance vs buncher phase of bunches of different charge, all produced from a laser spot of 0.8 mm, at the end of the bunching cavity with no solenoid field around the buncher. **(b)** ASTRA simulations of the minimum beam emittance achievable with a tuned solenoid field vs buncher phase for bunches of different charge, all produced from a laser spot of 0.8 mm, at the end of the bunching cavity.

suppress any emittance growth for charges up to 2 nC, for phases ranging from 0° to $\sim -50^\circ$ for bunches produced from a 0.8 mm laser spot. At phases lower than this, we begin to see that some emittance growth cannot be suppressed. However, even for the 2 nC bunch the emittance growth is reduced from a factor 4 at maximum compression to a factor 2. At phases lower than -100° the emittance still blows up to a large value. The solenoid field required to minimise emittance is similar for each laser spot size and bunch charge, due to space charge forces not being the dominant cause of emittance growth. At the peak acceleration phase, the optimum field is around 0.06 T. For bunches at maximum compression the optimum field strength is about 0.03 T. Bunches accelerated at a lower phase than the peak-energy phase have a lower rigidity. Therefore, if the solenoid is set to the strength that minimises emittance growth for the on-crest phase, then it can produce a beam waist of a very small size. At the beam waist the space charge forces grow significantly, which will increase the beam emittance.

3.4.4 Experimental Verification of Compression

Although simulations of bunch compression suggest that sub-ps bunch lengths are possible for high charges, only low-charge bunches were able to be successfully compressed to these bunch lengths previously. The main reason for this was a massive increase in beam losses as the buncher was de-phased. Therefore, experimental investigations into high charge bunch compression were performed on CLEAR. To avoid beam losses it was important to adjust the strengths of the buncher solenoid magnet and beam orbit correctors as the RF phase was adjusted. As the energy spread of the beam increases significantly in the bunching cavity when undergoing compression, it is important to ensure the beam is well centred along this element. If not, the dipole corrections given to the beam will introduce a large amount of dispersion to the beam, resulting in large beam sizes and high beam losses. The beam trajectory is monitored with the cavity BPMs. Taking care of the beam orbit, compression of bunches of several different charges produced from several different laser spot sizes were investigated experimentally.

Several beam jitters and experimental uncertainties make the comparison to simulation difficult. The RF phase of the gun is set experimentally by performing a phase scan for a small laser spot. The phase scan produces a variation in charge similar to that shown in simulation in Figure 3.10. The drop off in charge is recorded as $\sim 80^\circ$ and the operational phase is set around 35° lower. From a more time-consuming measurement of the bunch energy with phase, the uncertainty in the gun phase is estimated at $\pm 5^\circ$. The RF phase of the gun varies throughout the day due to the ambient temperature of the room in which the klystrons and waveguides are situated, so this phase scan of the gun is performed regularly. As they are powered by the same klystron the phases of the buncher and the gun vary similarly. The laser spot size and beam charge vary shot-to-shot by around 5 % and 10 %. There is a timing jitter for the arrival of the RF pulse in the gun relative to the laser pulse which causes a phase jitter of $\pm 1^\circ$. The bunch lengths are measured with the RF deflecting cavity as mentioned in section 3.1.3.

In Figures 3.24 and 3.25, there are two examples of the comparison between simulated and measured bunch length. Figure 3.24 is for a bunch charge of 0.5 nC generated from a laser spot of 0.6 mm and Figure 3.25 is for a bunch of 0.3 nC generated from a laser spot of

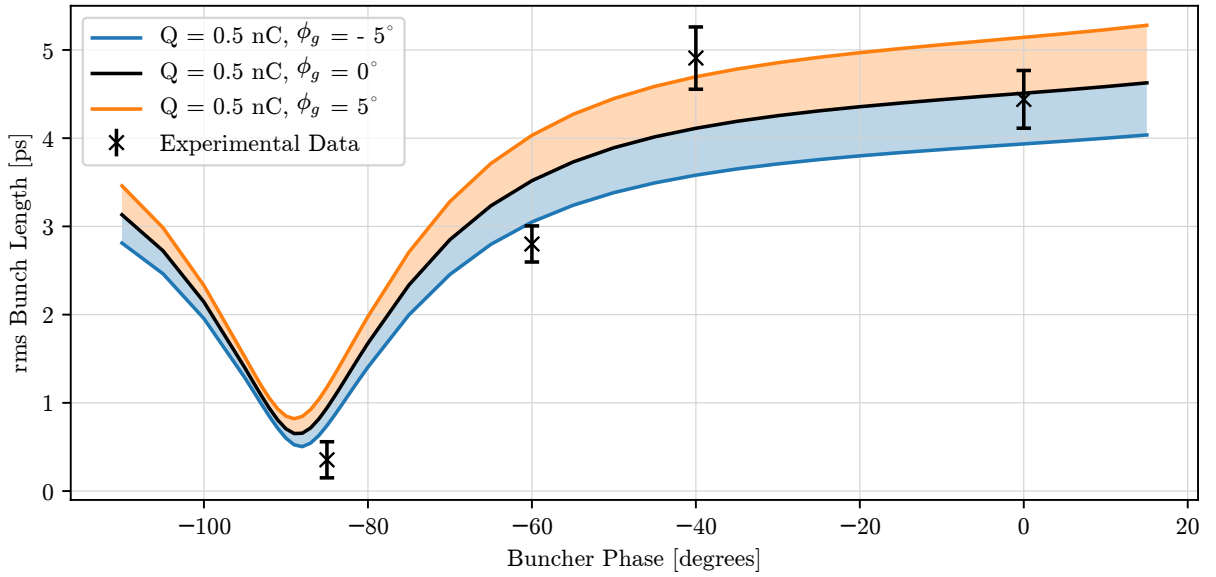


Figure 3.24: Comparison between ASTRA simulation and experimental data of the bunch length vs buncher phase of a bunch charge 0.5 nC created from a laser spot of 0.6 mm. A range of $\pm 5^\circ$ in gun phase is shown. The error bars show the statistical uncertainty.

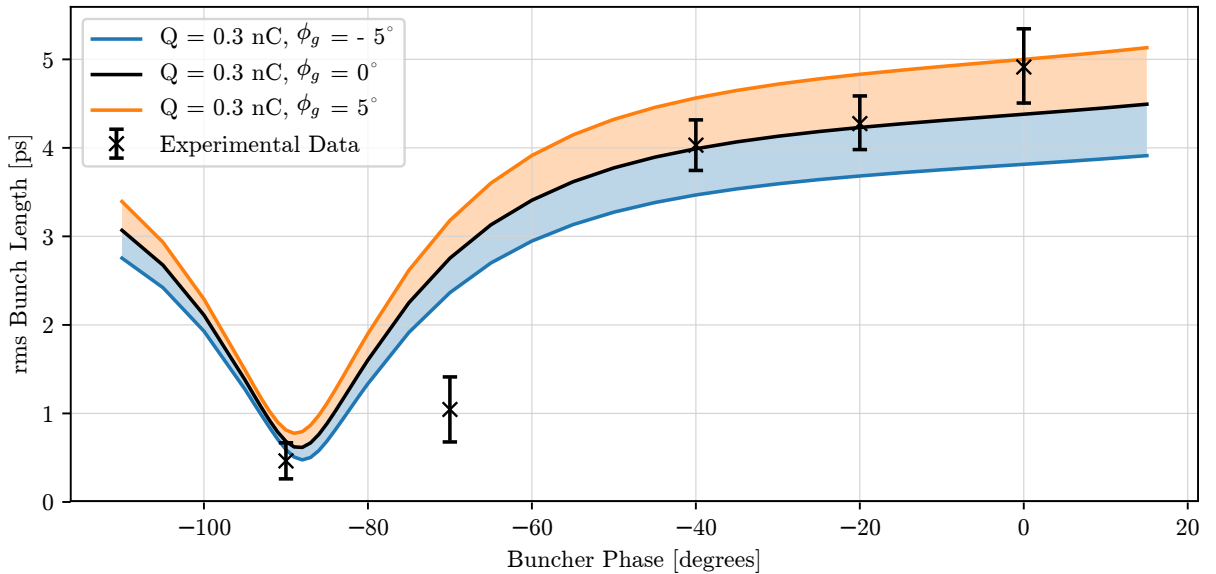


Figure 3.25: Comparison between ASTRA simulation and experimental data of the bunch length vs buncher phase of a bunch charge 0.3 nC created from a laser spot of 0.5 mm. A range of $\pm 5^\circ$ in gun phase is shown. The error bars show the statistical uncertainty.

0.5 mm. In each case the simulated bunch length with the gun phase set to the peak energy phase is shown in black. As the ambient temperature surrounding the klystrons fluctuated significantly during the phase scan, there was uncertainty in the gun phase. Therefore, the effect of a gun phase variation of 5° in simulation is also shown. There is reasonable

agreement between simulation and experiment in both cases. The bunch length does not drop significantly over the first 60° . The minimum bunch length achieved experimentally is similar to the minimum produced in simulation and occurs at a similar RF phase in both cases. However, for the 0.5 nC case the minimum length was slightly shorter in experiment at 0.31 ± 0.2 ps. The length measurement at a phase of -75° for the 0.3 nC bunch is likely an outlying measurement caused by poor beam profile fitting.

Further agreement with simulation can be seen in Figure 3.26, which shows the minimum lengths achieved for bunches of several charges produced from a laser spot of 0.5 mm compared to simulation. The highest charge bunch compressed experimentally for this spot size was 0.8 nC, which was compressed to a bunch length of 0.8 ± 0.2 ps. Due to the laser power being limited when these measurements were taken, no higher-charged bunches were compressed. If there continues to be agreement between experiment and simulation for this spot size it should be possible to create sub-ps bunches for charges up to 1.25 nC. Following this experimental demonstration of bunch compression on CLEAR, sub-ps bunches are routinely provided to users [84]

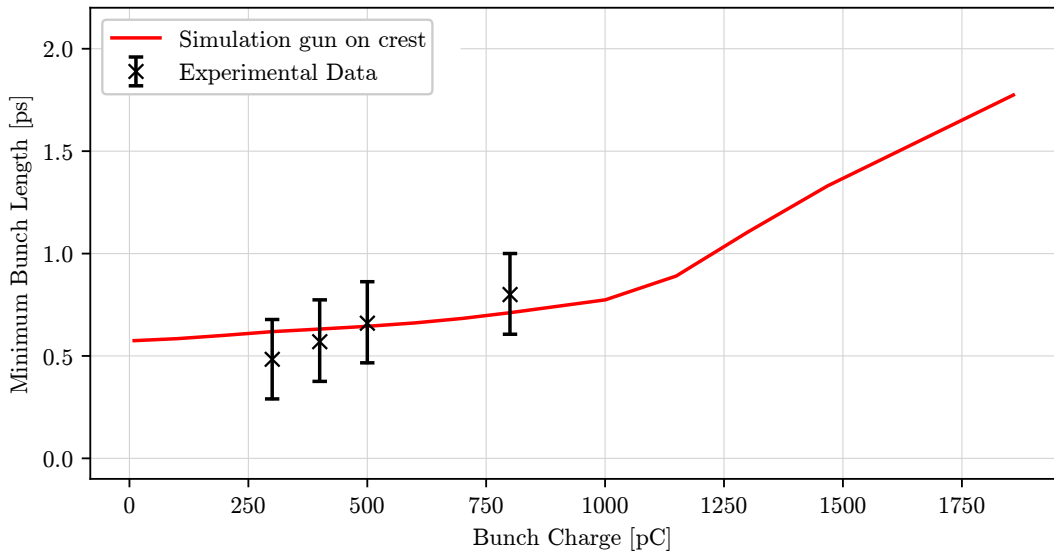


Figure 3.26: Comparison of the minimum bunch lengths achievable in ASTRA simulation and experimentally vs bunch charge for bunches produced from a 0.5 mm laser spot. The error bars show the statistical uncertainty.

3.4.5 Compression at Reduced Gun Phases

It is evident from experimental studies of bunch compression that the phase of the RF gun has a large effect on the minimum bunch length achievable. To investigate this effect, simulations of bunch compression with different gun phases were undertaken. The phase of the gun was varied between 25° and 50° , and a phase scan of the buncher was then performed. The same three spot sizes were used to act as a reference. As was shown in Figure 3.10, the amount of charge extracted at low gun phases was lower than the charge of the full bunch. The total charge of the bunch was, therefore, adjusted such that the bunch charge leaving the gun was equivalent to the stated level. For each different gun phase the strength of the gun solenoid was re-optimised to provide the minimum emittance.

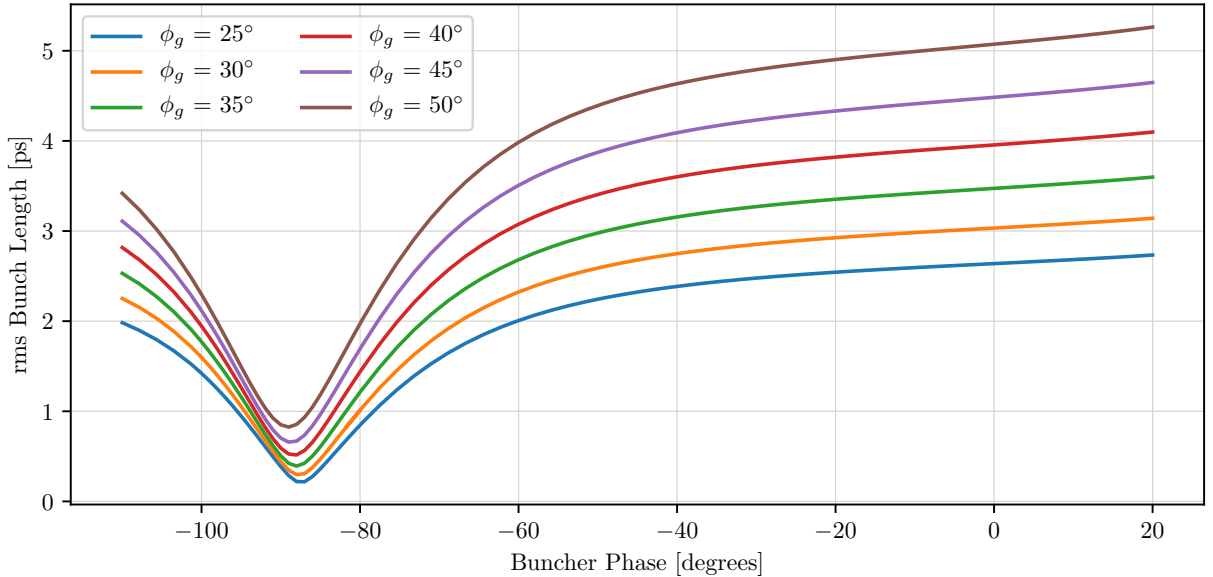


Figure 3.27: ASTRA simulation of the bunch length vs buncher phase for bunches of charge 0.5 nC produced from a 0.8 mm laser spot, and accelerated at different gun phases.

As shown in Section 3.4.1, bunches accelerated at lower gun phases have a shorter bunch length at the entrance to the bunching cavity. Consequently, bunches accelerated at lower gun phases have shorter bunch lengths following the bunching cavity, for all buncher phases. An example of the difference in bunch length at different buncher phases for a 0.5 nC bunch produced from a 0.8 mm laser spot is shown in Figure 3.27. When accelerated on the peak-energy phase of the bunching cavity, there is a small increase in bunch length at the exit of the bunching cavity relative to the entrance for higher charge bunches. As the buncher phase is reduced there is a similar relationship with bunch length for all gun phases. There

is a small reduction over the first 60° , followed by a large reduction towards a minimum around zero crossing, and a subsequent increase in length at lower phases. The minimum bunch length for a 0.5 nC bunch was around 0.2 ps at a gun phase of 20° , compared to 0.8 ps for a gun phase of 45° .

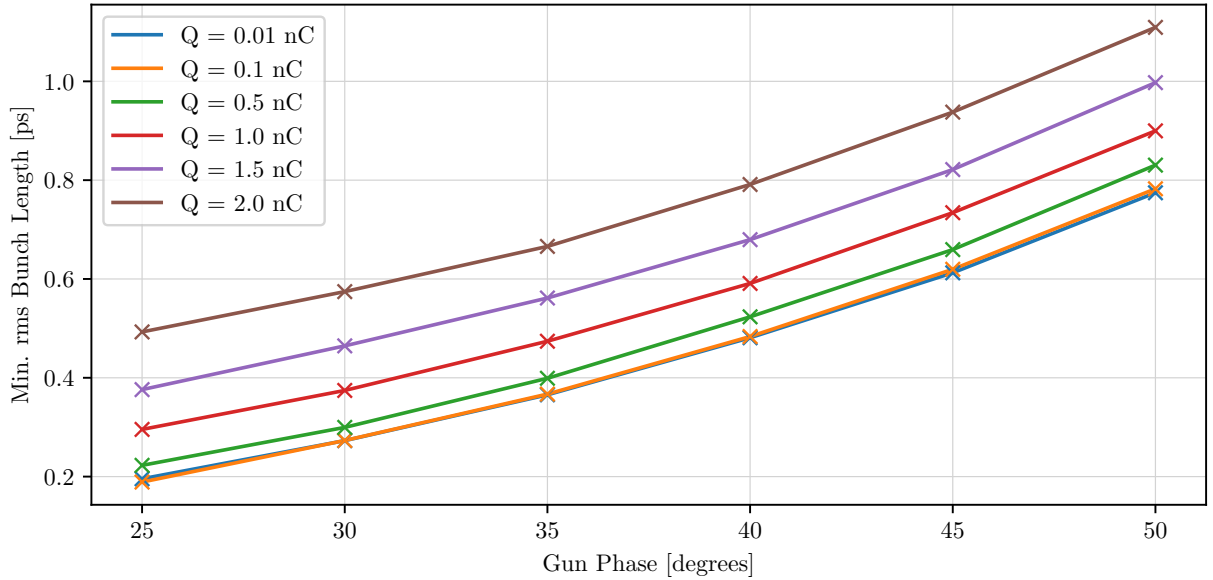


Figure 3.28: The minimum bunch lengths achievable for bunches of different charge, produced from a laser spot of 0.8 mm, vs RF gun phase.

The minimum bunch length achievable reduces with gun phase for all charges investigated, as can be seen in Figure 3.28. The reduction in minimum bunch length with gun phase is greater after compression in the bunching cavity, than the reduction of bunch length, shown in Figure 3.12, for bunches at the entrance to the bunching cavity. For example, at the entrance to the bunching cavity, a 0.5 nC bunch, generated from a 0.8 mm laser spot, is a factor 1.7 times shorter when accelerated at a gun phase of 25° , than the same bunch accelerated at a gun phase of 45° . After passing through the buncher at the maximum compression phase, the 25° bunch is a factor 3.0 times shorter. The reason for this extra compression is that accelerating a bunch at a lower gun phase causes a velocity bunching effect where the velocity of the bunch tail is higher than the bunch head, which is then amplified in the buncher.

As with bunches accelerated on the peak accelerating phase of the gun, the minimum bunch length following the buncher was longest for bunches produced from a 0.4 mm laser spot and shortest for a 1.2 mm spot. For bunches produced from a 0.4 mm spot, the bunch

length reduction caused by lowering the gun phase was only marginally greater than the reduction in bunch length at the entrance to the bunching cavity. Furthermore, as the charge extracted from the gun reduces significantly at lower gun phases, a 0.4 mm spot is not suitable for generating ultra-short high-charge bunches.

For ultra-short bunches accelerated at reduced gun phases to be useful to users, the beam quality must not drop significantly. As shown previously in Figure 3.14, the energy spread of bunches at the entrance to the bunching cavity depends on the gun phase. For a bunch of 0.01 nC charge, the minimum energy spread was seen at a gun phase of 45° . As the phase of the gun was reduced the energy of spread grew to a local maximum at 20° . For higher bunch charges, the minimum energy spread was found at lower gun phases and there was a different growth rate in energy spread as the gun phase was reduced.

However, when accelerated at the peak-energy phase through the bunching cavity there is a decrease in energy spread with gun phase for all bunch charges, shown in Figure 3.29a. The reduction in energy spread through the bunching cavity is larger for lower gun phases. The reduction in bunch length at lower gun phases is due to those bunches having a shorter bunch length at the entrance of the bunching cavity, thus being accelerated by a more uniform electric field. The reduction in bunch length is large enough to override the increase in initial energy spread exiting the gun. As the reduction in bunch length with gun phase is lower for a bunch produced from a 0.4 mm laser spot than those produced from a 0.8 mm laser spot, the reduction in energy spread is also smaller. As expected, the reduction is larger for bunches produced from a 1.2 mm laser spot.

A similar relationship between gun phase and energy spread holds at the phase of minimum bunch length (Fig. 3.29b). Again, this is due to a reduced bunch length entering the bunching cavity. The relative reduction in energy spread is, however, smaller for bunches accelerated at the minimum bunch length phase than the peak-energy phase of the buncher. For example, a bunch of charge 0.5 nC accelerated on-crest in the buncher, has an energy spread a factor 3 lower at a gun phase of 25° than a phase of 45° . Whereas, the energy spread of bunches accelerated at a gun phase of 25° is only a factor 1.7 lower than bunches accelerated at a gun phase of 45° , for the minimum bunch length phase of the buncher.

Reducing the gun phase only made a small difference to the beam emittance. When no

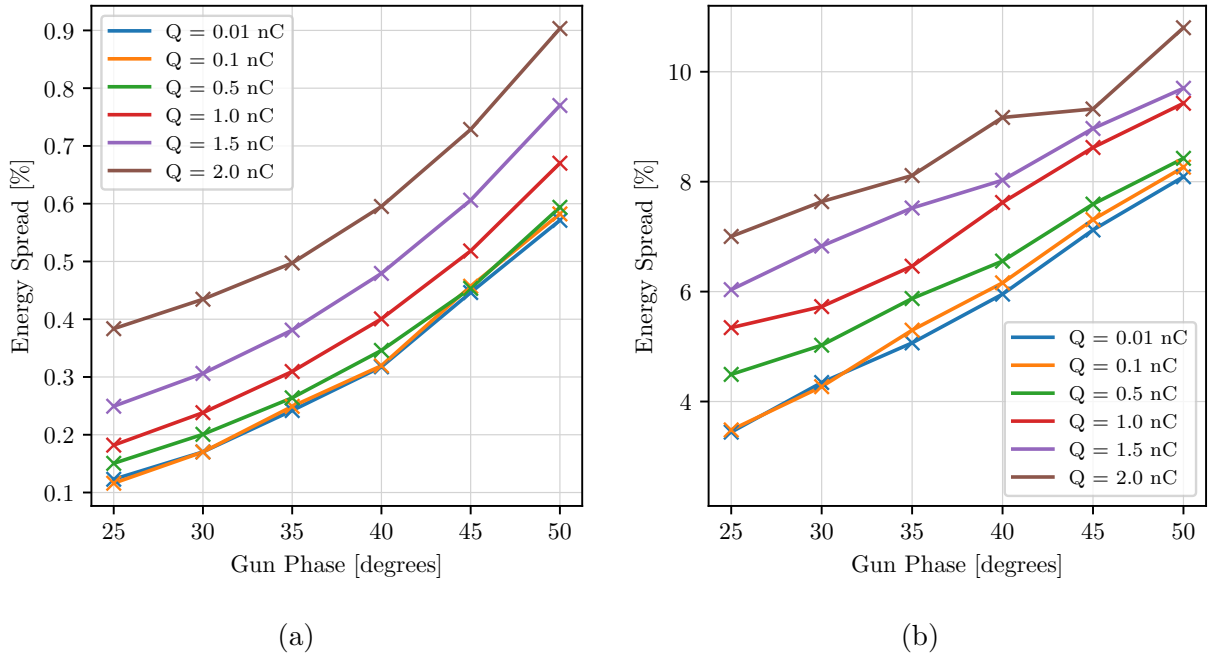


Figure 3.29: ASTRA simulations of the energy spread of bunches of different charge, all produced from a laser spot of 0.8 mm, at the end of the bunching cavity set to, **(a)** the peak accelerating phase, and **(b)** the phase of minimum bunch length vs RF gun phase.

solenoid field is present around the gun, reducing the gun phase increases the emittance, as shown in Figure 3.15. However, by adjusting the strength of the gun solenoid, it was possible to minimise this emittance growth significantly, as shown in Figure 3.30. Following this minimisation there was still a small emittance growth with lower gun phases. The emittance growth was relatively larger for lower-charge bunches than high charge bunches, with the emittance of the 0.01 nC bunch growing by a factor 1.5 from 45° to 25°, compared to emittance growth of a factor 1.1 for a bunch of 2 nC over the same phase range. As the emittance growth for low-charge bunches is mainly driven by RF effects the emittance growth cannot be suppressed as effectively with the solenoid. However, in higher charge bunches the emittance growth is mainly driven by space charge forces, therefore, solenoid compensation is relatively more effective across different gun phases.

When accelerating at the peak-energy phase through the buncher, it is possible to optimise the buncher solenoid to suppress emittance growth through the buncher, as was shown for bunches accelerated at a gun phase of 45° (Fig. 3.23b). With each different gun phase, the buncher phase at which the emittance suppression begins to fail is similar to the 45° case at a buncher phase of around -50° . There is a similar rise in emittance at the minimum

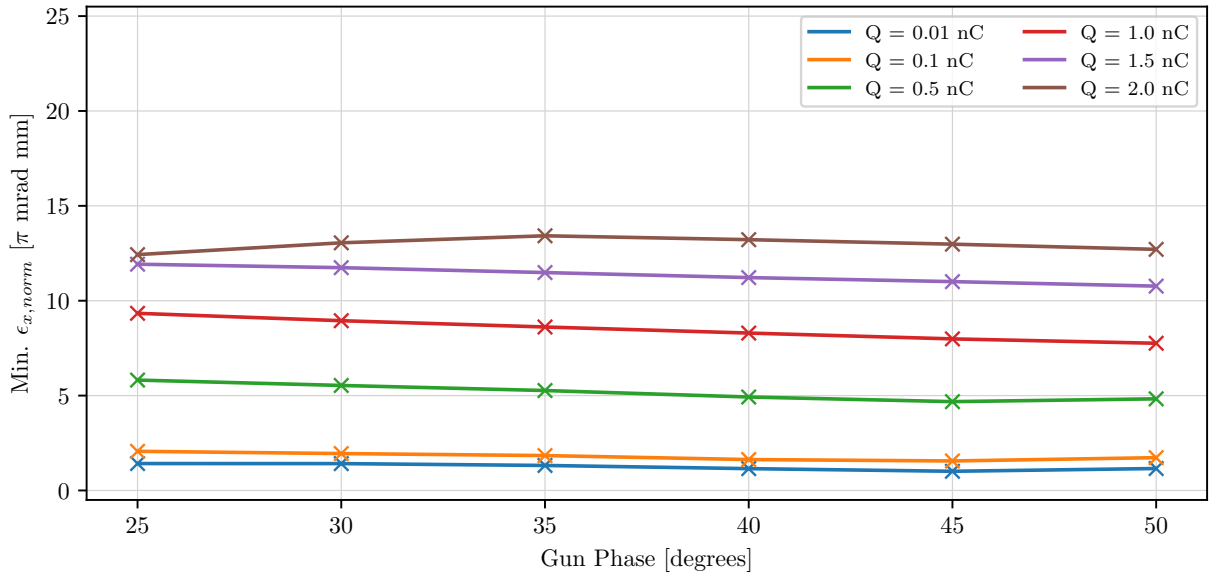


Figure 3.30: The minimum emittance achievable at the entrance of the bunching cavity, following an optimisation of the gun solenoid vs gun phase for bunches of different charge, produced from a laser spot of 0.8 mm.

bunch length phase for each gun phase. Again the relative emittance growth between the maximum acceleration and minimum length phases is higher for higher charge bunches. A bunch of charge 2 nC, generated from a laser spot of 0.8 mm, undergoes an increase in emittance of around a factor 2 relative to the maximum acceleration phase for each gun phase. The strength of the buncher solenoid required to minimise the emittance growth is very similar for each gun phase as the beam energy is only slightly changed by the change in gun phase.

By reducing the gun phase experimentally it was possible to reduce the minimum bunch lengths achievable on CLEAR. The gun phase was reduced by 20° as in simulation, which allowed compression of a 0.5 nC bunch to 0.2 ± 0.1 ps and a 0.3 nC bunch to a length that was likely shorter than 0.2 ± 0.1 ps. Both of these results were produced from a 0.5 mm laser spot and show good agreement with the simulated reduction in bunch length. It must be noted that producing a bunch of higher charge than 0.5 nC at a phase 20° lower than the peak-energy phase was not possible experimentally, due to the total charge extracted from the RF gun being too low.

For providing users who require moderately short bunches of length between 2 ps and 3 ps, with charges lower than 1 nC, it is often easier to just de-phase the gun and leave the

three following cavities on their peak-energy phases. By doing this, the operator is able to reduce the bunch length sufficiently without increasing the emittance, energy, and energy spread significantly, thereby reducing the time needed to optimise beam transport.

3.5 Summary

Since beginning operation in 2017, the CLEAR user facility has served a wide range of users, each requiring a different beam set up. One of the most commonly requested beam characteristics is a short bunch length. In order to assess the extent to which these requests could be realised, studies of bunch compression in CLEAR were undertaken.

By simulating the effect of the RF phase of the gun, it was suggested that the laser spot used to produce the beams should be larger than 0.4 mm in order to produce high-charge short bunches. The optimum phase for producing high quality bunches was shown to be between the peak accelerating phase and -15° of this phase depending on the bunch charge. At these phases, both the emittance and energy spread was minimised. However, due to the large space-charge forces present for a 0.4 mm laser spot, high-charge bunches could not be extracted fully at these phases and the bunch lengths were very long. By increasing the laser spot to 0.8 mm these two issues could be overcome. The space-charge forces present in the gun also caused a large emittance growth for high-charge bunches. Simulations of the gun solenoid suggest that this emittance growth can be compensated by up to a factor 2.

Following the optimisation of the gun parameters, it was shown in simulation that high amounts of bunch compression could be performed. By adjusting the phase of the bunching cavity, it was shown that for laser spots of 0.8 mm or higher, bunches of 2 nC in charge could be compressed to less than 1 ps in length. In these simulations, the emittance of the beam increased rapidly as the bunch was compressed. However, it was demonstrated that the solenoid magnets that surround the cavity could be used to suppress this emittance growth.

Some experimental verification of this bunch compression was performed. By measuring the bunch length at several different RF phases we saw some agreement with simulation. Further to this, by looking at the minimum lengths achievable experimentally for several bunches of different charge, we were able to show good agreement with simulation and compression of a bunch of charge 0.8 nC to a length of 0.8 ± 0.2 ps. Presently bunches of

less than 1 ps in bunch length are routinely provided to users.

It was noted that the minimum length achievable was often less than in simulation with the RF phase of the gun on the peak accelerating phase. Further simulations were undertaken to investigate the effect of reducing the phase of the RF gun. It was shown that by reducing the phase of the gun it is possible to reduce the minimum bunch length. It was also demonstrated that reducing the gun phase does not significantly reduce the quality of the bunch. It was shown that reducing the gun phase could lead to a reduction in the energy spread of the beam. Furthermore, the beam emittance only slightly increased as the gun phase was reduced. When the gun phase was reduced experimentally it was possible to significantly reduce the minimum bunch length achievable in compression. In addition to this, reducing the gun phase, whilst leaving the following accelerating cavities at a maximum acceleration phase, simplifies the experimental procedure required to achieve bunch lengths of 2 - 3 ps. Again, bunches compressed using the gun phase and the buncher phase are routinely provided to users on CLEAR. Additionally, high-charge bunches compressed using both the gun and the buncher phase would be short enough for acceleration in the eSPS linac.

Further experimental work must be undertaken to improve the stability of the machine in order to provide a more detailed comparison with simulation. In addition, the highest charge compressed to a sub-ps bunch length experimentally was 0.8 pC. As users may require higher charges than this, further experimental studies of higher charges should be done.

Further simulation should be undertaken to assess potential upgrades of the CLEAR beamline. A new klystron to power either the gun or bunching cavity would allow independent control of the RF fields of the two structures. Potential operation with a higher gun field could mean that higher charge is extracted at lower phases allowing operation at more optimal compression phases for high-charge bunches. Furthermore, tuning of the accelerating field of the bunching cavity could aid compression further. In addition to a new klystron a new laser may be purchased in the future. A shorter laser pulse may allow a reduction in bunch length from the gun and should, therefore, be studied in detail.

Chapter 4

Potential Upgrades to CLEAR

The CLEAR facility is constructed of components originally used in several other facilities from CERN's past, most recently CTF3. Because of this, the accelerator is not necessarily optimised for all of the needs of potential users. It would be possible to extend the range of available beams, and improve machine performance with changes to the existing hardware of both the injector and experimental beamline. These upgrades are particularly relevant to the eSPS project as there is more space to install additional hardware in the new beam hall. The following chapter will discuss changes to the injector aimed towards providing users with shorter, higher-charge, and higher-quality bunches, namely with the installation of a new laser system and a new klystron.

4.1 Reduced laser pulse length

The first potential upgrade of CLEAR to be discussed would be to install a new laser system for the photoinjector. The current laser system has a pulse length of 4.7 ps. Several photoinjector facilities presently in operation use laser systems able to produce shorter pulses than at CLEAR, such as: the European XFEL [178], with a laser of pulse length 3.1 ps; the SwissFEL injector [145, 179], which uses a laser of pulse length that can be varied between 1.2 ps and 4.2 ps; and the CLARA injector linac [76], which uses a laser of pulse length 76 fs. By using a shorter laser pulse it would be possible to reduce the bunch length at the peak accelerating phase and should allow shorter bunches to be produced through velocity bunching. Shorter bunches, that may be easy to produce experimentally, would be useful for various users, such as for the generation of THz radiation, and the testing

of novel bunch length diagnostics using Electro-Optical sampling and Cherenkov radiation techniques. Furthermore, the ability to produce shorter bunches would be advantageous in the scenario in which the CLEAR injector was reused in the eSPS.

A new laser system would also carry additional benefits. Charge jitter is strongly correlated with the laser power incident on the photocathode. Recent consolidation of the present laser system has reduced the power jitter significantly [156]. It has been shown that with careful setup of the laser system, a charge jitter of $\sim 1\%$ rms, and 5% peak-to-peak can be achieved. Typically, however, the charge stability on CLEAR is not as good. A new laser system could both have better stability and be easier to set up. Furthermore, any new laser could be installed closer to the gun than at present. The CLEAR laser is currently installed a distance of 75 m from the photocathode for historic reasons. Such a long optical line makes alignment difficult and increases the amount of position jitter. With careful setup it is possible to reduce the position jitter of the laser on the photocathode to $\sim 10 \mu\text{m}$. Again, the laser system is not typically this stable and could be improved with a new laser. In addition, the repetition rate of bunch trains in CLEAR could be increased with the installation of a new laser system. Presently, the maximum repetition rate of bunch trains is 10 Hz. The RF system could be reconfigured to increase the repetition rate of the RF pulses, but it is likely that the laser system cannot. A higher repetition rate would be useful to many users requiring a high integrated number of electrons to be incident on their experiment. One particular interest would be for studies of FLASH RT. As FLASH studies require their dose to be delivered in less than ~ 0.1 s, only a maximum of two trains can be delivered at present. By upgrading to 100 Hz, 10 trains could be delivered, a potentially significant increase in the dose delivered on FLASH timescales.

To investigate the effect of a new laser, with a shorter pulse length, on bunch length, further ASTRA simulations were performed. Similar to the simulations performed in Chapter 3, the RF phase of the gun was optimised first, followed by the solenoid strength, and then the buncher RF phase and solenoid strength. The same six bunch charge values were investigated, in the range 0.01 - 2.0 nC, generated from laser spots of the same sizes, 0.4, 0.8 and 1.2 mm. Again the peak electric field in the gun and buncher were set to 80 MV/m and 18 MV/m respectively. The maximum strength of the gun solenoid was set to 0.3 T to investigate whether the gun solenoid would need to be upgraded along with the laser system.

The maximum field strength in the buncher solenoid was set to 0.1 T. The laser pulse length was varied in the range 1 - 5 ps.

4.1.1 RF Gun

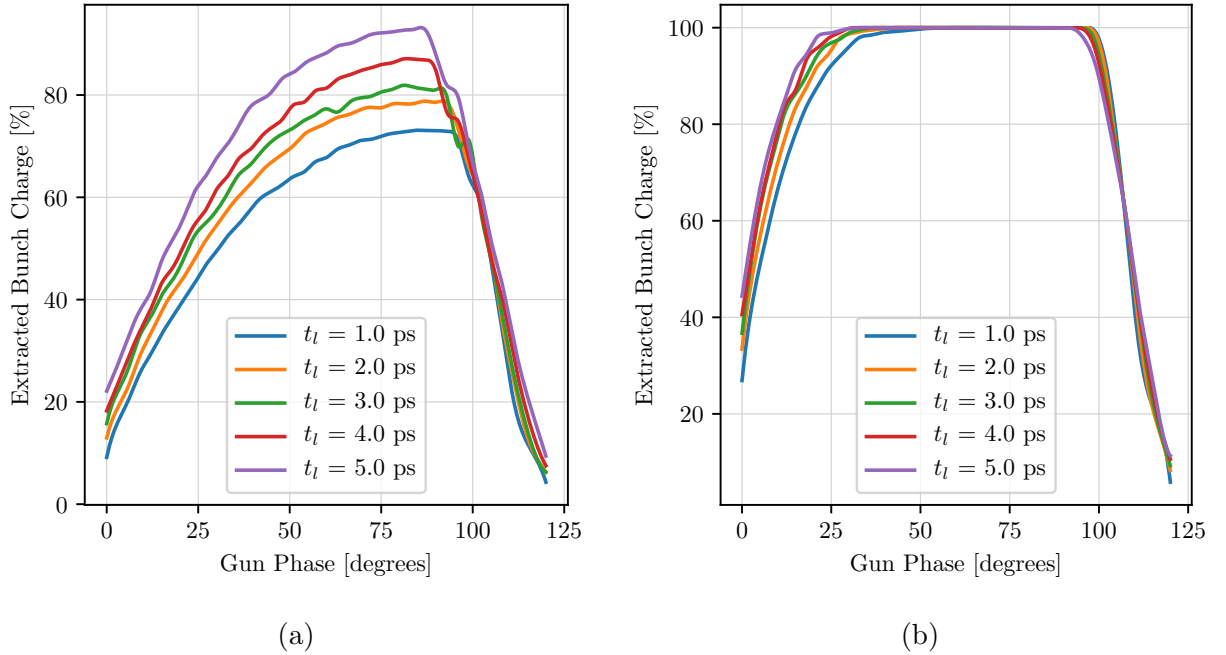


Figure 4.1: ASTRA simulation of the percentage bunch charge extracted from the RF gun for a 2 nC total charge, produced by laser pulses of different length and a laser spot of **(a)** 0.4 mm, and **(b)** 0.8 mm, vs gun phase.

Producing high-charge bunches from a laser spot of 0.4 mm was more difficult for shorter laser pulse lengths. Figure 4.1a shows the percentage charge extracted from a 2 nC bunch produced from a 0.4 mm laser spot as the phase of the gun was varied. The reduction in pulse length means that the charge density of the bunch around the cathode is higher, which increases the shielding effect of the mirror charge. The extracted charge was over 20% lower at the peak accelerating phase of the gun for a bunch produced from a laser pulse of 1 ps relative to one of 5 ps. As mentioned in Section 3.4.1, it was possible to increase the total bunch charge to allow a charge of 2 nC to be extracted from the gun when a laser pulse length of 4.7 ps was used. However, this was not possible for charges of 1.5 nC or above produced from a laser spot of 0.4 mm, and with a pulse length of less than 3 ps. As previously shown, by increasing the laser spot the charge density is reduced, thereby decreasing the shielding effect of the mirror charge and increasing the total amount of charge extracted. Figure 4.1b

shows the extracted charge for a 2 nC bunch produced from a 0.8 mm laser spot. The reduction in extracted charge with reduced laser pulse is significantly lower than with a 0.4 mm laser spot, with only a 2 nC bunch generated from a laser pulse of 1 ps not being extracted fully at the peak accelerating phase. When the laser spot is increased to 1.2 mm more charge is extracted. As it is impossible to extract some higher charge bunches with 1 ps and 2 ps laser pulses from a laser spot of 0.4 mm, this laser spot size was not investigated further.

The variation in energy was similar for all charges and laser pulse lengths. There were some small variations in energy at phases lower than the peak-energy phase, similar to those shown in Figure 3.11, due to the bunch not being fully extracted.

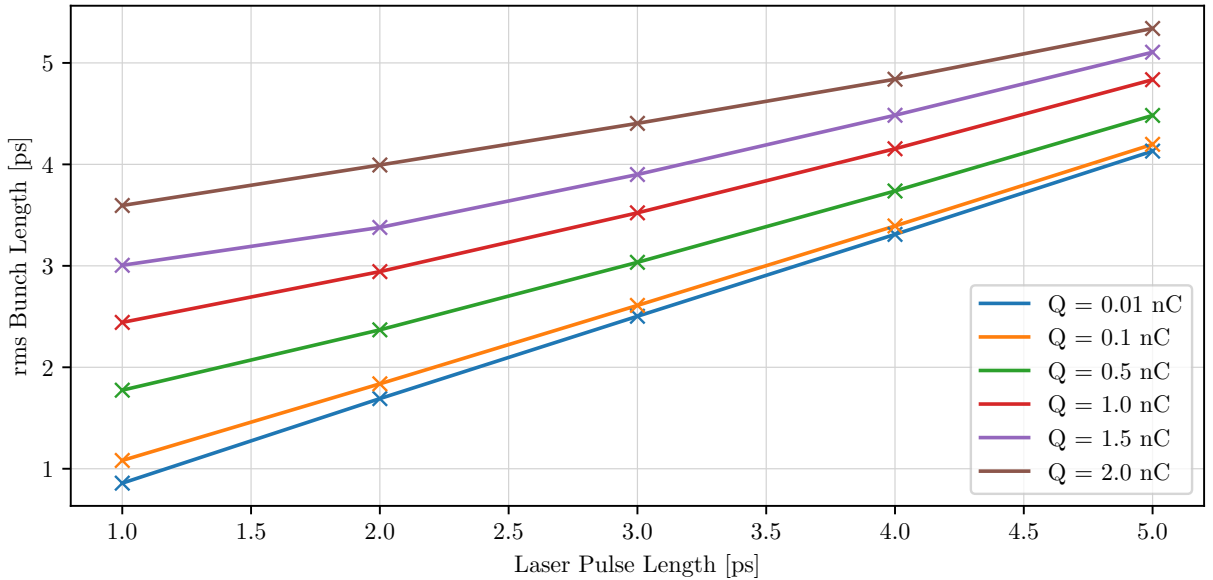


Figure 4.2: The bunch length at the entrance of the bunching cavity of bunches of various charge, generated from a laser spot of 0.8 mm, accelerated at the maximum energy phase of the RF gun vs the laser pulse length.

The bunch length at the entrance to the bunching cavity for bunches generated from a 0.8 mm laser spot, accelerated at the peak-energy phase is shown in Figure 4.2. For low-charge bunches the bunch length is similar to the laser pulse length. However, some velocity bunching occurs which reduces the length. For example, bunches of charge of 0.01 nC are around 15% shorter than the initial laser pulse length. Bunches of higher charge are longer due to the increased space-charge forces in the gun and the drift between the gun and the buncher. Increased space-charge forces mean that the reduction in bunch length with laser

pulse length is smaller for higher charged bunches. The difference in bunch length between a 0.01 nC bunch and a 2 nC bunch produced with a laser pulse of 5 ps is a factor 1.3, whereas the difference is a factor 4.2 when both bunches are produced from a 1 ps pulse length. By using a laser spot size of 1.2 mm, the space-charge forces are reduced. In low-charge bunches this results in only a small difference in bunch length compared to the 0.8 mm laser spot. However, the bunch lengths of high-charge bunches are more similar to the lengths of low charge bunches for all laser pulse lengths investigated. For example, a 2 nC bunch produced from a laser pulse length of 1 ps is a factor 3.3 longer than a 0.01 nC bunch, and a 2 nC bunch is only a factor 1.2 longer when produced from a 5 ps laser pulse. As shown previously, it is possible to decrease the bunch length by operating at phases lower than the peak-energy phase. However, the relative reduction in bunch length is lower for shorter laser pulses and higher bunch charge as the increase in space-charge forces overcomes any velocity bunching.

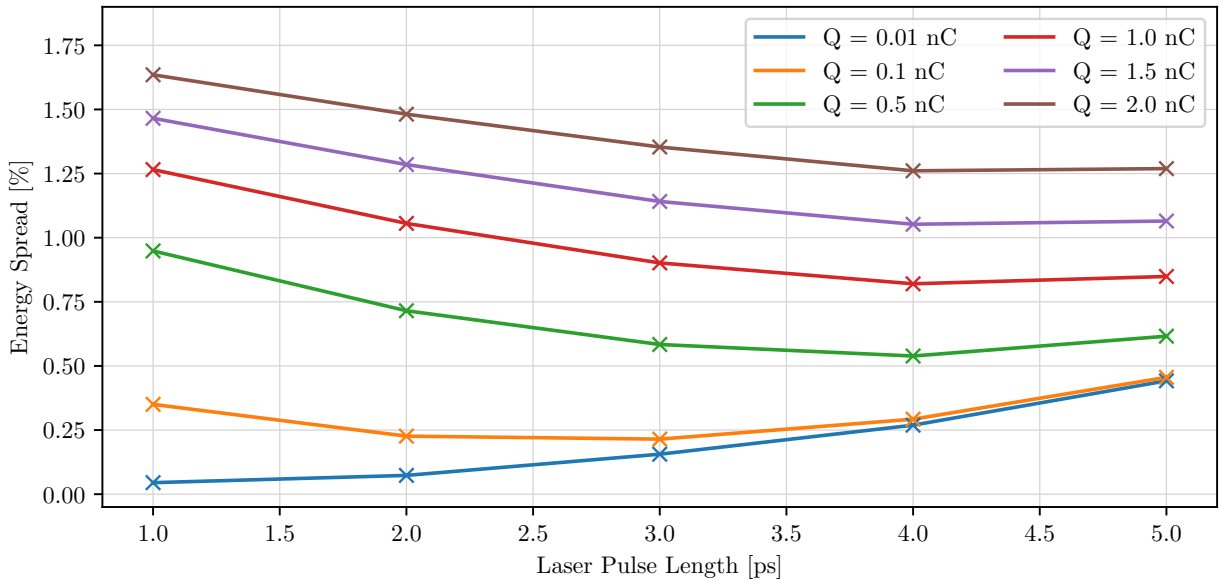


Figure 4.3: The energy spread at the entrance of the bunching cavity of bunches of various charge, generated from a laser spot of 0.8 mm, accelerated at the maximum energy phase of the RF gun vs the laser pulse length.

The energy spread at the peak accelerating phase of the gun for different charge bunches, produced from a 0.8 mm laser spot, with different laser pulse lengths is shown in Figure 4.3. For bunches of charge 0.01 nC, the energy spread decreases with laser pulse length. The decrease is due to the bunch length being lower in the gun, and the electrons, therefore,

being accelerated by a more uniform electric field. There is also a reduction in energy spread seen for bunches of charge 0.1 nC from laser pulse lengths of 5 ps to 3 ps, and all other bunch charges between 5 ps and 4 ps. However, the increased space-charge forces for higher bunch charges produced from shorter laser pulse lengths cause an increase in energy spread over the drift following the gun cancelling any reduction due to shorter bunch lengths. Furthermore, the reduction in bunch length is lower for high-charge bunches.

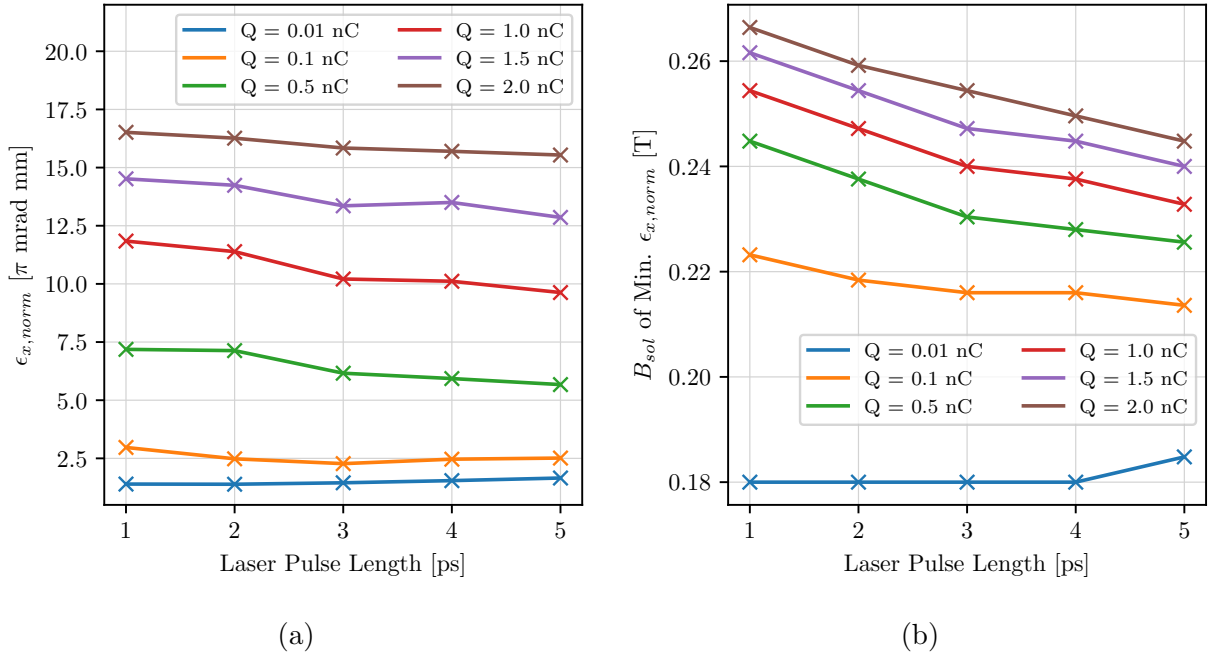


Figure 4.4: **(a)** The minimum emittance and **(b)** the solenoid strength required to minimise emittance of bunches of different charge produced from a laser spot of 1.2 mm vs laser pulse length.

A reduction in laser pulse length does not cause a significant increase in emittance, as shown in Figure 4.4a. Emittance growth in bunches of charge 0.01 nC is driven by the RF field in the gun and thermal effects on the cathode. With shorter laser pulse lengths there is a reduction in emittance for this bunch charge as the RF contribution to emittance growth is lower. However, at higher bunch charges emittance growth is driven mainly by space-charge effects. There is an increase in emittance of $\sim 10\%$ for bunches of charge more than 0.1 nC. The increase is similar for bunches generated from both 0.8 mm and 1.2 mm laser spots. The increase in space-charge forces can mostly be compensated by the solenoid magnet. However, as shown in Figure 4.4b, when the laser pulse length is reduced there is a linear increase in the solenoid field strength required to suppress emittance growth for all

charges higher than 0.01 nC. For many charges and laser pulse lengths the solenoid strength is higher than the current maximum of 0.24 T. Therefore, for effective operation with shorter laser pulses, the solenoid control system must be upgraded.

4.1.2 Bunching Cavity

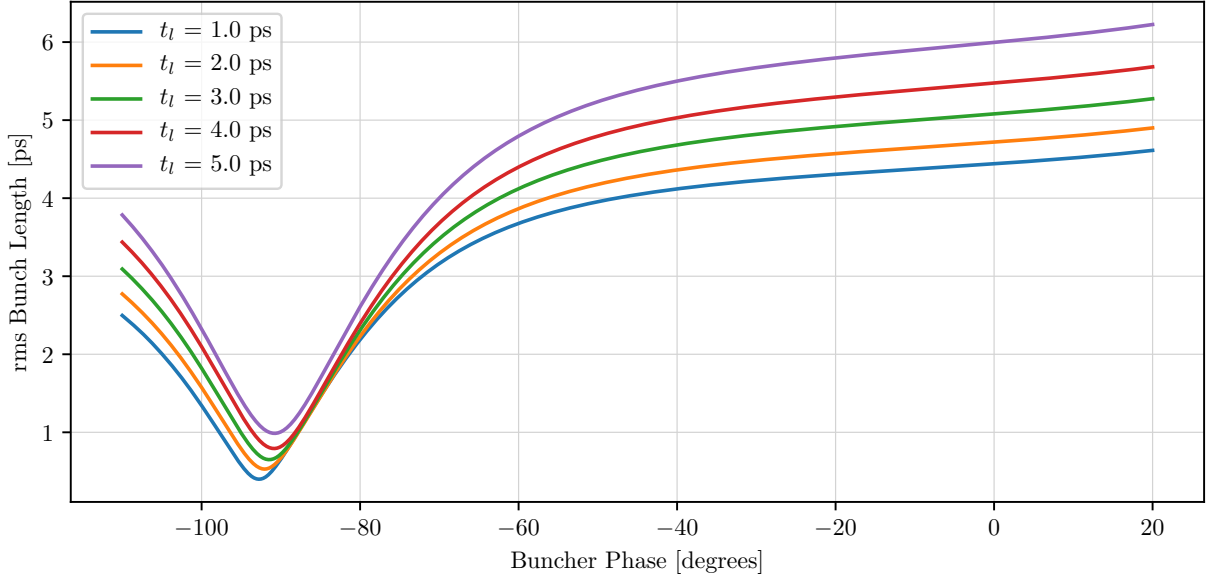


Figure 4.5: ASTRA simulation of the bunch length vs buncher phase for bunches of 2 nC produced from a 0.8 mm laser spot and different laser pulse lengths.

Following investigation of the RF gun, the phase of the bunching cavity was varied to investigate the ability to perform velocity bunching with bunches produced from shorter laser pulses. For tracking through the buncher, the phase of the gun was set to the maximum energy phase and the solenoid was set to minimise emittance growth. The energy of all bunches was similar to that shown in Figure 3.17. The bunch length was shorter for bunches produced from shorter laser spots for all buncher phases, as shown in Figure 4.5. For all charges above 1 nC there is a small increase in bunch length around the peak-energy phase due to space-charge forces early in the buncher. The relative increase is larger for shorter laser pulses due to the increased charge density. For the example shown in Figure 4.5, there is a 22% increase in bunch length for a 1 ps laser pulse length and only a 12% increase for a 5 ps laser pulse length. For all laser pulse lengths there is a small reduction in bunch length over the first 60° followed by a more rapid drop off towards zero crossing. For bunches produced by a shorter pulse length, the minimum length occurs at a lower phase due to the

increase in space-charge forces.

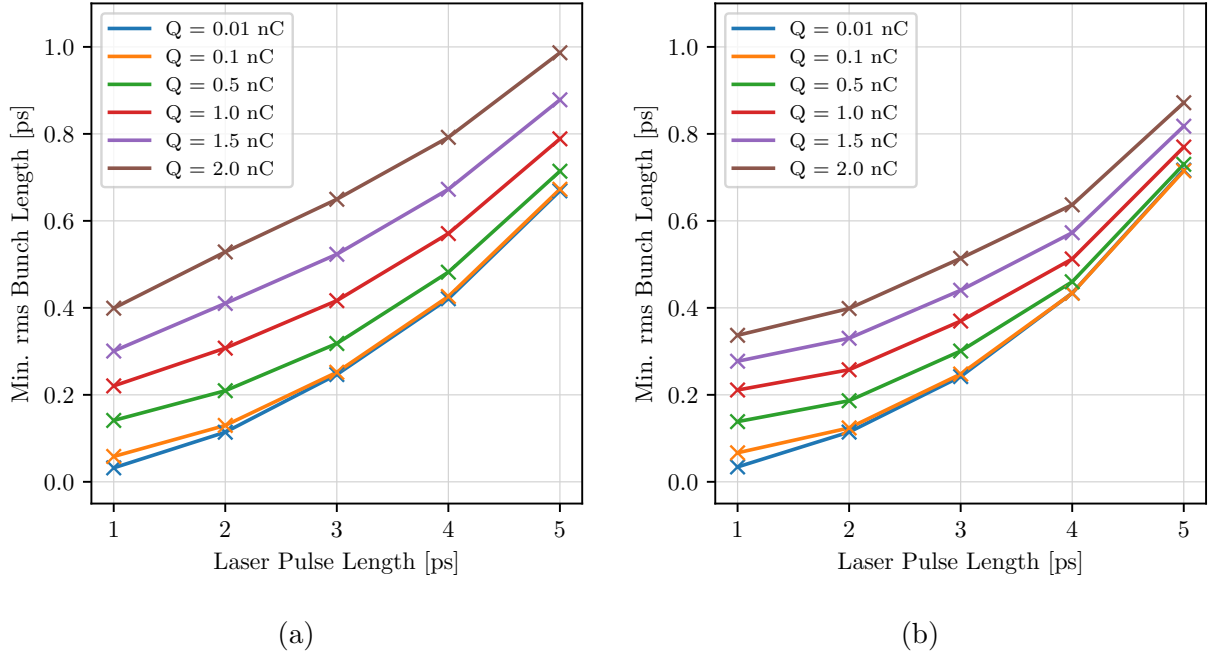


Figure 4.6: The minimum bunch lengths achievable for bunches of different charge produced from a laser spot of **(a)** 0.8 mm, and **(b)** 1.2 mm, vs laser pulse length.

The minimum achievable bunch length is significantly shorter for bunches produced from a shorter laser pulse, as shown in Figure 4.6. For bunches of charge 0.01 nC and 0.1 nC, bunch lengths of less than 100 fs are possible to produce with a 1 ps laser pulse length. It would also be possible to produce a bunch of charge 2 nC with a bunch length of less than 0.5 ps with a 1 ps laser pulse length. The reduction in bunch length is larger for lower-charge bunches than higher-charge bunches. Using a laser with a 1 ps pulse length, bunches of charge 0.1 nC could be compressed to a length a factor 10 times shorter than the current CLEAR setup. Whereas, the reduction in bunch length achievable for a 2 nC is just a factor 2.3. Again, this is due to the magnitude of space-charge forces present at maximum compression. When bunches are generated from a laser spot of size 1.2 mm, there is a reduction in bunch length relative to 0.8 mm (Fig. 4.6b). The relative magnitude of the reduction is similar to that shown in Figure 3.19 for all laser pulse lengths.

The variation in energy spread with buncher phase is similar for all laser pulse lengths, as shown in Figure 4.7 for bunches of 2 nC produced from a laser spot of 0.8 mm. For all laser pulse lengths, the minimum energy spread is produced at a phase slightly below the maximum energy phase, with the minimum occurring at a slightly lower phase for shorter

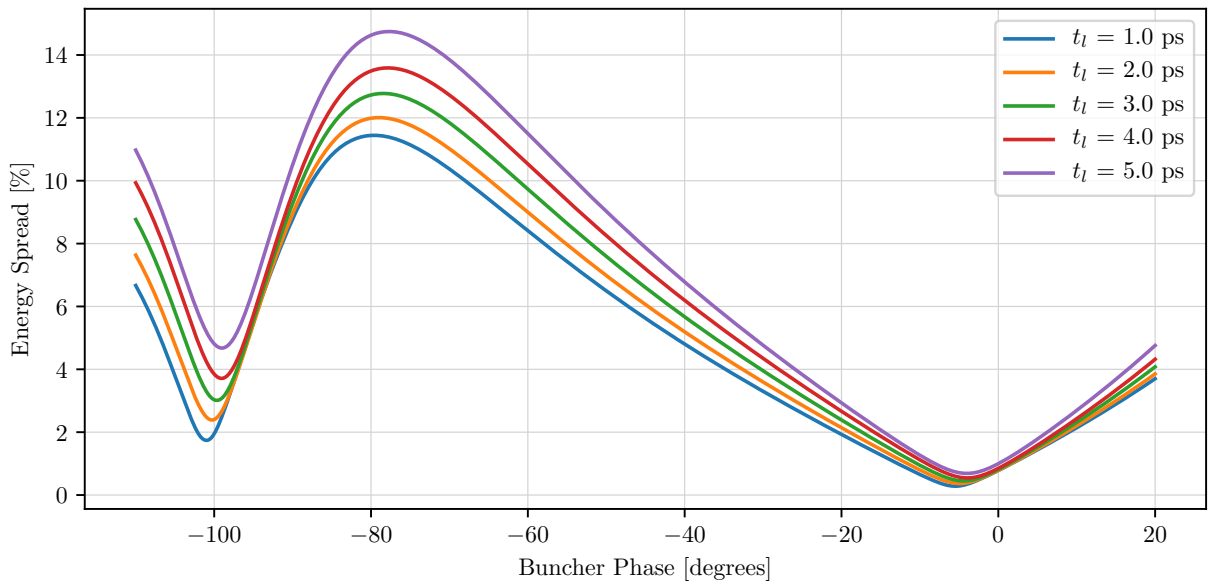


Figure 4.7: ASTRA simulation of the energy spread vs buncher phase for bunches of 2 nC, generated from a 0.8 mm laser spot and different laser pulse lengths.

laser pulse lengths. With all pulse lengths, there is a rise in energy spread towards a phase of -80° , where there is a maximum followed by a rapid decline towards a local minimum at a phase of $\sim -100^\circ$. The energy spread is lower for bunches produced from a shorter laser pulse for all phases investigated.

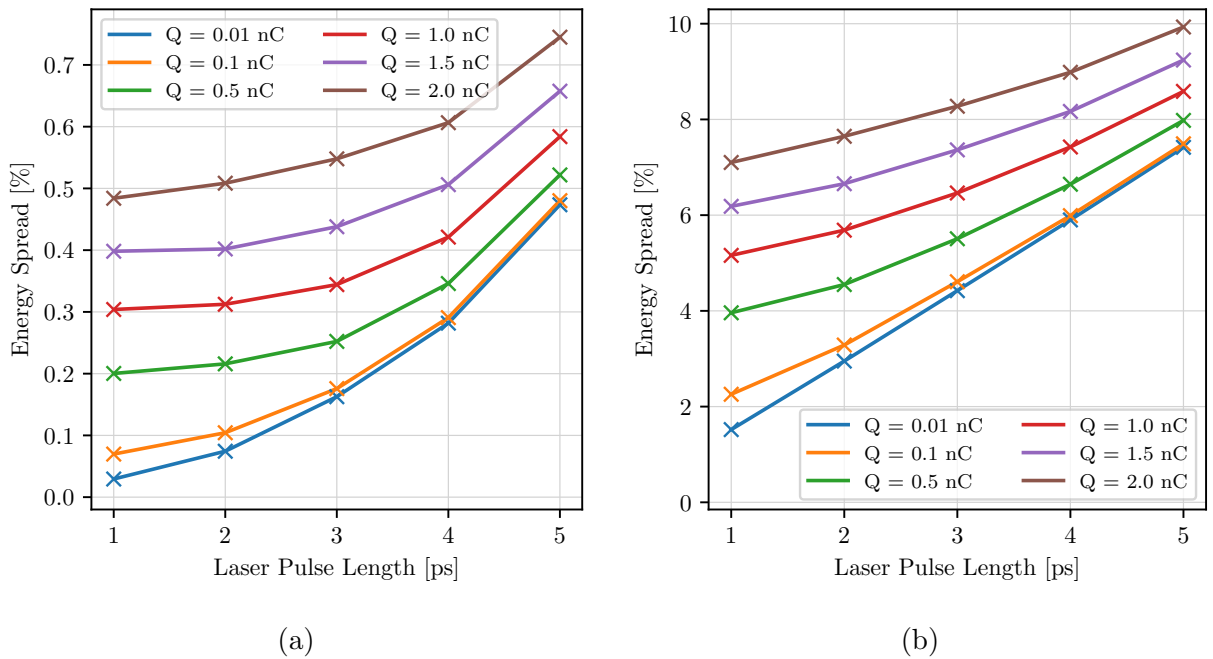


Figure 4.8: The energy spread of bunches of different charge, all produced from a laser spot of 0.8 mm at the end of the bunching cavity set to, **(a)** the peak accelerating phase, and **(b)** the phase of minimum bunch length, vs laser pulse length.

The energy spread at the maximum energy phase of the bunching cavity is shown in Figure 4.8a. Bunches produced from a shorter laser pulse have a smaller energy spread at the exit of the buncher. The reduction in energy spread with laser pulse length is due to the reduction in bunch length at the entrance of the bunching cavity. The reduction in bunch length overcomes the rise in energy spread at the entrance of the bunching cavity that was seen in Figure 4.3. The reduction in energy spread with laser pulse length is greatest for bunches of charge 0.01 nC and decreases with increased charge. The reason for this decrease in reduction with charge is due to both the energy spread at the entrance of the buncher and the change in bunch length. The initial energy spread of high-charge bunches is higher when they are produced from a shorter laser pulse (Fig. 4.3). Furthermore, the reduction in bunch length with laser pulse length is lower at the cavity entrance for high-charge bunches. A similar reduction in energy spread is seen at the phase of minimum bunch length, as shown in Figure 4.8b. Again the reduction in energy spread is greater for lower-charge bunches and is due to the reduction in bunch length with laser pulse length.

The buncher solenoid was optimised at each different phase to reduce emittance growth. There was no significant change in emittance with laser pulse length. At the peak accelerating phase it was possible to suppress emittance growth to the level seen at the entrance of the bunching cavity, as shown in Figure 4.9a. As shown previously, it was not possible to fully eliminate emittance growth around the phase of maximum bunch length compression. As shown in Figure 4.9b there was an increase in emittance relative to the emittance at the entrance of the cavity, but there was little variation with laser pulse length.

4.2 Additional Klystron

Another possible upgrade to CLEAR would be to install an additional klystron to power the RF structures. At present the same klystron is used to power the RF field in the gun and the bunching cavity. Mechanical phase shifters are installed on the waveguides to the gun and buncher, allowing the phases of both elements to be controlled independently. The RF power to the gun can be reduced with an attenuator. However, it is not currently possible to increase the electric field in the gun or adjust the electric field of the buncher independently of the gun. There is currently sufficient space in the klystron gallery above the CLEAR

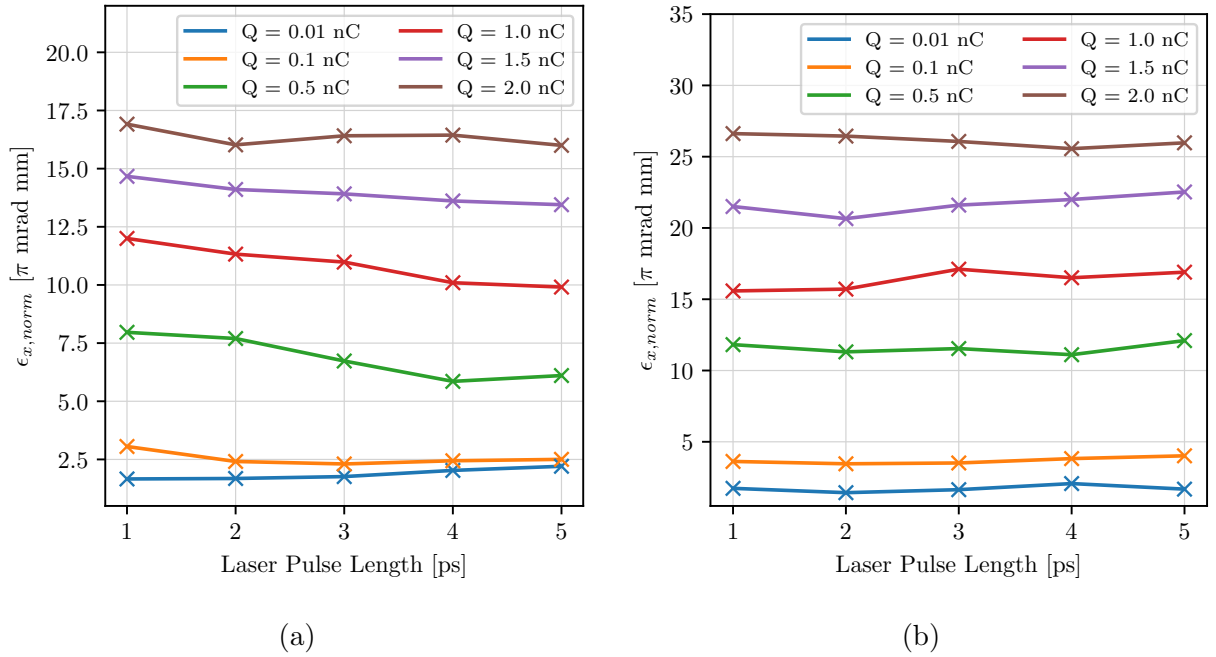


Figure 4.9: The minimum normalised emittance for bunches of different charge produced from a laser spot of 1.2 mm, accelerated at **(a)** the maximum energy phase in the buncher, and **(b)** the phase of the minimum bunch length, vs laser pulse length.

accelerator to install a new klystron. Furthermore, if the CLEAR linac is moved from its present location for use as the injector to the eSPS [45], there should be sufficient space for the new klystron. The following section will investigate the potential advantages of this upgrade, focusing on velocity bunching with a lower buncher field as well as using a higher accelerating field in the gun.

4.2.1 Reduced Buncher Field

The installation of an additional klystron would allow the strength of the electric field in the bunching cavity to be controlled independently. Operating with an adjustable accelerating field would allow the minimum achievable beam energy to be reduced to lower than the current 60 MeV minimum. It may also allow shorter bunches to be produced through velocity bunching. Bunch compression with velocity bunching relies on the generation of a velocity difference between the head and the tail of the bunch. As the bunch is accelerated during the bunching process the velocity difference becomes smaller. It has been shown that by operating with a lower field gradient in the bunching cavity, it is possible to improve the compression that can be achieved [141].

The current accelerating field strength in the bunching cavity is 18 MV/m, which cannot be reduced without also reducing the gun field strength. To investigate any possible improvement in bunch compression that can be achieved with a lower buncher field, ASTRA simulations were performed. Again, to ease comparison, bunches of the same charge, generated from the same laser spot sizes as described in Chapter 3 were simulated. The optimisation of the gun phase and solenoid was identical to that performed in Section 3.4.2, with the gun phase set to the peak-energy phase and the solenoid strength set to minimise emittance growth. The maximum electric field strength of the buncher was set to 7.5, 10.0, 12.5, 15.0, 17.5, and 20 MV/m. The phase of the bunching cavity was then varied to investigate velocity bunching.

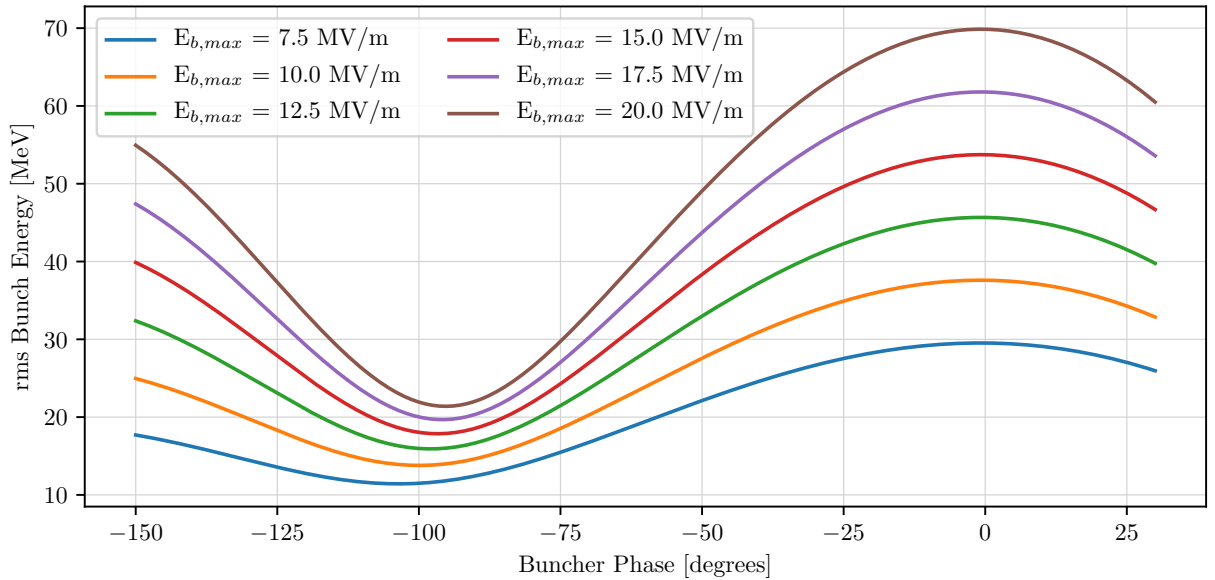


Figure 4.10: ASTRA simulation of the bunch energy of a 0.5 nC bunch, generated from a laser spot of 0.8 mm, vs the phase of buncher, for several different maximum buncher electric field strengths.

An example of the variation in energy with phase for a bunch of 0.5 nC generated from a laser spot of 0.8 mm is shown in Figure 4.10. For all bunches simulated, the maximum bunch energy, at a phase of 0° , increases linearly with the maximum field strength of the buncher. For a field strength of 7.5 MV/m, the bunch energy was 30 MeV, half the present minimum. Being able to produce beams of this energy would potentially be of use to many users, in particular for medical and irradiation experiments. There is a sinusoidal relationship between energy and phase for all of the bunches accelerated at all fields. However, the energy mini-

imum occurs at a lower phase for bunches accelerated at a lower buncher field. Furthermore, the reduction in minimum energy is not linear with the reduction in accelerating field. For the example shown in Figure 4.10, the difference between the energy minimum of bunches accelerated at 7.5 MV/m and 10.0 MV/m is 2.4 MeV, compared to just 1.7 MeV difference for 17.5 MV/m and 20.0 MV/m. The reason for both of these effects is that bunches that enter the cavity at a phase lower than zero crossing are initially decelerated before slipping to an accelerating phase. At a lower field in the buncher, it takes longer for the bunch to move to an accelerating phase, reducing the total energy that is gained by the end of the buncher.

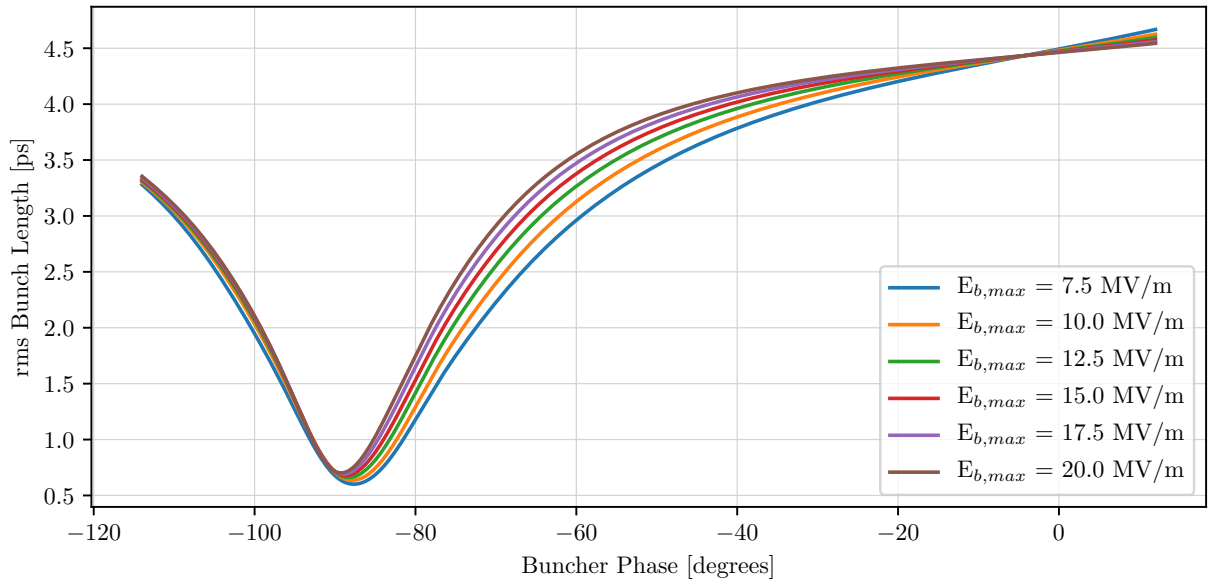


Figure 4.11: ASTRA simulation of the bunch length of a 0.5 nC bunch, generated from a laser spot of 0.8 mm, vs the phase of buncher, for several different maximum buncher electric field strengths.

The lengths of bunches accelerated at lower fields are shorter for most buncher phases below the maximum energy phase, as shown for a bunch of 0.5 nC generated from a laser spot of 0.8 mm in Figure 4.11. However, for charges of 0.5 nC and above there is a small increase in bunch length between the maximum energy phase and $\sim -10^\circ$, for lower accelerating fields relative to high accelerating fields. The increase is caused by space-charge forces present early in the buncher when the bunch energy is still low. The elongation is larger for higher charge bunches as well as bunches produced from a smaller laser spot, where the space-charge forces are higher. For phases below $\sim -10^\circ$, the velocity difference between the head

and tail of the bunches is larger for lower accelerating fields, resulting in a larger amount of compression. The minimum bunch length is also shorter for bunches accelerated at a lower buncher field. The minimum length is achieved at slightly lower phases for higher electric field strengths. Furthermore, the curve around the minimum bunch length is broader for lower buncher fields than higher fields. The increased width around the minimum bunch length would make operation at short lengths easier as it would be less sensitive to phase jitters and drifts.

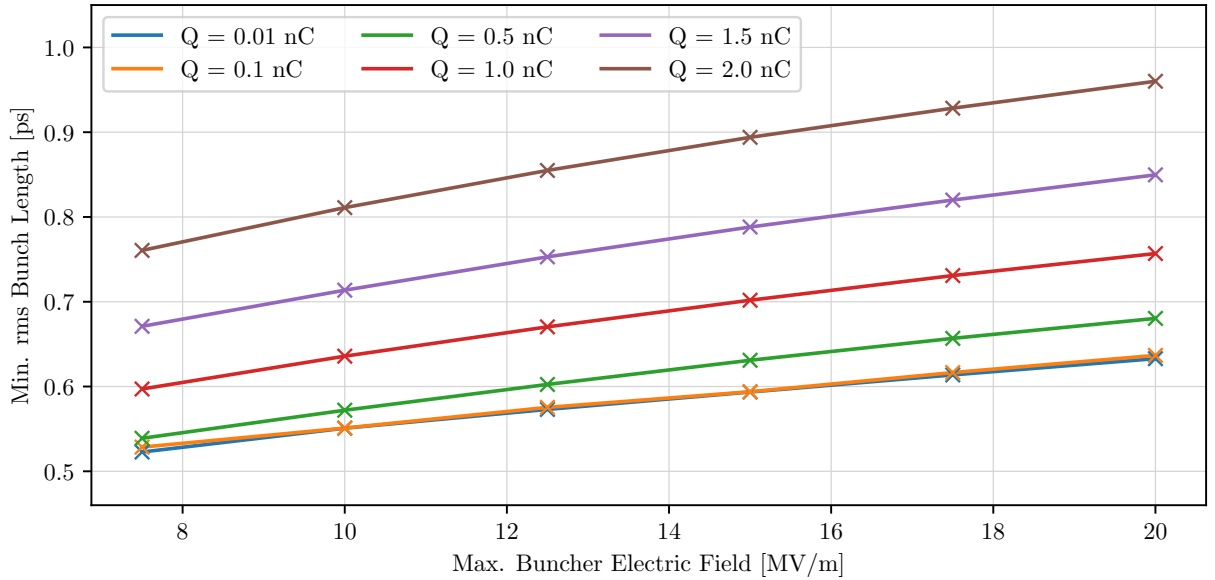


Figure 4.12: The minimum bunch lengths achievable for bunches of different charges, generated from a laser spot of 0.8 mm, vs maximum electric field in the bunching cavity.

The minimum bunch length achievable for all bunch charges investigated was shorter when velocity bunching was performed at lower accelerating gradients, as shown in Figure 4.12. The reduction in bunch length with reduced field is slightly greater for high-charge bunches than low charge bunches. For example, a 0.01 nC bunch generated from a laser spot of 0.8 mm was 20% shorter when velocity bunching was performed at a gradient of 7.5 MV/m than when performed at 20 MV/m. Whereas, a 2 nC bunch produced from the same spot was 26% shorter over the same difference in buncher field. The additional compression is because when accelerated at a lower buncher field, the minimum length is achieved at a higher bunch energy than when it is accelerated at a lower field. As the energy is higher, the space-charge forces are lower, which means there is less space charge induced elongation. The relative decrease in bunch length with buncher field strength is similar for

all three laser spot sizes investigated. It is likely that when operating at a lower gun phase, a similar reduction in bunch length with buncher field will be possible. However, this will need to be studied following a decision to install a new klystron.

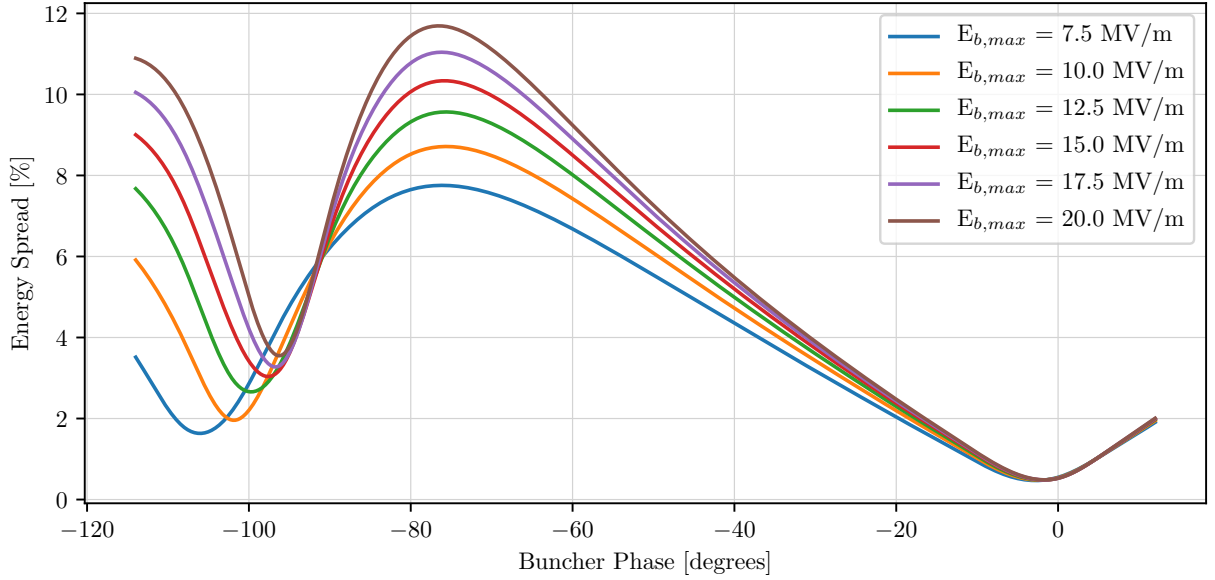


Figure 4.13: ASTRA simulation of the energy spread of a 0.5 nC bunch, generated from a laser spot of 0.8 mm, vs the buncher phase, for several different maximum buncher electric field strengths.

As with other potential upgrades to CLEAR it is important to assess the effect on beam quality. The variation in energy spread with buncher phase for bunches of 0.5 nC generated from a laser spot of 0.8 mm accelerated at different buncher fields is shown in Figure 4.13. Around the maximum acceleration phase, the energy spread is very similar for all buncher fields. As the phase is reduced the energy spread increases for all accelerating fields until a phase of around -80° , which is followed by a reduction in energy spread. The energy spread between 0° and -80° is lower for lower buncher fields. At zero crossing, the energy spread is similar for all buncher fields. At phases lower than zero crossing the energy spread continues to decrease to a local minimum. The buncher phase at which this local minimum occurs is lower for lower buncher fields. The energy spread at the local minimum is also lower for lower buncher fields. Bunches accelerated at phases lower than zero crossing are initially decelerated, and slip in phase towards a higher accelerating phase. Bunches accelerated by a lower field spend longer at a phase that reduces their energy spread. Furthermore, bunches accelerated at a lower field have a shorter bunch length, which also reduces the energy spread.

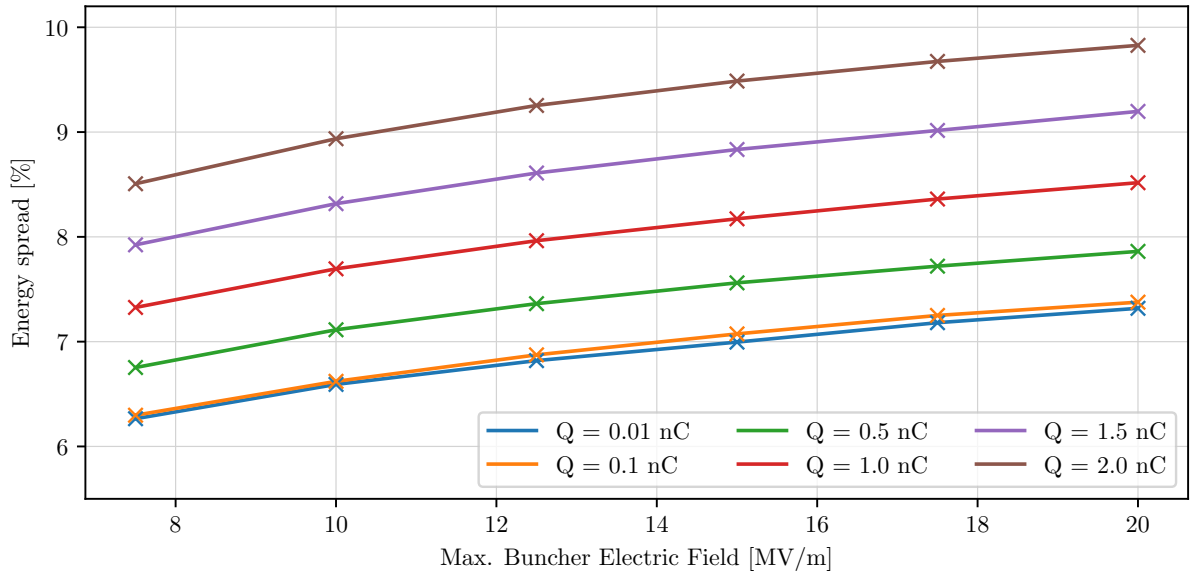


Figure 4.14: The energy spread for bunches of different charges, generated from a laser spot of 0.8 mm, at the phase of minimum bunch length in the bunching cavity vs maximum electric field in the bunching cavity.

The energy spread at the phase of maximum bunch compression is lower at lower accelerating fields for all bunch charges investigated (Fig 4.14). As the effect is mostly due to the slipping of RF phase, there is very little difference in the reduction of energy spread for different bunch charges. For a laser spot of 0.8 mm, there is a 15% reduction in energy spread for a 2 nC bunch between a field of 20 MV/m and 7.5 MV/m, and a 16% reduction for a charge of 0.01 nC. There is also no difference in the relative reduction of energy spread for bunches produced from different laser spots.

For both bunch length compression and for on-crest acceleration it is important that operating the bunching cavity at a lower accelerating field does not degrade the emittance significantly. The strength of the solenoid magnet that surrounds the buncher cavity was, therefore, optimised to reduce emittance growth. When no solenoid field is present around the bunching cavity, the increased space-charge forces present when bunches are accelerated at lower gradients caused the emittance to grow for all buncher phases. The normalised emittance achievable when the solenoid is optimised for bunches of different charge, generated from a 0.8 mm laser spot, accelerated at different field gradients at the maximum energy and minimum bunch length phases, is shown in Figure 4.15. When accelerated on the

maximum accelerating phase (Fig. 4.15a) there is a small increase in normalised emittance for lower accelerating gradients. The increase is larger for higher-charge bunches and is caused by the higher space-charge forces present in the early part of the bunching cavity for lower acceleration gradients. The strength of the solenoid magnet required to suppress the emittance growth is lower for bunches accelerated at a lower gradient, as the bunches have a lower rigidity.

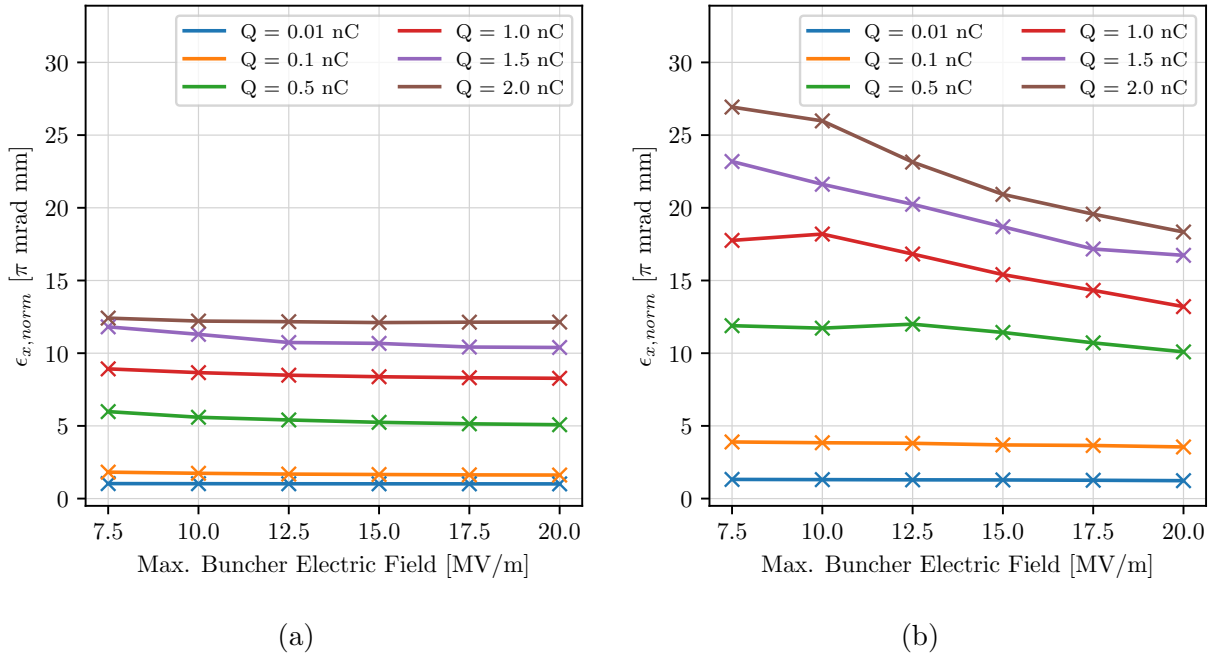


Figure 4.15: The minimum emittance of bunches of different charge, all produced from a laser spot of 0.8 mm, at the end of the bunching cavity set to (a) the maximum energy phase, and (b) the phase of minimum bunch length vs the maximum electric field in the buncher.

When accelerating at the phase of minimum bunch length, the growth in emittance with reduced buncher field is harder to suppress (Fig. 4.15b). For low-charge bunches, the emittance growth with reduced accelerating field is suppressed almost entirely. However, for bunches of higher charge the growth is more difficult to suppress. When the accelerating field is reduced from 20 MV/m to 7.5 MV/m the normalised emittance at the exit of the bunching cavity of a 0.5 nC bunch, generated from a laser spot of 0.8 mm, grows by 17%. For a 2 nC bunch, generated from the same laser spot, the growth in normalised emittance is 47%. Again, this growth is caused by the additional space charge forces present at the beginning of the bunching cavity.

It must be noted that the electric field strength of the buncher could also be reduced with the installation of an attenuator to the waveguide between the present klystron and the bunching cavity. Such an attenuator would be significantly less expensive than the installation, operation and maintenance of a new klystron.

4.2.2 Higher Gun Field

The installation of a second klystron would allow the field of the RF gun to be increased above the present maximum field strength of 80 MV/m. Several S-band photoinjectors operate with higher maximum electric field strengths in their RF guns. For example: the baseline for the CLARA photoinjector is to operate at 100 MV/m [76], with plans to increase to the gradient up to 120 MV/m; the RF gun at the LCLS operates at 120 MV/m [180]; and the SPARC RF gun also operates at a gradient of 120 MV/m [181]. By operating at a higher field, it may be possible to reduce some of the problems caused by space-charge, such as emittance growth and bunch length increase in high-charge bunches. It would also be possible to extract more charge from the photocathode as the effect on the mirror charge would be reduced.

The present CLEAR gun has not been extensively tested at higher field gradients, and several potential issues will need to be investigated prior to, and during the commissioning of a new klystron. Operating the gun at a higher field will lead to higher levels of dark current than are currently present. For example, when operated at 120 MV/m, the S-band RF gun at LCLS produced a charge of 0.6 nC spread over a 2 μ s RF pulse [180], an order of magnitude higher than the current CLEAR setup. A dark current this high could lead to significant issues for some users. However, it must be noted that for other users requiring irradiations over long periods of time, at low to medium charge, this level of dark current could be useful. Furthermore, operating at a higher gradient than at present would increase the likelihood of field breakdowns in the gun. It would also lead to increased degradation of the photocathode, meaning that it has to be replaced on a more regular basis. A dedicated study of these issues will need to be undertaken if a new klystron is installed.

To investigate the beam dynamics of operating the gun at a higher electric field, simulations were undertaken in ASTRA. As with other upgrades of the CLEAR facility, bunches

of the same charge (0.01 - 2 nC), generated from the same laser spots (0.4, 0.8, 1.2 mm) as described in Chapter 3 were investigated. The bunches were simulated from the photocathode to the beginning of the bunching cavity with maximum field gradients in the gun of 80, 90, 100, 110, and 120 MV/m. Bunches accelerated at higher field gradients have a higher rigidity, therefore, the maximum strength of the gun solenoid was set to 0.4 T. Following an optimisation of the gun, the bunches were tracked through the bunching cavity. The field gradient of the bunching cavity was set to 18 MV/m and the maximum strength of the buncher solenoid was set to 0.1 T.

4.2.2.1 RF Gun

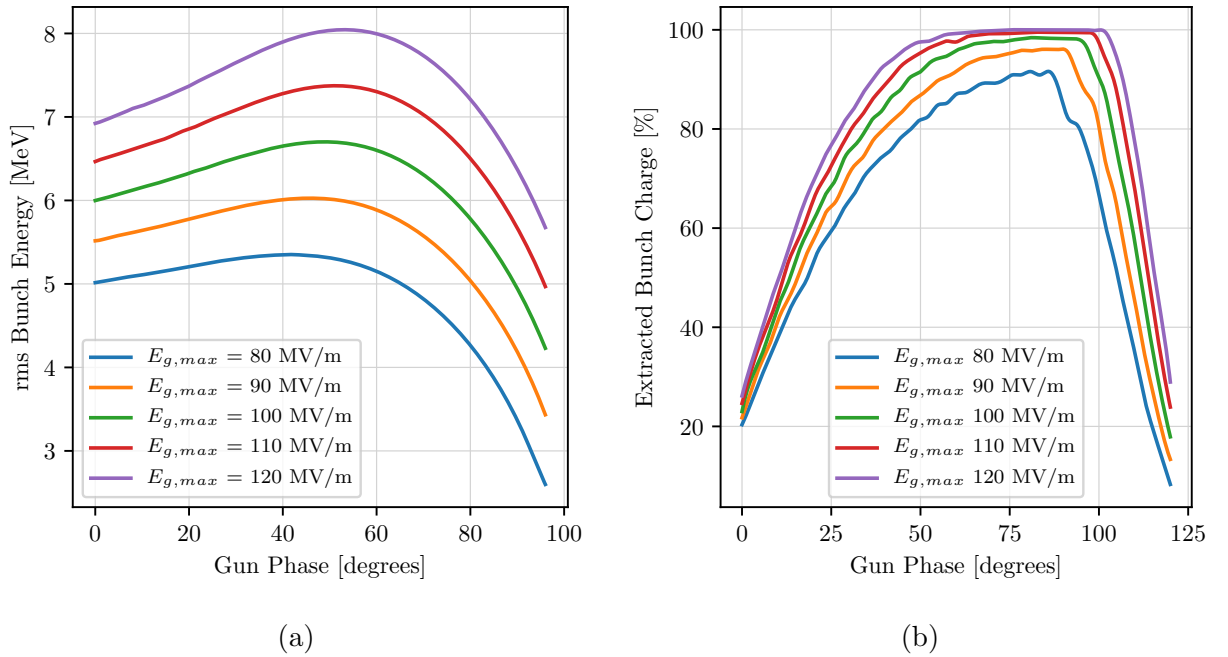


Figure 4.16: ASTRA simulation of **(a)** the energy, and **(b)** the percentage bunch charge extracted from the RF gun for a bunch of 2 nC total charge, generated from a 0.4 mm laser spot and accelerated at different gun electric fields, vs gun phase.

The energy of the bunch increases with the field in the gun as shown in Figure 4.16a. The gain in maximum energy was linear with electric field strength, with a gain of 0.65 MeV with a 10 MV/m increase in field strength. The maximum energy occurs at a higher phase for higher electric field gradients. The phase of maximum energy occurs between 40° and 45° for a field gradient of 80 MV/m depending on the bunch charge and laser spot size, with higher-charge bunches generated from a smaller laser spot occurring at lower phases. The

phase of maximum energy is $\sim 10^\circ$ higher for bunches accelerated with a field gradient of 120 MV/m.

When the maximum electric field was increased, a greater amount of charge was extracted from the RF gun. Figure 4.16b shows the level of extracted bunch charge for a 2 nC bunch generated from a laser spot of 0.4 mm. For the current field gradient of 80 MV/m, less than 80% of the 2 nC bunch was extracted at the peak-energy phase. Whereas over 95% of the bunch charge was extracted for a field of 120 MV/m. The higher field at the cathode means that the effect of the mirror charge is lower, resulting in a greater amount of charge being extracted. As was true with previous simulations, 100% of the bunches generated from 0.8 mm and 1.2 mm laser spots was extracted.

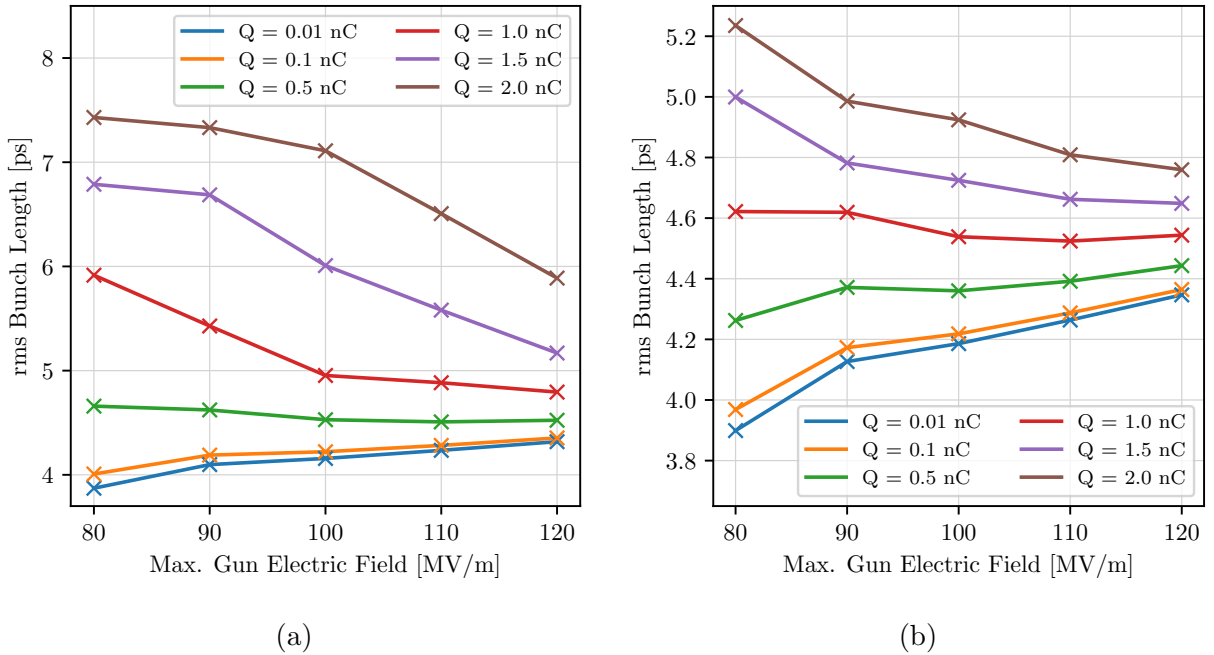


Figure 4.17: The bunch length at the entrance of the bunching cavity for bunches of various charge, generated from a laser spot of (a) 0.4 mm, and (b) 0.8 mm accelerated at the maximum energy phase of the RF gun vs maximum electric field strength in the gun.

The bunch length at the entrance to the bunching cavity for bunches generated from 0.4 mm and 0.8 mm laser spots and accelerated at the maximum energy phase in the gun is shown in Figure 4.17. For low-charge bunches, where the bunch is not significantly elongated by space-charge forces, the bunch length increased with gun field. The reason for this increase is that the phase of maximum energy is higher for these bunches, meaning that less velocity bunching occurs in the gun and the drift following the gun. For 0.01 nC and 0.1 nC bunches

the increase was identical for all laser spot sizes, as there is not a significant difference in the space-charge force present. However, bunches of higher charge are shorter when accelerated at a higher electric field in the gun. The decrease in bunch length is due to the space-charge forces in the gun and the following drift being lower. As the space-charge forces are higher when a smaller laser spot is used, the relative decrease in bunch length with gun field is larger when a laser spot of 0.4 mm is used compared to 0.8 mm. The relative decrease is smaller when the bunches are generated from a 1.2 mm laser spot compared with either a 0.4 mm or 0.8 mm laser spot.

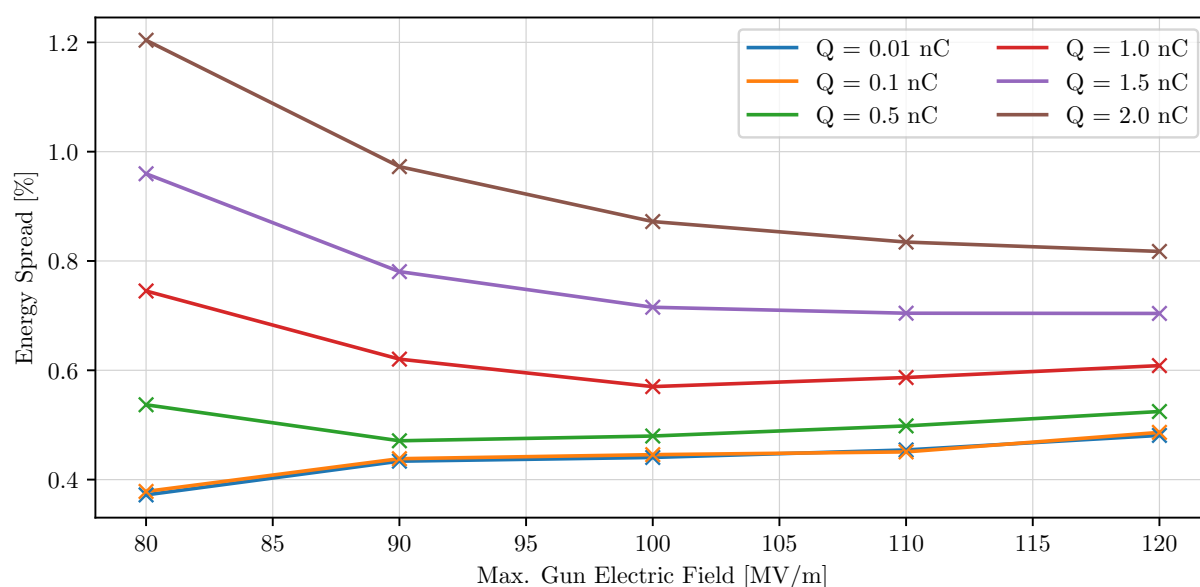


Figure 4.18: The energy spread at the entrance of the bunching cavity for bunches of various charge, generated from a laser spot of 0.8 mm, accelerated at the maximum energy phase of the RF gun vs maximum electric field strength in the gun.

As shown in Figure 4.18, there is an increase in energy spread at the phase of maximum energy for bunches of charge 0.01 nC and 0.1 nC accelerated at higher electric fields. The increase in energy spread at higher fields is due to the bunches being longer in the gun than bunches accelerated at lower fields. Bunches of charge 1.5 nC and 2 nC are shorter in the gun when accelerated at a higher electric field. Therefore, the energy spread of such bunches decreases with higher gun fields. Furthermore, the effects of space-charge forces are lower for bunches accelerated at a higher field. Therefore, there is a smaller increase in energy spread over the drift between the gun and bunching cavity. Both of these effects result in an overall decrease in energy spread. The energy spread of 0.5 nC bunches decreases between

80 MV/m and 90 MV/m, and then increases at higher gun fields. The bunch length for bunches of 0.5 nC charge increase with gun field, causing the energy spread directly after the gun to increase. However, between 80 MV/m and 90 MV/m, there is a significant drop in space-charge forces in the drift following the gun resulting in a larger energy spread at the lowest gun field strength. There is a similar reduction in space-charge forces in the drift for 1.0 nC bunches. However, there is also a bunch length reduction between 80 MV/m and 110 MV/m. The combination of the two effects cause the energy spread to decline to a minimum at 100 MV/m. When bunches are generated from a laser spot of 0.4 mm the effect of space-charge forces is more significant. Furthermore, the decrease in bunch length in the gun is also greater. For a 0.4 mm laser spot there is a larger decrease in energy spread of high-charge bunches than when using a 0.8 mm laser spot. When bunches are generated from a laser spot of 1.2 mm, the effects of space-charge forces are lower than a 0.8 mm spot, and the decrease in bunch length is not as large. Therefore, the decrease in energy spread is not as large. For a field of 120 MV/m, the energy spread is similar for bunches of all charge, and for all laser spot sizes investigated.

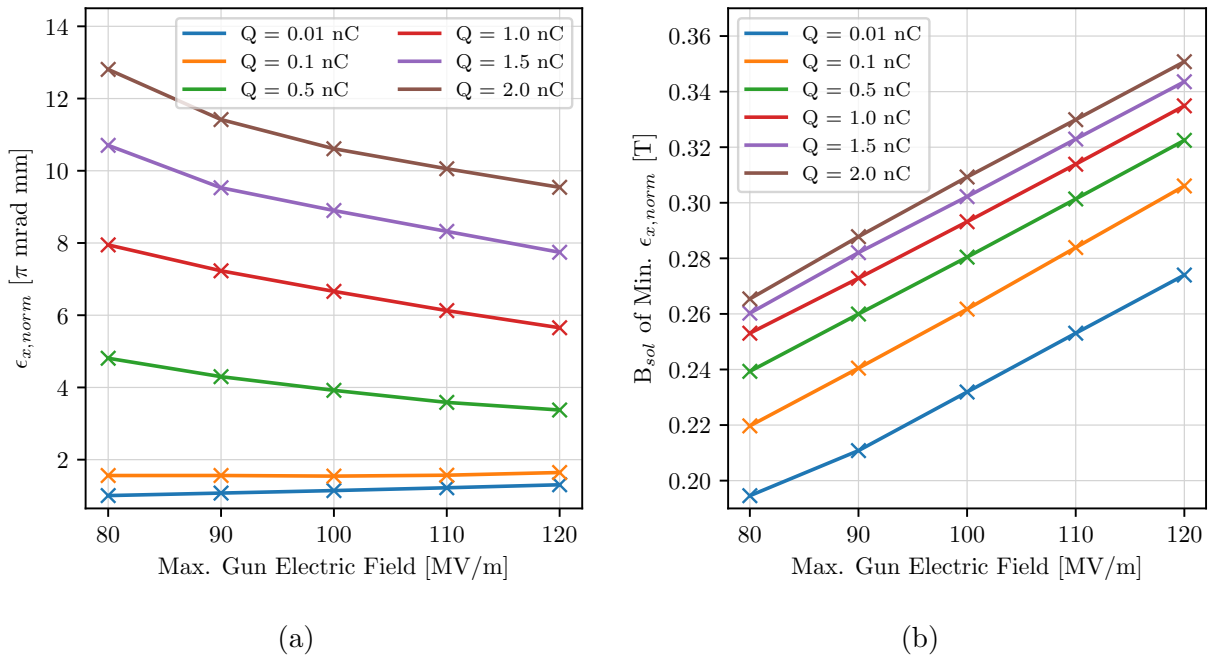


Figure 4.19: **(a)** The normalised emittance, following an optimisation of the gun solenoid, at the entrance of the bunching cavity for bunches of various charge, generated from a laser spot of 0.8 mm, accelerated at the maximum energy phase of the RF gun vs gun field strength. **(b)** The magnetic field strength of the solenoid magnet required to minimise emittance growth vs gun field strength.

Figure 4.19a shows the normalised emittance of bunches produced from a 0.8 mm laser spot for different gun gradients following an optimisation of the gun solenoid. For bunches of charge 0.01 nC, the emittance growth is mainly driven by RF and thermal effects, thus there is a small increase in emittance with RF field. For bunches of higher charge, the main driver of emittance growth is space-charge. Space-charge forces are lower for bunches accelerated at a higher gun field, and so the emittance is smaller. The relative drop in emittance is around 40% for all bunch charges of 0.5 nC or higher investigated. The relative reduction is similarly 40% for bunches of charge 0.5 nC or higher, generated from a laser spot of 1.2 mm. When bunches are generated from a 0.4 mm laser spot, the relative reduction in emittance growth is only around 30%. As bunches accelerated at a higher field in the gun have a higher rigidity, the magnetic field required to minimise emittance growth is higher, as shown in Figure 4.19b. The maximum solenoid strength needed to minimise the emittance growth was significantly higher than the current maximum of 0.24 T. Lower solenoid fields were needed to minimise the emittance growth of bunches generated from a 1.2 mm laser spot, and higher solenoid field strength were needed for a 0.4 mm laser spot. The highest field required was 0.38 T for a 2 nC bunch, generated from a 0.4 mm laser spot. As the current solenoid was not designed to operate at such fields, the maximum possible field strength will need to be investigated if the gun is to be operated effectively at a higher accelerating field. If it is not possible to extend the range, then an entirely new solenoid will need to be manufactured.

4.2.2.2 Bunching Cavity

As previously, bunches were tracked through the bunching cavity to investigate the effect of operating the gun at a higher field on bunch compression. The phase of the gun was set to the maximum energy phase and the gun solenoid was set to reduce emittance growth. The variation of energy with the phase of the buncher for a 1 nC bunch, generated from a laser spot of 0.8 mm, is shown in Figure 4.20. As bunches accelerated by higher fields in the gun have a higher energy entering the bunching cavity, the maximum energy following the cavity is higher. The absolute difference in energy between a bunch accelerated by a gun with fields of 80 MV/m and 120 MV/m is the same at the entrance as the exit of the cavity. The energy varies sinusoidally with buncher phase for all bunches accelerated at different gun

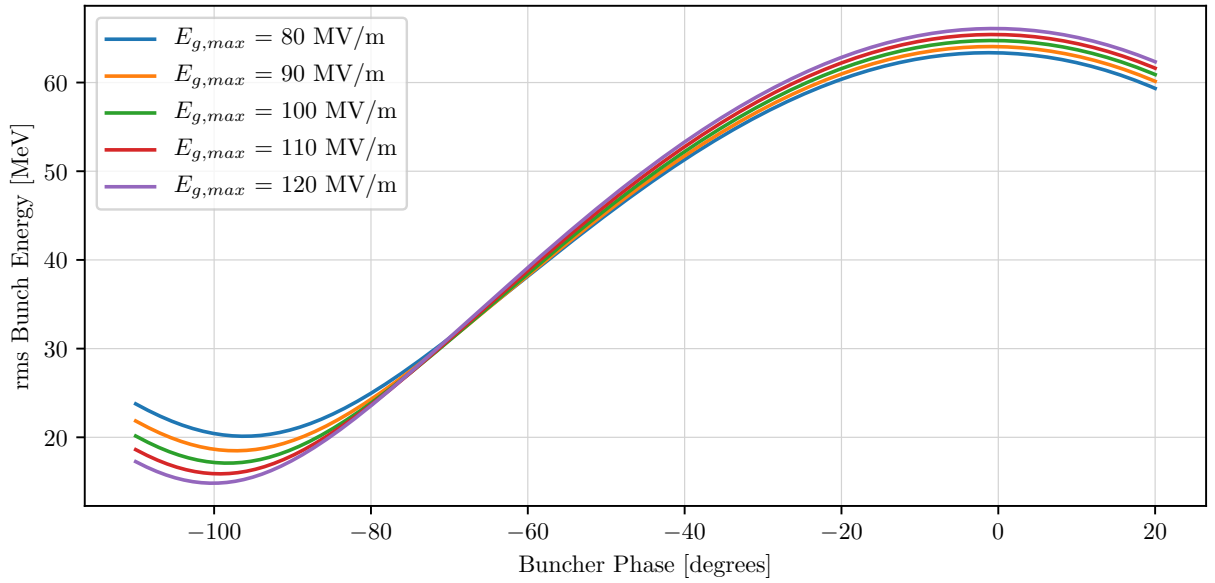


Figure 4.20: ASTRA simulation of the bunch energy of a 1.0 nC bunch, generated from a laser spot of 0.8 mm, vs the phase of the buncher, for several different maximum gun electric field strengths.

fields towards a minimum approximately at zero crossing. However, the minimum energy is lower for bunches accelerated at a higher gun field. The minimum also occurs at a slightly lower phase for bunches accelerated with higher gun fields. The reason for this is that as these bunches have a higher energy entering the cavity they sit at decelerating phases for a longer time than bunches accelerated with a lower field, thereby gaining less energy.

The variation in bunch length with phase is similar for all gun fields investigated. Bunches of 1 nC generated from a 0.8 mm laser spot, as shown in Figure 4.21, have a similar bunch length at the entrance of the bunching cavity (Fig. 4.17b) regardless of the gun field. At the phase of maximum energy there is some elongation in bunch length measured at the end of the bunching cavity due to space-charge forces in the early stages. The elongation in bunch length is reduced for bunches accelerated at higher gun fields as the space-charge forces are lower. For each gun field there is a similar variation in bunch length towards a minimum around zero crossing. The minimum bunch length occurs at a slightly lower phase for bunches accelerated with a higher gun field.

The minimum bunch length of bunches generated from 0.4 mm and 0.8 mm laser spots accelerated at by different gun fields are shown in Figure 4.22. Space-charge forces are more significant for bunches produced from a 0.4 mm laser spot than a 0.8 mm laser spot. The

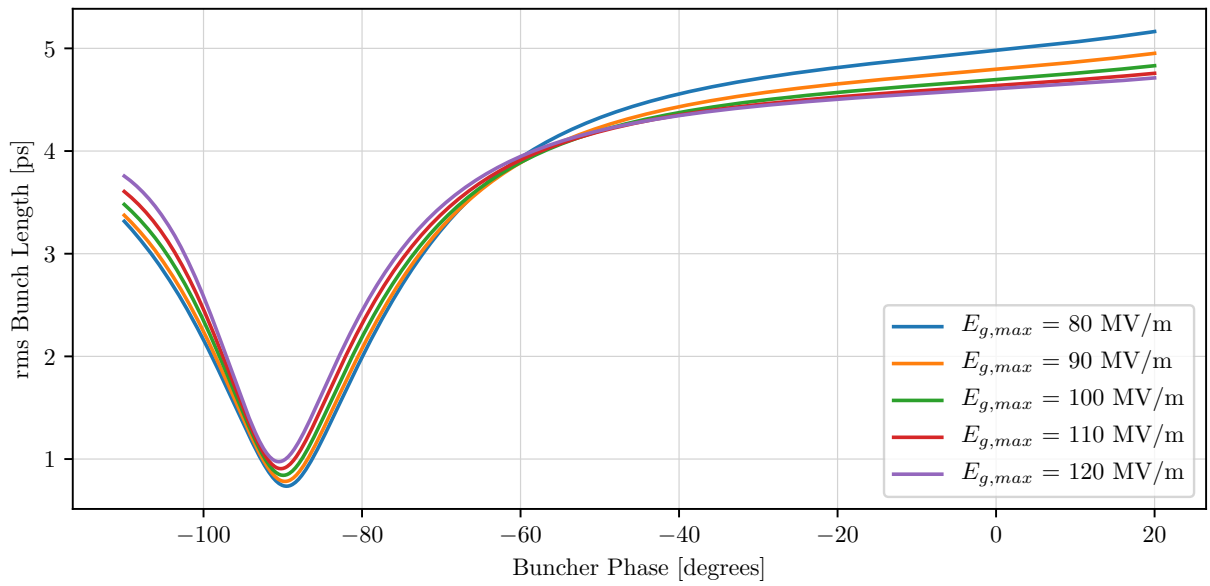


Figure 4.21: ASTRA simulation of the bunch length of a 1.0 nC bunch, generated from a laser spot of 0.8 mm, vs the phase of the buncher, for several different maximum gun electric field strengths.

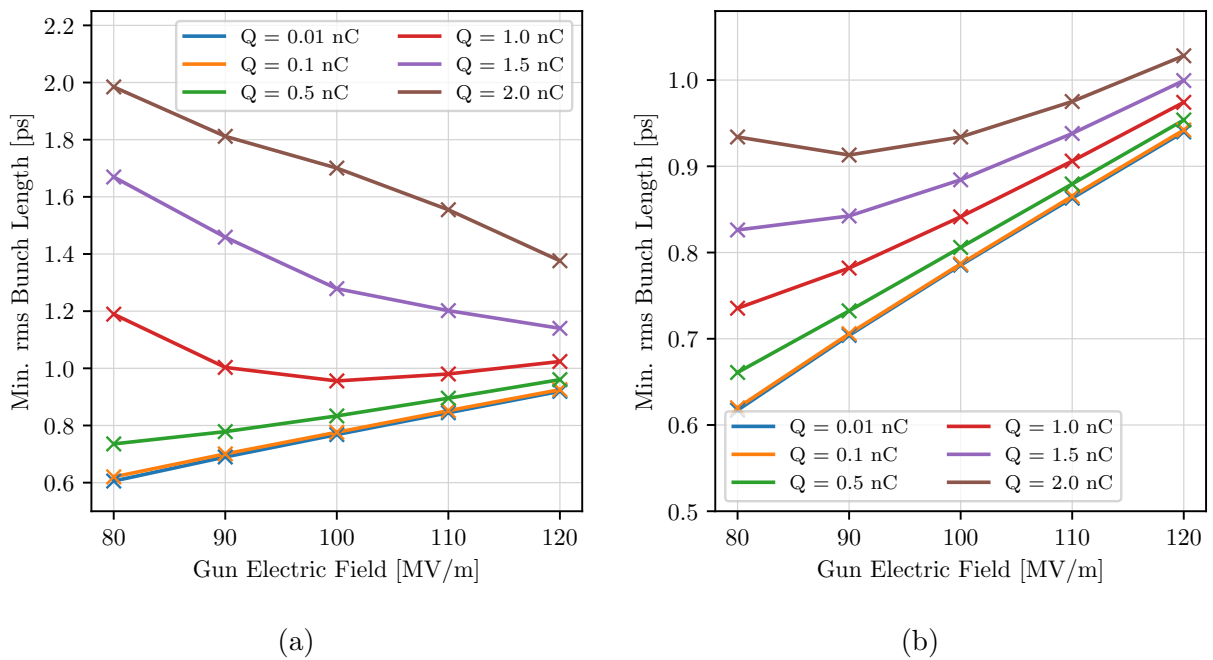


Figure 4.22: The minimum bunch lengths achievable for bunches of different charge produced from a laser spot of (a) 0.4 mm, and (b) 0.8 mm, vs maximum electric field strength in the gun.

bunch length of bunches of 1.5 nC and 2 nC produced from an 0.4 mm laser spot decrease with the electric field strength of the gun. The decrease in bunch length is due both to the bunch length being shorter at the entrance to the cavity as well as the reduction of

space-charge forces in the cavity. The compression factor is higher for bunches accelerated at higher gun fields, showing the effect of space-charge in the buncher. For a 2 nC bunch, the compression factor between the entrance and exit of the buncher is a factor 3.7 for a gun field of 80 MV/m and 4.3 for a gun field of 120 MV/m.

The minimum bunch length of bunches of charge 0.01 nC, 0.1 nC, and 0.5 nC produced from a 0.4 mm laser spot are not limited by space-charge forces in the buncher. The bunch length increases with gun field for these bunches. The increase is due to these bunches having a higher energy in the bunching cavity. A higher energy means that the difference in velocity between the head and the tail of the bunch that can be produced by de-phasing the cavity is lower. The compression factor is similar for these bunch charges at each gun field investigated and reduces with an increase in field. For a gun field of 80 MV/m the compression factor is 6.4, compared with 4.7 for a gun field of 120 MV/m. Bunches of charge 1 nC produced from a 0.4 mm laser spot experience a reduction in space-charge forces in the buncher. However, the compression factor remains constant at ~ 5 as the reduction in head-tail velocity difference cancels the reduction in space-charge forces.

Space-charge forces in the buncher are less significant for bunches produced from a laser spot of 0.8 mm. However, the reduction in head-tail velocity difference is identical for a bunch produced from a 0.4 mm laser spot. Because of this, the only reduction in bunch length with gun field is for a 2 nC bunch being accelerated at a 90 MV/m gun field relative to the same bunch being accelerated by a gun field of 80 MV/m. Space-charge forces do reduce the compression factor for 1.5 nC and 2 nC bunches relative to lower charge bunches, but only for gun fields below 100 MV/m. For bunches generated from a 1.2 mm laser spot, the effect of space-charge in the buncher is even lower. The compression factor at each different gun field is similar for all bunch charges investigated. The compression factor is only reduced in the 1.5 nC and 2 nC bunches, relative to lower charges, below a gun field of 100 MV/m, with the compression factor for a 2 nC bunch accelerated at a gun field of 80 MV/m only 7% less than a 0.1 nC bunch accelerated at the same gun field.

The energy spread of bunches accelerated at different gun fields is similar for buncher phases between the maximum energy phase and $\sim -60^\circ$, as shown in Figure 4.23. There is a small difference around the maximum energy phase, as shown in Figure 4.24a, due to the difference in bunch length at the entrance of the bunching cavity. Bunches that are initially

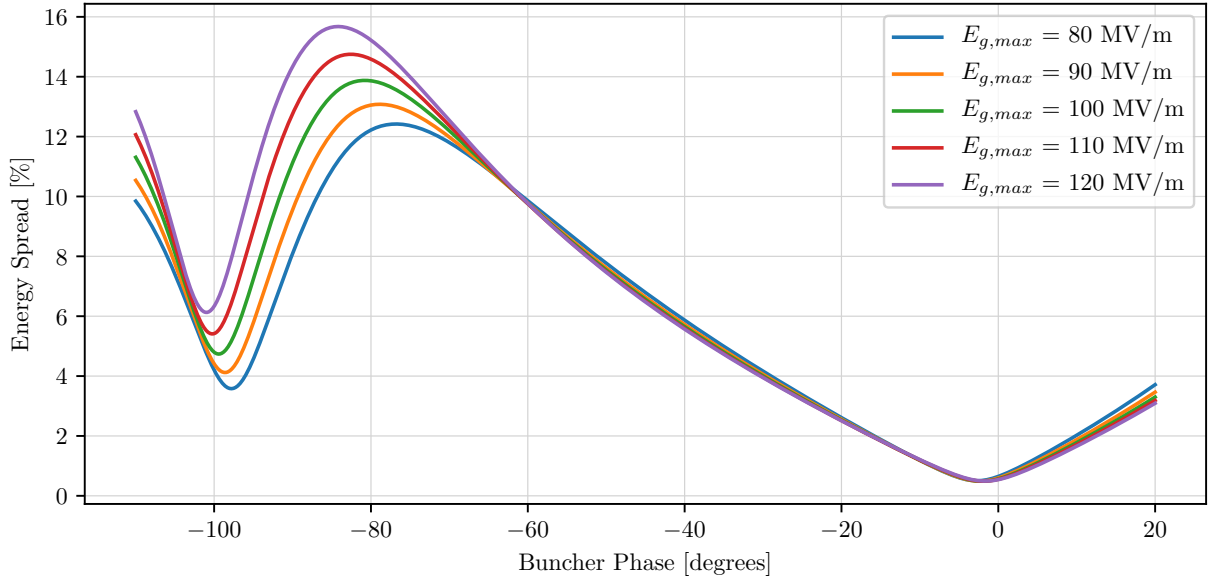


Figure 4.23: ASTRA simulation of the energy spread of a 1.0 nC bunch, generated from a laser spot of 0.8 mm, vs the phase of the buncher, for several different maximum gun electric field strengths.

shorter have a lower energy spread when accelerated on the peak-energy phase. At phases lower than $\sim -60^\circ$, there is an increase in the energy spread of bunches accelerated at higher gun fields relative to those accelerated at lower gun fields. As shown in Figure 4.24b, the increase in energy spread with gun field at the phase of minimum bunch length is common to all bunch charges investigated. The difference in energy spread is due to the incoming energy of the bunches. At low buncher phases, bunches slip in phase relative to the the RF towards a higher accelerating phase. The phase slippage causes the energy spread to decrease. Bunches accelerated at higher gun fields take longer to slip to a more accelerating phase and so have a higher energy spread. Furthermore, the buncher phase at which the energy spread begins to reduce is lower for bunches accelerated at a higher gun field.

The buncher solenoid was optimised to reduce emittance growth in the buncher. As shown in Figure 4.25a, at the phase of maximum acceleration it was possible to eliminate any emittance growth over the length of the buncher. Therefore, operating the gun at a higher electric field strength would slightly reduce the emittance of high-charge bunches when operating at the maximum energy phase. At the phase of minimum bunch length, shown in Figure 4.25b, there was a slight increase in emittance for higher gun fields. The increase is due to the minimum bunch length occurring at a lower buncher phase for bunches

accelerated at higher buncher fields. For high-charge bunches the minimum bunch length

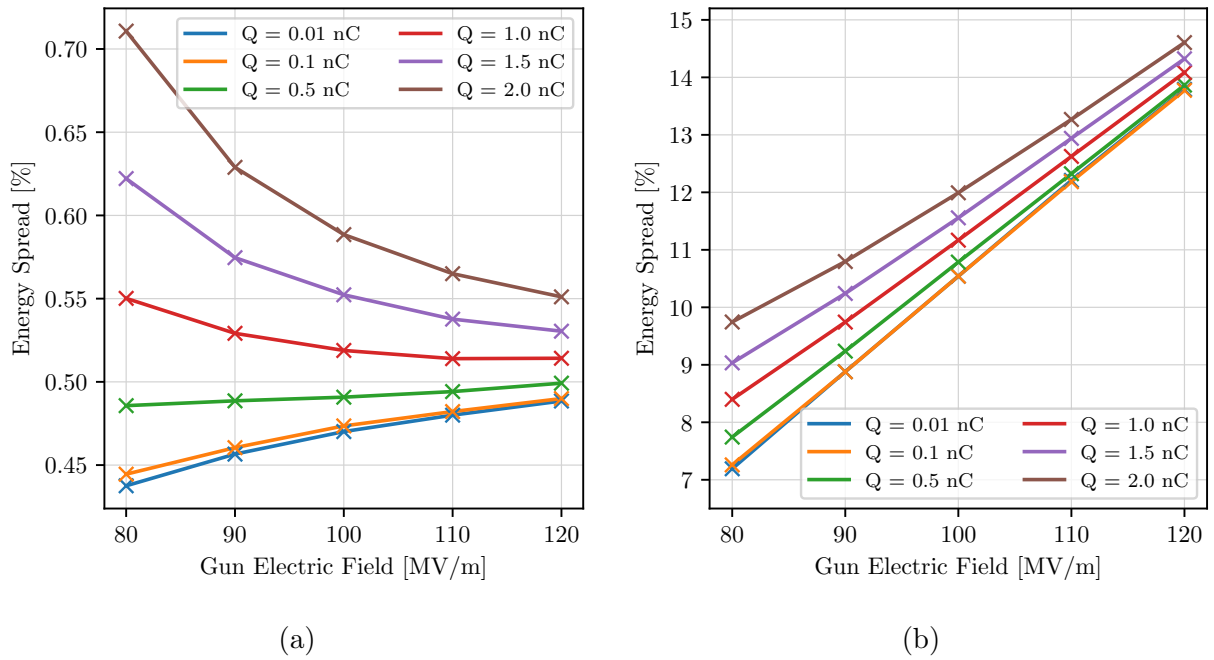


Figure 4.24: The energy spread of bunches of various charge generated from a laser spot of 0.8 mm vs the electric field strength in the RF gun at (a) the maximum energy phase of the buncher, and (b) the phase of minimum bunch length in the buncher.

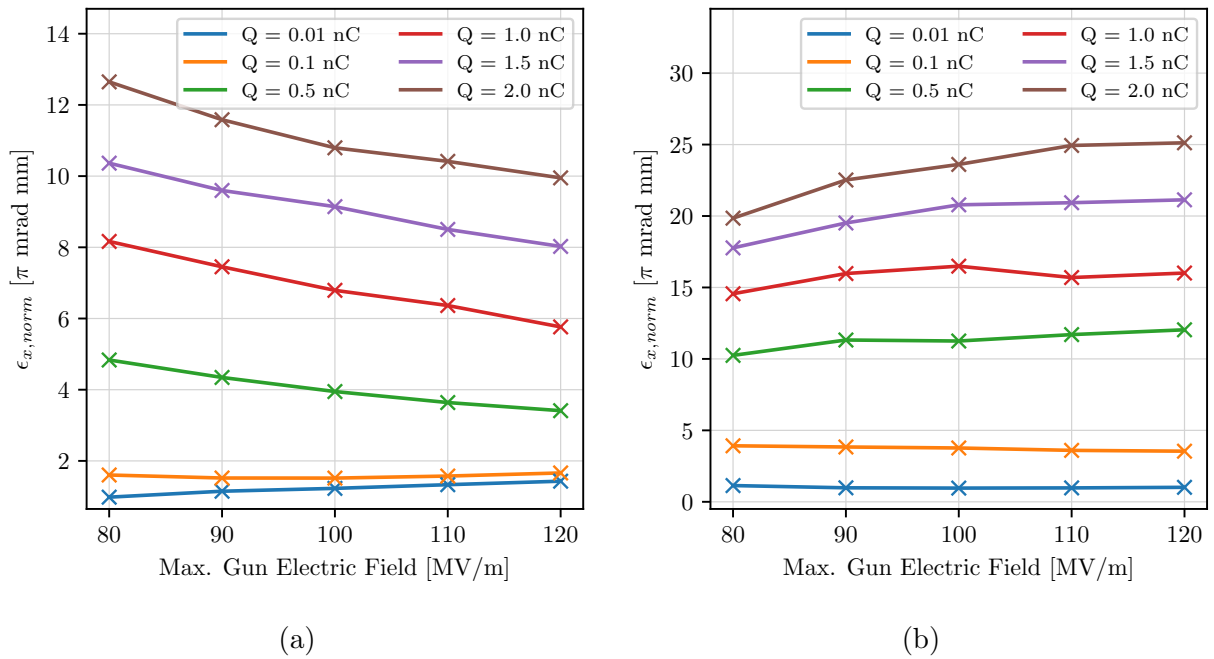


Figure 4.25: The minimum emittance of bunches of different charge, all produced from a laser spot of 0.8 mm, at the end of the bunching cavity set to (a) the maximum energy phase, and (b) the phase of minimum bunch length vs the maximum electric field in the gun.

is mostly below zero crossing where there is a large increase in emittance. The increase in emittance is more difficult to suppress. As the emittance at the entrance of the bunching cavity is larger for bunches generated from a 1.2 mm laser spot than a 0.8 mm laser spot, the emittance at the exit is also larger. At the maximum accelerating phase of the buncher, the emittance is $\sim 20\%$ higher for a 1.2 mm laser spot. There is, however, a smaller relative increase in emittance when accelerating at the phase of minimum bunch length. As bunches generated from a laser spot of 0.4 mm have a smaller emittance at the entrance to the bunching cavity, they have a smaller emittance at the exit. Using a field of 120 MV/m in the gun would allow the acceleration of a 2 nC bunch with an emittance of 6 mm mrad when accelerated at the peak-energy phase in the buncher. Using a laser spot of 0.4 mm to generate a 2 nC bunch would result in a $\sim 40\%$ decrease in emittance relative to a 0.8 mm laser spot. At the phase of the minimum bunch length the emittance of bunches generated from a 0.4 mm laser spot is also lower, with a 2 nC bunch accelerated at a gun field of 120 MV/m having an emittance of 15 mm mrad.

By operating the gun at a higher field strengths, it would likely be easier to extract high-charge bunches from a smaller laser spot. Therefore, it would be possible to accelerate 2 nC bunches, with bunch lengths ~ 1 ps, with a smaller emittance than at lower gun fields. Although the effect of performing velocity bunching with a reduced gun phase was not investigated, it would be easier to do so at higher bunch charges which could reduce the minimum bunch length. It may also be possible to operate with a higher gun field and a lower buncher field in order to overcome space-charge forces in the gun, but not to decrease the head-tail velocity difference. Again this may reduce the minimum bunch length achievable. When operating with a shorter laser pulse it was difficult to extract the full charge of a bunch. By operating at a higher gun field it may be possible to extract a higher bunch charge for shorter laser pulses. Furthermore, it would likely reduce the amount of bunch elongation caused by space-charge in the drift between the gun and the buncher seen in Figure 4.2 allowing the generation of shorter, high-charge bunches.

4.3 Summary

As the daughter of several previous CERN accelerators, many of the components used on CLEAR are not optimised for the needs of some potential users and for use as an injector to the eSPS. It may be desirable, therefore, to upgrade some of the machine components to increase the range of parameters available. In this chapter, the installation of a new laser system, as well as an additional klystron were investigated. Beam dynamics simulations were performed in ASTRA to assess the potential benefits and problems manifested from such upgrades.

From these simulations, it is clear that installing a new laser system with a shorter laser pulse could significantly reduce the minimum bunch lengths possible at CLEAR. A flexible laser system that could provide laser pulses of between 1 ps and 5 ps would allow the bunch length to be altered whilst keeping the RF phases set to provide maximum acceleration. For bunches of 0.1 nC or lower it would be possible to create bunches that match the laser pulse length or are in fact shorter. Space-charge forces in the gun would not allow the same to be performed at higher charges. However, it would still be possible to alter the bunch length in this way, with the length of a 2 nC bunch alterable between 3.5 ps and 5.5 ps. Shorter bunch lengths could be achieved by performing velocity bunching, with the minimum possible bunch lengths being significantly shorter than the present system. For low-charge bunches it would be possible to achieve bunch lengths of below 100 fs and for a 2 nC bunch charge it would be possible to perform compression to a length shorter than 400 fs, 60% lower than the present system. Such shorter bunches would be useful to a variety of users such as, the generation of THz radiation, testing novel bunch length measurements, and for any potential use of the CLEAR injector in the eSPS.

It was shown that such bunches, produced from shorter laser pulse lengths, would not be significantly worse in quality than bunches produced with the present laser system. It was shown that although there was a small rise in the beam emittance with shorter laser pulses, most of the emittance growth could be compensated by the gun solenoid operating at a slightly higher field strength than is presently possible. In addition, it was shown that due to the reduction in bunch length demonstrated with reduced laser pulse length, there would be a reduction in the energy spread of these beams relative to the present setup. It

was noted that, in addition to the beam dynamics improvements, a new laser system could provide, it may also allow greater charge and position stability as well as having the ability to operate at a higher repetition rate.

The installation of an additional klystron was also investigated. It was shown that by using a new klystron, or by installing an RF attenuator to the present waveguide, to reduce the accelerating field gradient of the bunching cavity it would be possible to extend the range of beams available to users. Primarily, by reducing the gradient from the present 18 MV/m to 7.5 MV/m, it would be possible to reduce the minimum energy available on CLEAR to 30 MeV. Operating at a lower energy than present would be desirable to many users, particularly medical and irradiation experiments. By performing simulations of velocity bunching at lower accelerating gradients it was shown that the minimum bunch length could be reduced by over 20%. In addition, performing velocity bunching at a lower field gradient would potentially improve the stability of compressed bunches with the bunch length less sensitive to phase drifts or jitters. It was also shown that operating at a lower field gradient could reduce the energy spread at the minimum bunch length by $\sim 15\%$. However, it was shown that performing velocity bunching at a lower accelerating gradient would lead to a growth in emittance that could not be compensated. The growth in emittance was more significant for higher charge bunches, with the emittance of a 2 nC bunch produced from a 0.8 mm spot growing by up to 50% at lower buncher-field gradients.

Although a reduction in the field of the bunching cavity could be undertaken by installing an RF attenuator alone, by installing an additional klystron it would be possible to increase the maximum electric field present in the gun. It was shown that by increasing the maximum accelerating field in the gun it would be easier to extract bunches of high-charge from smaller laser spots. Furthermore, these high-charge bunches would undergo less bunch length elongation in the drift and bunching cavity when accelerated at the maximum energy phase. However, due to the reduction in head-tail velocity difference when performing velocity bunching, the minimum bunch length achievable increased with gun field for all but the bunches with the highest charge density. It was demonstrated that by operating the gun at a higher electric field gradient, the emittance of bunches leaving the gun could be reduced by up to 40%. Unfortunately, at the phase of minimum bunch length in the buncher the emittance of bunches grew with increased gun field. Although this is countered by the

ability to accelerate and compress high-charge bunches from smaller laser spot sizes that have a smaller emittance. It was shown that by using a 0.4 mm laser spot size and a gun field of 120 MV/m, it would be possible to accelerate a 2 nC bunch that had an emittance of 6 mm mrad at the peak accelerating phase of the buncher, and an emittance of 15 mm mrad at the phase of minimum bunch length. It must be noted that producing a 2 nC bunch of that emittance the maximum field strength of the gun solenoid would have to be increased significantly to at least 0.38 T. Therefore, a feasibility study of the maximum field strength should be performed.

By combining these upgrades it would likely be possible to improve machine performance further. When investigating using a shorter laser pulse length it was difficult to extract high-charge bunches from a 0.4 mm laser spot. By operating the gun at a higher field it should be possible to extract a greater amount of charge as well as reduce the bunch length of bunches leaving the gun. Furthermore, it would be possible to extract more bunch charge at lower gun phases, and so enhance the effect shown in Section 3.4.5. To overcome the increase in minimum bunch length seen for bunches accelerated at higher gun fields, it may be possible to operate with a higher gun field and a lower buncher field. The combinations of the effects of various upgrades should be investigated further before these upgrades are commissioned. In addition, the technical limitations of the RF gun and the surrounding solenoid should be investigated. In particular an experimental study should be undertaken into operating the CLEAR gun at a higher field strength, observing dark current, breakdown rate and photocathode degradation.

Further upgrades to the CLEAR injector should also be investigated. It has been proposed to install a new electron gun in the CLEAR hall [84]. The beam dynamics of this gun, and the possible beams that it would be able to provide to users should be investigated in detail. An analysis of this would allow a decision to be made about whether the gun is used as part of the current CLEAR beamline or as part of a second, independent beamline. Another possible upgrade would be the construction of a second experimental beamline. The beamline would branch off from the present beamline via a dogleg bend, and would contain space to install in-air and in-vacuum experiments. The optics of this beamline should be investigated, optimising for new beam conditions such as strong-focusing or large irradiation spot sizes.

Furthermore, as RF power is due to be connected to the X-band accelerating structure installed on the experimental beamline, beams should be simulated through the structure. Particular focus should be directed onto the increase of beam energy that would be possible as well as any effects in the longitudinal or transverse beam dynamics operating the structure would cause.

Chapter 5

Generation of Uniform Beam Profiles

Irradiation experiments performed at CLEAR require beams that are as uniform as possible as non-uniform transverse beam profiles can lead to uncertainty in the dose that is incident on the target. The electron beams produced at CLEAR tend to have Gaussian beam profiles. Therefore, to increase the uniformity of the dose, the beam size is often increased to a significantly larger size than the target, thereby reducing the total dose incident on the target and the maximum dose rate. If it was possible to generate an entirely uniform beam profile in a CLEAR-like facility, then the total dose and dose rate could be increased. Furthermore, by producing a uniform beam profile it would be possible to collimate a beam to deliver dose to experimental target with an arbitrary transverse shape. A beam with a uniform profile, collimated to match the tumour shape, would also be useful in VHEE-RT, minimising the dose given to healthy tissue.

Photoinjectors used in free electron lasers (FELs) often produce electron bunches that have either 2D-uniform or 3D-uniform ellipsoid beam profiles in order to reduce the emittance of the beam and increase brightness [182]. 3D-uniform ellipsoids also have the added advantage in that the space-charge forces inside the bunch are linear. In FELs, both longitudinal and transverse space-charge forces can be used to distort the phase space of the bunches towards uniform profiles. In the so-called blow-out regime, ultra-short laser pulses of length ~ 10 fs are used [183] to create high longitudinal space-charge forces. To utilise transverse space-charge forces ultra-low charge beams (~ 1 pC) are generated from small laser spots of $\lesssim 30\mu\text{m}$ [182]. In both methods, the uniformity can be improved by using laser pulses that are shaped in 3D [184]. However, neither of these methods of producing uniform beams are suitable for an irradiation facility. Ultra-short or shaped laser pulses are

complicated to set up and require regular maintenance. Furthermore, as the beams used to produce uniform beam profiles with transverse space-charge forces are targeted towards producing ultra-low-emittance beams, they are of too low charge to be useful for many irradiation experiments.

In this chapter the ability to produce electron beams with uniform transverse beam profiles with Gaussian lasers of pulse lengths of a few picoseconds is demonstrated. In addition, a simple irradiation facility that generates and uses such beams is proposed with start-to-end simulations of this facility presented.

5.1 Defining Uniformity

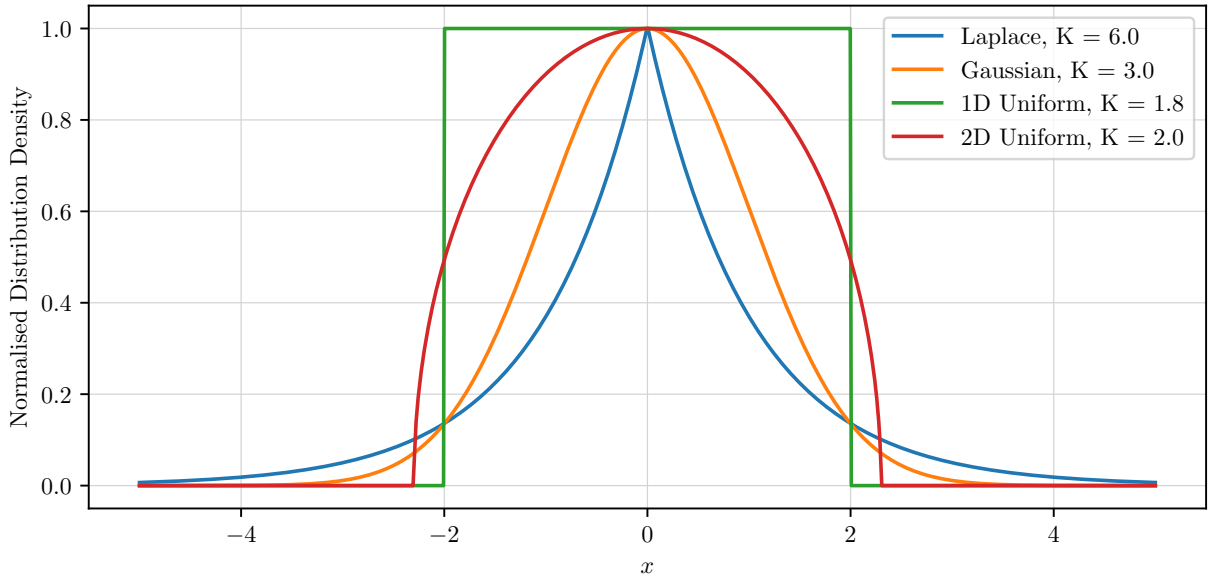


Figure 5.1: Sample distributions in x with their kurtosis labelled.

Before producing beams with uniform beam profiles it is important to define a measure of uniformity. One component of this definition is to look at the fourth moment, or kurtosis of the distribution. The kurtosis of a distribution in x , with a mean μ and standard deviation σ , is defined as,

$$K_x = \frac{\langle (x - \mu)^4 \rangle}{\sigma^4}. \quad (5.1)$$

The kurtosis measures the relative density of the tails of a distribution to the core [185]. Several distributions with different kurtosis are shown in Figure 5.1. The kurtosis of a Gaussian distribution is 3. Distributions, such as a Laplacian, which have a lower density

in the tails have a greater kurtosis. Distributions with relatively more populated tails have a lower kurtosis. A 1D uniform distribution has a kurtosis of 1.8. The kurtosis through one plane of a 2D uniform distribution is 2. Therefore, any beam profile that is uniform in $x - y$ will have a kurtosis of 2. As several non-uniform distributions can also have a kurtosis of 2 [186], care must be taken to check the uniformity. The uniformity is checked by comparing the variation in density over the transverse profile.

5.2 Generating Uniform Beams

Bunches produced in photoinjectors tend to exist in the space-charge regime, such that the interactions of particles within a bunch are dominated by the self field of the bunch. In the space-charge regime, non-linear space-charge forces cause the phase space of the bunch to distort in the manner illustrated in Figure 5.2. These space-charge forces cause bunches created in non-equilibrium to evolve towards stable states with a potential energy that is minimised [136]. If a bunch is initially created with a Gaussian distribution then the space-charge forces will cause particles in the core to move towards the tails. If the space-charge forces present in the photoinjector are low, the beam will continue to have a transverse beam profile similar to a Gaussian. If the space-charge forces are increased, then the tails of the Gaussian begin to become more populated and the bunch will have a more uniform transverse beam profile. When the space-charge forces are too high, the beam becomes highly peaked around its centre, with a diffuse surrounding halo. It is this principle that is used in FELs to produce uniform beam profiles for ultra low bunch charges [182]. However, it has not been demonstrated with bunch charges high enough to be useful in an irradiation facility or with simple laser optics.

In a photoinjector the evolution of the space-charge forces is determined by the bunch charge, the laser spot size, the laser pulse length, the strength of the RF field, the phase of the RF field, and the strength of solenoid field. It is, therefore, possible to control the space-charge driven evolution of the phase space of a bunch by changing these parameters. By simulating a modified version of the CLEAR gun using the ASTRA model, it is possible to demonstrate how the gun can be used to produce beams with uniform transverse beam profiles. In these initial simulations a bunch of charge 0.4 nC was produced from a laser pulse

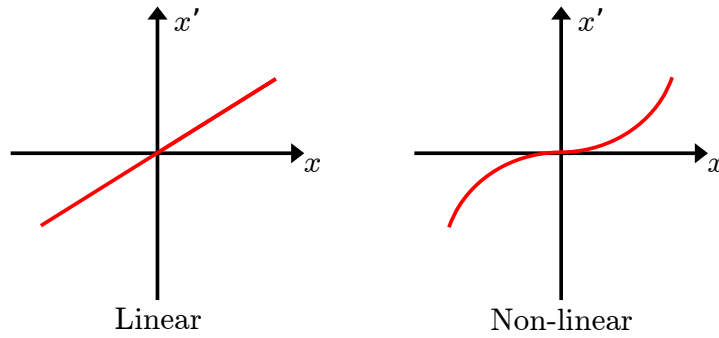


Figure 5.2: Transverse phase space of two sample distributions, one under the influence of linear forces and one under the influence of non-linear focusing forces.

of length 1 ps and Gaussian transverse shape of size 1.6 mm. The bunch was accelerated at the peak accelerating phase in the gun with an RF field of 110 MV/m. The strength of the solenoid magnet was varied showing how it could be used to control the uniformity of the transverse beam profile.

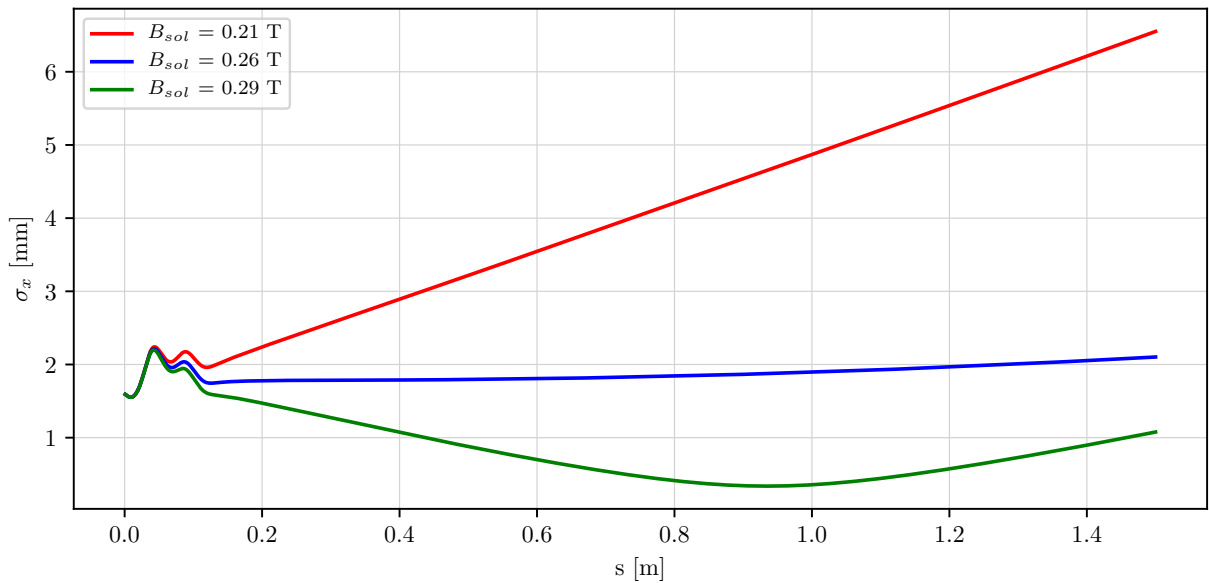


Figure 5.3: Horizontal beam size vs distance from the photocathode for a bunch of charge 0.4 nC generated from a laser spot of 1.6 mm with different solenoid magnetic field strengths.

The evolution of the beam size of three bunches focused by different solenoid fields is shown in Figure 5.3. Each magnetic field strength shown illustrates a separate space-charge evolution leading to three different transverse beam profiles. Slices of the transverse beam profile of each field at a distance of 1.5 m from the photocathode are shown in Figure 5.4. In each case the space-charge forces present in the gun are not strong enough to produce

uniform beam profiles at the exit of the gun. For a solenoid of strength 0.21 T, the beam is constantly diverging following the gun, resulting in a significant drop in space-charge forces with distance. The beam profile, therefore, remains similar to a Gaussian but with slightly more populated tails, with a $K_{x,y} = 2.56$. The bunch that is focused by a solenoid field of 0.26 T is only diverging a small amount during the drift. Therefore, the space-charge forces are almost constant during the drift causing the beam core to diffuse outwards creating a uniform beam profile with $K_{x,y} = 2.04$ at 1.5 m. For a solenoid field strength of 0.29 T the beam is converging as it leaves the gun towards a beam waist at 0.9 m from the photocathode. The evolution of phase space for this case at different distances from the photocathode is shown in Figure 5.5. At 0.3 m, just after the exit of the gun, the bunch profile is Gaussian like, with a $K_{x,y} = 2.65$. As the bunch moves towards the waist, the space-charge forces grow, and the beam moves towards a uniform distribution with a of $K_{x,y} = 2.07$ at a distance of 0.6 m. As the bunch reaches the waist, the space-charge forces cause an over-rotation in the phase space and a distribution with a sharp core develops. At a distance of 1.0 m from the photocathode the beam has $K_{x,y} = 3.90$, with the kurtosis growing with distance to $K_{x,y} = 7.57$. It must be noted that the transverse space-charge forces do not significantly affect the distribution in z .

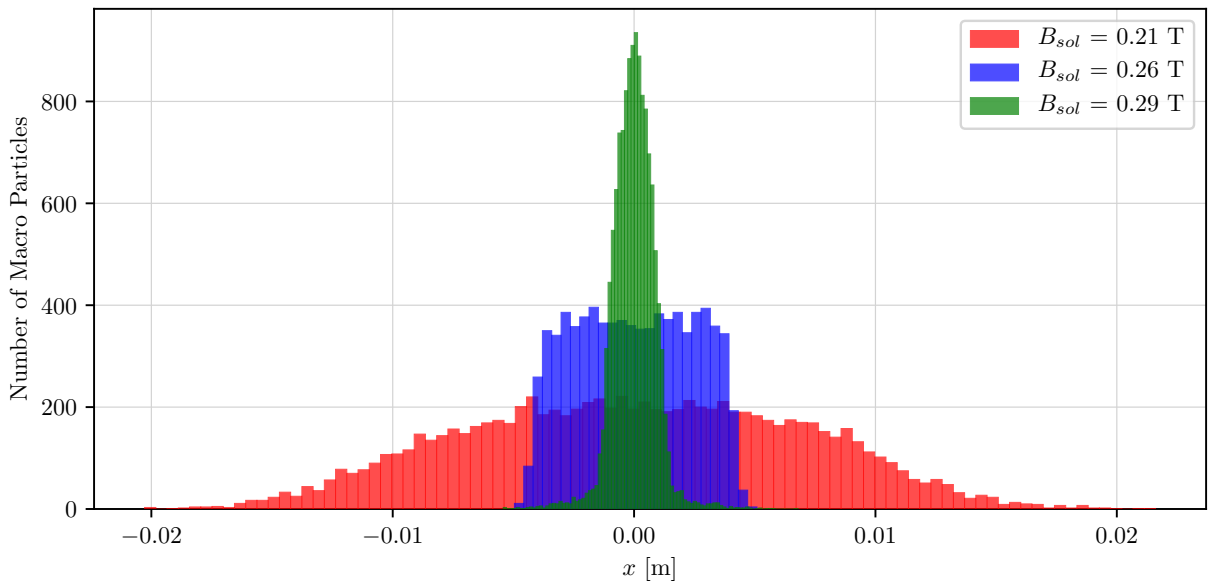


Figure 5.4: Particle distributions in x across a slice in y of width $\pm\sigma_y/4$ measured at a distance of 1.5 m from the photocathode for a bunch of charge 0.4 nC generated from a laser spot of 1.6 mm.

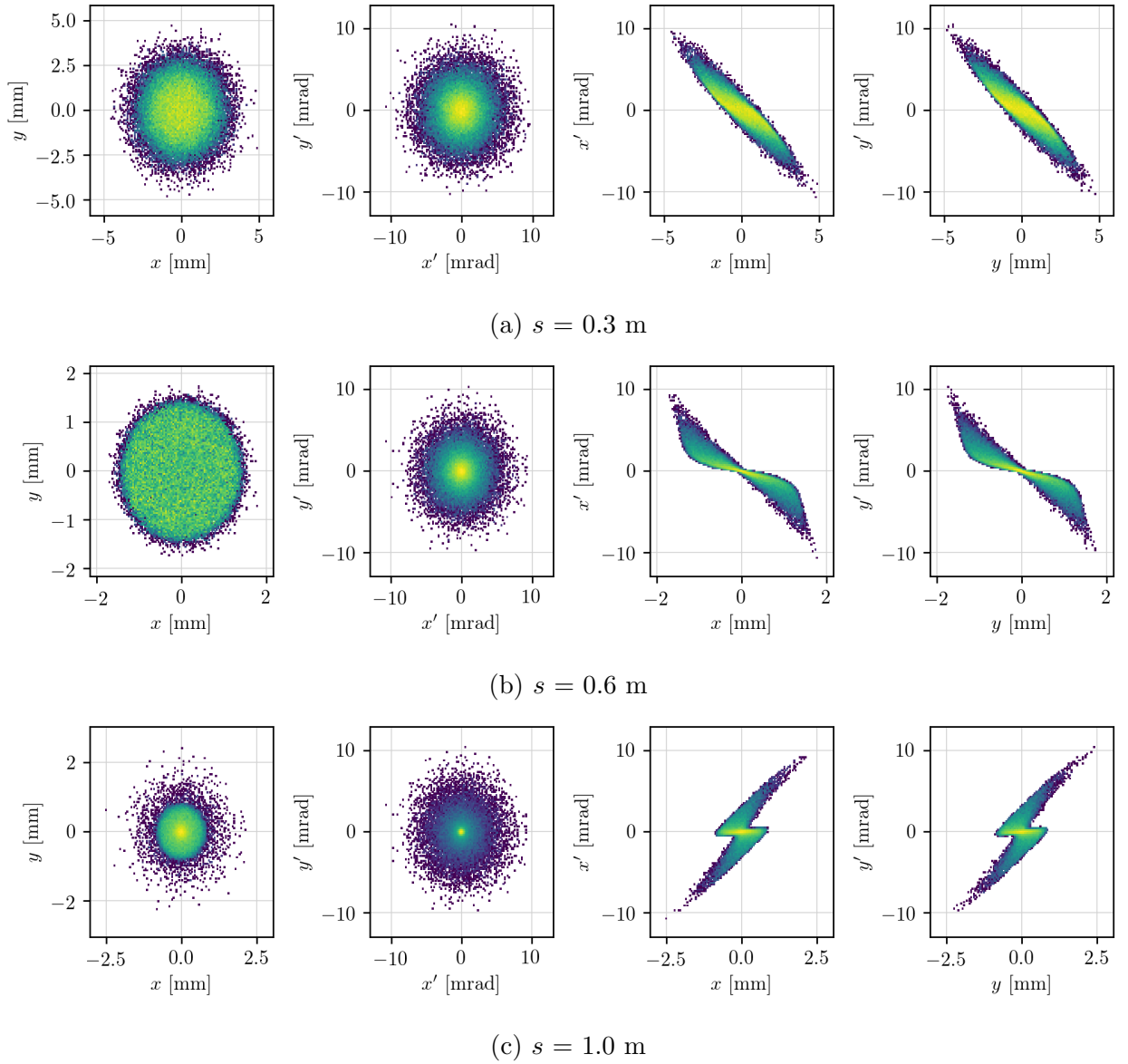


Figure 5.5: The phase space of a bunch of charge 0.4 nC generated from a laser spot of 1.6 mm focused by a solenoid magnet of strength 0.29 T measured at **(a)** $s = 0.3$ m, **(b)** $s = 0.6$ m, and **(c)** $s = 1.0$ m.

It is possible to adjust the position at which the beam has a uniform transverse beam profile by adjusting the solenoid strength only. The evolution of the kurtosis with distance for several different solenoid strengths is shown in Figure 5.6. As each beam is produced from a Gaussian laser spot the kurtosis at 0.0 m is 3. Space-charge forces cause the kurtosis to reduce with distance from the photocathode. All bunches focused with a solenoid strength higher than 0.26 T have a kurtosis of 2 at a distance less than 1.5 m. The stronger the magnetic field, the closer the point at which the kurtosis is 2 occurs to the photocathode. For solenoid strengths of 0.27 T or higher, there are two points at which the kurtosis is equal

to 2. In an operational facility the ability to change the distance at which a uniform beam profile is obtained simply by changing the solenoid strength would be useful. By placing a screen at a fixed position, closer to the gun than the target, the uniformity could be checked against the predicted distribution.

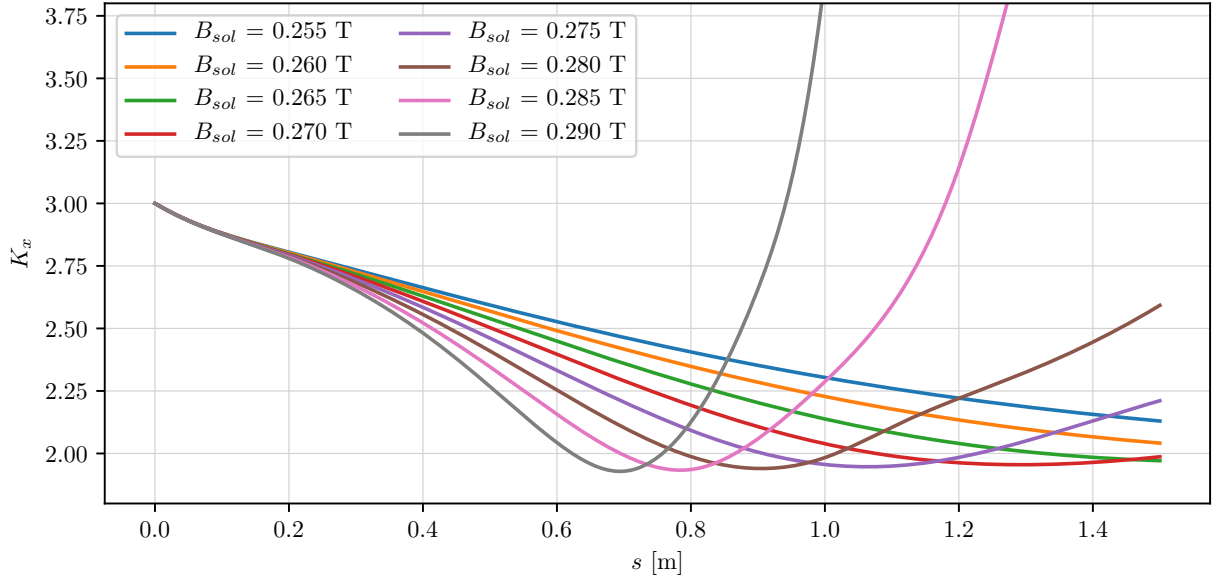


Figure 5.6: Kurtosis vs distance from the photocathode for a bunches of charge 0.4 nC generated from a laser spot of 1.6 mm and focused by different solenoid fields.

By tuning the solenoid magnet to produce a kurtosis of 2, minimisation of emittance growth is neglected. Figure 5.7 shows the evolution of emittance from the RF gun. At a distance of 1.5 m from the photocathode a focusing strength of 0.29 T produces a bunch with a significantly lower emittance than a focusing strength of 0.26 T. It may be possible to both minimise emittance growth and develop a uniform beam profile, as is the case for FELs, however, this was not achieved in this investigation.

Producing a uniform transverse beam profile using only a photoinjector has a limited use in an irradiation facility due to the low energy of the beam. However, as the space-charge forces drop significantly with increased energy, it is proposed that by rapidly accelerating the bunches following the photoinjector it would be possible to quickly reduce the space-charge forces, thus fixing an angle in phase space with uniform beam profile. There would be some phase space rotation as the bunch is accelerated, however, it would be possible to use magnetic elements following the accelerating cavities to rotate it back to a uniform profile in $x - y$.

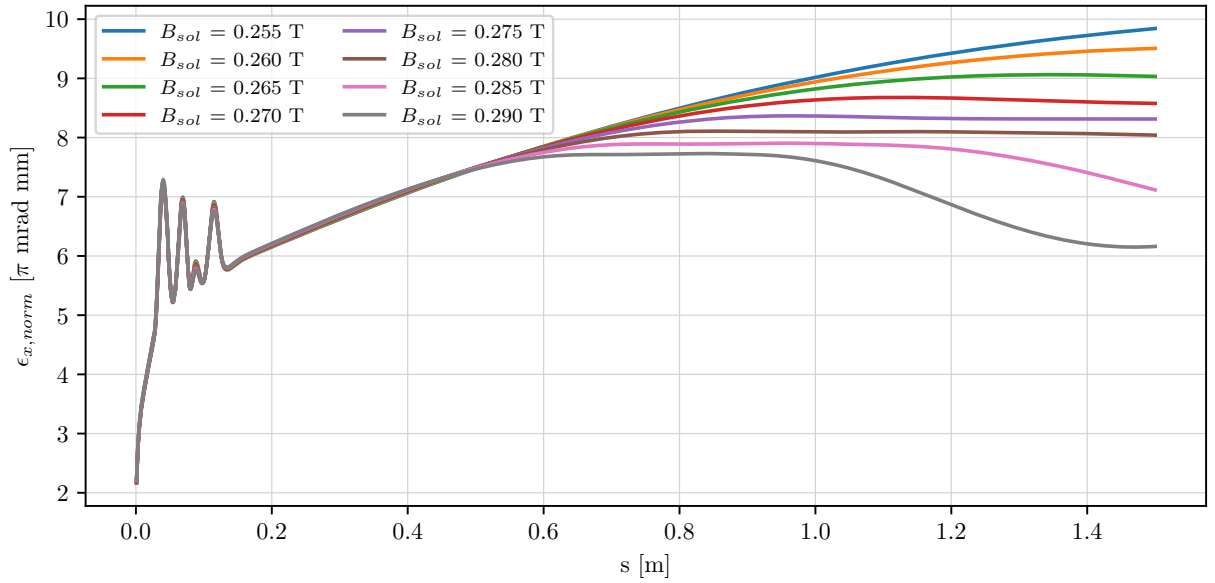


Figure 5.7: Normalised emittance vs distance from the photocathode for bunches of charge 0.4 nC generated from a laser spot of 1.6 mm and focused by different solenoid fields.

5.3 Proposed Linear Accelerator

To demonstrate the feasibility of producing transversely uniform electron beams for use in irradiation experiments or for VHEE-RT, a compact irradiation facility was proposed. The facility consists of the CLEAR photoinjector followed by eight, X-band, travelling-wave RF cavities similar to those used on CLIC [52]. The layout of the linear accelerator is shown in Figure 5.8. The accelerating structures are arranged on two modules, of four structures similar to those proposed to be used in the eSPS [45]. Each structure is 525 mm long, and there is a gap of 200 mm between the two modules. The iris of the structures was set to be the same as those proposed to be used in the eSPS, 3.7 mm at the entrance to the structure decreasing to 2.7 mm at the exit of the structure. Unlike the eSPS modules, there are no quadrupoles present in the linac, as the total length is short and the RF focusing forces are strong. Each RF module would have independent control of RF field strength and RF phase, and would be used to accelerate each beam to 100 MeV, which would allow the beams to be used for VHEE-RT. Following the linac would be a quadrupole matching section which would be used to rotate the phase space towards a uniform profile and shape the beam towards a target.

A single bunch was simulated from the photocathode to the entrance of the first X-band

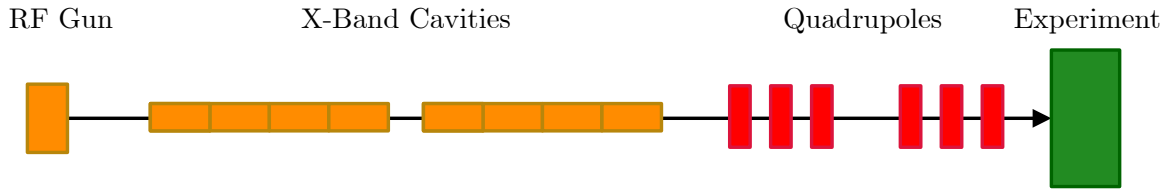


Figure 5.8: Diagram of the irradiation facility beamline.

structure using the ASTRA model detailed in Chapter 3. The bunch was simulated through the linac and matching section using the particle tracking code RF-Track [187, 188]. The RF-Track model simulates space-charge forces on the beam, and both transverse and longitudinal short-range wakefields. To simulate high-current beams, full beam-loading in the linac was assumed. Normalised real and imaginary components of the unloaded longitudinal field profile of one RF structure are shown in Figure 5.9a. In the RF-Track model, the phase of this field could be arbitrarily set. Beam-loading could then be added to the unloaded profile, with the phase of beam-loading set to be in phase with the beam. An example of the beam-loaded field profile is shown in Figure 5.9b.

In this initial proposal, bunches of charge 0.4 nC generated from a Gaussian laser profile at the photocathode were simulated. Laser spot sizes of 0.8 - 1.6 mm were considered. Due to the high-frequency of the X-band RF cavities it was necessary to keep the bunches short to reduce energy spread in the linac. As the aim of the proposed accelerator is to be simple to operate and maintain, a laser with a commonly used pulse length of 1 ps was used. Electric field strengths of between 80 and 120 MV/m were considered for the RF gun, and maximum field strengths of up to 50 MV/m were considered in the X-band structures. The X-band structures are able to operate at gradients of up to 100 MV/m, which would allow acceleration to a higher energy than 100 MeV, however, this was not considered in this initial investigation due to the large RF focusing forces at these gradients. A maximum gun solenoid field strength of 0.4 T was considered.

As the electron beam exits the RF gun at an energy of $\sim 5 - 10$ MeV, it has a low rigidity upon entrance to the first structure. Therefore, the high gradient of the X-band cavity produces a relatively strong RF focusing effect. The RF focusing can lead to a rapid reduction in bunch size and an increase in space-charge forces causing the phase space to

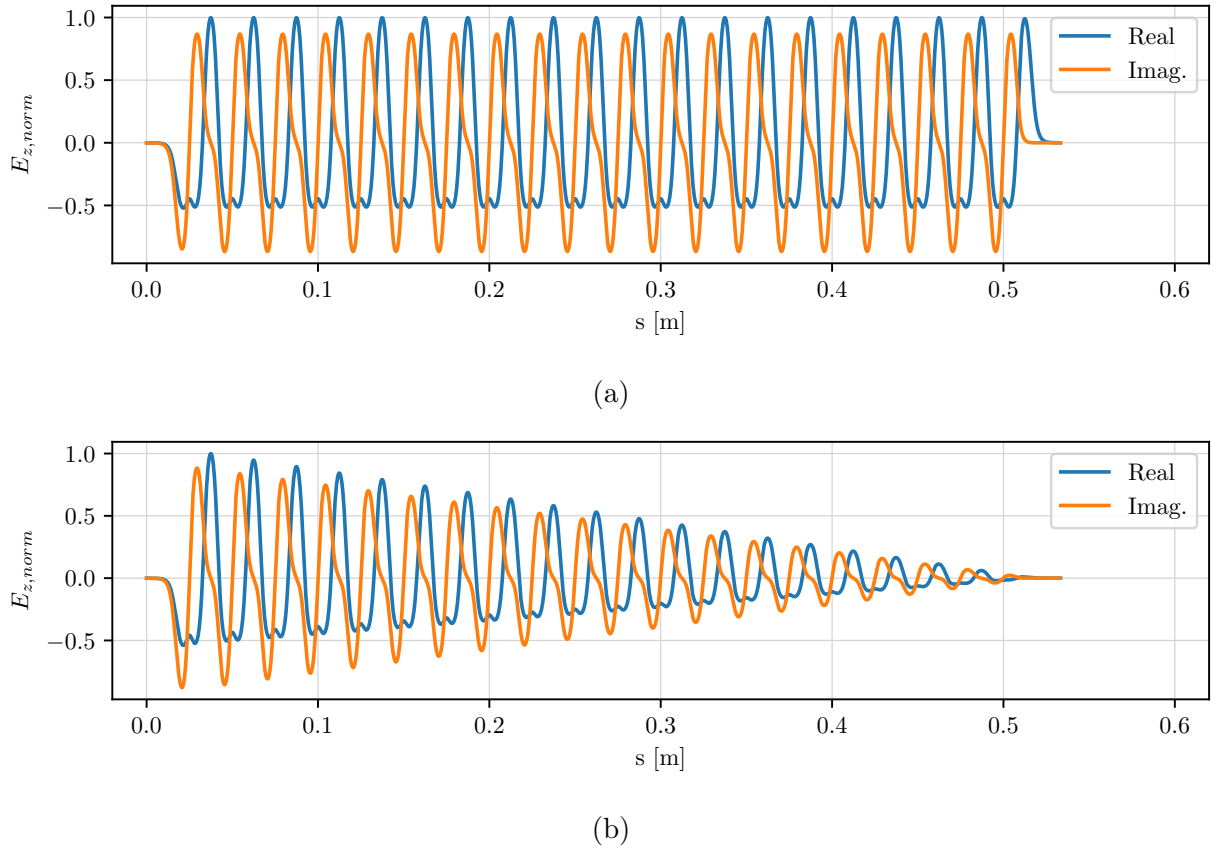


Figure 5.9: Real and imaginary longitudinal electric field profiles, normalised to the maximum real component, of the X-band cavities vs distance from the entrance to the cavity for **(a)** an unloaded cavity, and **(b)** a loaded cavity.

distort and move to a profile with a sharp core surrounded by a diffuse halo. The additional phase space distortion both leads to beam losses and makes it more difficult to recover a uniform beam profile at the end of the linac. It is possible to counteract the RF focusing by producing a bunch that is diverging at the entrance to the first cavity. Figure 5.10 shows the beam size through the linac of a 0.4 nC bunch produced at the linac entrance with a uniform transverse distribution of radius 2 mm, $\epsilon_{x,n} = \epsilon_{y,n} = 10 \pi$ mm mrad, length 1 ps, energy of 5.5 MeV, energy spread of 1%, and different values of $\alpha_{x,y}$. The bunches were tracked using the RF-Track model with the RF phase of both modules set to the maximum accelerating phase. The maximum field gradient of the structures was set to 25 MV/m. The aperture of each accelerating structure was approximated to vary linearly between 3.7 mm and 2.7 mm.

Bunches that are not diverging at the entrance to the linac see significant focusing forces from the RF field. The focusing forces cause the largest effect in the first metre of the linac

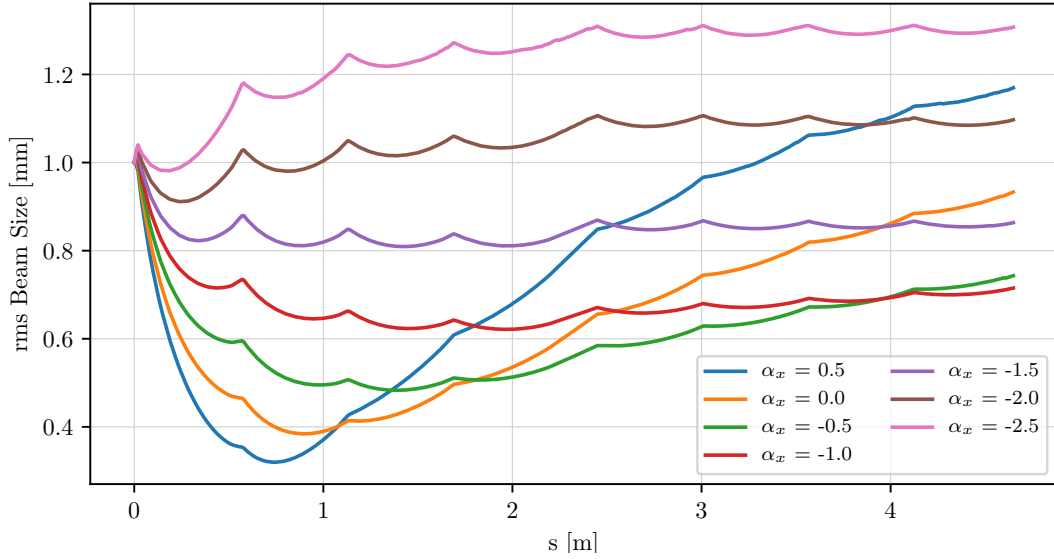


Figure 5.10: Beam size vs distance from the entrance to the first X-band structure for a 0.4 nC bunch produced with different $\alpha_{x,y}$.

when the beam rigidity is low, with no significant reduction in beam size seen in the second accelerating module. The bunch produced with $\alpha_{x,y}$ of 0, is focused to a waist less than 0.4 mm, whilst still at energies lower than 20 MeV. Because of this, space-charge forces cause the phase space of the bunch to distort. For a beam that has a uniform beam profile at the entrance to the linac, this causes the phase space to move to a core halo distribution, for which a uniform profile cannot be recovered. Bunches that are initially diverging at the entrance to the linac see smaller reduction in beam size. Bunches with $\alpha_{x,y}$ lower than -1.5 see a very small amount of focusing have an almost constant beam size.

However, bunches produced with an $\alpha_{x,y}$ lower than -1.5 are too large for the narrow aperture of the structures and produce beam losses through the linac, as shown in Figure 5.11. There are also beam losses for the bunch produced with an $\alpha_{x,y}$ of 0, however, these are low. The bunch produced with an $\alpha_{x,y}$ of -1.0 sees no beam losses. In addition, the RF focusing is mostly eliminated in the linac. Therefore, any bunch produced by the gun should have a divergence of around $\alpha_{x,y} = -1$.

Because of the narrow aperture, it was necessary to keep the beam small upon entrance to the cavity to avoid beam losses. To produce a diverging beam with a small beam size it was preferable to have the cavity as close to the gun as possible. The current CLEAR photoinjector has a length of 1.5 m from the photocathode to the mirror and 2.4 m to the first accel-

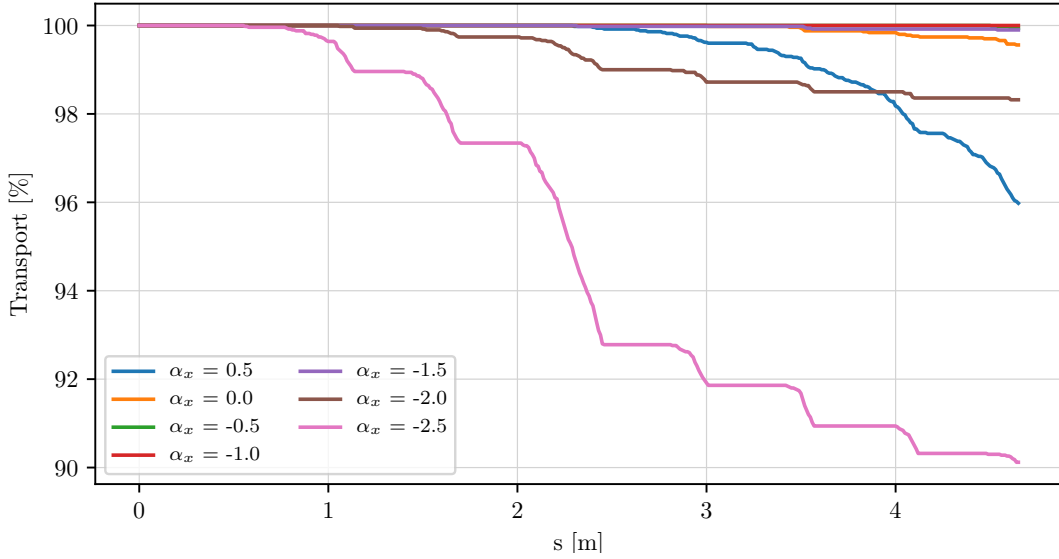


Figure 5.11: Beam transport vs distance from the entrance to the first X-band structure for a 0.4 nC bunch produced with different $\alpha_{x,y}$.

erating structure. Modern, compact photoinjectors such as the proposed AWAKE/CLEAR photoinjector [84], can have total lengths as low as 1.2 m from the cathode. Therefore, a length of 1.2 m was chosen between the gun and the linac.

5.4 Accelerator Optimisation

There are several parameters which need to be optimised to produce a 0.4 nC bunch which can be matched to a uniform beam profile, namely: the laser spot size; the RF field strength of the gun; the RF phase of the gun; the gun solenoid field strength; the accelerating field of both X-band modules; and the phase of both X-band modules. An optimisation of all of these parameters was performed using the MATLAB function `fminsearch` [189]. `fminsearch` uses a simplex search method to find a minimum of a merit function. The merit function for the optimisation targeted zero bunch losses in the linac, an energy of 100 MeV, an energy spread of $\leq 1\%$ at the linac exit, and a kurtosis of 2 across a projected plane in phase space at the linac exit. For the optimisation, a bunch of 2000 macro-particles was tracked from the photocathode to the linac exit. Following the optimisation of the beamline parameters, a bunch of 50,000 macro-particles was tracked through the linac and the results verified. The layout and optics of the quadrupole matching section were then optimised to recover a

uniform beam profile.

5.4.1 RF Gun

Following the optimisation, the RF field of the gun was set to 110 MV/m and the strength of the gun solenoid magnet set to 0.277 T. The phase of the RF cavity was set to 53° , which is $\sim 0.5^\circ$ less than the peak accelerating phase. The optimum laser spot size was 0.8 mm. The bunch diverges from the exit of the gun, as shown in Figure 5.12a. The beam is round in $x - y$ with a maximum particle radius of 3.2 mm at the linac entrance. Space-charge forces cause the bunch length to increase slightly from the 1 ps laser pulse length to 1.2 ps at the entrance to the linac, as shown in Figure 5.12b. The normalised emittance in both x and y is 6.71π mm mrad. The energy is 7.35 MeV and the energy spread is 1%.

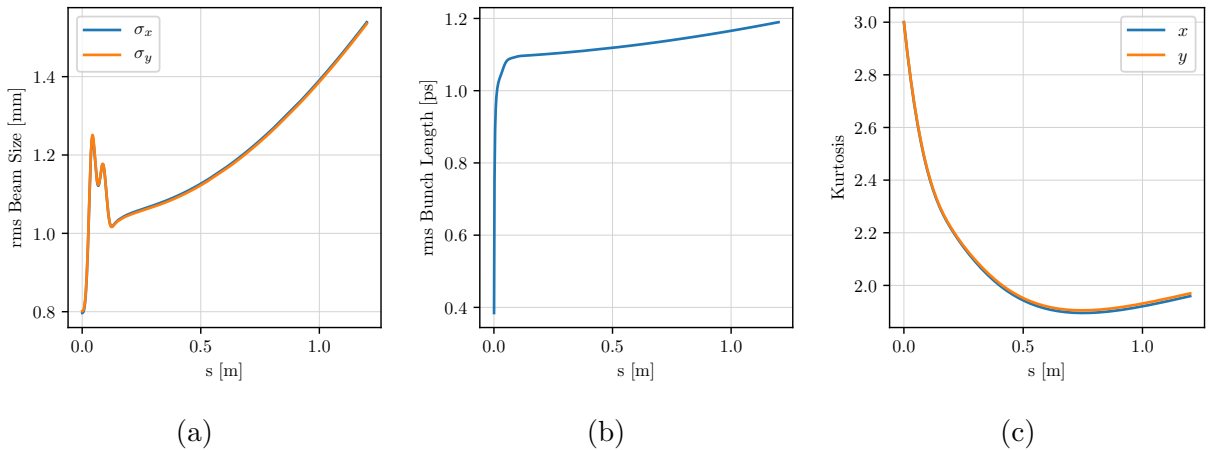


Figure 5.12: **(a)** The beam spot size, **(b)** the bunch length, and **(c)** the kurtosis of a 0.4 nC bunch generated from a laser spot of 0.8 mm, vs distance from the photocathode.

The phase space of the bunch at the entrance to the linac is shown in Figure 5.13. The beam profile is almost uniform in $x - y$, with a kurtosis of 1.97, suggesting slightly more populated tails than a true uniform distribution. The effect of the space-charge forces in rotating the position-momentum phase space is clear. The beam is symmetric between x and y in both position and momentum phase space. The evolution of the Kurtosis is shown in Figure 5.12c. The kurtosis is exactly 2 at 0.4 m, and then decreases to a minimum at 0.7 m, before it rises again. As the beam is uniform at 0.4 m, a BTV screen could be inserted here to verify the beam set up experimentally. A BTV could also be inserted close to the linac entrance, as it was previously shown that by changing the solenoid strength it is possible to

change the uniformity of the bunch with distance from the photocathode.

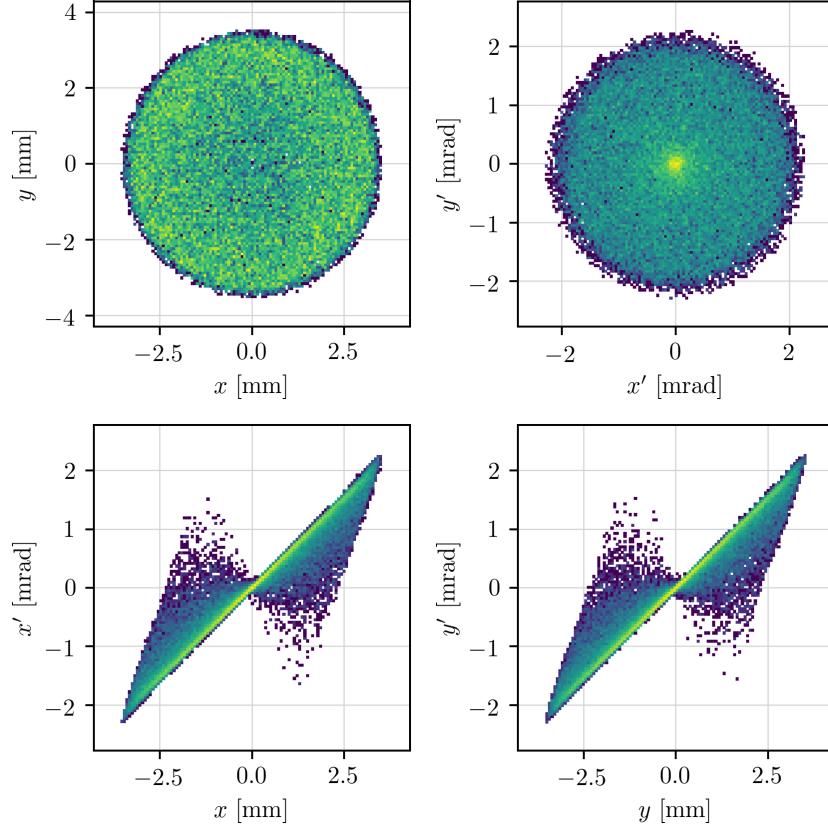


Figure 5.13: Transverse phase space of a 0.4 nC bunch, 1.2 m from the photocathode, generated from a laser spot of 0.8 mm.

The bunch produced in the optimisation does not have a uniform longitudinal profile such as distributions produced with ultra-short laser pulses. Unlike in transverse phase space, the longitudinal space-charges are not significant enough to produce a uniform distribution in longitudinal phase space, shown in Figure 5.14. However, the distribution of particles in z is not Gaussian. The longitudinal space-charge forces that are present cause the tails of the longitudinal distribution to become slightly more populated, and the distribution has a kurtosis of 2.5. Because of this, the space-charge forces along the rest of the linac are non-linear. To produce a uniform longitudinal distribution a shorter laser pulse is required. However, this is a well documented phenomenon and is out of the scope of this discussion [183].

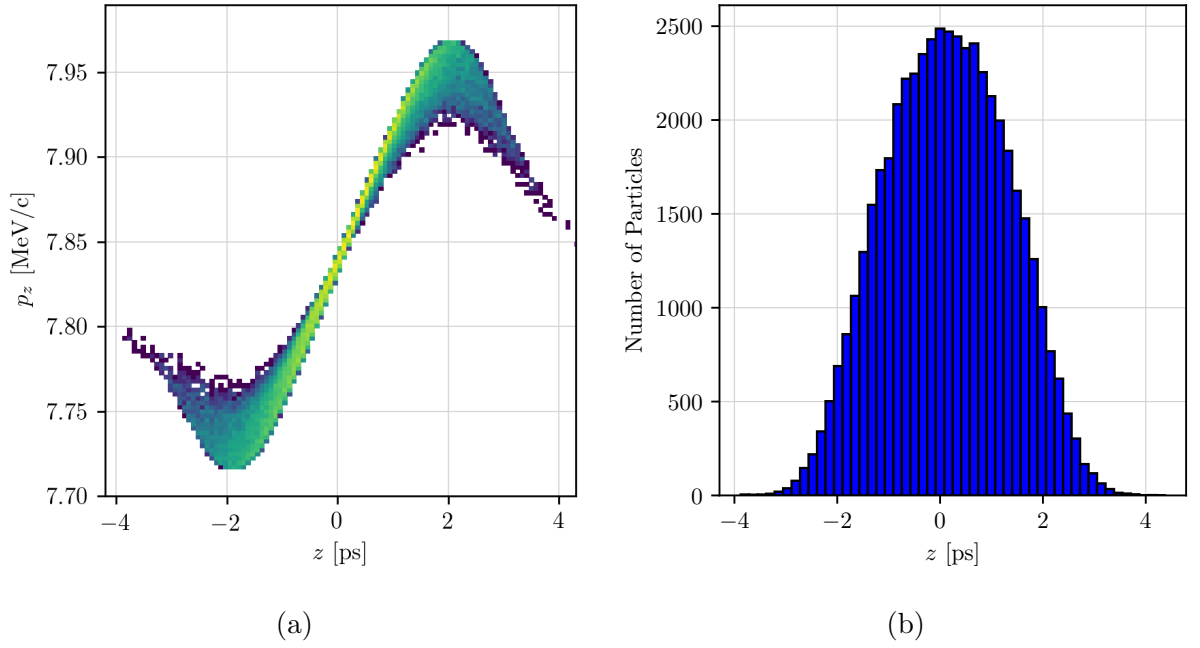


Figure 5.14: Longitudinal phase space of a 0.4 nC bunch, 1.2 m from the photocathode, generated from a laser spot of 0.8 mm.

| Energy | ΔE | $\epsilon_{x,n}$ | l_z | $\sigma_{x,rms}$ |
|------------|------------|--------------------|---------|------------------|
| 100.02 MeV | 0.77% | 6.71 μm | 1.15 ps | 0.35 mm |

Table 5.1: Beam Parameters at the linac exit.

5.4.2 Linac

The energy gain of the bunch through the linac is shown in Figure 5.15. To achieve 100 MeV, the loaded gradient of the first module was set to 27.6 MV/m with the second set to 26.7 MV/m. The effect of beam loading is shown, with a non-constant energy gain in each structure. The phase of the first module, as the beam enters, is set to -15.3° and the phase of the second structure, as the beam enters, is set to 7.8° . The average energy gain per structure in both modules is ~ 11.6 MeV. The main beam parameters at the exit of the linac are shown in Table 5.1. Both the energy spread of the bunch and the bunch length are slightly reduced in the linac. The energy spread at the exit of the linac is 0.77%, and the bunch length is 1.15 ps.

As the beam is strongly diverging at the entrance to the linac, the bunch core does not reach a small waist whilst at a low energy. The rms beam size is largest at its lowest energy and decreases through the linac, as shown in Figure 5.16. The beam is equal in size in x and

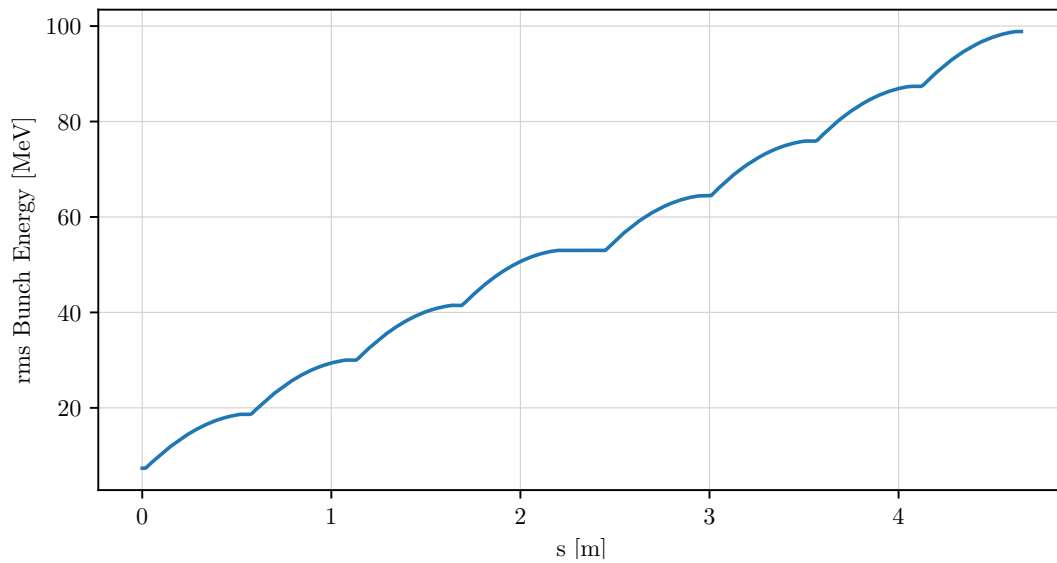


Figure 5.15: Bunch energy vs distance from the entrance of the first X-band cavity for a bunch of charge 0.4 nC generated from a laser spot of 0.8 mm.

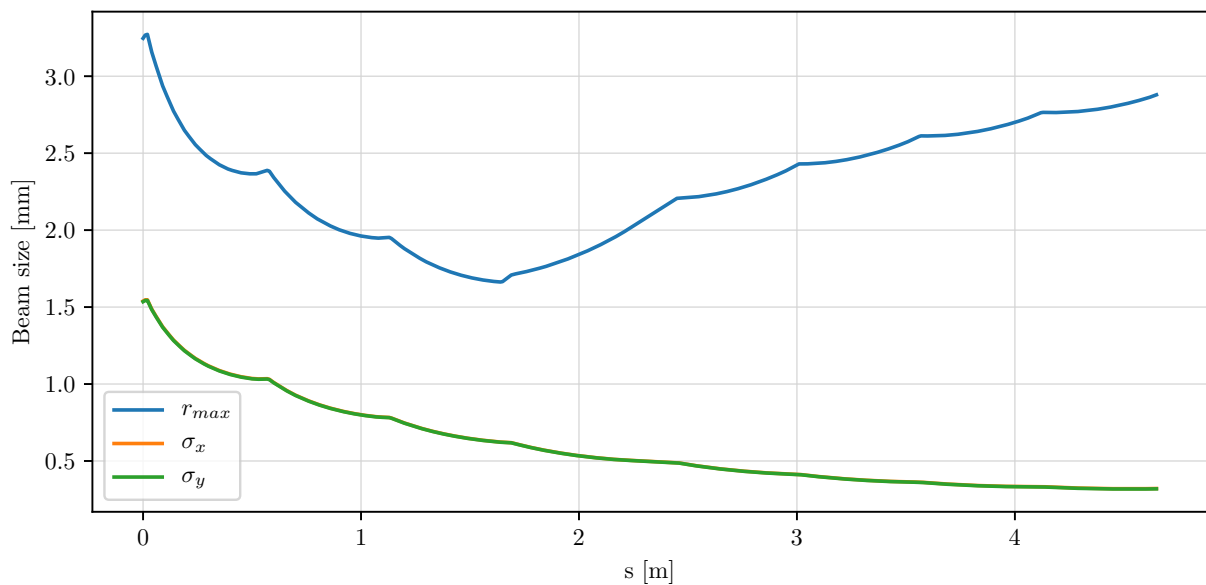


Figure 5.16: Maximum particle radius and rms bunch size vs distance from the entrance of the first X-band cavity for a bunch of charge 0.4 nC generated from a laser spot of 0.8 mm.

y . As there is no small waist at the entrance to the linac, the space-charge forces decrease through the linac. The radius of the particle furthest from the bunch core does, however, reach a minimum size in the linac, after which it grows. Over the linac, the maximum radius is not large enough to lead to any losses. The difference between the maximum particle radius and the rms beam size is due to the changing distribution of the bunch. The bunch

changes from a near uniform bunch at the linac entrance to a bunch with a dense core, with low rms size, and a surrounding halo. The phase space of the bunch at the end of the linac is shown in Figure 5.17. Phase space rotation results in the distribution in $x - y$ being non-uniform, with a sharp core with a kurtosis of 12.8.

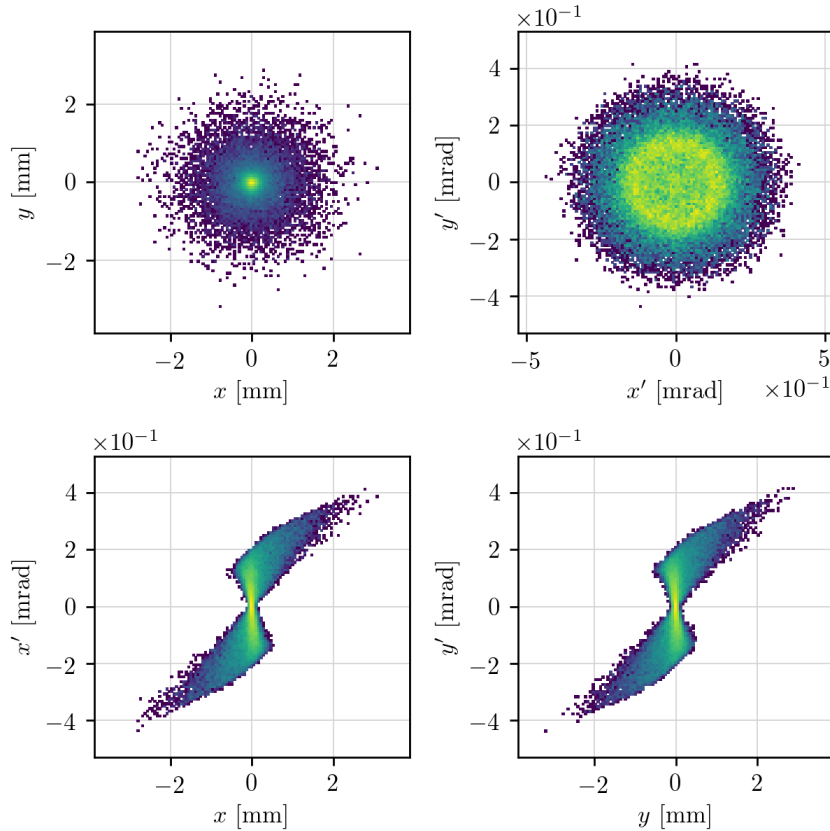


Figure 5.17: Transverse phase space of a 0.4 nC bunch at the exit of the linac.

The longitudinal phase space is shown in Figure 5.18a. Although the energy spread is less than 1% there is a long energy tail of over 3 MeV. The tail may cause chromatic issues when attempting to manipulate the beam with the quadrupole matching section. However, it is not possible to reduce the tail using just the RF phase and field strength of either the gun or the X-band structures. The only way to reduce the tail is to use a shorter laser pulse. The distribution in z is very similar at the exit of the linac to the entrance, with a Gaussian-like profile, with more populated tails. The kurtosis of the longitudinal distribution is identical to the linac entrance at 2.5.

As the space-charge forces drop as the beam moves through the linac, the phase space still contains an axis at which a uniform profile exists. A projected phase space is shown

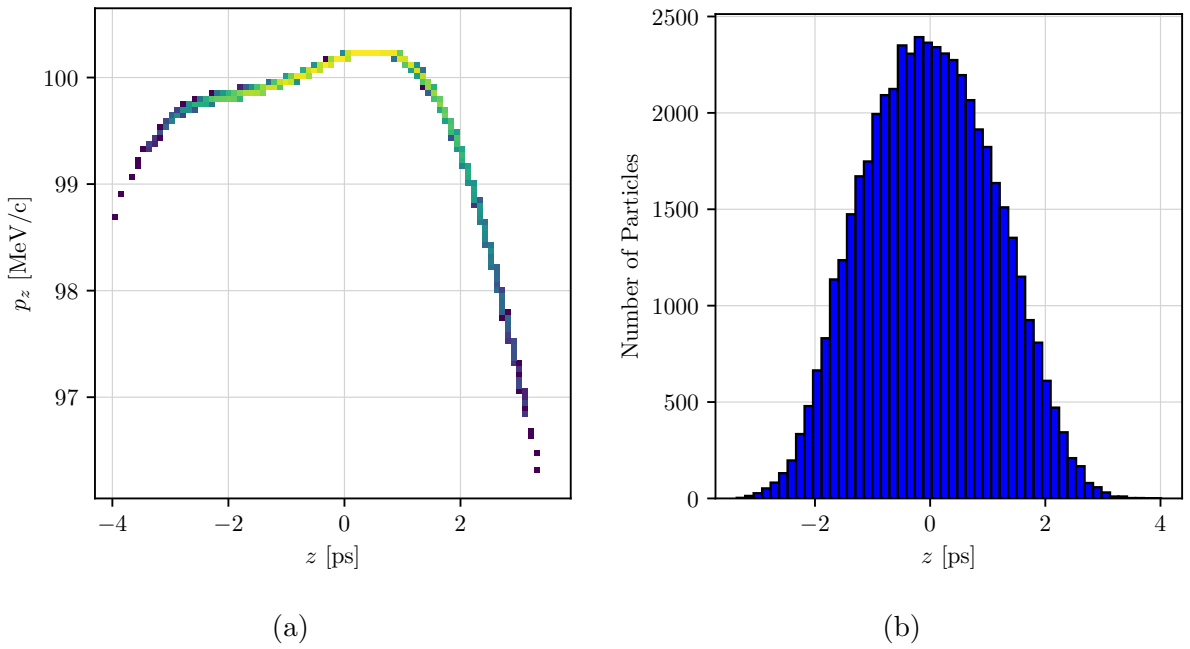


Figure 5.18: Longitudinal phase space of a 0.4 nC bunch at the exit of the linac.

in Figure 5.19. To produce this projection $x - x'$ and $y - y'$ were rotated by an angle of 81.9° . The beam is uniform in the projected phase space with a kurtosis of 2.01 in xx' and 2.00 in yy' . As there is a uniform angle in phase space, it should be possible to use a quadrupole matching section, with the correct phase advance, to produce a physical beam with a uniform distribution in $x - y$.

5.4.3 Quadrupole Matching Section

To verify the possibility of recovering a uniform beam distribution following the linac, a simple quadrupole matching section was simulated. The quadrupole section consists of two triplets, using quadrupoles of length 0.5 m. The first triplet begins a distance of 0.5 m from the linac exit, allowing for the installation of beam diagnostics and vacuum pumps. Between each magnet in the triplets there is a drift of 0.5 m. There is a drift of 1.5 m between the two triplets, again allowing the installation of diagnostics and other equipment.

An optimisation of the quadrupole magnets was undertaken to produce uniform beam profiles of several different sizes. The 50,000 macro-particle beam was tracked using RF-Track from the exit of the linac to an experimental target location, 0.3 m from the exit of the final quadrupole. The strengths of the quadrupole magnets were varied to produce a

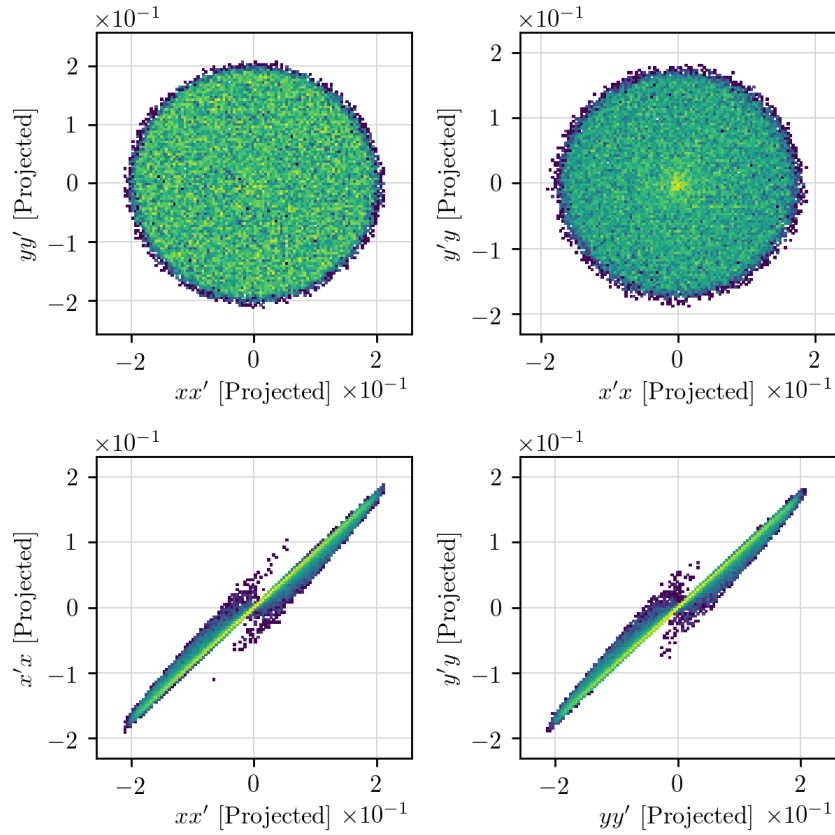


Figure 5.19: Projected transverse phase space of a 0.4 nC bunch at the exit of the linac.

bunch of kurtosis 2 and three separate diameters, small, medium and large such that 98% of the macro-particles fell within a diameter 5 mm, 10 mm, and 20 mm respectively. These beam sizes were chosen to span the range of commonly requested beam sizes for irradiation experiments at CLEAR. A maximum focusing gradient of 15 T/m was set. It must be noted that these optimisations are not meant to present the best layout for a matching section following the linac, just the ability to recover a uniform beam. Further work must, therefore, be done to optimise the optical layout, particularly targeting a more compact layout.

The phase space for each of the three beams is shown in Figure 5.20. The small-diameter bunch has a circular beam profile of maximum radius 3.0 mm. The bunch has a tail of width 0.5 mm with a population of 2%. Therefore, the target of 98% of the bunch within a 5 mm diameter was met. The bunch is uniform in $x - y$, with a kurtosis of 2.004 in x and 1.994 in y . There is a small peak in the centre of the distribution which is 0.25 mm in diameter and has a population of 8% higher than the rest of the distribution. The peak is an optical artefact

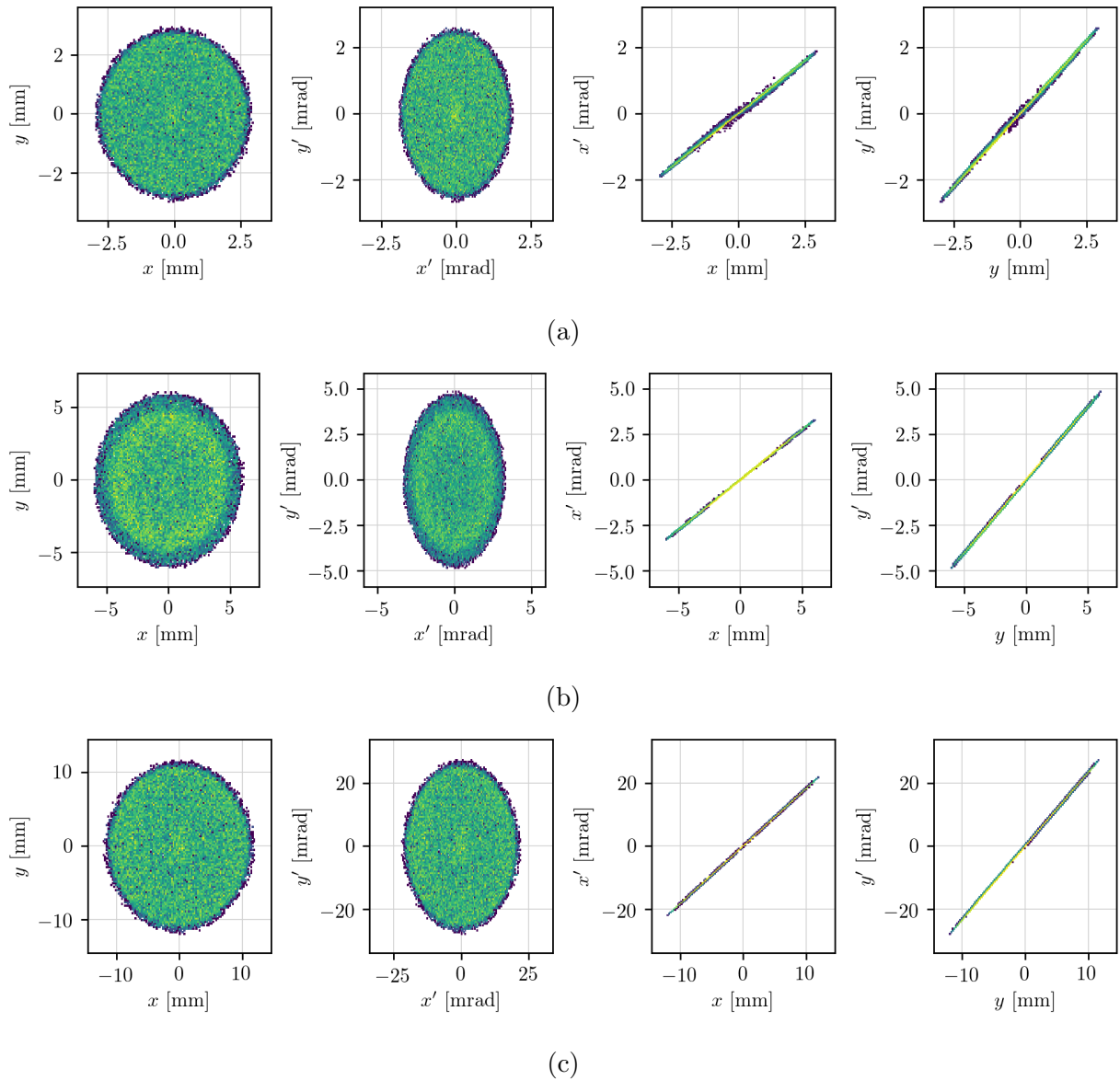
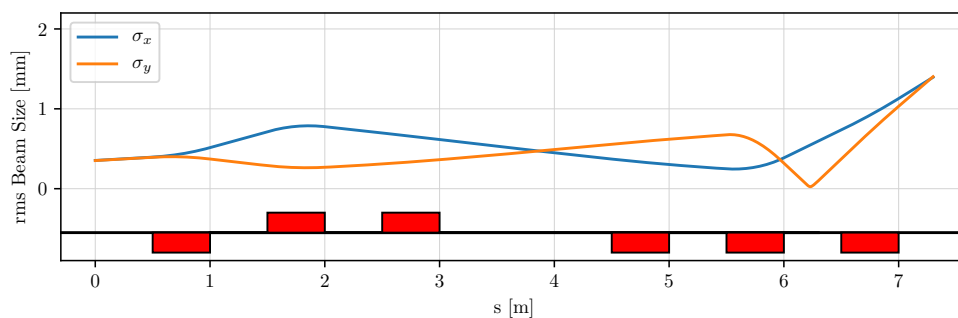


Figure 5.20: Transverse phase space measured at the experimental target location 0.3 m from the exit of the final quadrupole for the (a) small-, (b) medium-, and (c) large-diameter beam optics.

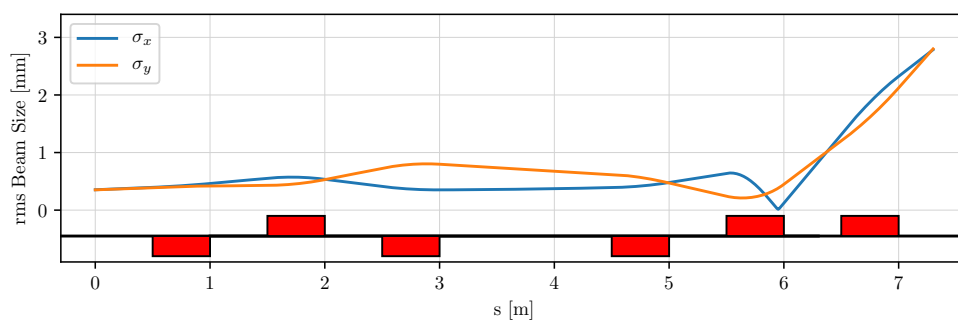
and could be removed with further optical optimisation. The momentum distribution is also quite uniform, although there is a sharper peak in the centre.

The medium-diameter bunch is slightly less uniform than the small-radius bunch with a kurtosis in x of 2.004 and in y of 1.992. The bunch also appears to have a lower population in the centre than the surrounding area. The population of the centre is about 5% lower than the population a radius 3.5 mm away. Again, this is an optical feature and could be removed with further optimisation. The total radius of the distribution is 6.1 mm, with a tail of 1 mm containing 2% of particles. Again, the momentum space is also quite uniform.

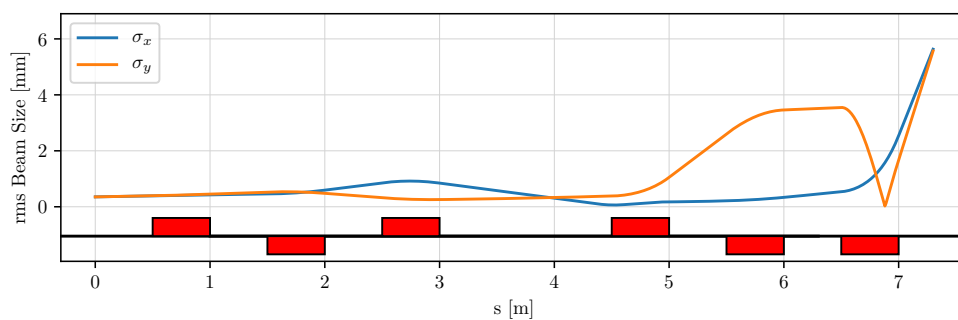
The large-diameter bunch has a slightly elliptical profile, with a total radius in x of 12.0 mm and a total radius in y of 11.7 mm. The tails of the distribution are 1.5 mm thick, resulting in a 98% radius in x of 10.5 mm and 10.2 mm in y . The beam is quite uniform in $x - y$ with a kurtosis of 1.995 in x and 2.005 in y . As with the small diameter bunch, there is a small peak at the centre of the distribution. The peak is 1 mm in radius and has a population 3% higher than the rest of the distribution.



(a)



(b)



(c)

Figure 5.21: Beam size vs distance from the linac exit for the (a) small-, (b) medium-, and (c) large-diameter beam optics.

All three beams have large divergence at the location of the target. The evolution in bunch size for all three bunches across the matching section is shown in Figure 5.21. All three

optical arrangements have relatively small beam sizes across the majority of the matching section before undergoing a blow up in the final triplet. Therefore, the beam pipe aperture could be small for the matching section and similar diagnostics to those used at CLEAR could be installed. In addition beam losses would likely be low in all three optics. It should be noted that none of the quadrupoles were either focusing or de-focusing for all three optics layouts. Therefore, in a physical facility the polarity of each of the magnet power supplies should be able to be reversed.

Following the exit of the final quadrupole, the uniformity of the beam profile was constant. Figure 5.22 shows the beam profile of the large-diameter beam at several distances from the exit of the final quadrupole. The radii in x and y change with distance, but the uniformity remains constant. At a distance of 0.1 m from the final quadrupole the beam has a size of $7.6 \times 6.3 \text{ mm}^2$, at a distance of 0.5 m from the final quadrupole the beam is $16.46 \times 17.2 \text{ mm}^2$, and at a distance of 1 m the beam has a size of $28.0 \times 30.9 \text{ mm}^2$. The maximum beam radius for the large-diameter optics is shown in Figure 5.23. The radius grows constantly to a maximum of 60 mm at a distance of 2 m from the final quadrupole. Therefore, in the proposed irradiation facility the beam optics could be configured to target a uniform beam size at one location, and the beam size changed by only moving the position of the target. Operating with a single beam optics would make the experimental programme significantly more efficient. As the beam uniformity does not change with distance it would be possible to collimate the beam at one location upstream of the target and shield the experimental target from any secondary particles produced in the collimator. As such a facility would likely operate with an in-air test stand; the effect of scattering from the vacuum window and the air itself should be investigated.

5.4.4 Stability

As non-linear space-charge forces are used to generate the uniform beam profile it was important to check whether the beam quality and uniformity is reduced by the typical variations present in a photoinjector. Therefore, scans of photoinjector parameters were performed to the tolerances experienced at CLEAR. The scans were performed for bunches of 50,000 macro-particles tracked in RF-Track without beam losses. The RF phase was scanned by $\pm 1^\circ$, the RF gradient in the gun by $\pm 1\%$, the bunch charge by $\pm 2\%$, the laser

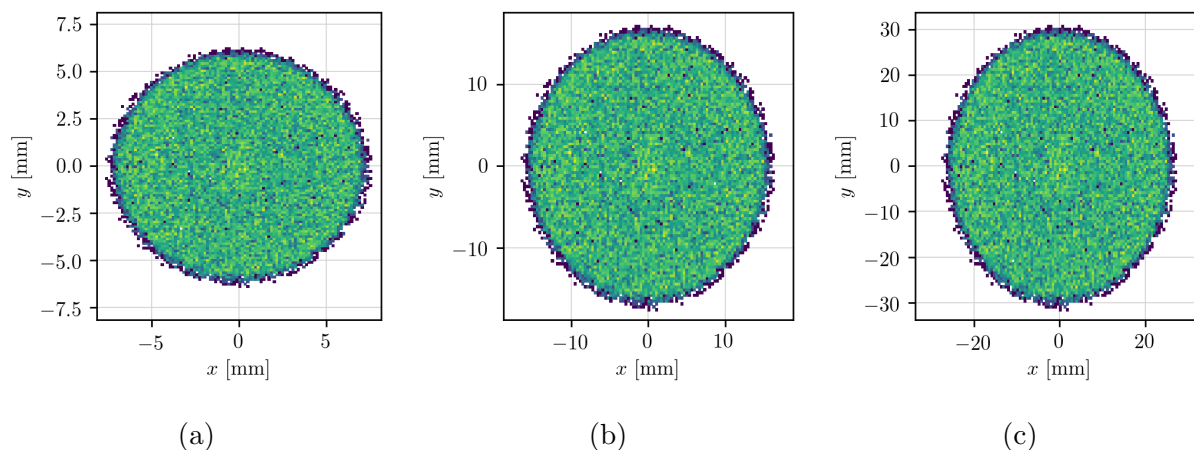


Figure 5.22: Transverse beam profiles for the large-beam optics measured (a) 0.1 m, (b) 0.5 m, and (c) 1.0 m, from the exit of the final quadrupole.

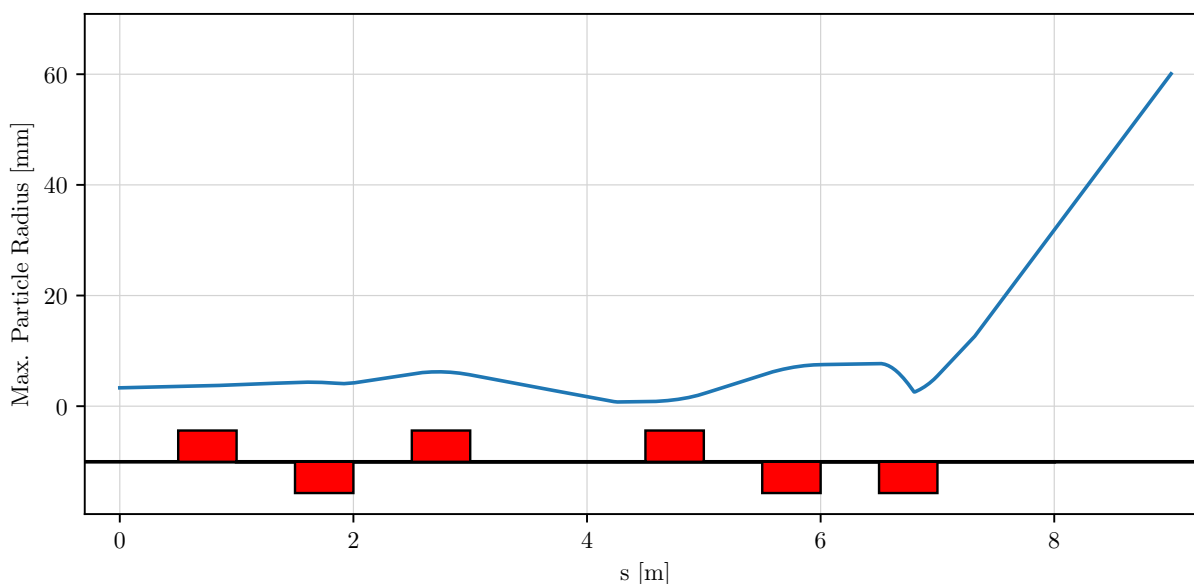


Figure 5.23: Maximum particle radius vs distance from the linac exit for the large beam optics.

spot size by $\pm 5\%$, and the laser pulse length by $\pm 10\%$. A small linear response to these variations was seen at the exit of the linac for the parameters shown in Table 5.1, as well as the beam size, and kurtosis at the projected angle in phase space. The maximum variation in each of these parameters across the variation range is shown in Table 5.2. In most cases the percentage change in the beam parameters was lower than the magnitude of the variation. The largest effects were seen on the beam size at the exit of the linac. Any changes in beam size could produce beam losses and, therefore, should be investigated further. The beam uniformity was assessed across the same angle in phase space as the nominal bunch. The

kurtosis of the bunch was recorded at this angle. No significant changes in the kurtosis were demonstrated. To demonstrate the effect that these variations at the linac exit would have on the final beam profile, the variation tracking should be performed from the photocathode through the entire matching section to the target.

| Parameter | Variation | Energy | ΔE | $\epsilon_{x,n}$ | l_z | $\sigma_{x,rms}$ | $K_{x,y}$ |
|------------------------|---------------------|---------|------------|------------------|-------|------------------|-----------|
| $\Delta\phi_{gun}$ | $\pm 1^\circ$ | 0.001 % | 0.01 % | 0.15 % | 0.8 % | 1.0 % | 0.02 % |
| ΔE_{gun} | ± 1.0 % | 0.06 % | 0.005 % | 0.4 % | 0.5 % | 4.0 % | 1.5 % |
| ΔQ_{bunch} | ± 2.0 % | 1.0 % | 0.005 % | 1.5 % | 0.3 % | 0.3 % | 0.15 % |
| $\Delta\sigma_{laser}$ | ± 5.0 % | 0.03 % | 0.02 % | 2.0 % | 1.0 % | 7.0 % | 0.8 % |
| Δt_{laser} | ± 0.1 ps (10 %) | 0.03 % | 0.09 % | 2.5 % | 6.0 % | 4.0 % | 1.0 % |

Table 5.2: Maximum amplitude of variations of beam parameters across a specified variation tolerance.

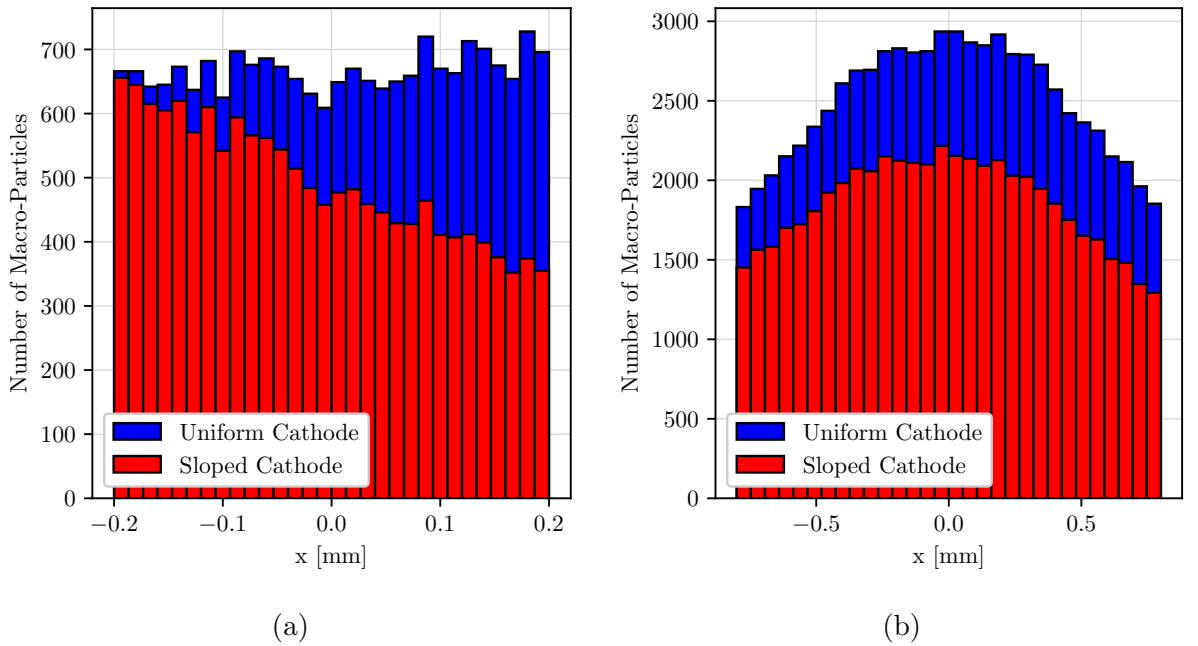


Figure 5.24: Beam profiles of bunches produced on photocathode with a uniform quantum efficiency, and one produced with a quantum efficiency with a 50% gradient for (a) a uniform, and (b) a Gaussian laser spot.

As the source photocathodes are unlikely to have a uniform quantum efficiency the effect of cathode non-uniformities was investigated. As the beam is produced in the high space-charge regime, the effect of cathode non-uniformities is likely to be suppressed. If an area of low quantum efficiency produces a lower number of electrons the charge density will be lower in this area. As the charge density is lower, electrons from areas of higher charge density will quickly flow into that area resulting in a smooth distribution. To investigate

the effect of photocathode non-uniformities, a cathode with a quantum efficiency that varied linearly, from high to low, was simulated. To model this “sloped cathode”, an initial Gaussian distribution of 100,000 particles was generated. The beam profile in x was split into 1000 bins. A fraction of the particles were then removed from each bin. No particles were removed from the first bin, and up to 50% of particles were removed from the final bin. Particles were removed from the bins between the first and last such that the number removed varied linearly between the first and last. The charge of the remaining distribution was then normalised to 0.4 nC. Figure 5.24a shows a uniform distribution modelled with a sloped cathode, with no particles removed from the first bin and 50% of particles removed from the final bin.

As most of the particles in a Gaussian distribution are located within $\pm 1\sigma$ the effect of a sloped quantum efficiency is less pronounced. A slice of the particle distribution for a 0.8 mm laser spot and a quantum efficiency slope of 50% is shown in Figure 5.24b. The effect of the change in quantum efficiency is most visible over the tails and not the core. Because of this, the effect on the beam uniformity and size at the entrance to the linac is very small, as shown in Figure 5.25. The kurtosis of the beam is similar to the nominal case. When tracked through the linac the effect on the beam parameters is very small. For a 50% gradient in quantum efficiency the emittance is 0.8% higher than a uniform cathode, the beam spot is 1% smaller, and the kurtosis along the projected angle in phase space is 0.3% higher. As any effects caused by non-uniform cathodes are likely to be static over each operating period any changes could be corrected when the beam is set up.

5.5 Summary

Generating electron beams with uniform beam profiles would be useful in irradiation facilities and for VHEE-RT. It has previously been shown that by using lasers with ultra-short pulses or transversely shaped profiles, uniform beams can be produced in FEL facilities to provide beams with low emittance.

By using a modified version of the CLEAR photoinjector it was shown that it is possible to produce beams that have a uniform beam profile with a Gaussian laser spot and picosecond laser pulse. By selecting the parameters of the photoinjector carefully the space-charge

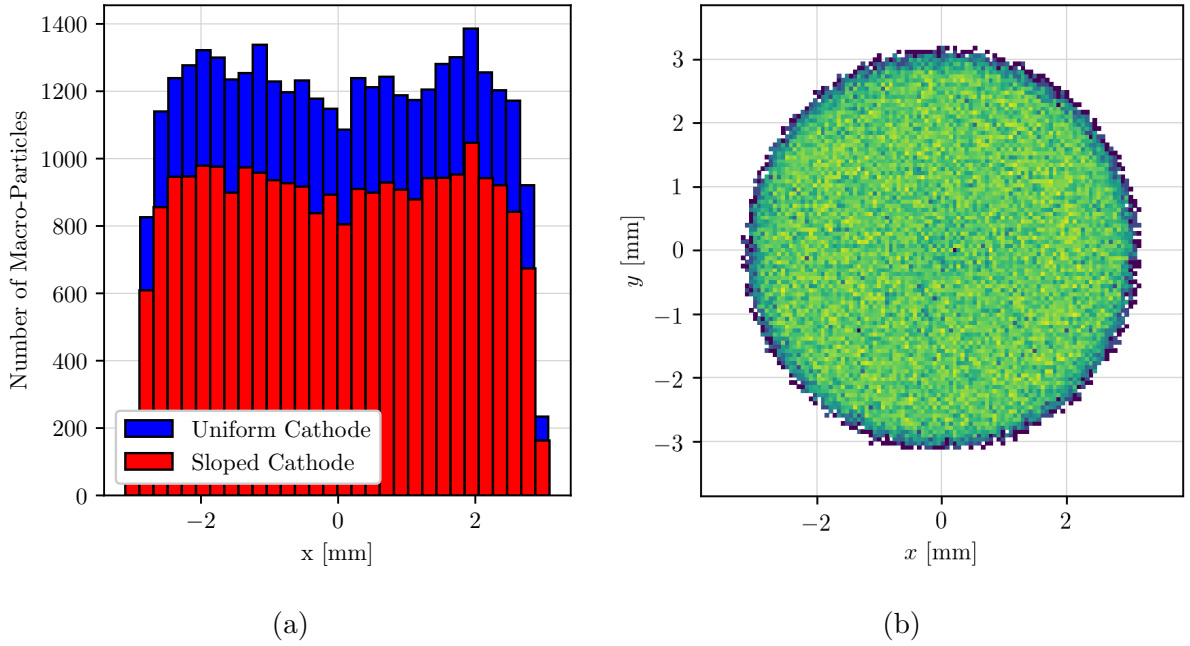


Figure 5.25: **(a)** Particle distributions in x across a slice in y of width $\pm\sigma_y/4$ measured at a distance of 1.2 m from the photocathode for bunches produced with a uniform cathode and a cathode with a 50% slope in quantum efficiency. **(b)** The transverse profile for a bunch produced from a cathode with a 50% slope in quantum efficiency at a distance of 1.2 m.

forces could be balanced in order to create a uniform transverse distribution. The level of uniformity at different distances could be controlled by altering the parameters of the photoinjector, particularly the focusing strength of the solenoid magnet. It was proposed that by rapidly accelerating a uniform bunch it would be possible to stop the space-charge evolution of the bunch, and allow a uniform bunch to be produced at high energy.

To investigate the possibility of producing a high-energy uniform bunch, a simple irradiation facility was proposed. The facility consists of the CLEAR photoinjector followed by eight X-band accelerating structures similar to the type used for CLIC. The accelerator was then followed by two quadrupole triplets which were able to match the beam to uniform distributions at a target.

An optimisation of the irradiation facility was undertaken. To prevent RF focusing forces from distorting the beam whilst at low energy, the beam was set to be diverging at the entrance to the first X-band structure. The beam was tracked to the end of the X-band accelerator to an energy of 100 MeV. It was shown that at the exit of the linac there indeed was an angle in phase space that had a uniform profile.

The quadrupole matching section was then optimised in order to reclaim this uniform profile. By doing this, uniform bunches of three different diameters were achieved at a distance of 0.3 m from the exit of the final quadrupole. It was shown that the beam remains uniform with distance from the photocathode which could be used to alter the beam size incident upon a target or collimate the beam to a required shape.

As producing a uniform beam profile relies on non-linear space-charge forces, the stability against typical variations present in a photoinjector was investigated. The change in beam parameters seen was proportional to the variation. The magnitude of the changes to beam parameters was mostly smaller than the magnitude of the variation itself. In addition, the effects of photocathode non-uniformities were investigated. As the bunches are produced in a high space-charge regime, the effect of these photocathode non-uniformities was shown to be minimal.

As this proposed beamline was a proof of concept beamline rather than a finalised design, further analysis of its design should be undertaken. The new analysis should target further optimisation of the gun and linac, as well as the matching section following the linac. The current design of the matching section is of a similar length to the linac and injector combined. Therefore, work should be done to produce a more compact beamline. In addition, scattering effects should be investigated around the target to ascertain whether scattering from the air or a vacuum window reduces the beam uniformity.

Furthermore, the optimisation presented was performed for a single bunch, of a single charge, accelerated to a single energy. Therefore, further energies and bunch charges should be investigated. In addition the same investigations should be repeated for bunch trains of different lengths.

Following a finalisation of the machine design, full start-to-end simulations of beam variations should be performed. Particular focus should be to investigate the effect on the beam at the target location. Additional imperfections, such as the misalignment of components or variations in the linac and matching section, should also be investigated. Variations may cause losses in the linac and should, therefore, be investigated.

Chapter 6

Conclusions

6.1 Summary

Significant developments in the understanding of particle physics have occurred in the past century. A large number of these developments have been produced in particle colliders, with the highest energy being the LHC. It is widely acknowledged that if there is to be a new particle collider the most likely candidate would be an e^+e^- collider for use as a Higgs factory. CLIC is one of several proposed designs for an e^+e^- collider. CLIC would use compact, X-band cavities which would operate at high acceleration gradients. The research effort undertaken for CLIC has begun to allow the use of high-gradient accelerating structures and technology for other applications. Projects are underway to use CLIC technology in several facilities such as: DEFT, to perform VHEE-RT and potentially induce the FLASH effect; CompactLight, a compact free electron laser, and the eSPS which would be used to search for light dark matter.

The CLEAR user facility was developed from the CLIC test facility, CTF3. Since 2017 CLEAR has provided beams for a wide range of user experiments. The parameters of the beams provided are tuned to the individual needs of each experiment. One of the most commonly requested beam parameters is to have bunches of less than 1 ps in length. Bunches of this length were previously only available for low charges, of charge up to 0.1 nC. Using an ASTRA model of the CLEAR beamline it was demonstrated that it should be possible to produce bunches of less than 1 ps in length for charges up to 2 nC using the velocity bunching technique. Additionally it was shown that by tuning the solenoid magnets it is possible to suppress the emittance growth that occurs during compression. The ability to compress

high-charge bunches by velocity bunching was confirmed experimentally, with bunches up to 0.8 nC compressed to lengths of less than 1 ps. Furthermore it was shown that by reducing the phase of the RF gun bunches of charge 0.5 nC could be compressed to lengths of 0.2 ps.

Upgrades to the CLEAR facility were proposed and investigated using ASTRA. It was demonstrated that by installing a new laser system with pulse lengths as short as 1 ps it would be possible to reduce the minimum bunch length achievable by up to 60%. The beam quality was not significantly affected by such an upgrade, with any emittance growth suppressed with minor changes to the power supply of the gun solenoid. A new laser may also be more stable than the present system and be able to operate at a higher repetition rate.

Additionally the installation of a new klystron was proposed which would allow the gun to operate with an accelerating field gradient as well as allow the bunching cavity to operate at a lower gradient. By increasing the gun field it would be possible to extract more charge from the gun, particularly from smaller laser spot sizes. Although the minimum bunch length achievable when a high field is used would be longer than that for a low field for all but the very highest bunch charges generated from smaller laser spots. By reducing the field present in the buncher it would be possible, however, to reduce the minimum bunch length by $\sim 20\%$. Additionally, the minimum beam energy available to users would be reduced from 60 MeV to 30 MeV.

As the beams produced by CLEAR have Gaussian-like transverse profiles the dose delivered to an irradiation experiment is non-uniform. It was shown that a modified version of the CLEAR photoinjector could be used to produce uniform transverse profiles using space-charge forces only. The distance at which the beam had a uniform profile could be varied by only changing the strength of the solenoid magnet. A compact irradiation facility was proposed, using the CLEAR photoinjector followed by eight high-gradient X-band cavities similar to those proposed for CLIC, to accelerate the uniform beam, thereby preventing the space-charge induced evolution in transverse phase space. The parameters of this facility were optimised and it was shown that a quadrupole matching section could be installed at the end of the linac to produce uniform beam profiles of various sizes. It was shown that the effect used in these simulations was stable to the typical variations seen in CLEAR as well as to cathode non-uniformities.

6.2 Future Work

Beams that are compressed to short bunch lengths are regularly used on CLEAR. However, further experimental work should be done to compress higher-charge bunches than has been shown in this thesis. Furthermore, the stability of the beam should be improved with feedback systems in order to aid the comparison of experiment to simulation.

The three upgrades presented in this thesis should be combined in simulation. By using a higher gun field it may be easier to extract more charge for shorter laser pulse lengths. It may also allow the extraction of higher-charge bunches at lower RF phases. Therefore, this should also be investigated.

Further upgrades to the CLEAR facility should be investigated. The beam dynamics of the new electron source should be characterised and the configuration to which it will be installed finalised, either as part of the existing facility or as a new beamline. A second experimental beamline branching off via a dogleg bend should be studied. The optics of this should be assessed and the layout optimised. Furthermore, the dynamics of the beam through the X-band cavity installed on the CLEAR beamline should be studied before it is connected to a klystron.

The design of the proposed irradiation facility in Chapter 5 should be optimised further. The optimisation should target different bunch charges and characteristics. The optical matching section following the linac should be a particular target of this optimisation, aiming to reduce its physical size. In addition, multi-bunch effects should be studied and included in the optimisation. When this optimisation is mature, further work should be undertaken into the stability of the beamline. Variations should be tracked from the photocathode to the target. Additional misalignments and variations must also be investigated and beam losses caused by variations should be studied.

Bibliography

- [1] Paul H. Frampton and Jihn E. Kim. *History of particle theory: Between Darwin and Shakespeare*. World Scientific Publishing Co., Jan. 2020, pp. 1–213. ISBN: 9789811224669. DOI: 10.1142/11948.
- [2] J.J. Thomson. “Cathode Rays”. In: *Philosophical Magazine* 44 (1897), pp. 293–316.
- [3] J.J. Thomson. “On the Structure of the Atom”. In: *Philosophical Magazine* 6 7 (1904), pp. 237–265. DOI: 10.1080/14786440409463107.
- [4] E. Rutherford. “The scattering of α and β particles by matter and the structure of the atom ”. In: *The London, Edinburgh, and Dublin Philosophical Magazine and Journal of Science* 21.125 (May 1911), pp. 669–688. ISSN: 1941-5982. DOI: 10.1080/14786440508637080.
- [5] Ernest Rutherford. “Collisions of α Particles with Light Atoms. IV. An Anomalous Effect in Nitrogen.” In: *The London, Edinburgh and Dublin Philosophical Magazine and Journal of Science, 6th series* 37 (1919), p. 581. URL: <https://web.lemoyne.edu/~giunta/rutherford.html>.
- [6] J. Chadwick. “Possible existence of a neutron”. In: *Nature* 129.3252 (Feb. 1932), p. 312. ISSN: 00280836. DOI: 10.1038/129312a0. URL: <https://www.nature.com/articles/129312a0>.
- [7] J Chadwick. “The existence of a neutron”. In: *Proceedings of the Royal Society of London. Series A, Containing Papers of a Mathematical and Physical Character* 136.830 (June 1932), pp. 692–708. ISSN: 0950-1207. DOI: 10.1098/rspa.1932.0112.
- [8] Fayyazuddin and Riazuddin. *A modern introduction to particle physics, third edition*. World Scientific Publishing Co., Jan. 2011, pp. 1–657. ISBN: 9789814338851. DOI: 10.1142/8064.
- [9] K. Kodama et al. “Observation of tau neutrino interactions”. In: *Physics Letters, Section B: Nuclear, Elementary Particle and High-Energy Physics* 504.3 (Apr. 2001), pp. 218–224. ISSN: 03702693. DOI: 10.1016/S0370-2693(01)00307-0.
- [10] Peter W. Higgs. “Broken symmetries and the masses of gauge bosons”. In: *Physical Review Letters* 13.16 (Oct. 1964), pp. 508–509. ISSN: 00319007. DOI: 10.1103/PhysRevLett.13.508. URL: <https://journals.aps.org/prl/abstract/10.1103/PhysRevLett.13.508>.
- [11] ATLAS Collaboration. “Observation of a new particle in the search for the Standard Model Higgs boson with the ATLAS detector at the LHC”. In: *Phys.Lett.* B716 (2012), pp. 1–29. DOI: 10.1016/j.physletb.2012.08.020.

- [12] S. Chatrchyan et al. “Observation of a new boson at a mass of 125 GeV with the CMS experiment at the LHC”. In: *Physics Letters, Section B: Nuclear, Elementary Particle and High-Energy Physics* 716.1 (Sept. 2012), pp. 30–61. ISSN: 03702693. DOI: 10.1016/j.physletb.2012.08.021.
- [13] P A Zyla et al. “Review of Particle Physics”. In: *PTEP* 2020.8 (2020), p. 083C01. DOI: 10.1093/ptep/ptaa104.
- [14] Gianfranco Bertone, Dan Hooper, and Joseph Silk. “Particle dark matter: Evidence, candidates and constraints”. In: *Phys. Rept.* 405 (2005), pp. 279–390. DOI: 10.1016/j.physrep.2004.08.031.
- [15] Lawrence M. Krauss, Salah Nasri, and Mark Trodden. “Model for neutrino masses and dark matter”. In: *Physical Review D - Particles, Fields, Gravitation and Cosmology* 67.8 (Apr. 2003), p. 085002. ISSN: 15502368. DOI: 10.1103/PhysRevD.67.085002. URL: <https://journals.aps.org/prd/abstract/10.1103/PhysRevD.67.085002>.
- [16] Laurent Canetti, Marco Drewes, and Mikhail Shaposhnikov. “Matter and antimatter in the universe”. In: *New Journal of Physics* 14 (2012), p. 95012. DOI: 10.1088/1367-2630/14/9/095012. URL: <http://www.njp.org/>.
- [17] Helmut Wiedemann. *Particle Accelerator Physics*. Graduate Texts in Physics. Cham: Springer International Publishing, Jan. 2015. ISBN: 978-3-319-18316-9. DOI: 10.1007/978-3-319-18317-6. URL: <http://link.springer.com/10.1007/978-3-319-18317-6>.
- [18] E. Wilson and B. J. Holzer. “Beam Dynamics”. In: *Particle Physics Reference Library*. Springer International Publishing, 2020, pp. 15–50. URL: <http://cds.cern.ch/record/2743947>.
- [19] Oliver Bruning et al. *LHC Design Report*. Tech. rep. 2004. DOI: 10.5170/CERN-2004-003-V-1. URL: <https://cds.cern.ch/record/782076>.
- [20] G Apollinari et al. “High-Luminosity Large Hadron Collider (HL-LHC) Preliminary Design Report”. In: (2015). DOI: 10.5170/CERN-2015-005. URL: <http://dx.doi.org/10.5170/CERN-2015-005>.
- [21] *LEP design report*. Vol. CERN-LEP-84-01. Geneva: CERN, 1983. URL: <http://cds.cern.ch/record/98881>.
- [22] Alain Blondel and Frank Zimmermann. “A High Luminosity e+e- Collider in the LHC tunnel to study the Higgs Boson”. In: (Dec. 2011). URL: <http://arxiv.org/abs/1112.2518>.
- [23] C. Adolphsen et al. *European Strategy for Particle Physics – Accelerator R&D Roadmap*. Vol. CERN-2022-001. Jan. 2022. ISBN: 9789290836216. DOI: 10.23731/CYRM-2022-001. URL: <https://cds.cern.ch/record/2800190>.
- [24] Hiroaki Aihara et al. *The International Linear Collider. A Global Project*. Vol. SLAC-PUB-17412. Jan. 2019. URL: <http://arxiv.org/abs/1901.09829>.
- [25] M Aicheler et al. *A Multi-TeV Linear Collider Based on CLIC Technology*. Ed. by M Aicheler. Vol. CERN-2021-007. CERN, 2012. DOI: 10.5170/CERN-2012-007.
- [26] The CLIC et al. *Updated baseline for a staged Compact Linear Collider*. Vol. CERN-2016-004. Aug. 2016. DOI: 10.5170/CERN-2016-004. URL: <http://dx.doi.org/10.5170/CERN-2016-004>.

- [27] Aidan Robson et al. *The Compact Linear $e+e-$ Collider (CLIC): Accelerator and Detector*. Vol. CLICdp-Note-2018-009. Dec. 2018. URL: <https://cds.cern.ch/record/2652255?ln=en>.
- [28] Lyn Evans and Shinichiro Michizono. *The International Linear Collider Machine Staging Report 2017*. Tech. rep. KEK-2017-3, 2017. URL: <https://cds.cern.ch/record/2293461/>.
- [29] A. Abada et al. “FCC-ee: The Lepton Collider: Future Circular Collider Conceptual Design Report Volume 2”. In: *European Physical Journal: Special Topics* 228.2 (June 2019), pp. 261–623. ISSN: 19516401. DOI: 10.1140/epjst/e2019-900045-4. URL: <https://doi.org/10.1140/epjst/e2019-900045-4>.
- [30] The CEPC Accelerator Study Group. “The CEPC input for the European Strategy for Particle Physics - Accelerator”. In: (Jan. 2019). URL: <http://arxiv.org/abs/1901.03169>.
- [31] The CEPC Study Group. “CEPC Conceptual Design Report: Volume 1 - Accelerator”. In: (Sept. 2018). DOI: 10.48550/arxiv.1809.00285. URL: <https://arxiv.org/abs/1809.00285v1>.
- [32] A. Abada et al. “FCC-hh: The Hadron Collider: Future Circular Collider Conceptual Design Report Volume 3”. In: *European Physical Journal: Special Topics* 228.4 (July 2019), pp. 755–1107. ISSN: 19516401. DOI: 10.1140/epjst/e2019-900087-0.
- [33] Aidan Robson and Philipp Roloff. *Updated CLIC luminosity staging baseline and Higgs coupling prospects*. Vol. CLICdp-Note-2018-002. Dec. 2018. URL: <http://arxiv.org/abs/1812.01644>.
- [34] *Accelerator Overview — CLIC - Compact Linear Collider*. URL: <https://clic.cern/accelerator-overview>.
- [35] J. de Blas et al. *The CLIC potential for new physics*. Tech. rep. Dec. 2018. DOI: 10.23731/CYRM-2018-003. URL: <https://doi.org/10.23731/CYRM-2018-003>.
- [36] H. Abramowicz et al. “Higgs physics at the CLIC electron–positron linear collider”. In: *European Physical Journal C* 77.7 (July 2017), p. 475. ISSN: 14346052. DOI: 10.1140/epjc/s10052-017-4968-5. URL: <https://link.springer.com/article/10.1140/epjc/s10052-017-4968-5>.
- [37] H Abramowicz et al. “Published for SISSA by Springer Top-quark physics at the CLIC electron-positron linear collider The CLICdp collaboration”. In: *JHEP11* (2019), p. 3. DOI: 10.1007/JHEP11(2019)003. URL: <https://doi.org/10.1007/JHEP11>.
- [38] D. Allard et al. *CTF3 Design Report Preliminary Phase*. Vol. CERN-PS-2001-072-RF. Dec. 2001. URL: <https://cds.cern.ch/record/531815>.
- [39] R. Ruber et al. “The CTF3 Two-beam Test Stand”. In: *Nuclear Instruments and Methods in Physics Research, Section A: Accelerators, Spectrometers, Detectors and Associated Equipment* 729 (Nov. 2013), pp. 546–553. ISSN: 01689002. DOI: 10.1016/j.nima.2013.07.055.
- [40] R Zennaro. *Study of the machining and assembly tolerances for the CLIC accelerating structures*. Tech. rep. 2009. URL: [https://www.eurotev.org/reports_ _presentations/eurotev_reports/2008/e1532/EUR0TeV-Report-2008-081.pdf](https://www.eurotev.org/reports/_presentations/eurotev_reports/2008/e1532/EUR0TeV-Report-2008-081.pdf).

- [41] Helene Mainaud Durand et al. *Fiducialisation and initial alignment of CLIC component with micrometric accuracy*. Dec. 2016. URL: <https://cds.cern.ch/record/2237694>.
- [42] Chetan Gohil et al. *High-Luminosity CLIC Studies*. Vol. CERN-ACC-2019-0051. Aug. 2020. URL: <https://cds.cern.ch/record/2687090?ln=en>.
- [43] C. Gohil et al. “Luminosity performance of the Compact Linear Collider at 380 GeV with static and dynamic imperfections”. In: *Physical Review Accelerators and Beams* 23.10 (Oct. 2020), p. 101001. ISSN: 24699888. DOI: 10.1103/PhysRevAccelBeams.23.101001. URL: <https://journals.aps.org/prab/abstract/10.1103/PhysRevAccelBeams.23.101001>.
- [44] *FLASH radiation therapy: From biological research to a clinical facility (26 April 2021)*. Indico. URL: <https://indico.cern.ch/event/975980/>.
- [45] Torsten Åkesson. *A primary electron beam facility at CERN-eSPS Conceptual design report*. Vol. CERN-2020-008. 2020. ISBN: 9789290835844. DOI: 10.23731/CYRM-2020-008. URL: <https://doi.org/10.23731/CYRM-2020-008>.
- [46] Andrea Latina et al. “CompactLight Design Study”. In: *Proc. 60th ICFA Advanced Beam Dynamics Workshop (FLS’18), Shanghai, China, 5-9 March 2018*. JACOW Publishing, Geneva, Switzerland, June 2018, pp. 85–88. ISBN: 978-3-95450-206-6. DOI: 10.18429/JACOW-FLS2018-WEP1WC02. URL: <http://accelconf.web.cern.ch/AccelConf/fls2018/export/WEP1WC02-bib.htm>.
- [47] G. D’Auria et al. “Status of the compactlight design study”. In: *Proceedings of the 39th International Free-Electron Laser Conference, FEL 2019*. JACoW Publishing, 2019, pp. 738–741. ISBN: 9783954502103. DOI: 10.18429/JACoW-FEL2019-THP078.
- [48] M. Ferrario et al. “EuPRAXIA@SPARC.LAB Design study towards a compact FEL facility at LNF”. In: *Nuclear Instruments and Methods in Physics Research, Section A: Accelerators, Spectrometers, Detectors and Associated Equipment (2018)*. ISSN: 01689002. DOI: 10.1016/j.nima.2018.01.094.
- [49] X. F. D. Stragier, P. H. A. Mutsaers, and O. J. Luiten. “Smart*Light: A Tabletop, High Brilliance, Monochromatic and Tunable Hard X-ray Source for Imaging and Analysis.” In: *Microscopy and Microanalysis* 24.S2 (Aug. 2018), pp. 314–315. ISSN: 1431-9276. DOI: 10.1017/s1431927618013880. URL: <https://doi.org/10.1017/S1431927618013880>.
- [50] P. Craievich et al. “Novel X -band transverse deflection structure with variable polarization”. In: *Physical Review Accelerators and Beams* 23.11 (Nov. 2020), p. 112001. ISSN: 24699888. DOI: 10.1103/PhysRevAccelBeams.23.112001. URL: <https://journals.aps.org/prab/abstract/10.1103/PhysRevAccelBeams.23.112001>.
- [51] B. Marchetti et al. “Experimental demonstration of novel beam characterization using a polarizable X-band transverse deflection structure”. In: *Scientific Reports* 11.1 (Dec. 2021), p. 3560. ISSN: 20452322. DOI: 10.1038/s41598-021-82687-2. URL: <https://doi.org/10.1038/s41598-021-82687-2>.
- [52] M. Aicheler et al. “The Compact Linear Collider (CLIC) - Project Implementation Plan”. In: (Mar. 2019). DOI: 10.23731/CYRM-2018-004. URL: <http://arxiv.org/abs/1903.08655>
<http://dx.doi.org/10.23731/CYRM-2018-004>.

- [53] D Gamba et al. “The CLEAR user facility at CERN”. In: *Nucl. Instrum. Meth.* (2018). DOI: 10.1016/j.nima.2017.11.080.
- [54] R Corsini et al. “First Experiments at the CLEAR User Facility”. In: *Proc. 9th International Particle Accelerator Conference (IPAC’18), Vancouver, BC, Canada, Apr. 4.* JACOW Publishing, Geneva, Switzerland, June 2018, p. 4066. DOI: 10.18429/JACoW-IPAC2018-THPMF014.
- [55] K N Sjobak et al. “Status of the CLEAR Electron Beam User Facility at CERN”. In: *Proc. 10th International Particle Accelerator Conference (IPAC’19), Melbourne, Australia, 19-24 May 2019.* 2019. ISBN: 9783954502080. DOI: 10.18429/JACoW-IPAC2019-MOPTS054.
- [56] L.A. Dyks. *The CLEAR User Facility at CERN.* Dec. 2021. URL: <https://indico.cern.ch/event/1101548/#14-clear-report>.
- [57] M Tali et al. “High-Energy Electron-Induced SEUs and Jovian Environment Impact”. In: *IEEE Transactions on Nuclear Science* 64 (2017), p. 2016.
- [58] Maris Tali et al. “Mechanisms of Electron-Induced Single-Event Upsets in Medical and Experimental Linacs”. In: *IEEE Transactions on Nuclear Science* 65.8 (Aug. 2018), pp. 1715–1723. ISSN: 00189499. DOI: 10.1109/TNS.2018.2843388.
- [59] Maris Tali et al. “Mechanisms of electron-induced single-event latchup”. In: *IEEE Transactions on Nuclear Science* 66.1 (Jan. 2019), pp. 437–443. ISSN: 00189499. DOI: 10.1109/TNS.2018.2884537.
- [60] Daniel Soderstrom et al. “Electron-Induced Upsets and Stuck Bits in SDRAMs in the Jovian Environment”. In: *IEEE Transactions on Nuclear Science* 68.5 (May 2021), pp. 716–723. ISSN: 15581578. DOI: 10.1109/TNS.2021.3068186.
- [61] Andrea Coronetti et al. “SEU characterization of commercial and custom-designed SRAMs based on 90 nm technology and below”. In: *IEEE Radiation Effects Data Workshop.* Vol. 2020-November. Institute of Electrical and Electronics Engineers Inc., Nov. 2020. ISBN: 9780738110851. DOI: 10.1109/REDW51883.2020.9325822.
- [62] Andrea Coronetti. *Irradiation Activities in CLEAR - CLEAR Review (16 March 2021)* · Indico. 2021. URL: <https://indico.cern.ch/event/1015632/#4-irradiation-activities-in-cl>.
- [63] Pasquale Arpaia et al. “Beam-based alignment of the CLIC high-gradient X-Band accelerating structure using beam-screen”. In: *I2MTC 2019 - 2019 IEEE International Instrumentation and Measurement Technology Conference, Proceedings.* Vol. 2019-May. May 2019. ISBN: 9781538634608. DOI: 10.1109/I2MTC.2019.8827121. URL: <https://cds.cern.ch/record/2751634>.
- [64] Antonio Gilardi. “Measurements of wakefields and bunch length with beam in linear electron accelerators: a case study at the CLEAR facility”. PhD thesis. 2021. URL: <https://cds.cern.ch/record/2766988>.
- [65] *CLIC Workshop 2019 (21-25 January 2019): Tests of Wakefield Monitors at CLEAR* · Indico. 2019. URL: <https://indico.cern.ch/event/753671/contributions/3285765/>.
- [66] J R Towler et al. “Development and Test of High-Resolution Cavity BPMs for the CLIC Main Beam Linac”. In: *Proceedings of IBIC2015, Melbourne, Australia.* 2015. ISBN: 9783954501762. DOI: DOI:10.18429/JACoW-IBIC2015-TUPB060.

- [67] *CLIC Workshop 2019 (21-25 January 2019): An acquisition system for cavity BPM* · Indico. URL: <https://indico.cern.ch/event/753671/contributions/3272592/>.
- [68] R. Corsini et al. “Status of VHEE Radiotherapy Related Studies at the CLEAR User Facility at CERN”. In: *Proceedings of IPAC2021* (Aug. 2021), pp. 2704–2707. DOI: 10.18429/JACoW-IPAC2021-WEPAB044.
- [69] L.A. Dyks et al. *HSE Occupational Health & Safety and Environmental Protection Preliminary irradiation tests of surgical masks with 200 MeV electrons at CLEAR*. Tech. rep. Geneva: CERN, Feb. 2021.
- [70] Thibaut Lefevre. *Diagnostics and THz Activites - CLEAR Review (7 February 2019)* · Indico. URL: <https://indico.cern.ch/event/781404/#5-diagnostics-and-thz-activiti>.
- [71] Stefano Mazzone. *Beam Diagnostics R&D - CLEAR Review (16 March 2021)* · Indico. 2021. URL: <https://indico.cern.ch/event/1015632/#9-beam-diagnostics-rd>.
- [72] R. Kieffer et al. “Experimental Observation of ”shadowing” in Optical Transition Radiation”. In: *Physical Review Letters* 120.9 (2018). ISSN: 10797114. DOI: 10.1103/PhysRevLett.120.094802.
- [73] D Alves et al. “Cherenkov Diffraction Radiation as a Tool for Beam Diagnostics”. In: *Proc. IBIC’19*. 2019. ISBN: 9783954502042. DOI: 10.18429/JACoW-IBIC2019-THA001.
- [74] Eugenio Senes. “Development of a beam position monitor for co-propagating electron and proton beams”. PhD thesis. 2020. URL: <http://cds.cern.ch/record/2753708>.
- [75] A. Curcio et al. “Noninvasive bunch length measurements exploiting Cherenkov diffraction radiation”. In: *Physical Review Accelerators and Beams* 23.2 (Feb. 2020), p. 22802. ISSN: 24699888. DOI: 10.1103/PhysRevAccelBeams.23.022802. URL: <https://journals.aps.org/prab/abstract/10.1103/PhysRevAccelBeams.23.022802>.
- [76] J.A. Clarke. *CLARA Conceptual Design Report*. Tech. rep. 2013. URL: <https://www.ukri.org/publications/clara-conceptual-design-report/>.
- [77] K Lasocha et al. “Feasibility Study of ChDR Diagnostic Device in the LHC”. In: *Proceedings of IPAC2021*. 2021, pp. 2139–2142. ISBN: 9783954502141. DOI: 10.18429/JACoW-IPAC2021-TUPAB283.
- [78] S Benítez et al. “Development and Testing of a Cherenkov Beam Loss Monitor In CLEAR Facility”. In: *Proceedings of IPAC2021*. JACOW Publishing, Geneva, Switzerland, Aug. 2021, pp. 2640–2643. ISBN: 9783954502141. DOI: 10.18429/JACoW-IPAC2021-WEPAB021.
- [79] E. Gschwendtner et al. “AWAKE, The Advanced Proton Driven Plasma Wakefield Acceleration Experiment at CERN”. In: *Nuclear Instruments and Methods in Physics Research, Section A: Accelerators, Spectrometers, Detectors and Associated Equipment* 829 (Sept. 2016), pp. 76–82. ISSN: 01689002. DOI: 10.1016/j.nima.2016.02.026.
- [80] Edda Gschwendtner. *AWAKE and Plasma Applications - CLEAR Review (16 March 2021)* · Indico. 2021. URL: <https://indico.cern.ch/event/1015632/#6-awake-and-plasma-application>.

- [81] J. Bauche et al. “A magnetic spectrometer to measure electron bunches accelerated at AWAKE”. In: *Nuclear Instruments and Methods in Physics Research, Section A: Accelerators, Spectrometers, Detectors and Associated Equipment* 940 (Oct. 2019), pp. 103–108. ISSN: 01689002. DOI: 10.1016/j.nima.2019.05.067. URL: <https://doi.org/10.1016/j.nima.2019.05.067>.
- [82] E Adli et al. “Acceleration of electrons in the plasma wakefield of a proton bunch”. In: *Nature* 562.18 (Aug. 2018), p. 485. DOI: 10.1038/s41586-018-0485-4. URL: <https://www.nature.com/articles/s41586-018-0485-4>.
- [83] R. Pan et al. “Electro-Optical Bunch Profile Measurement at CTF3”. In: *Proc. 4th Int. Particle Accelerator Conf. (IPAC'13)*. Shanghai, China, 2013, pp. 658–660.
- [84] L. A. Dyks et al. “Consolidation and Future Upgrades to the CLEAR User Facility at CERN”. In: *Proceedings of IPAC2021* (Aug. 2021), pp. 2700–2703. DOI: 10.18429/JACoW-IPAC2021-WEPAB043.
- [85] C. A. Lindstrøm et al. “Overview of the CLEAR plasma lens experiment”. In: *Nuclear Instruments and Methods in Physics Research, Section A: Accelerators, Spectrometers, Detectors and Associated Equipment* 909 (Nov. 2018), pp. 379–382. ISSN: 01689002. DOI: 10.1016/j.nima.2018.01.063.
- [86] A. E. Dyson, C. Thornton, and S. M. Hooker. “A compact, low cost Marx bank for generating capillary discharge plasmas”. In: *Review of Scientific Instruments* 87.9 (Sept. 2016), p. 093302. ISSN: 0034-6748. DOI: 10.1063/1.4961913. URL: <https://aip.scitation.org/doi/abs/10.1063/1.4961913>.
- [87] C. A. Lindstrøm et al. “Emittance Preservation in an Aberration-Free Active Plasma Lens”. In: *Physical Review Letters* 121.19 (Nov. 2018), p. 194801. ISSN: 10797114. DOI: 10.1103/PhysRevLett.121.194801. URL: <https://journals.aps.org/prl/abstract/10.1103/PhysRevLett.121.194801>.
- [88] K. N. Sjobak et al. “Strong focusing gradient in a linear active plasma lens”. In: *Physical Review Accelerators and Beams* 24.12 (Dec. 2021), p. 121306. ISSN: 2469-9888. DOI: 10.1103/PhysRevAccelBeams.24.121306. URL: <https://link.aps.org/doi/10.1103/PhysRevAccelBeams.24.121306>.
- [89] B Green et al. “High-Field High-Repetition-Rate Sources for the Coherent THz Control of Matter”. In: (2016). DOI: 10.1038/srep22256. URL: www.nature.com/scientificreports/.
- [90] A. Curcio et al. “Beam-based sub-THz source at the CERN linac electron accelerator for research facility”. In: *Physical Review Accelerators and Beams* 22.2 (Feb. 2019), p. 020402. ISSN: 24699888. DOI: 10.1103/PhysRevAccelBeams.22.020402. URL: <https://journals.aps.org/prab/abstract/10.1103/PhysRevAccelBeams.22.020402>.
- [91] A. Curcio et al. “Diffractive shadowing of coherent polarization radiation”. In: *Physics Letters, Section A: General, Atomic and Solid State Physics* 391 (Mar. 2021). ISSN: 03759601. DOI: 10.1016/j.physleta.2020.127135.
- [92] Michele Blago. “Convolutional neural networks and photonic crystals for particle identification at high energy collider experiments”. PhD thesis. Cambridge: University of Cambridge, 2021. URL: <https://doi.org/10.17863/CAM.78867>.

- [93] Luca Labate et al. “Toward an effective use of laser-driven very high energy electrons for radiotherapy: Feasibility assessment of multi-field and intensity modulation irradiation schemes”. In: *Scientific Reports* 10.1 (Dec. 2020), p. 17307. ISSN: 20452322. DOI: 10.1038/s41598-020-74256-w. URL: <https://www.nature.com/articles/s41598-020-74256-w>.
- [94] May Abdel-Wahab et al. “Global Radiotherapy: Current Status and Future Directions—White Paper”. In: *JCO Global Oncology* 7 (June 2021), pp. 827–842. ISSN: 26878941. DOI: 10.1200/go.21.00029. URL: <https://ascopubs.org/doi/10.1200/GO.21.00029>.
- [95] Maria Grazia Ronga et al. “Back to the future: Very high-energy electrons (vhees) and their potential application in radiation therapy”. In: *Cancers* 13.19 (Oct. 2021), p. 4942. ISSN: 20726694. DOI: 10.3390/cancers13194942. URL: <https://doi.org/10.3390/cancers13194942>.
- [96] Michael Goitein. *Radiation Oncology: A Physicist’s-Eye View*. Biological and Medical Physics, Biomedical Engineering. New York, NY: Springer New York, 2007. ISBN: 978-0-387-72644-1. DOI: 10.1007/978-0-387-72645-8. URL: <http://link.springer.com/10.1007/978-0-387-72645-8>.
- [97] Hermann Holthusen. “Erfahrungen über die Verträglichkeitsgrenze für Röntgenstrahlen und deren Nutzenanwendung zur Verhütung von Schäden”. In: *Strahlentherapie* 57.254 (1936), 51a.
- [98] William D. Bloomer and Samuel Hellman. “Normal Tissue Responses to Radiation Therapy”. In: *New England Journal of Medicine* 293.2 (July 1975), pp. 80–83. ISSN: 0028-4793. DOI: 10.1056/NEJM197507102930206. URL: <http://www.nejm.org/doi/abs/10.1056/NEJM197507102930206>.
- [99] Cyrus Chargari et al. “Optimize and refine therapeutic index in radiation therapy: Overview of a century”. In: *Cancer Treatment Reviews* 45 (Apr. 2016), pp. 58–67. ISSN: 15321967. DOI: 10.1016/j.ctrv.2016.03.001.
- [100] Agnese Lagzda et al. “Influence of heterogeneous media on Very High Energy Electron (VHEE) dose penetration and a Monte Carlo-based comparison with existing radiotherapy modalities”. In: *Nuclear Instruments and Methods in Physics Research, Section B: Beam Interactions with Materials and Atoms* 482 (Nov. 2020), pp. 70–81. ISSN: 0168583X. DOI: 10.1016/j.nimb.2020.09.008.
- [101] Samy Hanna. *RF Linear Accelerators for Medical and Industrial Applications*. 1st ed. Artech House, Mar. 2012. ISBN: 9781608070916.
- [102] Andrea Peeters et al. “How costly is particle therapy? Cost analysis of external beam radiotherapy with carbon-ions, protons and photons”. In: *Radiotherapy and Oncology* 95.1 (Apr. 2010), pp. 45–53. ISSN: 01678140. DOI: 10.1016/j.radonc.2009.12.002.
- [103] C. DesRosiers et al. “150-250 MeV electron beams in radiation therapy”. In: *Physics in Medicine and Biology* 45.7 (July 2000), pp. 1781–1805. ISSN: 00319155. DOI: 10.1088/0031-9155/45/7/306. URL: <https://iopscience.iop.org/article/10.1088/0031-9155/45/7/306%20https://iopscience.iop.org/article/10.1088/0031-9155/45/7/306/meta>.

- [104] K. Kokurewicz et al. “Focused very high-energy electron beams as a novel radiotherapy modality for producing high-dose volumetric elements”. In: *Scientific Reports* 9.1 (Dec. 2019), pp. 1–10. ISSN: 20452322. DOI: 10.1038/s41598-019-46630-w. URL: www.nature.com/scientificreports.
- [105] Karolina Kokurewicz et al. “An experimental study of focused very high energy electron beams for radiotherapy”. In: *Communications Physics* 4.1 (Dec. 2021), pp. 1–7. ISSN: 23993650. DOI: 10.1038/s42005-021-00536-0. URL: <https://www.nature.com/articles/s42005-021-00536-0>.
- [106] Agnese Lagzda. “VHEE Radiotherapy Studies at CLARA and CLEAR Facilities”. PhD thesis. 2019. URL: https://www.research.manchester.ac.uk/portal/files/156333514/FULL_TEXT.PDF.
- [107] L. Whitmore et al. “Focused VHEE (very high energy electron) beams and dose delivery for radiotherapy applications”. In: *Scientific Reports* 11.1 (Dec. 2021), p. 14013. ISSN: 20452322. DOI: 10.1038/s41598-021-93276-8. URL: <https://doi.org/10.1038/s41598-021-93276-8>.
- [108] A. Subiel et al. “Dosimetry of very high energy electrons (VHEE) for radiotherapy applications: Using radiochromic film measurements and Monte Carlo simulations”. In: *Physics in Medicine and Biology* 59.19 (Oct. 2014), pp. 5811–5829. ISSN: 13616560. DOI: 10.1088/0031-9155/59/19/5811. URL: <https://iopscience.iop.org/article/10.1088/0031-9155/59/19/5811%20https://iopscience.iop.org/article/10.1088/0031-9155/59/19/5811/meta>.
- [109] Rachel Delorme et al. “First theoretical determination of relative biological effectiveness of very high energy electrons”. In: *Scientific Reports* 11.1 (Dec. 2021), p. 11242. ISSN: 20452322. DOI: 10.1038/s41598-021-90805-3. URL: <https://doi.org/10.1038/s41598-021-90805-3>.
- [110] K. L. Small et al. “Evaluating very high energy electron RBE from nanodosimetric pBR322 plasmid DNA damage”. In: *Scientific Reports* 11.1 (Dec. 2021), p. 3341. ISSN: 20452322. DOI: 10.1038/s41598-021-82772-6. URL: <https://doi.org/10.1038/s41598-021-82772-6>.
- [111] Vincent Favaudon et al. “Ultrahigh dose-rate FLASH irradiation increases the differential response between normal and tumor tissue in mice”. In: *Science Translational Medicine* 6.245 (July 2014). ISSN: 19466242. DOI: 10.1126/scitranslmed.3008973. URL: <https://www.science.org/doi/abs/10.1126/scitranslmed.3008973>.
- [112] Marco Durante, Elke BräUer-Krisch, and Mark Hill. *Faster and safer? FLASH ultrahigh dose rate in radiotherapy*. 2018. DOI: 10.1259/bjr.20170628.
- [113] D. L. Dewey and J. W. Boag. “Modification of the oxygen effect when bacteria are given large pulses of radiation”. In: *Nature* 183.4673 (1959), pp. 1450–1451. ISSN: 00280836. DOI: 10.1038/1831450a0. URL: <https://www.nature.com/articles/1831450a0>.
- [114] C. D. Town. *Effect of high dose rates on survival of mammalian cells [9]*. 1967. DOI: 10.1038/215847a0. URL: <https://www.nature.com/articles/215847a0>.
- [115] R. J. Berry et al. “Survival of mammalian cells exposed to x rays at ultra-high dose-rates.” In: *The British journal of radiology* 42.494 (1969), pp. 102–107. ISSN: 00071285. DOI: 10.1259/0007-1285-42-494-102. URL: <https://pubmed.ncbi.nlm.nih.gov/4975207/>.

- [116] Pierre Montay-Gruel et al. “Irradiation in a flash: Unique sparing of memory in mice after whole brain irradiation with dose rates above 100 Gy/s”. In: *Radiotherapy and Oncology* 124.3 (Sept. 2017), pp. 365–369. ISSN: 18790887. DOI: 10.1016/j.radonc.2017.05.003.
- [117] Luis A. Soto et al. “FLASH Irradiation Results in Reduced Severe Skin Toxicity Compared to Conventional-Dose-Rate Irradiation”. In: *Radiation Research* 194.6 (Aug. 2020), pp. 618–624. ISSN: 0033-7587. DOI: 10.1667/RADE-20-00090. URL: <https://bioone.org/journals/radiation-research/volume-194/issue-6/RADE-20-00090/FLASH-Irradiation-Results-in-Reduced-Severe-Skin-Toxicity-Compared-to/10.1667/RADE-20-00090.full>.
- [118] Karen Levy et al. “Abdominal FLASH irradiation reduces radiation-induced gastrointestinal toxicity for the treatment of ovarian cancer in mice”. In: *Scientific Reports* 10.1 (Dec. 2020). ISSN: 20452322. DOI: 10.1038/s41598-020-78017-7. URL: <https://pubmed.ncbi.nlm.nih.gov/33303827/>.
- [119] M. C. Vozenin, J. H. Hendry, and C. L. Limoli. “Biological Benefits of Ultra-high Dose Rate FLASH Radiotherapy: Sleeping Beauty Awoken”. In: *Clinical Oncology* 31.7 (July 2019), pp. 407–415. ISSN: 14332981. DOI: 10.1016/j.clon.2019.04.001.
- [120] Marie Catherine Vozenin et al. “The Advantage of FLASH Radiotherapy Confirmed in Mini-pig and Cat-cancer Patients”. In: *Clinical Cancer Research* 25.1 (Jan. 2019), pp. 35–42. ISSN: 15573265. DOI: 10.1158/1078-0432.CCR-17-3375. URL: <http://clincancerres.aacrjournals.org/>.
- [121] Jean Bourhis et al. “Treatment of a first patient with FLASH-radiotherapy”. In: *Radiotherapy and Oncology* 139 (Oct. 2019), pp. 18–22. ISSN: 18790887. DOI: 10.1016/j.radonc.2019.06.019.
- [122] Jeffrey C. Buchsbaum et al. *FLASH Radiation Therapy: New Technology Plus Biology Required*. July 2021. DOI: 10.1016/j.ijrobp.2021.01.053.
- [123] Joseph D. Wilson et al. “Ultra-High Dose Rate (FLASH) Radiotherapy: Silver Bullet or Fool’s Gold?” In: *Frontiers in Oncology* 9 (Jan. 2020), p. 1563. ISSN: 2234-943X. DOI: 10.3389/fonc.2019.01563. URL: <https://www.frontiersin.org/article/10.3389/fonc.2019.01563/full>.
- [124] Jeannette Jansen et al. “Does FLASH deplete oxygen? Experimental evaluation for photons, protons, and carbon ions”. In: *Medical Physics* 48.7 (July 2021), pp. 3982–3990. ISSN: 0094-2405. DOI: 10.1002/mp.14917. URL: <https://onlinelibrary.wiley.com/doi/10.1002/mp.14917>.
- [125] Daria Boscolo et al. “May oxygen depletion explain the FLASH effect? A chemical track structure analysis”. In: *Radiotherapy and Oncology* 162 (Sept. 2021), pp. 68–75. ISSN: 18790887. DOI: 10.1016/j.radonc.2021.06.031. URL: <https://doi.org/10.1016/j.radonc.2021.06.031>.
- [126] Binwei Lin et al. “FLASH Radiotherapy: History and Future”. In: *Frontiers in Oncology* 11 (May 2021), p. 1890. ISSN: 2234-943X. DOI: 10.3389/fonc.2021.644400. URL: <https://www.frontiersin.org/articles/10.3389/fonc.2021.644400/full>.
- [127] Ranald MacKay et al. *FLASH radiotherapy: Considerations for multibeam and hypofractionation dose delivery*. Nov. 2021. DOI: 10.1016/j.radonc.2021.09.011. URL: <https://doi.org/10.1016/j.radonc.2021.09.011>.

- [128] Nolan Esplen, Marc S. Mendonca, and Magdalena Bazalova-Carter. *Physics and biology of ultrahigh dose-rate (FLASH) radiotherapy: A topical review*. Nov. 2020. DOI: 10.1088/1361-6560/abaa28. URL: <https://doi.org/10.1088/1361-6560/abaa28>.
- [129] Pierre Montay-Gruel et al. “Hypofractionated FLASH-RT as an effective treatment against glioblastoma that reduces neurocognitive side effects in mice”. In: *Clinical Cancer Research* 27.3 (Feb. 2021), pp. 775–784. ISSN: 15573265. DOI: 10.1158/1078-0432.CCR-20-0894. URL: <http://clincancerres.aacrjournals.org/>.
- [130] Giuseppe Felici et al. “Transforming an IORT Linac Into a FLASH Research Machine: Procedure and Dosimetric Characterization”. In: *Frontiers in Physics* 8 (Sept. 2020), p. 374. ISSN: 2296-424X. DOI: 10.3389/fphy.2020.00374. URL: <https://www.frontiersin.org/article/10.3389/fphy.2020.00374/full>.
- [131] Pierre Montay-Gruel et al. “X-rays can trigger the FLASH effect: Ultra-high dose-rate synchrotron light source prevents normal brain injury after whole brain irradiation in mice”. In: *Radiotherapy and Oncology* 129.3 (Dec. 2018), pp. 582–588. ISSN: 18790887. DOI: 10.1016/j.radonc.2018.08.016. URL: <https://pubmed.ncbi.nlm.nih.gov/30177374/>.
- [132] Magdalena Bazalova-Carter and Nolan Esplen. “On the capabilities of conventional x-ray tubes to deliver ultra-high (FLASH) dose rates”. In: *Medical Physics* 46.12 (Dec. 2019), pp. 5690–5695. ISSN: 0094-2405. DOI: 10.1002/mp.13858. URL: <https://onlinelibrary.wiley.com/doi/10.1002/mp.13858>.
- [133] Simon Jolly et al. “Technical challenges for FLASH proton therapy”. In: *Physica Medica* 78 (Oct. 2020), pp. 71–82. ISSN: 11201797. DOI: 10.1016/j.ejmp.2020.08.005. URL: <https://linkinghub.elsevier.com/retrieve/pii/S1120179720301964>.
- [134] Patrik Gonçalves Jorge et al. “Dosimetric and preparation procedures for irradiating biological models with pulsed electron beam at ultra-high dose-rate”. In: *Radiotherapy and Oncology* 139 (Oct. 2019), pp. 34–39. ISSN: 18790887. DOI: 10.1016/j.radonc.2019.05.004. URL: <https://doi.org/10.1016/j.radonc.2019.05.004>.
- [135] Anna Subiel et al. “Challenges of dosimetry of ultra-short pulsed very high energy electron beams”. In: *Physica Medica* 42 (Oct. 2017), pp. 327–331. ISSN: 1724191X. DOI: 10.1016/j.ejmp.2017.04.029. URL: <http://dx.doi.org/10.1016/j.ejmp.2017.04.029>.
- [136] Thomas P. Wangler. *RF Linear Accelerators*. Wiley, Jan. 2008. ISBN: 9783527406807. DOI: 10.1002/9783527623426. URL: <https://onlinelibrary.wiley.com/doi/book/10.1002/9783527623426>.
- [137] Rob Appleby et al. *The Science and Technology of Particle Accelerators*. CRC Press, Dec. 2020. DOI: 10.1201/9781351007962. URL: <https://www.taylorfrancis.com/books/oa-mono/10.1201/9781351007962/science-technology-particle-accelerators-rob-appleby-graeme-burt-james-clarke-hywel-owen>.
- [138] J. Haimson. “Electron bunching in travelling wave linear accelerators”. In: *Nuclear Instruments and Methods* 39.1 (Jan. 1966), pp. 13–34. ISSN: 0029554X. DOI: 10.1016/0029-554X(66)90040-1.
- [139] S. G. Anderson et al. “Pulse compression via velocity bunching with the LLNL Thomson X-ray source photoinjector”. In: *Proceedings of the IEEE Particle Accelerator Conference*. Vol. 5. 2003, pp. 2957–2959. DOI: 10.1109/pac.2003.1289779.

- [140] L. Serafini. “Velocity bunching in photo-injectors”. In: *AIP Conference Proceedings*. Vol. 581. 1. AIP Publishing, Feb. 2001, pp. 87–106. DOI: 10.1063/1.1401564. URL: <http://aip.scitation.org/doi/abs/10.1063/1.1401564>.
- [141] Huang Rui-Xuan and Li Wei-Wei. “Velocity bunching in travelling wave accelerator with low acceleration gradient”. In: *Chinese Physics C* 38.5 (2014), p. 57004. DOI: 10.1088/1674-1137/38/5/057004.
- [142] M. Ferrario et al. “Experimental demonstration of emittance compensation with velocity bunching”. In: *Physical Review Letters* 104.5 (Feb. 2010), p. 054801. ISSN: 00319007. DOI: 10.1103/PHYSREVLETT.104.054801/FIGURES/5/MEDIUM. URL: <https://journals.aps.org/prl/abstract/10.1103/PhysRevLett.104.054801>.
- [143] J. S. Fraser et al. “High-brightness photoemitter injector for electron accelerators”. In: *IEEE Particle Accelerator Conference*, Vancouver, 1985. URL: <https://ui.adsabs.harvard.edu/abs/1985paac.confT...F/abstract>.
- [144] Richard L. Sheffield. “High-brightness electron injectors: A review”. In: *IEEE Particle Accelerator Conference*. Williamsburg, 1989. DOI: 10.1109/pac.1989.73365.
- [145] R Ganter. *SwissFEL Conceptual Design Report*. Tech. rep. 2012.
- [146] D Kayran et al. “First Test Results from SRF Photoinjector for the R&D ERL at BNL”. In: *Proceedings of the 5th International Particle Accelerator Conference*. Dresden, 2014. URL: [doi:10.18429/JACoW-IPAC2014-MOPRI064](https://doi.org/10.18429/JACoW-IPAC2014-MOPRI064).
- [147] Eric Chevallay et al. “PHIN photo-injector as the CLIC drive beamsource”. In: *J. Phys.: Conf. Ser.* Vol. 347. 2012, p. 12036. DOI: 10.1088/1742-6596/347/1/012036.
- [148] Lawrence Ives, Eric Montgomery, and Kevin Jensen. “High efficiency, long-life photocathodes”. In: *AIP Conference Proceedings 1812*. Vol. 1812. 2017. ISBN: 9780735414808. DOI: 10.1063/1.4975889. URL: <https://doi.org/10.1063/1.4975889>.
- [149] Andrew Burrill et al. “Multi-alkali photocathode development at brookhaven national lab for application in superconducting photoinjectors”. In: *Proceedings of the IEEE Particle Accelerator Conference*. Vol. 2005. 2005, pp. 2672–2674. ISBN: 0780388593. DOI: 10.1109/PAC.2005.1591224.
- [150] C Travier. “An introduction to photo-injector design”. In: *Nuclear Instruments and Methods in Physics Research Section A: Accelerators, Spectrometers, Detectors and Associated Equipment* 340(1) (Jan. 1993), pp. 26–39.
- [151] K Flöttmann. *Note on the thermal emittance of electrons emitted by cesium telluride photo cathodes*. Feb. 1997. URL: <https://cds.cern.ch/record/331841>.
- [152] Öznur Mete. “Study and Experimental Characterization of a Novel Photo Injector for the CLIC Drive Beam”. PhD thesis. Laussane: École Polytechnique Fédérale De Lausanne, 2011. DOI: 10.5075/EPFL-THESIS-5020. URL: <https://infoscience.epfl.ch/record/163549>.
- [153] Bruce E Carlsten. “Space-Charge Induced Emittance Compensation in High-Brightness Photoinjectors”. In: *articleAccelerators, Vol.49*. Vol. 49. 1995, pp. 27–65.
- [154] *CLEAR / CLEARLayout · GitLab*. URL: <https://gitlab.cern.ch/CLEAR/clearlayout>.
- [155] J. Brossard et al. “Construction of the probe beam photo-injector of CTF3”. In: *Proceedings of 10th European Particle Accelerator Conference (EPAC 06)*. Vol. 060626. Edingburgh, Scotland, 2006, pp. 828–830.

- [156] E Granados et al. *Capabilities and performance of the CLEAR facility photo-injector laser*. Tech. rep. Sept. 2019. URL: <https://cds.cern.ch/record/2705786>.
- [157] R. Belbéoch et al. *Rapport d'études sur le projet des linacs injecteur de LEP (LIL)*. 1982. URL: <https://cds.cern.ch/record/136636>.
- [158] D Blechschmidt and D J Warner. *Parameters of the LEP injector Linacs*. Feb. 1988. URL: <https://cds.cern.ch/record/2641876>.
- [159] F Dupont. "Status of the LEP e+- injector linacs". In: 1983. URL: <https://cds.cern.ch/record/156719>.
- [160] R. Belbeoch. *Pouvoir de résolution dans la mesure de la distribution longitudinale des paquets à la sortie du groupeur du linac pre-injecteur de LEP*. Tech. rep. Orsay: LAL PI 85-06/T, Apr. 1986.
- [161] Bruno Jean-Marie Cassany et al. *CLEAR photo*. Aug. 2019. URL: <http://cds.cern.ch/record/2687673>.
- [162] *High-precision current transformers and analog electronics*. URL: <https://www.bergoz.com/>.
- [163] Alban Mosnier et al. "The Probe Beam Linac in CTF3". In: *Proceedings of EPAC 2006, Edinburgh, Scotland*. 2006. URL: <https://cds.cern.ch/record/1078543?ln=en>.
- [164] Wilfrid Farabolini et al. "Video Profile Monitors Development for the CTF3 Probe Beam Linac". In: *Proceedings of EPAC08, Genoa, Italy*. 2008. URL: <http://cds.cern.ch/record/1183147>.
- [165] Carlos Eduardo Cocha Toapaxi. *Assessment performance and emittance measurements tests of Basler digital camera vs. the standard BTV system at CLEAR*. Tech. rep. Geneva: CERN, Aug. 2019. URL: <https://cds.cern.ch/record/2686221>.
- [166] Marek Gasior. "An Inductive Pick-Up for Beam Position and Current Measurements". In: *Dipac*. January 2003. 2003, pp. 53–55. URL: <http://accelconf.web.cern.ch/accelconf/d03/papers/CT01.pdf>.
- [167] A D'elia, R Fandos, and L Sjøby. *High-Bandwidth Wall Current Monitors*. Tech. rep. Nov. 2009. URL: <https://cds.cern.ch/record/1262855>.
- [168] R. Akre et al. "A transverse RF deflecting structure for bunch length and phase space diagnostics". In: *Proceedings of the IEEE Particle Accelerator Conference*. Vol. 3. 2001, pp. 2353–2355. DOI: 10.1109/pac.2001.987379.
- [169] Pasquale Arpaia et al. "Enhancing particle bunch-length measurements based on Radio Frequency Deflector by the use of focusing elements". In: *Scientific Reports* 10.1 (Dec. 2020), p. 11457. ISSN: 20452322. DOI: 10.1038/s41598-020-67997-1. URL: <https://doi.org/10.1038/s41598-020-67997-1>.
- [170] Luca Sabato et al. "A Measurement Method Based on RF Deflector for Particle Bunch Longitudinal Parameters in Linear Accelerators". In: *IEEE Transactions on Instrumentation and Measurement* 70 (2021). ISSN: 15579662. DOI: 10.1109/TIM.2020.3009342.
- [171] L. Garolfi et al. "Beam dynamics studies and instrumentation tests for bunch length measurements at CLEAR". In: *Proceedings of the 29th Linear Accelerator Conference, LINAC 2018* (2018), pp. 74–77. DOI: 10.18429/JACOW-LINAC2018-MOP0020.

- [172] Klaus Floettmann. *A Space Charge Tracking Algorithm*. Tech. rep. Hamburg: Desy, 2000. URL: <https://www.desy.de/~mpyflo/>.
- [173] S Lidia et al. “An Injector for the Proposed Berkley Ultrafast X-ray Light Source”. In: *Proceedings of the 2003 Particle Accelerator Conference*. Portland, 2003. URL: <https://accelconf.web.cern.ch/p03/PAPERS/WPAB021.PDF>.
- [174] J. P. Carneiro et al. “Transverse and longitudinal beam dynamics studies at the Fermilab photoinjector”. In: *Physical Review Special Topics - Accelerators and Beams* 8.4 (Apr. 2005), pp. 1–7. ISSN: 10984402. DOI: 10.1103/PHYSREVSTAB.8.040101/FIGURES/5/MEDIUM. URL: <https://journals.aps.org/prab/abstract/10.1103/PhysRevSTAB.8.040101>.
- [175] M. Hüning and H. Schlarb. “Measurement of the beam energy spread in the TTF photo-injector”. In: *Proceedings of the IEEE Particle Accelerator Conference 3* (2003), pp. 2074–2076. DOI: 10.1109/PAC.2003.1288783.
- [176] F. Zhou et al. “Commissioning of the SLAC Linac Coherent Light Source II electron source”. In: *Physical Review Accelerators and Beams* 24.7 (July 2021), p. 073401. ISSN: 24699888. DOI: 10.1103/PHYSREVACCELBEAMS.24.073401/FIGURES/14/MEDIUM. URL: <https://journals.aps.org/prab/abstract/10.1103/PhysRevAccelBeams.24.073401>.
- [177] *CLEAR / CLEARAstra · GitLab*. URL: <https://gitlab.cern.ch/CLEAR/CLEARAstra>.
- [178] E. Colby et al. “Design and construction of high brightness RF photoinjectors for TESLA”. In: *Proceedings of the IEEE Particle Accelerator Conference*. Vol. 2. IEEE, 1995, pp. 967–969. DOI: 10.1109/pac.1995.505097.
- [179] A Trisorio et al. “New Concept for the SwissFEL Gun Laser”. In: *Proceedings of FEL2013, New York, NY, USA*. 2013. ISBN: 9783954501267. URL: <https://accelconf.web.cern.ch/FEL2013/papers/tupso88.pdf>.
- [180] D. H. Dowell et al. “Measurement and analysis of field emission electrons in the LCLS gun”. In: *Proceedings of the IEEE Particle Accelerator Conference*. 2007, pp. 1299–1301. ISBN: 1424409179. DOI: 10.1109/PAC.2007.4441062.
- [181] A. Cianchi. “The status of the SPARC project”. In: World Scientific Pub Co Pte Lt, Apr. 2010, pp. 477–484. DOI: 10.1142/9789814307017{_}0044.
- [182] O. J. Luiten et al. “How to realize uniform three-dimensional ellipsoidal electron bunches”. In: *Physical Review Letters* 93.9 (Aug. 2004), p. 094802. ISSN: 00319007. DOI: 10.1103/PhysRevLett.93.094802.
- [183] Luca Serafini. “The short bunch blow-out regime in RF photoinjectors”. In: *AIP Conference Proceedings*. Vol. 413. 1. AIP Publishing, Dec. 1997, pp. 321–334. DOI: 10.1063/1.54425. URL: <http://aip.scitation.org/doi/abs/10.1063/1.54425>.
- [184] M Gross et al. “Emittance Reduction of RF Photoinjector Generated Electron Beams by Transverse Laser Beam Shaping”. In: (June 2019), pp. 1958–1960. DOI: 10.18429/JACoW-IPAC2019-TUPTS012. URL: <http://www.desy.de/~mpyflo/>.
- [185] Anders Kallner. “Formulas”. In: *Laboratory Statistics*. Elsevier, Jan. 2018, pp. 1–140. DOI: 10.1016/b978-0-12-814348-3.00001-0.

- [186] Peter H. Westfall. “Kurtosis as Peakedness, 1905–2014. R.I.P.” In: *The American Statistician* 68.3 (July 2014), pp. 191–195. ISSN: 0003-1305. DOI: 10.1080/00031305.2014.917055. URL: <http://www.tandfonline.com/doi/abs/10.1080/00031305.2014.917055>.
- [187] Andrea Latina. “RF-Track Reference Manual”. In: (June 2020). DOI: 10.5281/ZENODO.3887085. URL: <https://zenodo.org/record/3887085>.
- [188] A Latina. “Update of the Tracking Code RF-Track”. In: *Prodceedings of IPAC’21*. Campinas, SP, Brazil: JACOW Publishing, Geneva, Switzerland, Aug. 2021, pp. 4180–4182. ISBN: 9783954502141. DOI: 10.18429/JACoW-IPAC2021-THPAB203.
- [189] *Find minimum of unconstrained multivariable function using derivative-free method - MATLAB fminsearch*. URL: <https://www.mathworks.com/help/matlab/ref/fminsearch.html>.